RESONANT BRILLOUIN SCATTERING IN II-VI, III-V AND III-VI SEMICONDUCTORS

（II-VI, III-V および III-VI 族半導体における共鳴ブリルアン散乱に関する研究）

Sadao Adachi

Department of Electronics, Osaka University

March 1980

RESONANT BRILLOUIN SCATTERING IN II-VI, III-V AND III-VI SEMICONDUCTORS

Thesis

Submitted to the Faculty of Engineering

of

Osaka University

by

Sadao Adachi

In Partial Fulfillment of the Requirements

for

the Degree of Doctor of Engineering

March 1980

ACKNOWLEDGMENTS

The author would like to express his appreciation to Professor J. Nakai for stimulating and helpful advice, criticism and continual encouragement throughout the course of this work. He also wishes to acknowledge Associate Professor C. Hamaguchi for helpful discussions and encouragement. Special thanks are also due to Professor R. Bray of Purdue University, U.S.A., for valuable discussions throughout the course of this work.

He is indebted to Professor J. Koyama for continual encouragement and guidance throughout the graduate research. He thanks to Professors T. Hanawa, S. Nakamura, K. Ura and Y. Inuishi for critical reading of this thesis. He also wishes to thank Professors O. Kakusho, S. Kodama, Y. Matsuo, H. Ozaki and K. Terada for many helpful lectures and encouragement.

He is indebted to Dr. K. Ando of Nippon Telegraph and Telephone Public Corporation and M. Yamada of Kobe University for helpful discussions. He also would like to acknowledge helpful discussions with many members of the Semiconductor Research Group of Osaka University, in particular: Dr. T. Shirakawa, Dr. A. Moritani, Mr. K. Yamabe and Mr. M. Yokogawa.

He wishes to thank Professors M. Nakano and Y. Machi of Tokyo Electrical Engineering College for continual encouragement. He also wishes to acknowledge Dr. T. Taguchi for continual encouragement and helpful advices concerning crystal growth.

The financial support of the Japan Scholarship Foundation is greatly acknowledged.

The present work was supported in part by the Scientific Reserach Grant from the Ministry of Education, Japan.

TABLE OF CONTENTS

LIST OF TABLES

LIST OF FIGURES

Figure Page

Figure Page

Figure Page

Figure Page

Figure | Page

ABSTRACT

RESONANT BRILLOUIN SCATTERING IN II-VI, III-V AND III-VI SEMICONDUCTORS

by

Sadao Adachi

The present work deals with investigations of resonant Brillouin scattering in II-VI, III-V and III-VI semiconducting compounds by making use of the acoustoelectrically amplified phonon domain. This domain is formed in the piezoelectric semiconductor CdS upon the application of high electric fields, and propagates with the velocity of sound in the carrier drift direction. The intense phonon domains generated in CdS produce strong Brillouin-scattering signals with a reasonable S/N ratio and thus enable us the use of a non-coherent light source instead of a laser. This technique also enables us to discuss accurate resonance behaviors in a region close to the fundamental absorption edge of the semiconductors. In order to obtain the intense phonon domains in the weak piezoelectric semiconductors such as ZnSe, ZnTe, GaP, GaSe and GaS, we have used the amplified acoustical-domain injection method in which the

phonon domain excited in CdS is injected into the other end-bonded semiconductors through the thin indium layer with a high transmission efficiency. A series of experiments have been performed to establish the Brillouin-scattering mechanism in (a) the direct-gap, II-VI semiconductors ZnSe, ZnTe, $Zn_xCd_{1-x}Te$ and CdS, (b) the indirect-gap, III-V semiconductor GaP, and (c) the layer-type (indirect-gap), III-VI semiconductors GaSe and GaS.

The spectral dependence of the Brillouin-scattering cross sections in the II-VI semiconductors has shown resonant enhancement and cancellation in the region near the fundamental absorption edge, and new maxima have also been found in the dispersion curves very close to the ground-state exciton-energy regions. The Brillouin-scattering cross section is found to depend strongly on the lifetime-broadening effect of the intermediate electronic states near the resonance region. The spectral dependence of the Brillouin-scattering cross sections has shown a good agreement with the theoretical analysis based upon Loudon's light-scattering theory, assuming the virtual Wannier-Mott exciton transition, when the lifetime-broadening effect is taken into account.

The resonance data of Brillouin scattering have also been analyzed with a theoretical description based on the quasi-static approximation. This analysis indicates that for the allowed-scattering configuration the Brillouin-scattering efficiency can be predicted by the first derivative of the dielectric constant with respect to the incident-photon energy. The theoretical calculation has been performed by numerically differentiating the experimental data of the dielectric constant. The resonance behaviors of the Brillouin-scattering cross sections have been well interpreted by the quasi-static approximation when the nondispersive contribution is properly taken into account. Resonant forbidden Brillouin scattering by

the slow-TA phonon domain in CdS has been observed near the fundamental absorption edge. The data are in good agreement with a dielectric theory based on the second derivative of the dielectric constant with respect to the incident-photon energy. Although mechanism of the forbidden scattering observed here has not yet been completely explained, it may be pointed out that the strong longitudinal electric field associated with the piezo-electrically active slow-TA phonon domain is one of the causes.

In order to investigate some of the lifetime-broadening effects on the spectral dependence of the Brillouin-scattering cross sections, we have used two kinds of ZnTe and ZnSe single crystals and made the Brillouin-scattering measurements at room temperature and low temperature (77 K). It has been found that the lifetime-broadening energy does not depend strongly on the temperatures but on the kinds of the crystals. The lifetime-broadening energy of the high-quality ZnTe (ZnSe) determined from the Brillouin-scattering measurements is Γ = 26 meV (44 meV) at 77 K, which is very large compared with the value of $\Gamma \simeq 2$ meV (3 meV) obtained from reflectance spectrum. The results are interpreted in terms that the lifetime broadening is caused mainly by an interaction of the intermediate electronic states with the high-intensity phonon domains and the crystalline imperfections.

From a macroscopical point of view, the Brillouin-scattering cross section is proportional to the square of the corresponding photoelastic constant which can be obtained independently from the piezobirefringence experiment. The dispersion curves of the photoelastic constants, $p_{11} - p_{12}$ and p_{44} for ZnSe and ZnTe and p_{66} $[\frac{1}{2}(p_{11} - p_{12})]$, p_{44} and p_{31} for CdS, have been determined from the present data by introducing the piezo-birefringence analysis, where the lifetime-broadening effect is also taken into consideration as in the case of the Brillouin-scattering analysis.

In addition, we have reported a new method to analyze the piezobirefringence coefficient in an opaque region in which the stress-induced changes in both the real ($\Delta\varepsilon_1$) and imaginary part ($\Delta\varepsilon_2$) of the dielectric constant are properly taken into account. New coefficients, which determine the fractional contributions of $\Delta\varepsilon_1$ and $\Delta\varepsilon_2$ to the piezobirefringence coefficient, have been derived from an analytical point of view. The experimental data on Si [Chandrasekhar *et al.*] and ZnSe [present work] have been analyzed by using the present model. Good agreement between the experiment and calculation has been found. The present method provides a guiding principle for analyzing the piezobirefringence coefficient in an opaque region.

It is shown that the Brillouin-scattering efficiency is expressed by the first derivative of the dielectric constant with respect to the incident-light wavelength (or equivalently to the band-gap energy) which is the same as the expression for the first-derivative modulation spectroscopy. A detailed discussion is given on resonant Brillouin scattering in connection with the first-derivative modulation spectroscopy such as thermoreflectance, piezoreflectance and wavelength-modulation spectroscopy. A comparison of the Brillouin-scattering efficiencies derived experimentally with the first-derivative modulation spectra shows that they agree quite well with each other and also with the theoretical curves of the Brillouin-scattering efficiency when the lifetime broadening is taken into account in the Brillouin-scattering analysis.

Resonant Brillouin scattering in the indirect-gap, III-V semiconductor GaP by the TA phonons has been studied at room temperature in the region of the indirect absorption edge by making use of the acoustical-domain injection method. The spectral dependence of the Brillouin-scattering cross sections has shown a monotonic decrease (resonant cancellation) as the incident-photon

energy extends beyond the indirect-energy gap. The experimental dispersion curves have been well interpreted by a theoretical model of the indirect-gap resonance including an additional dielectric theory of the direct-gap resonance. The spectral dependence of the photoelastic constants, $|p_{11} - p_{12}|$ and $|p_{44}|$, has also been determined as a by-product of the Brillouin-scattering data.

Resonant Brillouin scattering in the layer-type (indirect-gap), III-VI semiconductors GaSe and GaS by the pure-TA phonon domains has been investigated at room temperature by making use of the acoustical-domain injection method. The measured spectral dependence of the Brillouin-scattering cross sections has shown resonant cancellation for both GaSe and GaS in the region of the fundamental absorption edges. The experimental data have shown a good agreement with the theoretical analyses based on the quasi-static approximation and Loudon's light-scattering theory. The resonant cancellation has been successfully interpreted by taking into account the direct-gap and indirect-gap resonance processes for GaSe and GaS, respectively. It has also been found that the Brillouin-scattering efficiency depends strongly on the lifetime-broadening effect of the intermediate-electronic states, as similar to the case for the direct-gap, II-VI semiconductros. Moreover, such analyses have clearly indicated that the nonresonant electronic transition is dominant in the Brillouin-scattering process even in the region near the fundamental absorption edge.

CHAPTER I

INTRODUCTION

Inelastic light scattering, namely Brillouin and Raman scattering, is a long-established phenomenon. Following the appearance of Maxwell's equation, Rayleigh[1] calculated in 1899 the scattering of light produced by a dielectric sphere with dimensions small compared to the wavelength of light and obtained the celebrated result that the intensity of the scattering varies as the reciprocal fourth power of the wavelength of exciting light (λ^4-law). In 1922, Brillouin[2] presented the foundations of the inelastic-light-scattering process by long-wavelength elastic sound waves. He predicted a Doppler shift of the light scattered by the elastic sound waves with a doublet called a Brillouin doublet at the light frequencies $\nu_0 \pm \Delta\nu$, where (θ: scattering angle)

$$\frac{\Delta\nu}{\nu_0} = 2n \frac{v}{c} \sin(\frac{\theta}{2}) \qquad ,$$

and where ν_0 is the frequency of the incident light wave, n is the refractive index of the medium, v is the sound velocity and c is the velocity of light in vacuum. In 1923, Smekal[3] developed the theory of light scattering by a system with two quantized energy levels. His theory contained the essential characteristics of the phenomena discovered by Raman[4] and, independently, by Landsberg and Mandelstam[5] in 1928.

The line width and frequency shift of the Brillouin doublets can provide

the lifetime and velocity of the scattering sound waves, respectively. The Brillouin doublets were first found experimentally by Gross[6] in 1930 and later confirmed by Meyer and Ramm[7] in 1932. The method of experimentation had become particularly useful since the advent of lasers in 1960 whose high spectral purity, coherence, collimation, power and directivity make them ideal light sources in light-scattering experiments. Such advantages of the laser, thus, quickly made the old mercury arcs obsolete as sources for light-scattering spectroscopy.

A large part of the research effort in light scattering was devoted to the study of excitations in fluids until about 1940. In the 1940's emphasis shifted to systematic investigations of single crystals in order to obtain information for the semi-empirical treatment of their crystal dynamics. Recently, a large part of the research effort in Brillouin and Raman scattering has also been devoted to the study of the properties of the low-frequency elementary excitations of solids.[8] A large group of crystal elementary excitations have been observed by such light-scattering spectroscopy. This group includes acoustical and optical phonons, surface and bulk polaritons, plasmons, magnons as well as electronic and vibrational excitations of isolated ions in crystals. More recently, considerable theoretical and experimental interest has been focused on resonant light scattering. Resonant light scattering has been found to be intimately related to the optical spectra of the crystal.

The resonant-Raman measurement has first been performed by Leite and Porto[9] in 1966 for CdS using the discrete lines of Ar^+ laser which cover the photon-energy range between 2.38 and 2.73 eV. Later, in 1970, Ralston *et al.*[10] have confirmed the resonance behavior in CdS and also established the existence of an antiresonance of the Raman-scattering cross sections for TO phonons immediately below the fundamental absorption edge. Such a structure is now understood as a cancellation between the contributions of the band edge and of higher

transitions; these contributions must thus have opposite signs. The recent availability of cw dye lasers has given considerable impetus to study of resonant Raman scattering, and as a matter of fact a lot of experiments on resonant Raman scattering have been performed up to date in various semiconductors.[8]

The resonant-Brillouin measurement, on the other hand, has first been performed by Pine[11] in 1972 for CdS from thermal phonons using a high-resolution Fabry-Perot interferometer. The resonance condition has been achieved by thermally tuning the fundamental absorption edge of this material through the incident radiation at 514.5 nm. The experimental Brillouin-scattering intensity has shown resonant enhancement near the intrinsic absorption edge and found to be roughly proportional to the square of the absorption coefficient, while a cancellation as observed in resonant Raman scattering has not been found.

The interaction of phonons with free carriers in semiconductors are the subject of many Brillouin-scattering studies. Hutson, McFee and White[12] and Hutson and White[13,14] have demonstrated that in piezoelectric semiconductors acoustical waves could be amplified by carriers with drift velocity exceeding the sound velocity. When the high drift fields are applied to piezoelectric semiconductors, the intense packets of acoustical waves (domains) are observed to travel along the sample at the sound velocity. These acoustical domains consist of amplified thermal phonons in a narrow band of frequency range between 0.1 and 6.0 GHz, and have an energy density a factor of the order of 10^9 above the thermal equilibrium value. Zucker and Zemon[15] have been first to examine the spectrum of these domains in CdS by means of Brillouin-scattering technique. Many subsequent Brillouin-scattering studies have been performed to study the generation and amplification mechanisms and dynamical characteristics of the acoustoelectrical domains in various piezoelectric semiconductors such as GaAs[16,17], CdS[18,19] and ZnO[20,21], and revealed that the domain-frequency

distribution in these materials initially peaks and downshifts as the domain propagates through the sample probably due to an anharmonic parametric conversion.[22-24]

Brillouin-scattering intensity is expected to be resonantly enhanced when the incident or scattered light approaches the electriionic transitions in the medium. Resonant Brillouin scattering by the acoustoelectrical domains has first been reported in GaAs by Garrod and Bray[25] in 1972. Thermal Brillouin scattering is much weaker, so laser sources are generally used with interferometric spectral analysis. They have used a particularly simple, but versatile, apparatus, because the intense acoustoelectrical domains provide strong Brillouin-scattering signals with a reasonable S/N ratio and permit the use of a conventional light source instead of a laser. They have found clear resonant enhancement and cancellation of the Brillouin-scattering cross sections in the region near the fundamental absorption edge. Subsequently, similar resonance behaviors have been observed in CdS from the acoustoelectrical domains by Hamaguchi and coworkers[26,27] and, independently, by Gelbart and Many.[28] Resonant Brillouin scattering has also been performed from the acoustoelectrical domains in CdS and ZnO by Berkowicz and Price[29] and Berkowicz and Skettrup[30] and in CdSe by Yamamoto *et al.*[31] The experimental data have also clearly shown resonant enhancement and cancellation in the region near the fundamental absorption edges. Such studies are restricted to piezoelectric semiconductors in which the acoustoelectrical instability can occur by the application of a high electric field and as a result produce the traveling acoustoelectrical domains consisting of piezoelectrically active transeverse-acoustical phonons (T2-mode phonons).

The overall objective of the present work is to analyze the resonant-Brillouin-scattering mechanisms in various semiconductors such as II-VI (ZnSe, ZnTe, $Zn_xCd_{1-x}Te$), III-V (GaP) and III-VI compounds (GaSe and GaS). Our first

objective is, thus, to measure accurately the spectral dependence of the Brillouin-scattering cross sections in such semiconductors. In order to do this, we make use of the acoustoelectrical domains instead of thermal phonons. This permits us the use of a conventional light source, *e.g.* xenon flash tube, instead of a laser and, thus, enable us to obtain the accurate experimental data.[27] The CdS single crystal is known to have the wurtzite-type crystal structure and to be strong piezoelectric semiconductor. The acoustoelectrical domains themselves were investigated in detail by many workers.[32] It is necessary to develop new technique for measuring resonant Brillouin scattering in non-piezoelectric or weak piezoelectric semiconductors such as ZnSe, ZnTe, GaP, GaSe and GaS. We introduce an acoustical-domain injection method[33,34] developed recently in our laboratory. This method enables us to inject the intense acoustoelectrical domains amplified in CdS into the other end-bonded semiconductors (ZnSe, ZnTe, etc.) through the thin indium layer with a high transmission efficiency.

In Chapter II, we review the resonant-light-scattering theories derived from microscopical and phenomenological aspects and indicate how it should be applied within the context of our experiments. Loudon[35,36] has first obtained the quantum-mechanical expression for resonant light scattering based on the 3rd-order time-dependent perturbations, where the intermediate electronic excitations of the crystal involved in the calculation are assumed to be free electron-hole pair states. The expression for the case in which the intermediate electronic states are Wannier-Mott excitons has been given by Ganguly and Birman.[37] Benedek and Fritsch[38] have constructed the Brillouin-scattering theory from phenomenological aspect. This theory predicts the intensity, polarization and spectral distribution of the scattered light as a function of the incident and scattered directions in the crystal. Based on these theories, we obtain the Brillouin-scattering cross sections for each

acoustical-mode phonon (i.e., transverse- and longitudinal-mode phonons) in the zincblende-type (ZnSe, ZnTe, etc.) and wurtzite-type crystal (CdS). We also calculate the matrix elements of the deformation-potential scattering for both types of crystals and discuss the intermediate-electronic-transition processes which play an important role in the resonant-Brillouin-scattering process. From a macroscopical point of view,[38] the Brillouin-scattering cross section is proportional to the square of the photoelastic constant which can be obtained independently from the piezobirefringence experiment. In order to determine the photoelastic constant from the Brillouin-scattering data (Chapter VI), we also present here the outline of the intrinsic-piezobirefringence theory.

Chapter III deals with the sample constraction, experimental procedure and methodology. Brillouin scattering from acoustoelectrically or piezoelectrically driven sound waves is easily observed using conventional light sources, and the angular dependence establishes either the sound velocity or frequency if one is known. Apparatus of this kind has first been used by Garrod and Bray[25] to study resonant Brillouin scattering in GaAs by the acoustoelectrical domains. In this Chapter, we also review the theory of acoustoelectrical amplification and obtain the relation between the incident and scattering angles for the sake of the Brillouin-scattering measurements. The theoretical analysis and application of the acoustical-domain injection method are also presented in this Chapter.

In Chapter IV, we present the experimental data of resonant Brillouin scattering in II-VI semiconductors ZnSe, ZnTe, $Zn_xCd_{1-x}Te$ and CdS. For the zincblende-type crystals such as ZnSe, ZnTe and $Zn_xCd_{1-x}Te$, the Brillouin-scattering measurements are performed by the T1- (slow TA) and T2-mode (fast TA) acoustical phonons using the acoustical-domain injection method. For the wurtzite-type, piezoelectric semiconductor CdS, we perform the Brillouin-scattering measurements by using the acoustoelectrically amplified T2-mode

(slow TA) phonon domains. When the traveling domain reaches the anode end of the specimen, part of the acoustical flux is reflected. It is well known[16,29] that the reflection is usually accompanied by mode conversion. The piezoelectrically inacitive pure-transverse TA phonon (T1-mode phonon) and pure-longitudinal PL phonon domains can be obtained by the mode conversion upon partial reflection of the T2-mode domains at the anode-end surface.[39,40] Thus, we also perform the Brillouin-scattering measurements in CdS by using these mode-converted phonon domains. The experimental data are compared with the theoretical prediction based upon Loudon's light-scattering theory assuming the free electron-hole pairs or Wannier-Mott excitons as the intermediate electronic states.

The qualitative features of resonant light scattering can be predicted from an expression based on the quasi-static approximation.[41] In this approximation, the phonons are assumed to act through the electron-phonon interactions like static perturbations of the electronic band structure of the crystal, which cause a change in the dielectric constant ε of the crystal. The dielectric theory of resonant light scattering shows that for the allowed scattering the two-band term of the first-order scattering efficiency (Brillouin or Raman tensor) is proportional to the first derivative of ε with respect to the incident-photon energy while for the forbidden scattering proportional to the second derivative of ε with respect to the incident-photon energy. In Chapter V, we discuss resonant Brillouin scattering in more detail from a view point of the quasi-static approximation. The resonance data presented in Chapter IV are reanalyzed by the quasi-static approximation. The resonance forbidden data observed in CdS are alos presented and analyzed in this Chapter. In order to obtain theoretical predictions, we calculate the derivative of ε with respect to the photon energy by numerical differentiation of the experimental optical constants. A comparison of theoretical curves between the quasi-static

approximation and Loudon's light-scattering theory are also made in this Chapter.

Chapter VI deals with the determination of the photoelastic constants in II-VI semiconductors ZnSe, ZnTe and CdS from the the Brillouin-scattering data. The Brillouin-scattering cross section is known to be proportional to the square of the corresponding photoelastic constant.[38] This constant can be obtained independently from the stress-induced birefringence (piezobirefringence) measurements. The investigation of the piezobirefringence in solids is an old topic of crystal optics.[42] We obtain the microscopical expression of the photoelastic constants and compare it with the experimental data. We also discuss the lifetime-broadening effect of the electronic states on the spectral dependence of the photoelastic constants. We report a new method to analyze the piezobirefringence coefficient in an opaque region in which the stress-induced changes in both the real ($\Delta\varepsilon_1$) and imaginary part ($\Delta\varepsilon_2$) of the dielectric constant are properly taken into account. New coefficients, which determine the fractional contributions of $\Delta\varepsilon_1$ and $\Delta\varepsilon_2$ to the piezobirefringence coefficient, are derived from an analytical point of view. This method provides a guiding principle for analyzing the piezobirefringence coefficient in an opaque region.

In Chapter VII, we report on a detailed study of the lifetime-broadening effect of the intermediate electronic states on resonant Brillouin scattering in ZnTe and ZnSe. In order to investigate some temperature effects on the lifetime broadening, we measure resonant Brillouin scattering at room temperature and low temperature (77 K). Moreover, we use two kinds of ZnTe and ZnSe single crystals to study some effects of the crystalline imperfections on the spectral dependence of the Brillouin-scattering cross sections. We show that the lifetime-broadening energy does not depend strongly on the temperature but on the kinds of the crystals.

In Chapter VIII, a discussion is given on resonant Brillouin scattering

in connection with the first-derivative modulation spectroscopy such as thermoreflectance, piezoreflectance and wavelength-derivative modulation spectroscopy. It is shown that the Brillouin-scattering efficiency is expressed by the first derivative of the dielectric constant with respect to the incident-light wavelength or equivalently to the band-gap energy, which is the same as the expression for the first-derivative modulation spectroscopy.[43,44] The light-scattering experiment yields more information than its conventional modulation counterpart. A measurement of the spectral dependence of the scattering efficiency yields the energies of critical points in a manner similar to more conventional modulation experiments. The spectrometer trace in which the scattered signal appears also yields the frequency of the corresponding excitation, without counterpart in the conventional modulation experiment. An absolute scattering intensity yields the tensorial constants, *e.g.*, deformation potential, which represent the interaction of the elementary excitation with the electronic transitions. In this Chapter, a detailed survey is given of a relation between the expressions for resonant Brillouin scattering based upon Loudon's light-scattering theory and the quasi-static approximation and also of a comparison of them with the first-derivative modulation spectroscopy. We try to make a comparison of the Brillouin-scattering efficiencies derived experimentally with the first-derivative modulation spectra obtained in some semiconductors.

Chapter IX deals with the resonance phenomena of the Brillouin-scattering cross sections in the III-V semiconductor GaP by the transverse-acoustical phonons in the region of the indirect-energy gap by making use of the acoustical-domain injection method. The GaP crystal is a more suitable material to study some of the indirect-gap resonance behaviors, since the energy separation between the indirect and direct gaps in this material is relatively large (the lowest indirect-gap energy is about 0.5 eV lower than the lowest direct-

gap one).[45] If this separation is small, the indirect-gap resonance should be masked off by the much stronger direct-gap one. We formulate a theory of resonant Brillouin scattering at the indrirect gap of semiconductors and compare it with the experimental data. It has been shown by Dixon[46] that the GaP crystal is exceptionally good material for use in light deflectors and modulators. In this Chapter, we also determine the spectral dependence of the photoelastic constants, $|p_{11} - p_{12}|$ and $|p_{44}|$, as a by-product of the Brillouin-scattering data.

In Chapter X, we present the experimental data of resonant Brillouin scattering in III-VI semiconductors GaSe and GaS obtained by making use of the acoustical-domain injection method. These semiconductors are layer-type compounds which present a strong anisotropic behavior of their physical properties due to the singularity of the crystal structures and have an indirect gap below the lowest direct gap.[47] The top of its valence band lies at Γ point and the bottom of the conduction band at M point. Relative minima of the conduction band at Γ point are situated a few tens of meV for GaSe and about 0.4 eV for GaS above the minima at M point. The experimental data are compared with the theoretical predictions based on the quasi-static approximation and Loudon's light-scattering theory including the indirect- and direct-gap resonances. The resonance processes are determined by the aid of group theory. The nonresonant electronic transitions are also found to be dominant in the Brillouin-scattering process.

Finally, in Chapter XI, the conclusions obtained in the present work are summarized.

In Appendix, we present the methodology and growth technique of the traveling heater method (THM) which is used in the present work to obtain high-quality ZnTe and $Zn_xCd_{1-x}Te$ single crystals.

CHAPTER II

THEORETICAL BACKGROUND

2.1 INTRODUCTION

A common feature of theoretical expressions for the Brillouin-scattering efficiency of a substance is the presence of terms which either diverge or become relatively large when the frequency of the exciting radiation is equal to an allowed optical-transition frequency of the substance. This predicted increase in the intensity of the scattered light, known as the resonant-Brillouin effect, is very familiar in the realm of Brillouin scattering from fluids. The quantum-mechanical expression of the first-order Brillouin and Raman scattering in solids has first been obtained by Loudon.[35] It has been pointed out that the most important Brillouin (Raman) scattering mechanism is always one in which the radiation interacts indirectly with the lattice *via* the free electron-hole pairs, where the electron-lattice interaction is treated by the deformation-potential approximation. The form of the first- and second-order Brillouin-scattering efficiency for the case in which the intermediate electron-hole pair states are Wannier-Mott excitons has been given by Ganguly and Birman.[37] Martin[48] has also treated the first-order Raman effect including the excitonic interaction in the hydrogenic approximation *via* numerical calculations by use of the Green's-function formulation. It has been found that the excitonic interaction may increase the strength of the Brillouin (Raman) scattering resonances compared with the free electron-hole pair model

proposed by Loudon[35] without greatly altering the resonance shape.

It can be easily understood from a macroscopical point of view[41] that the light-scattering phenomenon results from a change in the dielectric constant of a crystal arising from thermal vibrations of the constitutional lattices. This treatment is known to as dielectric theory of light scattering (quasi-static approximation). In the quasi-static approximation, the phonons are assumed to act (through the electron-phonon interactions) like static perturbations of the electronic band structure of the crystal, which causes a change in the dielectric constant of the crystal. The quasi-static approximation shows that the first-order scattering efficiency is proportional to the first derivative of the dielectric constant with respect to the incident-photon energy. The experimental Raman-scattering data in some semiconductors have recently been well interpreted in terms of this theoretical model.[49-61]

From a phenomenological point of view, the Brillouin-scattering cross section is proportional to the square of the photoelastic (elasto-optic) constant which can be obtained independently from the intrinsic piezobirefringence experiment. Benedek and Fritsch[38] have first obtained an accurate expression of Brillouin scattering in cubic crystals by incorporating the photoelastic constants. Such an analysis has been extended to the case of anisotropic media by Nelson *et al.*[62] and Hamaguchi[63] by taking into account the birefringence and internal reflection. Loudon[35] has also derived microscopical expressions for the photoelastic constants as by-products of his calculation of the first-order Brillouin effect.

In Section 2.2, we present the quantum-mechanical expression of resonant Brillouin scattering obtained from 3rd-order time-dependent perturbation calculations. The 3rd-order perturbation mechanism is known to be correspond to the case for the first-order direct-gap resonance process. The indirect-gap resonance process, on the other hand, can be interpreted by a 5th-order

perturbation mechanism. Details of the indirect-gap resonance process will be discussed elsewhere (Chapter IX). Section 2.2 also presents the selection roles of deformation-potential scattering (Section 2.2.2) and the macroscopical expressions of resonant Brillouin scattering based upon Benedek-Fritsch's theory (Section 2.2.3). In Section 2.3, we present the generalized expression of the photoelastic constant derived from the intrinsic biezobirefringence theory.[64] We will determine in Chapter VI the spectral dependence of the photoelastic constants in various semiconductors from the Brillouin-scattering data by introducing the piezobirefringence analysis.

2.2 RESONANT BRILLOUIN SCATTERING

2.2.1 Time-Dependent Perturbation Calculation

The collective excitations of semiconductors and insulators which participate in inelastic light scattering are lattice vibrations (acoustical and optical phonons) and plasma waves (plasmons) of the electron-gas of small-gap or doped semiconductors. They also include coupled photon-electronic excitation modes (polaritons) and coupled phonon-plasmon modes. In this subsection, we shall discuss first-order Brillouin-scattering process involving the acoustical phonons as elementary excitations.

The perturbation picture of the first-order Brillouin-scattering process is indicated in Fig. 2-1 (a) and consists of:

i) transmission of the incident photon ω_i into the crystal,

ii) annihilation of the photon with creation of an electron-hole pair (*via* H_{ER}),

iii) scattering of the electron-hole pair accompanied by creation (Stokes) or annihilation (anti-Stokes) of a phonon (*via* H_{EL}),

iv) annihilation of the scattered electron-hole pair and creation of the

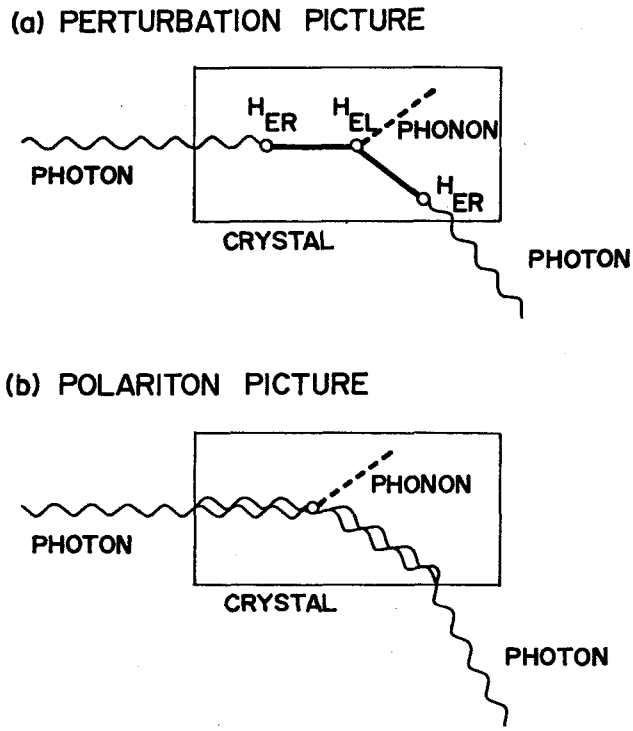

FIG. 2-1. Perturbation theory and polariton pictures of one-phonon Brillouin scattering. Single wavy lines: photons; double wavy lines: polaritons; straight solid lines: excitons; dashed lines: phonons.

scattered photon ω_s (*via* H_{ER}),

v) transmission of the photon ω_s out of the crystal.

When the incident-photon energy approaches the exciton resonance, we have to take into account the excitonic polariton states in the Brillouin-scattering process.[65] This polariton picture of the first-order Brillouin-scattering process is indicated in Fig. 2-1 (b). Brenig, Zeyher and Birman[66] have reported a theoretical analysis of resonant Brillouin scattering in crystals exhibiting spatial dispersion which included excitonic polaritons as the intermediate states in the Brillouin-scattering process. Their result predicts a multiplet of the Brillouin spectrum near the exciton resonance with line separations and efficiencies, depending strongly on the incident-photon energy because of the polariton dispersion. In the following, we consider the first-order Brillouin-scattering process and that the virtual intermediate state is assumed to be Wannier-Mott exciton,[37] and the polariton picture is not introduced in the calculations for simplicity. We perform a canonical transformation[67] to remove the lowest-order interaction terms in the Hamiltonian.

Let $H^{(0)}$ denotes the unperturbed Hamiltonian; then it can be written as

$$H^{(0)} = H_e + H_L + H_R \tag{2.1}$$

with

$$H_e = \sum_{\lambda K} E_{\lambda K} a^{\dagger}_{\lambda K} a_{\lambda K} \tag{2.2}$$

$$H_L = \sum_{\eta\xi} \hbar\omega_{\eta\xi} b^{\dagger}_{\eta\xi} b_{\eta\xi} \tag{2.3}$$

$$H_R = \sum_{\chi e} \hbar\omega_{\chi} c^{\dagger}_{\chi e} c_{\chi e} \quad , \quad \omega_{\chi} = (c/n)|\chi| \quad . \tag{2.4}$$

Here, $a^{\dagger}_{\lambda K}$ and $a_{\lambda K}$ are the creation-annihilation operators for the excitons having inner quantum-number λ and wave vector $\vec{K}$ formed from conduction c and valence band v, and $E_{\lambda K}$ denotes the exciton energy. $b^{\dagger}_{\eta\xi}$ and $b_{\eta\xi}$ are the creation-annihilation operators for the phonons having an energy quantum $\hbar\omega_{\eta\xi}$, where

$\vec{\eta}$ and $\vec{\xi}$ stand for the wave vector and unit polarization vector, respectively, and the system considered here is that a crystal has two ions per unit cell of mass M_1 and M_2. $c^{\dagger}_{\chi e}$ and $c_{\chi e}$ are the creation-annihilation operators for the photons having an energy momentum $\hbar\omega_{\chi}$, where $\vec{\chi}$ and $\vec{e}$ stand for the wave vector and unit polarization vector, respectively, c is the velocity of light in vacuum, and n is the refractive index. The commutation relations for the creation-annihilation operators are

$$[a_{\lambda K}(c,v),\ a^{\dagger}_{\lambda',K'}(c',v')] = \delta_{\lambda\lambda'}\delta_{KK'}\delta_{cc'}\delta_{vv'}, \tag{2.5a}$$

$$[b_{\eta\xi},\ b^{\dagger}_{\eta',\xi'}] = \delta_{\eta\eta'}\ \xi\xi', \tag{2.5b}$$

$$[c_{\chi e},\ c^{\dagger}_{\chi',e'}] = \delta_{\chi\chi'}\delta_{ee'}, \tag{2.5c}$$

Note that $a_{\lambda K}$ and $a^{\dagger}_{\lambda K}$ satisfy approximately the commutation relations for bosons, but this is immaterial as far as we confine ourselves to the electronic states in which the total number of excitons is zero or unity.

Next, we consider the perturbation Hamiltonians for the exciton-radiation (H_{eR}) and exciton−phonon (H_{eL}) interactions, as are depicted in Fig. 2-1 (a). The perturbed Hamiltonian terms can be given by

$$H^{(1)} = H^{(1)}_{eL} + H^{(1)}_{eR} \quad , \tag{2.6a}$$

$$H^{(2)} = H^{(2)}_{eL_{(1)}} + H^{(2)}_{eL_{(2)}} + H^{(2)}_{eR} \tag{2.6b}$$

The specific forms of the interaction terms are given as follows:

$$H^{(1)}_{eR} = \sum_{cv\lambda K\chi} \{f_{\chi e}(cv\lambda K)a^{\dagger}_{\lambda K}(c,v)c_{\chi e}\delta_{K,\chi} + f^{*}_{\chi e}(cv\lambda K)a_{\lambda K}(c,v)c_{\chi e}\delta_{K,-\chi}\} + \text{c.c.}, \tag{2.7a}$$

$$H^{(2)}_{eR} = \sum_{\substack{cv\lambda K\\ c'v'\lambda'K'\\ \chi e}} \{F_{\chi e}(cv\lambda K,c'v'\lambda'K')a^{\dagger}_{\lambda K}(c,v)a_{\lambda',K'}(c',v')c_{\chi e}\delta_{K-K',\chi}$$

$$+ F^{*}_{\chi e}(cv\lambda K,c'v'\lambda'K')a_{\lambda K}(c,v)a^{\dagger}_{\lambda',K'}(c',v')c_{\chi e}\delta_{K-K',-\chi}\} + \text{c.c.}, \quad (2.7b)$$

and

$$H^{(1)}_{eL} = \sum_{\substack{cv\lambda K\\ \eta\xi}} \{g_{\eta\xi}(cv\ K)a^{\dagger}_{\lambda K}(c,v)b^{\dagger}_{\eta\xi}\delta_{K.-\eta} + g^{*}_{\eta\xi}(cv\lambda K)a_{\lambda K}(c,v)b^{\dagger}_{\eta\xi}\delta_{K,\eta}\} \quad , \quad (2.8a)$$

$$H^{(2)}_{eL_{(1)}} = \sum_{\substack{cv\lambda K\\ c'v'\lambda'K'\\ \eta\xi}} G_{\eta\xi}(cv\lambda K,c'v'\lambda'K')a^{\dagger}_{\lambda K}(c,v)a_{\lambda',K'}(c',v')b^{\dagger}_{\eta\xi}\delta_{K-K',-\eta} \quad (2.8b)$$

$$H^{(2)}_{eL_{(2)}} = \sum_{\substack{cv\lambda K\\ \eta\xi\eta'\xi'}} \{d_{\eta\xi,\eta'\xi'}(cv\lambda K)a^{\dagger}_{\lambda K}(c,v)b^{\dagger}_{\eta\xi}b^{\dagger}_{\eta'\xi'}\delta_{K,-(\eta+\eta')}$$

$$+ d^{*}_{\eta\xi,\eta'\xi'}(cv\lambda K)a_{\lambda K}(c,v)b^{\dagger}_{\eta\xi}b^{\dagger}_{\eta'\xi'}\delta_{K,\eta+\eta'}\} \quad , \quad (2.8c)$$

where $f_{\chi e}$, $f^{*}_{\chi e}$, $F_{\chi e}$, $F^{*}_{\chi e}$, $g_{\eta\xi}$, $g^{*}_{\eta\xi}$, $G_{\eta\xi}$, $G^{*}_{\eta\xi}$, $d_{\eta\xi,\eta'\xi'}$, and $d^{*}_{\eta\xi,\eta'\xi'}$, are coupling parameters. The coupling parameters of Eqs. (2.7) and (2.8) contain the momentum matrix elements and the matrix elements of deformation-potential scattering, respectively. The matrix elements of deformation-potential scattering will be calculated in detail in Section 2.2.3. The perturbation terms (2.8a) and (2.8b) will give Stokes process. To get anti-Stokes, we have to include terms with the annihilation operator of the phonons "$b_{\eta\xi}$" in H_{eL} instead of the creation operator $b^{\dagger}_{\eta\xi}$.

We shall perform a canonical transformation to remove the lowest-order interaction terms in the Hamiltonian. The transformation is generally given by[67]

$$\tilde{Q} = e^{-S} Q\, e^{S} \quad , \quad (2.9)$$

where Q being any operator. The unitary transformation is the special case where $S^{\dagger} = -S$. Then, it is readily shown that

$$\tilde{Q} = Q + \sum_{n=1}^{\infty} \frac{[S_n, Q]}{n!} \quad , \tag{2.10}$$

where S_n is defined by the recurrence relation

$$S_n = [S, [S_{n-1}, Q]] \quad (S_1 = S) \quad . \tag{2.11}$$

The total Hamiltonian is taken from Eqs. (2.1) and (2.6) as

$$\mathcal{H} = \mathcal{H}^{(0)} + \mathcal{H}^{(1)} + \mathcal{H}^{(2)} \quad . \tag{2.12}$$

The transformated Hamiltonian $\tilde{\mathcal{H}}$ is, thus,

$$\begin{aligned} \tilde{\mathcal{H}} &= e^{-iS} \mathcal{H} \, e^{iS} \\ &= \mathcal{H} - i[S, \mathcal{H}] - \frac{1}{2}[S, [S, \mathcal{H}]] + \frac{i}{6}[S[S, [S, \mathcal{H}]]] + \cdots \, , \end{aligned} \tag{2.13}$$

where S is chosen such that

$$i[S, \mathcal{H}^{(0)}] = \mathcal{H}^{(1)} \quad . \tag{2.14}$$

Then

$$\begin{aligned} \tilde{\mathcal{H}} = {} & \mathcal{H}^{(0)} + \mathcal{H}^{(2)}_{eL_{(1)}} + \mathcal{H}^{(2)}_{eL_{(2)}} + \mathcal{H}^{(2)}_{eR} - \frac{i}{2}[S, \mathcal{H}^{(1)}] - i[S, \mathcal{H}^{(2)}_{eL_{(1)}} + \mathcal{H}^{(2)}_{eR}] \\ & - i[S, \mathcal{H}^{(2)}_{eL_{(2)}}] - \frac{1}{3}[S, [S, \mathcal{H}^{(1)}]] - \frac{1}{2}[S, [S, \mathcal{H}^{(2)}_{eL_{(1)}} + \mathcal{H}^{(2)}_{eR}]] \\ & - \frac{1}{2}[S, [S, \mathcal{H}^{(2)}_{eL_{(2)}}]] + \cdots \quad . \end{aligned} \tag{2.15}$$

If the eigenstates of $\mathcal{H}^{(0)}$ are represented by $|m\rangle$, etc, it is obvious from Eq.(2.14) that

$$\begin{aligned} i\langle m|[S, \mathcal{H}^{(0)}]|n\rangle &= i\langle m|S\mathcal{H}^{(0)} - \mathcal{H}^{(0)}S|n\rangle \\ &= i\{\langle m|S|n\rangle\langle n|\mathcal{H}^{(0)}|n\rangle - \langle m|\mathcal{H}^{(0)}|m\rangle\langle m|S|n\rangle\} \end{aligned}$$

$$= i\langle m|S|n\rangle(E_n - E_m)$$

$$= \langle m|H^{(1)}|n\rangle \quad , \tag{2.16}$$

where

$$E_m = \langle m|H^{(0)}|m\rangle \quad , \tag{2.17a}$$

$$E_n = \langle n|H^{(0)}|n\rangle \quad . \tag{2.17b}$$

Therefore, it is obvious that

$$\langle m|S|n\rangle = \frac{1}{i}\,\frac{\langle m|H^{(1)}|n\rangle}{E_n - E_m} \quad . \tag{2.18}$$

Using Eqs. (2.6a) and (2.18), we obtain

$$S = \frac{1}{i}\,(Q + Q' + P + P') \quad , \tag{2.19}$$

where

$$Q = -\sum_{\substack{cv\lambda K\\ \chi e}} \frac{f_{\chi e}(cv\lambda K)a^{\dagger}_{\lambda K}(c,v)c_{\chi e}}{E_{\lambda K} - \hbar\omega_{\chi e}}\,\delta_{K,\chi} + \text{c.c.}, \tag{2.20a}$$

$$Q' = \sum_{\substack{cv\lambda K\\ \chi e}} \frac{f^{*}_{\chi e}(cv\lambda K)a_{\lambda K}(c,v)c_{\chi e}}{E_{\lambda K} - \hbar\omega_{\chi e}}\,\delta_{K,-\chi} - \text{c.c.}, \tag{2.20b}$$

$$P = -\sum_{\substack{cv\lambda K\\ \eta\xi}} \frac{g_{\eta\xi}(cv\lambda K)a^{\dagger}_{\lambda K}(c,v)b^{\dagger}_{\eta\xi}}{E_{\lambda K} - \hbar\omega_{\eta\xi}}\,\delta_{K,-\eta} \quad , \tag{2.20c}$$

$$P' = \sum_{\substack{cv\lambda K\\ \eta\xi}} \frac{g^{*}_{\eta\xi}(cv\lambda K)a_{\lambda K}(c,v)b^{\dagger}_{\eta\xi}}{E_{\lambda K} - \hbar\omega_{\eta\xi}}\,\delta_{K,\eta} \quad . \tag{2.20d}$$

It can be found from Eq. (2.15) that $-\frac{1}{2}[S, [S, H^{(2)}_{eL_{(1)}} + H^{(2)}_{eR}]]$ is the lowest-order commutator that contributes to the first-order Brillouin-scattering effect. This commutator can be written as

$$-\frac{1}{2}[S, [S, H^{(2)}_{eL_{(1)}} + H^{(2)}_{eR}]] = \frac{1}{2}[Q + Q' + P + P', [Q + Q' + P + P', H^{(2)}_{eL_{(1)}} + H^{(2)}_{eR}]]$$

$$= \frac{1}{2}\{[(Q + Q' + P + P')(Q + Q' + P + P')(H^{(2)}_{eL_{(1)}} + H^{(2)}_{eR})$$

$$- (Q + Q' + P + P')(H^{(2)}_{eL_{(1)}} + H^{(2)}_{eR})(Q + Q' + P + P')]$$

$$- (Q + Q' + P + P')(H^{(2)}_{eL_{(1)}} + H^{(2)}_{eR})(Q + Q' + P + P')$$

$$+ (H^{(2)}_{eL_{(1)}} + H^{(2)}_{eR})(Q + Q' + P + P')(Q + Q' + P + P')\} . \qquad (2.21)$$

To select terms that contribute to the first-order Brillouin-scattering process from Eq. (2.21), we have to take into account the following conditions:

i) we reject process that contain $a_{\lambda K}|0>$ (because $a_{\lambda K}|0> = 0$),

ii) processes must return to the electronic ground state,

iii) processes must involve two photons and one phonon.

Thus, we obtain six terms $Q'H^{(2)}_{eR}P$, $Q'H^{(2)}_{eL_{(1)}}Q'$, $QH^{(2)}_{eR}P$, $QH^{(2)}_{eL_{(1)}}Q$, $P'H^{(2)}_{eR}Q'$ and $P'H^{(2)}_{eR}Q$ corresponding to the various time orderings of the absorption of the incident photon, the emission of the phonon and the emission of the scattered photon accompanied by three virtual excitonic transitions. Figure 2-2 shows the Feynman diagrams which describe the 3rd-order perturbation calculation of first-order Brillouin scattering by lattice vibrations involving intermediate exciton states; (a) $Q'H^{(2)}_{eR}P$, (b) $Q'H^{(2)}_{eR}Q'$, (c) $QH^{(2)}_{eR}P$, (d) $QH^{(2)}_{eL_{(1)}}Q$, (e) $P'H^{(2)}_{eR}Q'$ and (f) $P'H^{(2)}_{eR}Q$.

2.2.2 Brillouin-Scattering Cross Section

Suppose that one photon ω_i has been destroyed, and a photon ω_s and phonon ω_q have been created is given by [Fig. 2-2][35]

$$W = \frac{2\pi}{h^2} \sum_{\eta\chi} |<f|(Q'H^{(2)}_{eR}P + Q'H^{(2)}_{eL_{(1)}}Q' + QH^{(2)}_{eR}P + QH^{(2)}_{eL_{(1)}}Q + P'H^{(2)}_{eR}Q'$$

$$+ P'H^{(2)}_{eR}Q)|i>|^2 \cdot \delta(\omega_i - \omega_s - \omega_q)$$

$$= \frac{(2\pi)^3 a}{V} \sum_{\eta\chi} | R_{is}(-\omega_i, \omega_s, \omega_q) |^2 \cdot \delta(\chi_i - \chi_s - \eta)\delta(\omega_i - \omega_s - \omega_q) , \qquad (2.22)$$

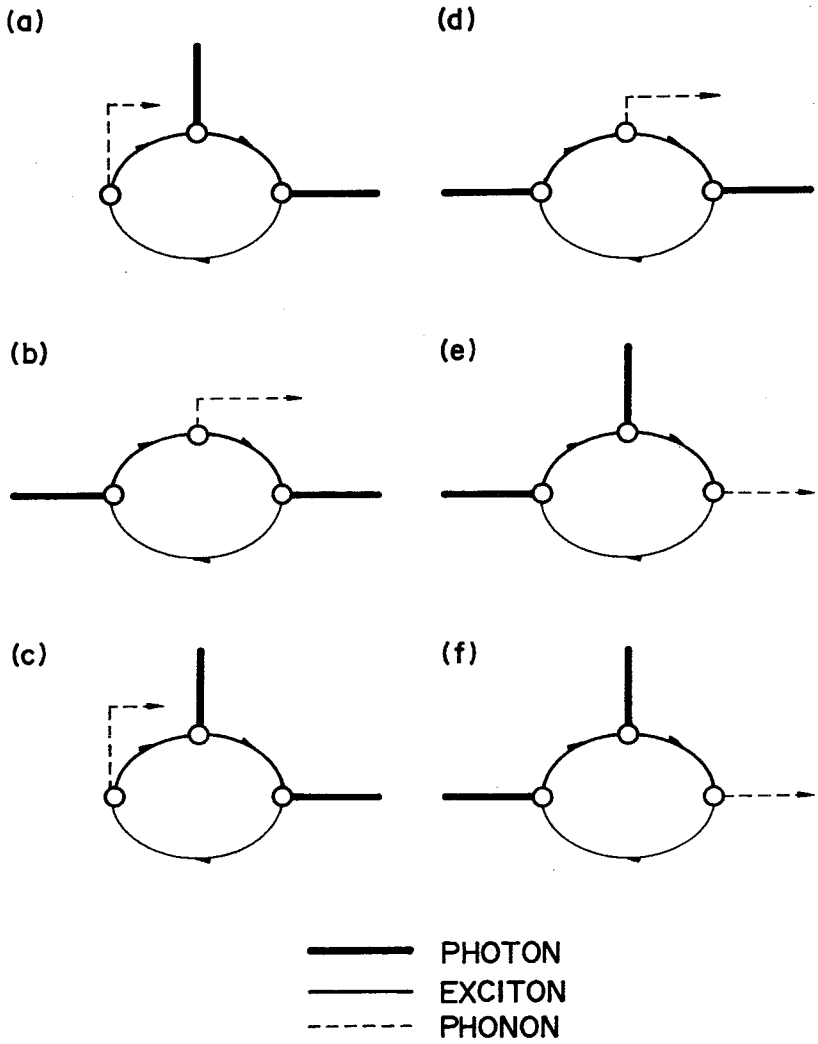

FIG. 2-2. Diagrams of six possible orderings of the interactions contributing to the first-order Brillouin-scattering process.

where $|i\rangle$ and $|f\rangle$ are the initial and final states of the system, respectively, **a** is a constant containing various physical parameters, and V is the crystal volume. R_{is} is the frequency-dependent Brillouin tensor. This tensor is represented by considering six terms of the first-order Brillouin-scattering process $Q'H_{eR}^{(2)}P$, etc., as follows:

$$R_{is}(-\omega_i, \omega_s, \omega_q) = \frac{1}{V}\sum_{\alpha,\beta}\Big[\frac{P^s_{0\beta}\Xi_{\beta\alpha}P^i_{\alpha 0}}{(\omega_\beta + \omega_s + \omega_q)(\omega_\alpha + \omega_s)} + \frac{P^s_{0\beta}\Xi_{\beta\alpha}P^i_{\alpha 0}}{(\omega_\beta - \omega_i + \omega_q)(\omega_\alpha - \omega_i)}$$

$$+ \frac{P^s_{0\beta}P^i_{\beta\alpha}\Xi_{\alpha 0}}{(\omega_\beta + \omega_s + \omega_q)(\omega_\alpha + \omega_q)} + \frac{P^s_{0\beta}P^i_{\beta\alpha}\Xi_{\alpha 0}}{(\omega_\beta - \omega_i + \omega_q)(\omega_\alpha + \omega_q)}$$

$$+ \frac{\Xi_{0\beta}P^s_{\beta\alpha}P^i_{\alpha 0}}{(\omega_\beta + \omega_s - \omega_i)(\omega_\alpha + \omega_s)} + \frac{\Xi_{0\beta}P^s_{\beta\alpha}P^i_{\alpha 0}}{(\omega_\beta + \omega_s - \omega_i)(\omega_\alpha - \omega_i)}\Big] , \tag{2.23}$$

where P and Ξ are the momentum matrix element and the matrix element of deformation-potential scattering, respectively, the subscript 0 indicates the electronic ground state and the subscripts α and β the intermediate electronic states, and $\hbar\omega_\alpha$ and $\hbar\omega_\beta$ are the optical energy gaps for the incident and scattered lights, respectively. The superscripts i and s of P indicate the components in the polarization directions of incident and scattered lights, respectively.

One can easily find that the second term on the right-hand side of Eq. (2.23) has the strongest divergence when $\hbar\omega_i$ is close to the band-gap energy $\hbar\omega_\alpha$, i.e., the second term is the most importance in the first-order Brillouin-scattering process. Thus, we now write the Brillouin tensor in the following form:

$$R_{is}(-\omega_i, \omega_s, \omega_q) \simeq \frac{1}{V}\sum_{\alpha,\beta}\frac{P^s_{0\beta}\Xi_{\beta\alpha}P^i_{\alpha 0}}{(\omega_\beta - \omega_i + \omega_q)(\omega_\alpha - \omega_i)} \quad . \tag{2.24}$$

The electronic transitions involved in the calculation of the Brillouin-scattering process may be conveniently described by a diagram of the type shown in Fig. 2-3 (a). The time order of the three electronic transitions shown in the figure is

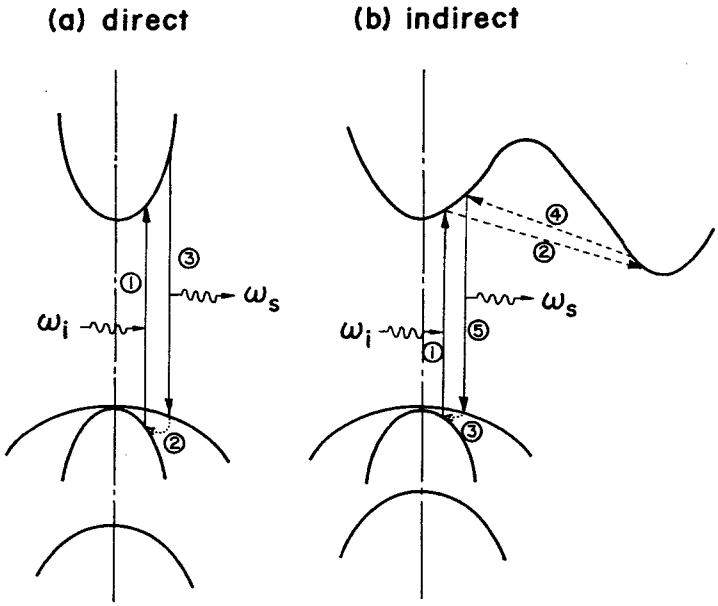

FIG. 2-3. Schematic diagrams of (a) direct-gap and (b) indirect-gap first-order Brillouin-scattering processes. ω_i and ω_s are the angular frequencies of the incident and scattered lights, respectively The numbers indicate the order of the electronic transitions.

the same as that for the case of Eq. (2.24). Similar diagram can be drawn for Brillouin scattering involving indirect-gap resonance process [see Fig. 2-3 (b)]. This type of process may be interpreted by the 5th-order perturbation calculation. One of the time orders of the electronic transitions is also shown in Fig. 2-3 (b) by the numbers [see Chapter IX].

The Brillouin-scattering cross section derived by Loudon has the following form:

$$\sigma_B = \left(\frac{e}{\hbar mc}\right)^4 \frac{\Phi}{2\rho v^2} \frac{\omega_s}{\omega_i} \left| R_{is}(-\omega_i, \omega_s, \omega_q) \right|^2 \quad , \qquad (2.25)$$

where ρ is the density of crystal, v is the sound velocity, and Φ and ω_q are the energy density and angular frequency of the acoustical phonons, respectively. The energy density Φ can be replaced by $k_B T$ in the case of Brillouin scattering by thermal phonons, where k_B is the Boltzman constant and T is the absolute temperature.

Let us now assume that the virtual intermediate electronic states are free electron-hole pairs. It is usually a good approximation to assume that the band edge in semiconductors is parabolic (spherical) in $\vec{k}$-space, i.e.,

$$\omega_\alpha(\vec{k}) = \omega_{g\alpha}(0) + \hbar k^2/2\mu \quad , \qquad (2.26a)$$

$$\omega_\beta(\vec{k}) = \omega_{g\beta}(0) + \hbar k^2/2\mu \quad , \qquad (2.26b)$$

where μ is the reduced effective mass being given by $\mu^{-1} = m_e^{*-1} + m_h^{*-1}$, and is assumed to be equal for the $|\alpha\rangle$ and $|\beta\rangle$ pair states for simplicity. Then, with the prescription

$$\frac{1}{V}\sum_k \longrightarrow \frac{2}{(2\pi)^2}\int_0^{k_m} k^2 dk \quad , \qquad (2.27)$$

Eq. (2.24) can be written as

$$R_{is} = \frac{2}{(2\pi)^2} P^s_{0\beta} \Xi_{\beta\alpha} P^i_{\alpha 0} \int_0^{k_m} \frac{k^2 dk}{(\omega_{g\beta} + \frac{\hbar k^2}{2\mu} - \omega_i + \omega_q)(\omega_{g\alpha} + \frac{\hbar k^2}{2\mu} - \omega_i)} , \quad (2.28)$$

where the P- and Ξ-matrix elements are assumed to be independent of k. Performing the integration, we finally obtain the expression of R_{is} in the case where the intermediate electronic states are assumed to be the free electron-hole pairs as[27]

$$R_{is} = \frac{2}{(2\pi)^2} \sum_{\alpha,\beta} \left(\frac{2\mu}{\hbar} \right)^{3/2} \frac{P^s_{0\beta} \Xi_{\beta\alpha} P^i_{\alpha 0}}{\omega_{g\beta} - \omega_{g\alpha} + \omega_q} \left[(\omega_{g\beta} - \omega_s)^{\frac{1}{2}} \tan^{-1}\left(\frac{\Delta\omega_{g\beta}}{\omega_{g\beta} - \omega_s} \right)^{\frac{1}{2}} \right.$$

$$\left. - (\omega_{g\alpha} - \omega_i)^{\frac{1}{2}} \tan^{-1}\left(\frac{\Delta\omega_{g\alpha}}{\omega_{g\alpha} - \omega_i} \right)^{\frac{1}{2}} \right] , \quad (2.29)$$

where $\hbar\Delta\omega_{g\alpha}$ and $\hbar\Delta\omega_{g\beta}$ are the combined widths of the conduction and valence bands, which are given by

$$\Delta\omega_{g\alpha} = \Delta\omega_{g\beta} = \hbar k_m^2/2\mu \quad . \quad (2.30)$$

The conservation of energy in the Brillouin-scattering process can be written as

$$\omega_i - \omega_s = \pm \omega_q \quad . \quad (2.31)$$

The plus and minus signs correspond to the Stokes and anti-Stokes processes, respectively. In Eq. (2.29), we used the condition of the Stokes process by replacing $\omega_i - \omega_q$ by ω_s.

Next, we obtain R_{is} assuming that the virtual intermediate electronic states are the Wannier-Mott exciton states.[37] The phenomenon of the excitons in crystals has been a subject of considerable interest for many years and has been summarized in general by Knox,[68] and in particular with respect to the group II-VI compounds

by Reynolds *et al.*[69] It can be considered that the excitonic transitions play an important role in the Brillouin-scattering process, because the Coulomb interaction is always present between the electrons and holes. The exciton state is expanded in terms of the Bloch functions for the perfect periodic lattice. The wave function of the exciton will be a linear combination of conduction- (ψ_{c,k_e}) and valence-band wave function (ψ_{v,k_h}). Since the electron-hole interaction is weak (Wannier-Mott exciton), only the lowest conduction band and highest valence band need be included in the expansion of the eigenstate Ψ, so that

$$\Psi(\vec{r}_e,\vec{r}_h) = \sum_{k_e,k_h} C(\vec{k}_e,\vec{k}_h)\psi^*_{c,k_e}(\vec{r}_e)\psi_{v,k_h}(\vec{r}_h) \quad . \tag{2.32}$$

Only small ranges of $\vec{k}$ about the two extrema contribute appreciably to the sum. Periodicity requires that the exciton wave vector $\vec{K}$ is a good quantum number and that

$$\vec{K} = \vec{k}_e + \vec{k}_h \quad . \tag{2.33}$$

The Fourier transform of $C(\vec{k}_e,\vec{k}_h)$ may be written as

$$\Phi_{K,n}(\vec{R},\vec{r}) = (BN)^{-\frac{1}{2}} \exp\,(i\vec{K}\vec{R})\ \phi_n(\vec{r}) \quad , \tag{2.34}$$

where B is the volume of a unit cell, N is the number of such cells in the crystal, and $\vec{R}$ and $\vec{r}$ are the center-of-mass coordinate and relative position, respectively, being given by

$$\vec{R} = (m^*_e\vec{r}_e + m^*_h\vec{r}_h)(m^*_e + m^*_h)^{-1}, \qquad \vec{r} = \vec{r}_e - \vec{r}_h \quad . \tag{2.35}$$

Equation (2.34) represents the wave function of the exciton's over-all motion in the crystal. The effective-mass approximation gives Eq. (2.34) as a solution of the Schrödinger-like equation,

$$[H_e(\vec{p} + \tfrac{1}{2}\vec{P} - \vec{p}_e) + H_h(-\vec{p} + \tfrac{1}{2}\vec{P} - \vec{p}_h) - \frac{e^2}{\varepsilon|\vec{r}|}\ ]\ \Phi = E\ \Phi \quad , \tag{2.36}$$

where $\vec{p}$, $\vec{P}$ are the momenta conjugate to $\vec{r}$, $\vec{R}$; and $\vec{p}_e$, $\vec{p}_h$ are $\hbar$ times $\vec{k}_e$, $\vec{k}_h$ (wave vectors at the band extrema). ε is the dielectric constant. E and Φ can be found by solving this equation. The energy of the exciton state is given by

$$E_{ex} = E_g + E \quad , \tag{2.37}$$

where

$$E_g = E_c(\vec{k}=0) - E_v(\vec{k}=0) \tag{2.38}$$

is the band-gap energy at $\vec{k} = 0$. The two-particle wave equation, Eq. (2.36), can be expressed as a sum of two separate terms if it is written in a coordinate system of the center-of-mass coordinate $\vec{R}$ (translational part) and the electron-hole separation coordinate $\vec{r}$ (rotational part). The translational part can be written as

$$-\frac{\hbar^2}{2M}\nabla_R{}^2\Phi_R(\vec{R}) = E_K\Phi_R(\vec{R}) \quad , \tag{2.39}$$

which describes just the motion of a free particle with a mass

$$M = m_e^* + m_h^* \quad . \tag{2.40}$$

This equation gives that

$$E_K = \hbar^2K^2/2M \quad , \qquad K = |\vec{K}| \ , \tag{2.41}$$

and

$$\Phi_R(\vec{R}) = \exp\ (i\vec{K}\vec{R}) \quad . \tag{2.42}$$

The rotational part, on the other hand, can be written as

$$[-\ (\frac{\hbar^2}{2\mu})\ \nabla_r{}^2 - \frac{e^2}{\varepsilon|\vec{r}|}\ ]\ \phi_n(\vec{r}) = E_n\phi_n(\vec{r}) \quad . \tag{2.43}$$

Equation (2.43) is similar to that for the hydrogenic problem, but with the electron charge replaced by $e/\sqrt{\varepsilon}$ and the free electron mass m replaced by the reduced exciton mass μ. Consequently, the eigen values of Eq. (2.43) can

be given as an analogy of the hydrogenic problem as

$$E_n = -\frac{G}{n^2} \quad , \qquad n = 1, 2, \cdots \quad , \tag{2.44}$$

where G is the exciton Rydberg (binding) energy given by

$$G = \frac{\mu e^4}{2\hbar^2\varepsilon^2} = 13.6 \left(\frac{\mu}{m_0}\right) \frac{1}{\varepsilon^2} \quad [\text{eV}] \quad . \tag{2.45}$$

The exciton Bohr radius is now given by

$$a_0^* = \frac{\hbar^2\varepsilon}{\mu e^2} = 0.53\, \varepsilon \left(\frac{m_0}{\mu}\right) \quad [\text{Å}] \quad . \tag{2.46}$$

The eigenvalue of Eq. (2.36) is, thus,

$$E = E_K + E_n = \frac{\hbar^2 K^2}{2M} - \frac{G}{n^2} \quad . \tag{2.47}$$

The exciton state can, thus, be written from Eq. (2.37) as

$$E^D_{exn} = E_g + \frac{\hbar^2 K^2}{2M} - \frac{G}{n^2} \quad . \tag{2.48}$$

It is clear from Eq. (2.43) that $\phi_n(\vec{r})$ is a hydrogenic wave function with substituted for m_0 (electron mass) and ε for ε_0 (dielectric constant of vacuum). Since $\phi_n(\vec{r})$ is a smooth function extending over a large region of the solid, it is usually called "envelope function". Because $\phi_n(\vec{r})$ describes the rotational motion of the exciton, it is characterized by three quantum numbers n (principal quantum number), l (azimuthal quantum number) and m (magnetic quantum number). However, it has been shown by Elliott[70] that only the s-rotational state (l = 0) is important for the optically created excitons. It is, therefore, sufficient for us to label the envelope function only with one quantum number n. For the simple case of two spherical bands of masses m_e^* and m_h^*, the envelope function of the n-th exciton state $\phi_n(0)$ can now be written as

$$|\phi_n(0)|^2 = \frac{V_0}{\pi a_0^{*3} n^3} = |\phi_1(0)|^2 \frac{1}{n^3} \quad , \tag{2.49}$$

where V_0 is the volume of the unit cell. A discrete series of lines, therefore, can be predicted at energy

$$E_{ex}^n = E_g + \frac{\hbar^2 K^2}{2M} - \frac{G}{n^2} \quad , \tag{2.50}$$

with intensity falling like n^{-3}. As the absorption edge is approached, the infinite number of lines will overlap so that it may be considered as a contunuum. In the true continuum where $h\nu - E_g > 0$, one obtains for the envelope function of the continuum exciton

$$|\phi_k(0)|^2 = \frac{\pi\alpha e^{\pi\alpha}}{N \sinh(\pi\alpha)} \quad , \tag{2.51}$$

where

$$\alpha = |G/(\hbar^2 k^2/2\mu)|^{\frac{1}{2}} \tag{2.52}$$

The continuum-exciton state corresponds to positive energy solutions of the hydrogen-like equation (2.43). The energy of the continuum-exciton states may be written as

$$E_{ex}^k = E_g + \frac{\hbar^2 K^2}{2M} + \frac{\hbar^2 k^2}{2\mu} \tag{2.53}$$

In the continuum, the rotational energy is much larger than the Coulomb interaction energy, and therefore the excitons behave like free particles with an effective mass μ. The exciton spectrum, thus, consists of a series of discrete parabolic bands below E_g at $\vec{K} = 0$, which merges into a continuum at higher energies, as is depicted in Fig. 2-4.

The Brillouin tensor R_{is} in the case where the intermediate electronic states are assumed to be the Wannier exciton states becomes, using Eqs. (2.24), (2.49) — (2.53),

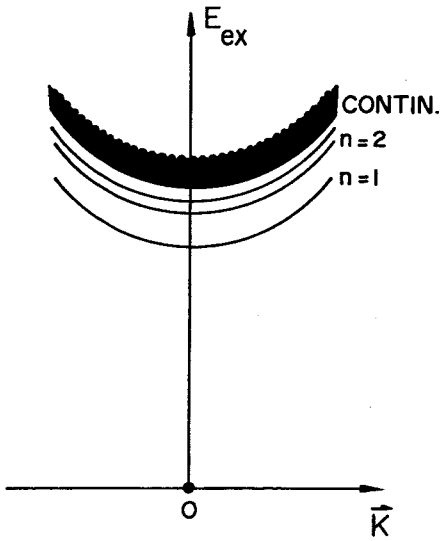

FIG. 2-4. Energy of the exciton bands for the Wannier-Mott excitons as a function of exciton momentum $\vec{k}$. The discrete "hydrogenic" states merge into the continuum states for $E > E_g$. The point 0 represents the energy of the unexcited crystal.

$$R_{is} = \sum_{\alpha,\beta} P^{s}_{0\beta}\Xi_{\beta\alpha}P^{i}_{\alpha 0}\left\{\frac{N}{V}\sum_{n}\frac{|\phi_n(0)|^2}{(\omega_{g\beta} - R^*/n^2 - \omega_s)(\omega_{g\alpha} - R^*/n^2 - \omega_i)}\right.$$

$$\left. + \frac{2}{(2\pi)^2}\int k^2 dk \frac{|\phi_k(0)|^2}{(\omega_{g\beta} + \frac{\hbar k^2}{2\mu} - \omega_s)(\omega_{g\alpha} + \frac{\hbar k^2}{2\mu} - \omega_i)}\right\}, \qquad (2.54)$$

where $\omega_{g\alpha} = E_{g\alpha}/\hbar$ and $\omega_{g\beta} = E_{g\alpha}/\hbar$, $R^* = G/\hbar$, and we have converted the summation of k for the continuum-exciton states into an integral using Eq. (2.27). Performing the integration, we finally obtain[71]

$$R_{is} = \sum_{\alpha,\beta}\frac{P^{s}_{0\beta}\Xi_{\beta\alpha}P^{i}_{\alpha 0}}{\omega_{g\beta} - \omega_{g\alpha} + \omega_q}\left\{\frac{1}{\pi a_0^{*3}}\sum_{n}\left(\frac{1}{\omega_{g\alpha}-R^*/n^2-\omega_i-i\Gamma_n^{\alpha D}/2\hbar} - \frac{1}{\omega_{g\beta}-R^*/n^2-\omega_s-i\Gamma_n^{\beta D}/2\hbar}\right)\right.$$

$$+ \frac{i}{4\pi}\left(\frac{2\mu}{\hbar}\right)^{3/2}(4\pi^2R^*)^{1/2}\left(\left[1 - \exp-\left(-\frac{4\pi^2R^*}{\omega_{g\alpha}-\omega_i-i\Gamma^{\alpha C}/2\hbar}\right)^{1/2}\right]^{-1}\right.$$

$$\left.\left. - \left[1 - \exp-\left(-\frac{4\pi^2R^*}{\omega_{g\beta}-\omega_s-i\Gamma^{\beta C}/2\hbar}\right)^{1/2}\right]^{-1}\right)\right\}. \qquad (2.55)$$

In the calculation, we have assumed that $[1 - \exp(-2\pi\alpha)]$ has no poles and the integration has been carried out by using the residue theorem. The first and second terms in the right-hand side of Eq. (2.55) correspond to the n-th discrete-exciton and unbound continuum-exciton contributions, respectively. It is well known that the excitonic transitions play a momentous role in the optical properties such as emission and absorption of photons in the band-edge region. They are affected strongly by a damping effect, i.e., a lifetime broadening. Such a damping effect has been introduced in Eq. (2.55) in a

phenomenological manner by replacing ω by $\omega + i\Gamma/2\hbar$, where $\Gamma_n^{\alpha D}$ and $\Gamma^{\alpha C}$ are the damping energies in the electronic state $|\alpha\rangle$ for the n-th discrete- and continuum-exciton states, respectively.

Figure 2-5 shows a typical example of the calculated line shapes of R_{is} [Eq. (2.55)] based on the simple two-band model ($\omega_{g\alpha} = \omega_{g\beta}$) with four different damping parameters, $\Gamma = 0$, $0.02E_g$, $0.04E_g$ and $0.06E_g$,[39] where we have made the following assumption in the calculations:

$$\Gamma = \Gamma_n^D = \Gamma^C \tag{2.56}$$

When the exciton states have an infinite lifetime ($\Gamma = 0$), the calculated line shape shows a divergence at the ground-state discrete-exciton energy E_{x1} ($n = 1$). The damping parameter broadens the resonance feature and decreases the Brillouin-scattering efficiency. Thus, a maximum of the Brillouin-scattering efficiency appears near the ground-state exciton energy. It is obvious that such a maximum shifts toward lower-energy side with increasing damping parameter. These results clearly suggest that the Brillouin-scattering efficiency depends strongly on the damping of the excited electronic states especially in the resonance-energy region. Details of the damping effect on resonant Brillouin scattering will be discussed in Chapter VII.

Figure 2-6 shows a typical example of the spectral dependence of the Brillouin-scattering cross section σ_B calculated from Eqs. (2.25) and (2.55). The vertical arrows indicate the positions of the E_0 and $E_0 + \Delta_0$ (spin-orbit splitting) gaps. The numerical parameters used are corresponding to those of ZnSe [see Chapter IV]. It has been taken into account the damping energy of $\Gamma = 0.024E_0$ in the calculation. The curve has also been calculated by taking into account the higher-gap contribution (i.e., nondispersive contribution) arising from such as the E_1, $E_1 + \Delta_1$ and E_2 gaps. The strong peaks appearing near the E_0-gap region are due to the discrete-exciton resonance contribution.

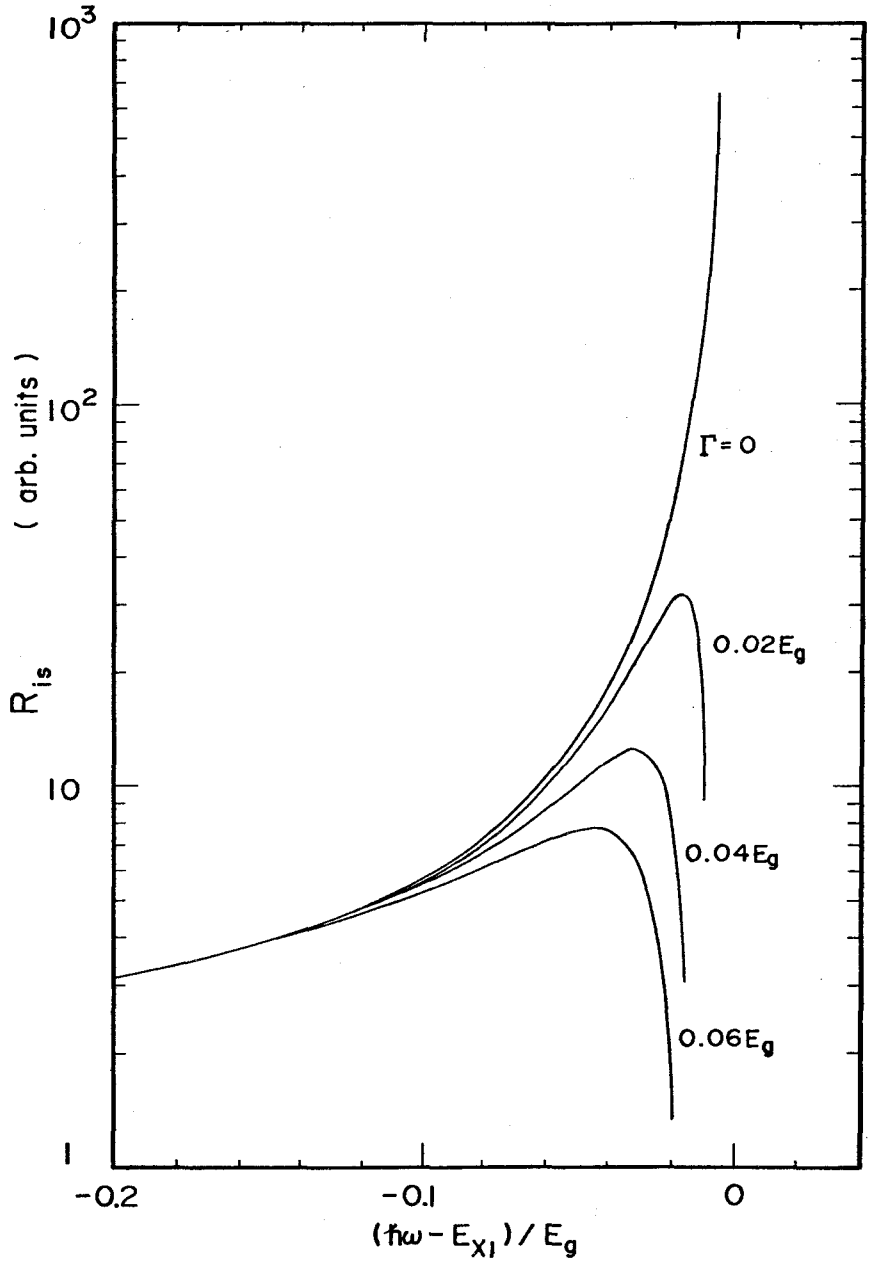

FIG. 2-5. Theoretical line shapes of R_{is} [Eq. (2.55)] based on the simple two-band model with taking account of four different damping parameters.

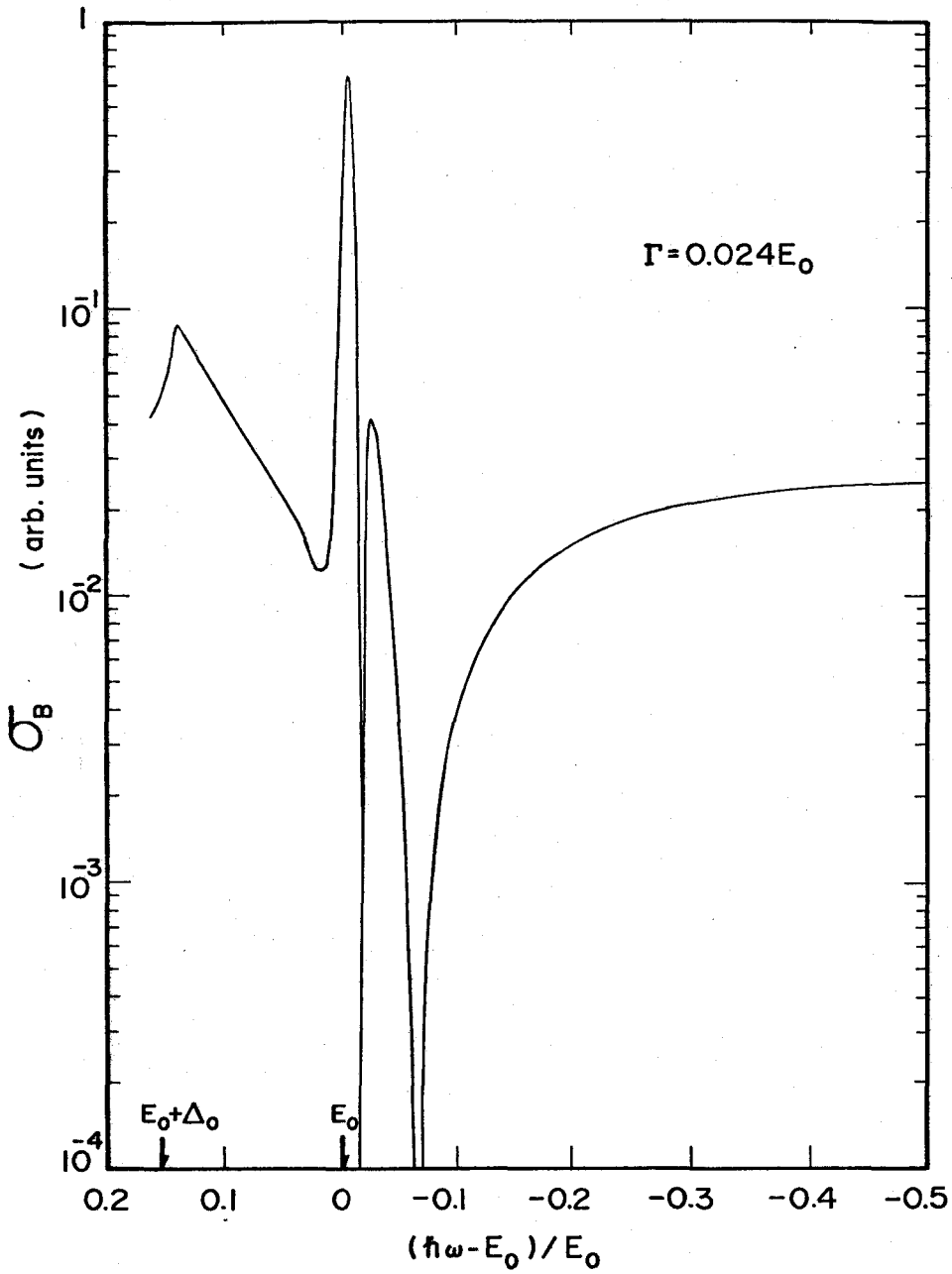

FIG. 2-6. Typical example of the spectral dependence of the Brillouin-scattering cross section σ_B calculated from Eqs. (2.25) and (2.55). The vertical arrows indicate the positions of the E_0 and $E_0+\Delta_0$ (spin-orbit splitting) gaps.

The resonance peak of the $E_0 + \Delta_0$ gap can also be clearly found in the figure. Moreover, the Brillouin-scattering cross section has narrow and sharp minima (dips) in the region below and near the E_0 gap. This phenomenon is usually called "resonant cancellation (or antiresonance)", which is corresponding to a cancellation of the resonant and nonresonant contributions, as will be discussed in more detail in Chapter IV.

The Wannier-Mott exciton model [Eq. (2.55)] may increase the Brillouin-scattering efficiency compared with the free electron-hole pair model [Eq. (2.29)] without greatly altering the resonance shape. If R* is very small (i.e., the exciton interaction is very small), Eqs. (2.49) and (2.51) can be approximated as

$$|\phi_n(0)|^2 \rightarrow 0 \quad (R^* \rightarrow 0) \quad , \tag{2.57}$$

$$|\phi_k(0)|^2 \sim \frac{1}{N} \quad . \tag{2.58}$$

In this limit, the contribution of the discrete exciton term becomes very small compared with that of the continuum exciton term, and therefore Eq. (2.55) agrees explicitly with Loudon's formulation of Eq. (2.29).

2.2.3 Deformation-Potential Scattering

The intermediate electronic states produced by the incident radiation interact with the acoustical phonons *via* deformation-potential interaction, resulting in a change in their electronic states. The transitions of the intermediate electronic states are determined by the transformation properties of the electronic states in crystals and the relevant acoustical phonon modes. Such a selection rule of the deformation-potential scattering determines the electronic transition process (two- or three-band process) which plays a dominant role in the resonant Brillouin-scattering process. The excitation of a phonon produces a displacement of the atoms of the lattice, and this displace-

ment perturbs the periodic potential acting on the electrons, leading to the electron-lattice interaction energy H_{EL}. The electron-lattice interaction is linear in the component u of the relative displacement (Bir & Pikus),[72] and a matrix element of H_{EL} is written as

$$\langle\beta|\ H_{EL}\ |\alpha\rangle = \Xi_{\beta\alpha} u/a \qquad , \tag{2.59}$$

where a is the lattice constant, included to give a conventional normalization, and $|\alpha\rangle$ and $|\beta\rangle$ are the electronic states. The deformation potential $\Xi_{\beta\alpha}$ is a matrix element of the derivative of the perturbed periodic potential with respect to u. The coupling parameters of Eqs. (2.8a) and (2.8b), thus, contain the following deformation potential:

$$\langle\beta|\ \Xi^{(i)}\ |\alpha\rangle = \langle\beta|\ \frac{\partial\phi}{\partial u_i}\ |\alpha\rangle \qquad , \tag{2.60}$$

where ϕ is the equilibrium periodic-lattice potential and $\Xi^{(i)}$ is the x, y or z component of Ξ. The deformation potential contained in the coupling parameters of Eq. (2.8c), on the other hand, can be expressed by the following form:

$$\langle\beta|\ \Xi^{(ij)}\ |\alpha\rangle = \langle\beta|\ \frac{\partial^2\phi}{\partial u_i \partial u_j}\ |\alpha\rangle \qquad , \tag{2.61}$$

because the electron-lattice interaction Hamiltonian $H^{(2)}_{eL_{(2)}}$ is bilinear in phonon operators and linear in exciton operators (which creates two phonons simultaneously and creates or annihilates an exciton). Now, let us calculate the matrix element $\Xi_{\beta\alpha}$ having a form of Eq. (2.60) in the cases of [A] zincblende-type crystal and [B] wurtzite-type crystal. We, however, do not calculate $\Xi_{\beta\alpha}$ having a form of Eq. (2.61) because the electron-lattice interaction Hamiltonian $H^{(2)}_{eL_{(2)}}$ does not act on the first-order Brillouin-scattering process, as already mentioned in Section 2.2.1.

[*A*] *Zincblende-Type Crystal*

The wave functions of the conduction (ψ_C) and valence band (ψ_V) for the zincblende-type crystals at $\vec{k} = 0$ are given by[73]

$$\psi_C = |\, S\uparrow >\tag{2.62}$$

$$\psi_{VA} = |A> = |\tfrac{3}{2}, \tfrac{1}{2}> = (\tfrac{1}{6})^{\frac{1}{2}} |\, 2Z\uparrow - (X+iY)\downarrow >\tag{2.63a}$$

$$\psi_{VB} = |B> = |\tfrac{3}{2}, \tfrac{3}{2}> = (\tfrac{1}{2})^{\frac{1}{2}} |\, (X+iY)\uparrow >\tag{2.63b}$$

$$\psi_{VC} = |C> = |\tfrac{1}{2}, \tfrac{1}{2}> = (\tfrac{1}{3})^{\frac{1}{2}} |\, Z\uparrow + (X+iY)\downarrow > ,\tag{2.63c}$$

where $\uparrow$ and $\downarrow$ indicate spin-up and spin-down, respectively, and X, Y and Z are the valence-band wave functions which transform as atomic p functions under the operations of the group of the tetrahedron and S is the conduction-band wave function which transforms as an atomic s function under the same operations. The wave functions for the valence-band states are taken in the (J, m_J) representations. The subscripts A, B and C of Eq. (2.63) indicate the Γ_8, Γ_8 and Γ_7 valence bands, respectively. In the zincblende-type crystals, the A and B valence bands are degenerate at $\vec{k} = 0$, and the magnitude of the splitting between the A (B) and C valence bands is denoted usually by Δ_{so} (spin-orbit splitting energy) [see Fig. 2-8].

In order to calculate Eq. (2.59), we use the orbital-strain Hamiltonian derived by Pikus and Bir[74,75] as the electron-lattice interaction Hamiltonian. This seems to be reasonable for the interaction between the electrons and acoustical phonons (Brillouin scattering). In the polar semiconductors, however, the deformation-potential type of electron-lattice interaction is augment for the case of the longitudinal optical (LO) phonon by an interaction H^F_{eL} due to the electric field associated with this phonon (Raman scattering). The matrix element of H^F_{eL} (Fröhlich interaction) can be given by[76,77]

$$<\beta|\, H^F_{eL}\, |\alpha> = \sum_q \frac{ie}{|\vec{q}|} \left(\frac{1}{\varepsilon_\infty} - \frac{1}{\varepsilon_0} \right)^{\frac{1}{2}} \left(\frac{2\pi\hbar\omega_{LO}}{V} \right)^{\frac{1}{2}} <\beta|\, e^{i\vec{q}\vec{r}}\, |\alpha> \quad ,\tag{2.64}$$

where $\vec{q}$ and ω_{LO} are the wave vector and angular frequency of LO phonon, respectively, and ε_0 is the static dielectric constant. If we let $\vec{q} \to 0$, then the matrix element mecomes diagonal in the electronic states [$|\alpha\rangle$ and $|\beta\rangle$].

The orbital-strain Hamiltonian H_{ec} and H_{ev} can be written as[74,75]

$$H_{ec} = a' \ (e_{xx} + e_{yy} + e_{zz}) \tag{2.65}$$

for the conduction band at $\vec{k} = 0$, and

$$H_{ev} = -a \ (e_{xx} + e_{yy} + e_{zz}) - 3b[(L_x^{\ 2} - \frac{1}{3}\mathbf{L}^2)e_{xx} + c.p.] - \frac{6d}{\sqrt{3}}\{[L_x, L_y]e_{xy} + c.p.\} \tag{2.66}$$

for the valence bands at $\vec{k} = 0$. In Eqs. (2.65) and (2.66), the parameters a' and a are the hydrostatic-pressure deformation potentials for the conduction and valence bands, respectively, and b and d are the uniaxial-deformation potentials appropriate to strains of tetragonal and rhombohedral symmetry, respectively. e_{ij} is the component of the strain tensor. L_i is the orbital-angular momentum operator, being given by[78]

$$L_x = \frac{\hbar}{\sqrt{2}}\begin{bmatrix} 0 & 1 & 0 \\ 1 & 0 & 1 \\ 0 & 1 & 0 \end{bmatrix} , \quad L_y = \frac{\hbar}{\sqrt{2}}\begin{bmatrix} 0 & -i & 0 \\ i & 0 & -i \\ 0 & i & 0 \end{bmatrix} , \quad L_z = \hbar\begin{bmatrix} 1 & 0 & 0 \\ 0 & 0 & 0 \\ 0 & 0 & -1 \end{bmatrix} , \tag{2.67a}$$

and

$$\mathbf{L}^2 = L_x^{\ 2} + L_y^{\ 2} + L_z^{\ 2} = \hbar^2\begin{bmatrix} 2 & 0 & 0 \\ 0 & 2 & 0 \\ 0 & 0 & 2 \end{bmatrix} . \tag{2.67b}$$

"c.p." in the right-hand side of Eq. (2.66) denotes cyclic permutations with respect to the indices, x, y and z, and the quantity in the square bracket indicates the symmetrized product:

$$[L_x, L_y] = \frac{1}{2}(L_xL_y + L_yL_x) . \tag{2.68}$$

The sound waves produce a displacement $u(\vec{r}, t)$ at $\vec{r}$, which can be given by the following plane-wave form:

$$u_l(\vec{r}, t) = \pi_l u_0 \exp[i(\vec{q}\vec{r} - \omega t)], \tag{2.69}$$

where $\vec{\pi}$ is a unit vector in the direction of the polarization of the sound wave, and the subscript l represents the component of the direction x, y or z. The strain components $e_{ij}(\vec{r}, t)$ are related to the elastic displacements $[u(\vec{r}, t)]$ in the dedium by [79]

$$e_{ij} = \frac{1}{2} \left(\frac{\partial u_i}{\partial r_j} + \frac{\partial u_j}{\partial r_i} \right) \quad . \tag{2.70}$$

The non-vanishing components of the strain tensor can, thus, be obtained from Eq. (2.70). As will be mentioned later [Chapter IV], we have measured the spectral dependence of the Brillouin-scattering cross sections from the T1- and T2-mode acoustical phonons in the zincblende-type crystals. The corresponding non-vanishing strain components obtained from Eq. (2.70) are as follows.

T1-mode acoustical phonons:

$$e_{xx} \text{ and } e_{yy} \text{ with } e_{xx} = - e_{yy} \tag{2.71}$$

T2-mode acoustical phonons:

$$e_{yz} \text{ and } e_{zx} \text{ with } e_{yz} = e_{zx} \quad , \tag{2.72}$$

where the T1- and T2-mode acoustical phonons propagate in the $[1\bar{1}0]$ and [001] directions, respectively, with shear polarization parallel to the [110] direction.

The orbital-strain Hamiltonians [Eqs. (2.65) and (2.66)], hence, become

$$\mathcal{H}_{ec} = 0 \tag{2.73a}$$

$$\mathcal{H}_{ev} = - 3b[(L_x^{\,2} - \tfrac{1}{3}\mathbf{L}^2)e_{xx} + (L_y^{\,2} - \tfrac{1}{3}\mathbf{L}^2)e_{yy}] \tag{2.73b}$$

for the T1-mode acoustical phonons, and

$$H_{ec} = 0 \tag{2.74a}$$

$$H_{ev} = -\frac{6}{\sqrt{3}}\, d\, \{[L_y, L_z]e_{yz} + [L_z, L_x]e_{zx}\} \tag{2.74b}$$

for the T2-mode acoustical phonons. It is obvious from Eq. (2.73a) and (2.74a) that the deformation-potential scattering of electrons in the conduction bands disappears for both the T1- and T2-mode acoustical phonons. The wave functions of the *p*-like valence bands [Eq. (2.63)] can now be written in the matrix representation as

$$|A\rangle = \left(\frac{2}{6}\right)^{\frac{1}{2}} \left\{ 2^{\frac{1}{2}} \begin{bmatrix} 0 \\ 1 \\ 0 \end{bmatrix} \alpha + \begin{bmatrix} 1 \\ 0 \\ 0 \end{bmatrix} \beta \right\} \tag{2.75a}$$

$$|B\rangle = -\begin{bmatrix} 1 \\ 0 \\ 0 \end{bmatrix} \alpha \tag{2.75b}$$

$$|C\rangle = \left(\frac{2}{3}\right)^{\frac{1}{2}} \left\{ 2^{-\frac{1}{2}} \begin{bmatrix} 0 \\ 1 \\ 0 \end{bmatrix} \alpha - \begin{bmatrix} 1 \\ 0 \\ 0 \end{bmatrix} \beta \right\} , \tag{2.75c}$$

where α and β indicate spin-up and spin-down, respectively. Substituting Eqs. (2.73b), (2.74b) and (2.75) into Eq. (2.59), one can find the deformation-potential scattering of holes in the valence bands. We obtain the following results:[71]

$$\begin{aligned} \Xi_{AA} &= \Xi_{BB} = \Xi_{CC} = 0 \\ \Xi_{BA} &= 3^{\frac{1}{2}} b \\ \Xi_{CB} &= 6^{\frac{1}{2}} b \\ \Xi_{AC} &= 0 \end{aligned} \tag{2.76}$$

for the T1-mode acoustical phonons, and

$$\Xi_{AA} = \Xi_{BB} = \Xi_{CC} = 0$$

$$\Xi_{BA} = d$$

$$\Xi_{CB} = d/2^{\frac{1}{2}} \tag{2.77}$$

$$\Xi_{AC} = 6^{\frac{1}{2}}d/2$$

for the T2-mode acoustical phonons. It is clear from Eq. (2.76) and (2.77) that the intraband deformation-potential scattering is forbidden for both the T1- and T2-mode acoustical phonons (i.e., the diagonal components are zero). Figure 2-7 shows the schematic diagrams of the electronic transitions involving (a) Ξ_{BA}, (b) Ξ_{CB} and (c) Ξ_{AC} which play a role in the first-order Brillouin-scattering process. Ξ_{BA}, for example, means that the excited holes in the A valence band (A excitons) are scattered by the deformation potential b (or d) to the B valence band (B excitons), corresponding to the matrix element Ξ_{BA}. Note that the matrix element $\Xi_{\beta\alpha}$ has the symmetry property:

$$\Xi_{\beta\alpha} = \Xi_{\alpha\beta} \quad , \tag{2.78}$$

since it is the matrix element of a real operator.

[*B*] *Wurtzite-Type Crystal*

Next, we obtain the matrix element $\Xi_{\beta\alpha}$ in the case of the wurtzite-type crystals based on the quasi-cubic model.[80,81] It has been pointed out by Hopfield[81] that the direct-band gap of wurtzite (at $\vec{k} = 0$) can be obtained from that of zincblende by the action of a small hexagonal crystal field. Under the spin-orbit interaction, represented by the matrix element Δ_{so} and that of the crystal field represented by Δ_c, the energy differences of the split valence bands (correspond to the A, B and C valence bands) are given by [see Fig. 2-8][81]

$$E_{BA} = E_{gB} - E_{gA}$$

$$= \frac{\Delta_{so} + \Delta_c}{2} - \sqrt{\left(\frac{\Delta_{so} + \Delta_c}{2}\right)^2 - \frac{2}{3}\Delta_{so}\Delta_c} \quad , \tag{2.79a}$$

FIG. 2-7. Schematic diagrams of the deformation-potential-scattering processes for the zincblende-type crystal. a) Ξ_{BA}; b) Ξ_{CB}; c) Ξ_{AC}.

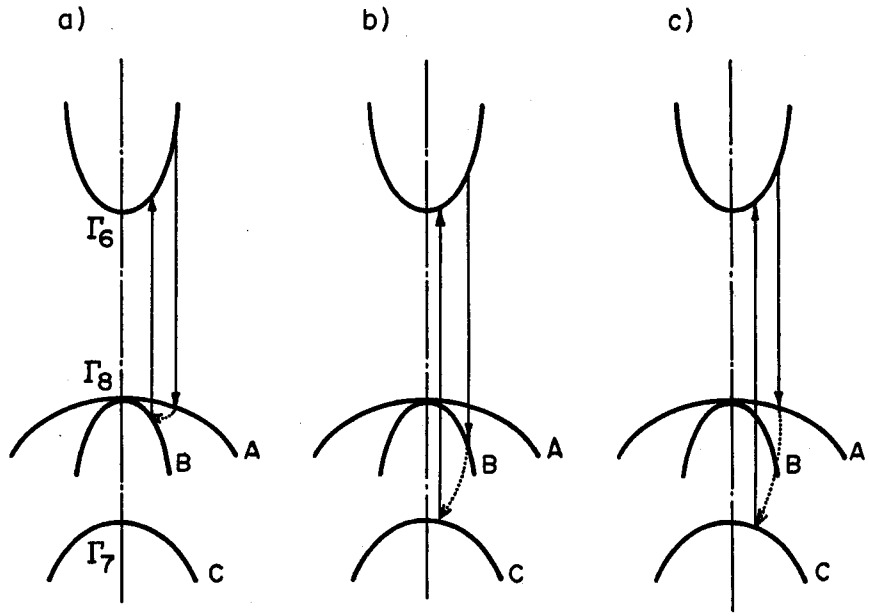

$$E_{CA} = E_{gC} - E_{gA}$$

$$= \frac{\Delta_{so} + \Delta_c}{2} + \sqrt{\left(\frac{\Delta_{so} + \Delta_c}{2}\right)^2 - \frac{2}{3}\Delta_{so}\Delta_c} \quad , \tag{2.79b}$$

$$E_{CB} = E_{gC} - E_{gB}$$

$$= 2\sqrt{\left(\frac{\Delta_{so} + \Delta_c}{2}\right)^2 - \frac{2}{3}\Delta_{so}\Delta_c} \quad . \tag{2.79c}$$

The corresponding wave functions of the three split valence bands are

$$|A\rangle : \quad S_+\uparrow \tag{2.80a}$$

$$|B\rangle : \quad \alpha_B S_-\uparrow + \alpha_C S_0\downarrow \tag{2.80b}$$

$$|C\rangle : \quad \alpha_C S_-\uparrow - \alpha_B S_0\downarrow \quad , \tag{2.80c}$$

where $\uparrow$ and $\downarrow$ represent spin-up and spin-down, respectively, and S_+, S_- and S_0 are defined by using the *p*-like basis functions S_x, S_y and S_z as follows:

$$S_+ = (S_x + iS_y)/2^{\frac{1}{2}} \quad , \tag{2.81a}$$

$$S_- = (S_x - iS_y)/2^{\frac{1}{2}} \quad , \tag{2.81b}$$

$$S_0 = S_z \quad . \tag{2.81c}$$

The admixture coefficients α_B and α_C are

$$\alpha_B = [1 + \frac{1}{2}(2 - \frac{3}{\Delta_{so}} E_{BA})^2]^{-\frac{1}{2}} \quad , \tag{2.82a}$$

$$\alpha_C = [1 + \frac{1}{2}(2 - \frac{3}{\Delta_{so}} E_{CA})^2]^{-\frac{1}{2}} \quad , \tag{2.82b}$$

$$\alpha_B^2 + \alpha_C^2 = 1 \quad . \tag{2.82c}$$

The wave function of the conduction band is *s*-like in character:

$$\psi_C : \quad |S\rangle \quad . \tag{2.83}$$

It has been shown that the orbital-strain Hamiltonian H_e for the s-like conduction band of wurtzite crystals at $\vec{k} = 0$ is given by[82]

$$H_{ec} = d_1 e_{zz} + d_2(e_{xx} + e_{yy}) \quad , \tag{2.84}$$

and for the p-like valence bands by

$$H_{ev} = (C_1+C_3L_z^2)e_{zz} + (C_2+C_4L_z^2)(e_{xx}+e_{yy}) + C_5(L_-^2e_+ + L_z^2e_-)$$
$$+ C_6([L_z, L_+]e_{-z} + [L_z, L_-]e_{+z}) \quad , \tag{2.85}$$

where the coefficients C_i and d_i are the deformation potentials, e_{ij} is the component of the strain tensor with $e_\pm = e_{xx} - e_{yy} \pm 2ie_{xy}$ and $e_{\pm z} = e_{xz} \pm ie_{yz}$, and L_i is the orbital-strain momentum operator having the same form as Eq. (2.67) and $L_\pm = (1/\sqrt{2})(L_x \pm iL_y)$.

The non-vanishing strain components of the wurtzite-type crystals are also obtained from Eq. (2.70) as

T1-mode acoustical phonons:

$$e_{xy} \tag{2.86}$$

T2-mode acoustical phonons:

$$e_{zx} \text{ and } e_{yz} \text{ with } e_{zx} = e_{yz} \quad , \tag{2.87}$$

where the T1-mode acoustical phonons in the wurtzite-type crystals propagate in the direction perpendicular to the c-axis with shear polarization parallel to the c-axis and the T2-mode acoustical phonons propagate in the direction perpendicular to the c-axis with shear polarization perpendicular to the c-axis, and the z-axis is parallel to the c-axis of the crystals.

The orbital-strain Hamiltonians [Eqs. (2.84) and (2.85)], hence, become

$$H_{ec} = 0 \tag{2.88a}$$

$$H_{ev} = C_5(L_-^2e_+ + L_z^2e_-) \tag{2.88b}$$

for the T1-mode acoustical phonons, and

$$H_{ec} = 0 \tag{2.89a}$$

$$H_{ev} = C_6([L_z, L_+]e_{-z} + [L_z, L_-]e_{+z}) \tag{2.89b}$$

for the T2-mode acoustical phonons. It is obvious from Eqs. (2.88a) and (2.89b) that the deformation-potential scattering of electrons in the conduction bands disappear for both the T1- and T2-mode acoustical phonons, as similar to the case for the zincblende-type crystals. The wave functions of the p-like valence bands [Eq. (2.80)] can be written in the matrix representation as

$$|A\rangle = \begin{bmatrix}1\\0\\0\end{bmatrix}\alpha \tag{2.90a}$$

$$|B\rangle = \alpha_B \begin{bmatrix}0\\0\\1\end{bmatrix}\alpha + \alpha_C \begin{bmatrix}0\\1\\0\end{bmatrix}\beta \tag{2.90b}$$

$$|C\rangle = \alpha_C \begin{bmatrix}0\\0\\1\end{bmatrix}\alpha - \alpha_B \begin{bmatrix}0\\1\\0\end{bmatrix}\beta \tag{2.90c}$$

Substituting Eqs. (2.88b), (2.89b) and (2.90) into Eq. (2.59), one can find the deformation-potential scattering of holes in the valence bands of the wurtzite-type crystals. We finally obtain the following results:

$$\begin{aligned} \Xi_{AA} &= \Xi_{BB} = \Xi_{CC} = 0 \\ \Xi_{BA} &= \alpha_B C_5 \\ \Xi_{CB} &= 0 \\ \Xi_{AC} &= \alpha_C C_5 \end{aligned} \tag{2.91}$$

for the T1-mode acoustical phonons,[39] and

$$\Xi_{AA} = \Xi_{BB} = \Xi_{CC} = 0$$

$$\Xi_{BA} = \frac{1}{2}\alpha_C C_6$$

$$\Xi_{CB} = \frac{1}{2} C_6 \qquad (2.92)$$

$$\Xi_{AC} = \frac{1}{2} \alpha_B C_6$$

for the T2-mode acoustical phonons.[27] It can be found from Eqs. (2.91) and (2.92) that the intraband deformation-potential scattering is forbidden for both the T1- and T2-mode acoustical phonons (i.e., $\Xi_{\alpha\alpha} = 0$).

The matrix elements of the deformation-potential scattering for longitudinal acoustical phonons in the wurtzite- or zincblende-type crystals can also be obtained by the same procedure as mentioned above. Now, we consider the case of the pure-longitudinal (PL) acoustical phonons in the wurtzite-type crystals (propagating in the direction perpendicular to the c-axis). From Eq. (2.70), the atomic displacement of the PL acoustical phonon produces the non-vanishing strain component e_{xx}. The orbital-strain Hamiltonians of Eqs. (2.84) and (2.85), thus, become

$$H_{ec} = d_2 e_{xx} \qquad (2.93a)$$

$$H_{ev} = (C_2 + C_4 L_z^2) e_{xx} + C_5 (L_-^2 e_+ + L_z^2 e_-) \quad . \qquad (2.93b)$$

Substituting Eqs. (2.90) and (2.93) into Eq. (2.59), we obtain the following matrix elements:

$$\begin{aligned}
\Xi_{AA} &= d_2 - (C_2 + C_4) \\
\Xi_{BB} &= d_2 - (C_2 + \alpha_B^2 C_4) \\
\Xi_{CC} &= d_2 - (C_2 + \alpha_C^2 C_4) \\
\Xi_{BA} &= \alpha_B C_5 \\
\Xi_{CB} &= \alpha_C C_5 \\
\Xi_{AC} &= \alpha_B \alpha_C C_4 \quad .
\end{aligned} \qquad (2.94)$$

It is interesting to point out that the intraband deformation-potential scattering [$\Xi_{\alpha\alpha}$] is allowed for the PL acoustical phonons (in addition to the interband ones [$\Xi_{\beta\alpha}$]), in contrast to those for the transverse acoustical phonons.

In order to determine the Brillouin-scattering process, we have to take into account the selection rules of the optical transitions (dipole transitions) in addition to those of the deformation-potential scattering. Let us now consider the selection rules of the optical transitions by the aid of group theory. The zincblende-type crystal has a Td point-group structure. It is well known that at $\vec{k} = 0$ the conduction band has Γ_6 symmetry and the A, B and C valence bands have Γ_8, Γ_8 and Γ_7 symmetries, respectively.[83] The polarization vector $\vec{E} \perp (\vec{x}, \vec{y}, \vec{z})$ of the point group Td belongs to Γ_5 symmetry. The optical transitions between the conduction and valence bands can be given by the direct product

$$\Gamma_8 \rightarrow \Gamma_6 \text{ (A, B excitons): } \Gamma_8 \times \Gamma_6 = \Gamma_3 + \Gamma_4 + \Gamma_5 \qquad (2.95a)$$

$$\Gamma_7 \rightarrow \Gamma_6 \text{ (C exciton): } \Gamma_7 \times \Gamma_6 = \Gamma_2 + \Gamma_5 \quad . \qquad (2.95b)$$

It is clear from Eq. (2.95) that the transitions contain the representation of $\vec{E} \perp (\vec{x}, \vec{y}, \vec{z})$ [i.e., Γ_5]. The wurtzite-type crystal, on the other hand, has a C_{6v} point-group structure. At the center of the Brillouin zone ($\vec{k} = 0$), the conduction band has Γ_7 symmetry and the A, B and C valence bands have Γ_9, Γ_7 and Γ_7 symmetries, respectively.[83] The polarization vectors $\vec{E} \perp \vec{c}$ and $\vec{E} \parallel \vec{c}$ of the point group C_{6v} belong to Γ_5 and Γ_1 symmetries, respectively. The direct products can be given by

$$\Gamma_9 \rightarrow \Gamma_7 \text{ (A exciton): } \Gamma_9 \times \Gamma_7 = \Gamma_5 + \Gamma_6 \qquad (2.96a)$$

$$\Gamma_7 \rightarrow \Gamma_7 \text{ (B exciton): } \Gamma_7 \times \Gamma_7 = \Gamma_1 + \Gamma_2 + \Gamma_5 \qquad (2.96b)$$

$$\Gamma_7 \rightarrow \Gamma_7 \text{ (C exciton): } \Gamma_7 \times \Gamma_7 = \Gamma_1 + \Gamma_2 + \Gamma_5 \quad . \qquad (2.96c)$$

The transitions $\Gamma_7 \rightarrow \Gamma_7$ contain the representations of both $\vec{E} \perp \vec{c}$ and $\vec{E} \parallel \vec{c}$, but the transition $\Gamma_9 \rightarrow \Gamma_7$ contains only the representation of $\vec{E} \perp \vec{c}$. It means that for $\vec{E} \parallel \vec{c}$ the optical transition between the conduction and A valence band is forbidden and for $\vec{E} \perp \vec{c}$ all the optical transitions are possible. In Fig. 2-8, we show such selection rules of the optical transitions along with the band models of the zincblende- and wurtzite-type crystals at $\vec{k} = 0$, where (a): zincblende ($\Delta_{so} = 0$), (b): zincblende ($\Delta_{so} \neq 0$) and (c): wurtzite ($\Delta_{so} \neq 0$, $\Delta_c \neq 0$).

2.2.4 Macroscopical Theory

Brillouin scattering in cubic crystals has been analyzed in detail from a macroscopical point of view by Benedek and Fritsh.[38] The theory predicted the intensity, polarization and spectral distribution of the scattered light as a function of the incident and scattered directions in the crystals. Nelson *et al.*[62] and Hamaguchi[63] have extended such analyses to the case of anisotropic media in which the birefringence effect is properly taken into account. In the following, we obtain expressions of the Brillouin-scattering intensities in the case of [A] zincblende-type crystal and [B] wurtzite-type crystal, based on Benedek-Fritsh's theory.

[A] Zincblende-Type Crystal

The electric field of the incident light in a medium is

$$\vec{E}(\vec{r}, t) = \vec{E}_0 \exp[i(\vec{k}_0\vec{r} - \omega_0 t)] \tag{2.97}$$

with

$$|\vec{k}_0| = n\omega_0/c \quad , \tag{2.98}$$

where $\vec{k}_0$ and ω_0 are the wave vector and angular frequency of the light wave, respectively. The light wave passing through the medium produces an oscillating dipole moment per unit volume or polarization $\vec{P}(\vec{r}, t)$ at each point $\vec{r}$. The

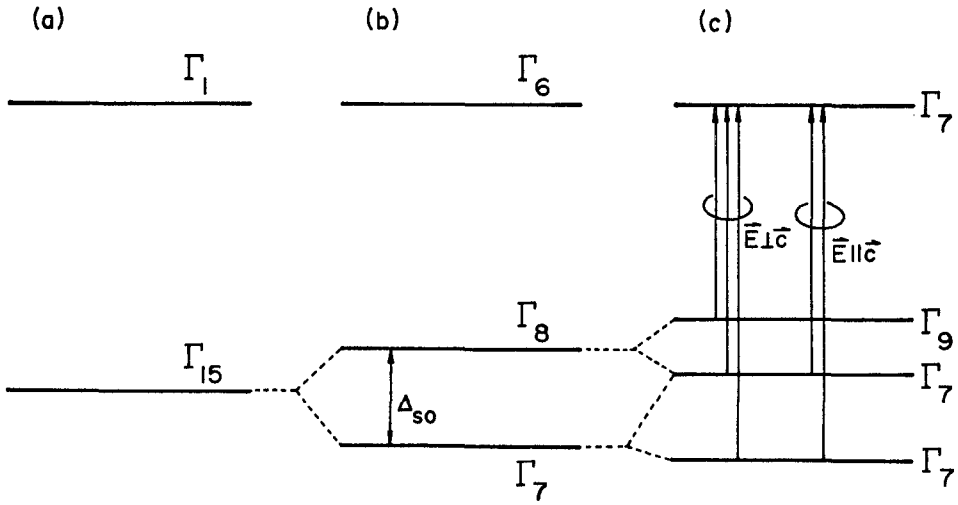

FIG. 2-8. Selection rules of the optical transitions along with the band models of the zincblende- and wurtzite-type crystals at $\vec{k} = 0$. (a) zincblende ($\Delta_{so}=0$); (b) zincblende ($\Delta_{so}\neq 0$); (c) wurtzite ($\Delta_{so}\neq 0$, $\Delta_{c}\neq 0$).

polarization at each point in the medium is

$$\vec{P}(\vec{r},\ t) = [\ \langle\alpha\rangle + \delta\alpha(\vec{r},\ t)\ ]\ \vec{E}(\vec{r},\ t) \qquad , \tag{2.99}$$

where α is the polarizability tensor which is decomposed into its time average part $\langle\alpha\rangle$ plus the time-space fluctuations $\delta\alpha(\vec{r},\ t)$ produced by the acoustical phonons. The electric field $d\vec{E}'$ scattered to the field point $\vec{R}$ by the oscillating polarization within a volume $|d\vec{r}| \ll \lambda^3$ [λ: wavelength of light] is now given by

$$d\vec{E}'(\vec{R},\ t) = [\ \frac{\vec{I}_{\vec{R}-\vec{r}} \times (\vec{I}_{\vec{R}-\vec{r}} \times \partial^2\vec{P}(\vec{R},\ t')/\partial t'^2)}{c^2|\vec{R} - \vec{r}|}\ |d\vec{r}|\ ] \ , \tag{2.100}$$

where I_{R-r} is the unit vector of R-r and t' is the retarded time, being given by

$$t' = t - \frac{n|\vec{R}-\vec{r}|}{c} \qquad . \tag{2.101}$$

In Eq. (2.101), n is the refractive index of the medium and c is the velocity of light in vacuum. If the frequency of the acoustical phonon is small compared with that of light, we can regard $\delta\alpha$ of Eq. (2.99) as a weak function of the time and write

$$\partial^2\vec{P}(\vec{r},\ t)/\partial t^2 = -\omega_0{}^2\vec{P}(\vec{r},\ t) \qquad . \tag{2.102}$$

The oscillating moments of Eq. (2.99) radiate or scatter electromagnetic energy in all directions. Substituting Eqs. (2.99) and (2.102) into Eq. (2.100) and carrying out the integration over the illuminated volume V at the retarded time t', we find that if $\vec{R} \gg \vec{r}$,

$$\vec{E}_s(\vec{R},\ t) = -(\ \frac{\omega_0}{c}\ )^2\ \frac{\exp[i(\vec{k}_0\vec{R} - \omega_0 t)}{R}\ \vec{I}_k$$

$$\times\ [\vec{I}_k \times \int_V \vec{P}(\vec{r},t')\exp[-i(\vec{k}_s\vec{r} - \omega_0 t)]|d\vec{r}|]\ , \tag{2.103}$$

where

$$\vec{I}_k \simeq \vec{I}_{\vec{R}-\vec{r}} \ (\vec{R} \gg \vec{r}) \quad , \qquad \vec{k}_s = n\omega_0 \vec{I}_k / c \quad , \tag{2.104}$$

and we have used the approximation that

$$| \vec{R} - \vec{r} | \simeq | \vec{R} | \quad . \tag{2.105}$$

The fluctuation of the polarization tensor of Eq. (2.103) [Eq. (2.99)] can be expressed in terms of its spatial Fourier component:

$$\delta\alpha(\vec{r}, t') = \left(\frac{1}{2\pi} \right)^{3/2} \sum_{\mu} \int |d\vec{q}| \delta\alpha^{\mu}(\vec{q}) \exp\{i[\vec{q}\vec{r} \pm \omega_{\mu}(\vec{q})t']\}. \tag{2.106}$$

In Eq. (2.106), $2\pi/|\vec{q}|$ is the wavelength of the fluctuation, $\omega_{\mu}(\vec{q})$ is the frequency of the fluctuation corresponding to this wavelength. The index μ denotes the possibility of a number of branches in the dispersion relation connecting $\vec{q}$ and $\omega_{\mu}(\vec{q})$. The wave vector of the fluctuation which produces the light scattering in the direction $\vec{I}_k$ is that which satisfies the implicit equation:

$$\vec{q} = \vec{k} - \vec{k}_0 \quad , \tag{2.107}$$

where

$$\vec{k} = \frac{n}{c} [\ \omega_0 \pm \omega_{\mu}(\vec{q}) \ ] \ \vec{I}_k \quad . \tag{2.108}$$

Substituting Eq. (2.106) into Eq. (2.103), we obtain

$$\vec{E}_s(\vec{R}, t) = -\left(\frac{\omega_0}{c}\right)^2 \frac{(2\pi)^{3/2}}{4\pi R} \sum_{\mu} \exp i\{\vec{k}\vec{R} - [\omega_0 \pm \omega_{\mu}(\vec{q})]t\}$$

$$\times \vec{I}_k \times [\vec{I}_k \times (\delta\varepsilon^{\mu}(\vec{q})\vec{E}_0)] \quad , \tag{2.109}$$

where we have replaced $\delta\alpha$ by $\delta\varepsilon/4\pi$ [ε: dielectric constant tensor].
The total power $dI_s(\vec{q}, \vec{R})$ in all frequencies scattered into a solid angle $d\Omega$ at the field point $\vec{R}$ is proportional to the mean square field strength:

$$dI_s(\vec{q}, \vec{R}) = \frac{c}{8\pi} <|\vec{E}_s(\vec{q}, t)|^2>R^2 d\Omega \tag{2.110}$$

The fluctuation in the dielectric constant appearing in Eq. (2.109) results from the fact that this constant depends on the state of the strain of the solid. The strains themselves fluctuate at each point because of the pasage of the sound waves. The elastic strains are connected with the elastic displacements through Eq. (2.70). In general, for small strains, the change in the dielectric tensor component $\delta\varepsilon_{ij}(\vec{r}, t)$ is a linear function of the elastic-strain components $e_{kl}(\vec{r}, t)$, i.e.,

$$-\frac{\delta\varepsilon_{ij}(\vec{r}, t)}{\varepsilon_{ii}\varepsilon_{jj}} = \sum_{kl} p_{ijkl} e_{kl}(\vec{r}, t) \quad , \tag{2.111}$$

where p_{ijkl} is the component of the photoelastic tensor. Each tensor for the zincblende-type crystals has the following form:

dielectric constant tensor: $[\varepsilon]$

$$[\varepsilon] = \begin{bmatrix} \varepsilon_{11} & 0 & 0 \\ 0 & \varepsilon_{11} & 0 \\ 0 & 0 & \varepsilon_{11} \end{bmatrix} \quad , \quad \varepsilon_{11} = n^2 \quad , \tag{2.112}$$

strain tensor: $[e]$

$$[e] = \begin{bmatrix} e_{11} & e_{12} & e_{13} \\ e_{21} & e_{22} & e_{23} \\ e_{31} & e_{32} & e_{33} \end{bmatrix} \tag{2.113}$$

photoelastic constant tensor: $[p]$

$$[p] = \begin{bmatrix} p_{11} & p_{12} & p_{13} & 0 & 0 & 0 \\ p_{12} & p_{11} & p_{12} & 0 & 0 & 0 \\ p_{12} & p_{12} & p_{11} & 0 & 0 & 0 \\ 0 & 0 & 0 & p_{44} & 0 & 0 \\ 0 & 0 & 0 & 0 & p_{44} & 0 \\ 0 & 0 & 0 & 0 & 0 & p_{44} \end{bmatrix} . \tag{2.114}$$

In Eq. (2.112), n is the refractive index ofthe crystal. Note that the strain [e] is the symmetric tensor.

We may write $\delta\varepsilon_{ij}(\vec{r}, t)$ using Eqs. (2.112) — (2.114) as

$$\varepsilon_{ij}(\vec{r}, t) = [p_{44}e_{ij}(\vec{r}, t) + (p_{11}-p_{12}-p_{44})\delta_{ij}e_{ii}(\vec{r}, t) + p_{12}(\sum_{l} e_{ll}(\vec{r}, t)\delta_{ij}] \times \varepsilon_{11}^{2} \quad . \tag{2.115}$$

The elastic-strain components $e_{kl}(\vec{r}, t)$ are functions of the position vector $\vec{r}$. Using the Fourier transformation of $e_{kl}(\vec{r}, t)$ into $e_{kl}(\vec{q}, t)$, we obtain the fluctuation of the electric displacement in the crystal:

$$\delta\vec{D}^{\mu}(\vec{q}, t) \equiv \delta\varepsilon^{\mu}(\vec{q}, t)\vec{E}_0 = \frac{\varepsilon_{11}^{2}}{i} u^{\mu}(\vec{q}, t)|\vec{q}||\vec{E}_0|\vec{\zeta}^{\mu} \ , \tag{2.116}$$

where

$$\vec{\zeta}^{\mu} = p_{44}[\vec{\pi}^{\mu}(\vec{I}_q\cdot\vec{I}_E) + (\vec{\pi}^{\mu}\cdot\vec{I}_E)\vec{I}_q] + p_{12}(\vec{\pi}^{\mu}\cdot\vec{I}_q)\vec{I}_E + \sum_{l}(p_{11}-p_{12}-2p_{44}) \cdot(\vec{\pi}^{\mu})_l(\vec{I}_q)_l(\vec{I}_E)_l\vec{I}_l \quad . \tag{2.117}$$

In Eq. (2.117), $\vec{\pi}^{\mu}$ is the unit vector in the direction of the polarization of the sound wave, $\vec{I}_q$ is the unit vector in the direction of propagation of the sound wave, with components $(\vec{I}_q)_l$ along the cube axes, l = x, y, z. $\vec{I}_l$ (l = x, y or z) is the unit vector along the cube axis. The direction of $\vec{\zeta}^{\mu}$ is determined by the relative directions of $\vec{q}$, $\vec{E}_0$ and $\vec{\pi}^{\mu}$. We note that in the Brillouin-scattering experiments one observes not $\vec{\zeta}^{\mu}$ but the vector $\vec{\xi}^{\mu}$ which is related to $\vec{\zeta}^{\mu}$ by

$$\vec{\xi}^{\mu} = \vec{I}_k \times (\vec{I}_k \times \vec{\zeta}^{\mu}) \quad , \tag{2.118}$$

where $\vec{I}_k$ is the unit vector of scattered light.

From Eqs. (2.109), (2.110) and (2.116), we finally obtain the Brillouin-scattering intensity of light scattered into the internal solid angle Ω during

the optical-path length b as

$$dI_s(\Omega) = I_0 \frac{\pi^2 \varepsilon_{11}^4}{\lambda_0^4} \sum_{\mu=1}^{3} \frac{|\vec{\xi}^{\mu}|^2}{2\rho v_\mu^2} \Phi^\mu d\Omega\, b \quad , \tag{2.119}$$

where I_0 is the incident-light intensity and λ_0 is the wavelength of the light in vacuum. The summation in Eq. (2.119) indicates that one must include contributions from the three different acoustical phonon modes, i.e., those from two transverse phonon modes and one longitudinal phonon mode. Φ^μ is the energy density of the acoustical phonons. The thermal-phonon occupation number $n_\mu(\vec{q})$ is given by

$$n_\mu(\vec{q}) = 1/[\ \exp(\hbar\omega_\mu(\vec{q})/k_B T) - 1\ ] \quad . \tag{2.120}$$

In the case of $\hbar\omega_\mu(\vec{q}) \ll k_B T$, Eq. (2.120) can be written in good approximation as

$$n_\mu(\vec{q}) \simeq k_B T/\hbar\omega_\mu(\vec{q}) \quad . \tag{2.121}$$

Thus, the energy density Φ^μ of Eq. (2.119) can be replaced by $k_B T$ in the case of Brillouin scattering by thermal phonons $[\Phi^\mu = n_\mu(\vec{q})\hbar\omega_\mu(\vec{q}) \simeq k_B T]$. It should be noted here that the internal solid angle Ω is not equal to the external solid angle Ω' due to the fact that the refractive index in the medium is different from that in vacuum. Assuming small cone angles, one obtains[63]

$$d\Omega \simeq \frac{\cos\theta_d}{n\sqrt{n^2 - \sin^2\theta_d}}\, d\Omega' \quad , \tag{2.122}$$

where θ_d is the external scattering angle. The scattering cross section is now

$$\sigma_B = \frac{\pi^2 \varepsilon_{11}^4}{\lambda_0^4} \sum_\mu \frac{\Phi^\mu}{2\rho v_\mu^2} |\vec{\xi}^{\mu}|^2 \frac{\cos\theta_d}{n\sqrt{n^2 - \sin^2\theta_d}} \quad , \tag{2.123}$$

where σ_B is defined as the Brillouin-scattering intensity per unit path length

per unit external solid angle. Next, we evaluate the Brillouin-scattering cross sections in the zincblende-type crystals for two special phonon modes (a) T1-mode acoustical phonons and (b) T2-mode acoustical phonons by the aid of the above results.

(a) T1-Mode Acoustical Phonons:

The T1-mode phonons propagate in the $[1\bar{1}0]$ direction with shear polarization parallel to the [110] direction. We adopt the configuration that the incident-light polarization is parallel to the [110] direction [see Fig. 3-1 (a)]. The vectors $\vec{\pi}$, $\vec{I}_q$ and $\vec{I}_E$, thus, become

$$\vec{\pi} = (1/\sqrt{2},\ 1/\sqrt{2},\ 0) \quad , \tag{2.124a}$$

$$\vec{I}_q = (1/\sqrt{2},\ -1/\sqrt{2},\ 0) \quad , \tag{2.124b}$$

$$\vec{I}_E = (1/\sqrt{2},\ 1/\sqrt{2},\ 0) \quad . \tag{2.124c}$$

Substituting Eq. (2.124) into Eqs. (2.117) and (2.118), one obtains $\vec{\zeta}^{T1}$ as

$$\vec{\zeta}^{T1} = \frac{1}{2}(p_{11} - p_{12})\vec{I}_q \tag{2.125}$$

and $\vec{\xi}^{T1}$ as

$$\vec{\xi}^{T1} = \frac{1}{2}(p_{11} - p_{12})\cos\theta_i{}'\ \vec{I}_s \quad , \tag{2.126}$$

where $\theta_i{}'$ is the incident angle incide the specimen, and the vector $\vec{I}_s$ stands for the unit vector lying in the scattering plane. The scalar product of $\vec{I}_s$ and $\vec{I}_E$ is given by

$$\vec{I}_s \cdot \vec{I}_E = 0 \quad , \tag{2.127}$$

which means that the scattered-light polarization is explicitly perpendicular to the incident-light polarization. Substituting Eq. (2.126) into Eq. (2.123), we obtain

$$\sigma_B = \frac{\pi^2 \varepsilon_{11}^{\ 4}}{\lambda_0^{\ 4}} \frac{\Phi^{T1}}{C_{11}-C_{12}} [\tfrac{1}{2}(p_{11}-p_{12})\cos\theta_i' |\vec{I}_s|]^2 \frac{\cos\theta_d}{n\sqrt{n^2-\sin^2\theta_d}} , \quad (2.128)$$

where C_{ij} is the component of the elastic stiffness tensor which has the same form as Eq. (2.114). In Eq. (2.128), we used the following relation:

$$v_{T1} = [(C_{11} - C_{12})/2\rho]^{\frac{1}{2}} \quad . \quad (2.129)$$

(b) T2-Mode Acoustical Phonons:

The T2-mode phonons propagate in the [001] direction with shear polarization parallel to the [110] direction. We adopt the configuration that the incident-light polarization is parallel to the [110] direction [see Fig. 3-1(b)]. The vectors $\vec{\pi}$, $\vec{I}_q$ and $\vec{I}_E$ are, thus, written as

$$\vec{\pi} = (1/\sqrt{2},\ 1/\sqrt{2},\ 0) \quad , \quad (2.130a)$$

$$\vec{I}_q = (0,\ 0,\ 1) \quad , \quad (2.130b)$$

$$\vec{I}_E = (1/\sqrt{2},\ 1/\sqrt{2},\ 0) \quad . \quad (2.130c)$$

Substituting Eq. (2.130) into Eq. (2.117) and (2.118), one obtains $\vec{\zeta}^{T2}$ as

$$\vec{\zeta}^{T2} = p_{44}\, \vec{I}_q \quad , \quad (2.131)$$

and $\vec{\xi}^{T2}$ as

$$\vec{\xi}^{T2} = p_{44}\cos\theta_i'\, \vec{I}_s \quad . \quad (2.132)$$

The scattered-light polarization is also explicitly perpendicular to the incident-light polarization, because

$$\vec{I}_s \cdot \vec{I}_E = 0 \quad . \quad (2.133)$$

Substituting Eq. (2.132) into Eq. (2.123), we obtain

$$\sigma_B = \frac{\pi^2 \varepsilon_{11}^{\ 4}}{\lambda_0^{\ 4}} \frac{\Phi^{T2}}{2C_{44}} [p_{44}\cos\theta_i' |\vec{I}_s|]^2 \frac{\cos\theta_d}{n\sqrt{n^2-\sin^2\theta_d}} \quad , \tag{2.134}$$

where C_{44} is the component of the elastic stiffness tensor, and we used the following relation:

$$v_{T2} = (C_{44}/\rho)^{\frac{1}{2}} \quad . \tag{2.135}$$

[*B*] *Wurtzite-Type Crystal*

The macroscopical theory of Brillouin scattering in the wurtzite-type crystals offers the closest analogy with that in the zincblende-type crystal [*A*]. One must, however, take into account the anisotropic nature of the optical properties (i.e., birefringence effect) in these crystals, since the scattered and incident lights have sometimes different polarizations. For the wurtzite-type crystals, the dielectric constant tensor [ε], strain tensor [e] and photoelastic constant tensor [p] can be written as

$$[\varepsilon] = \begin{bmatrix} \varepsilon_{11} & 0 & 0 \\ 0 & \varepsilon_{11} & 0 \\ 0 & 0 & \varepsilon_{33} \end{bmatrix} \quad , \tag{2.136}$$

with

$$\varepsilon_{11} = n_o^{\ 2} \quad \text{and} \quad \varepsilon_{33} = n_e^{\ 2} \quad , \tag{2.137}$$

$$[e] = \begin{bmatrix} e_{11} & e_{12} & e_{13} \\ e_{21} & e_{22} & e_{23} \\ e_{31} & e_{32} & e_{33} \end{bmatrix} \quad , \tag{2.138}$$

and

$$[p] = \begin{bmatrix} p_{11} & p_{12} & p_{13} & 0 & 0 & 0 \\ p_{12} & p_{11} & p_{13} & 0 & 0 & 0 \\ p_{31} & p_{31} & p_{33} & 0 & 0 & 0 \\ 0 & 0 & 0 & p_{44} & 0 & 0 \\ 0 & 0 & 0 & 0 & p_{44} & 0 \\ 0 & 0 & 0 & 0 & 0 & p_{66} \end{bmatrix} , \qquad (2.139)$$

with

$$p_{66} = \frac{1}{2} (p_{11} - p_{12}) \quad . \qquad (2.140)$$

In Eq. (2.137), n_o and n_e are the refractive indices for the ordinary and extraordinary rays, respectively. If the birefringence effect is taken into account, the wave vectors $\vec{k}_0$ [Eq. (2.98)], $\vec{k}_s$ [Eq. (2.104)] and $\vec{k}$ [Eq. (2.108)] appeared in [*A*] become[63]

$$\vec{k}_0 = \frac{n_i \omega_0}{c} \vec{1}_{k_0} \quad , \qquad (2.141)$$

$$\vec{k}_s = \frac{n_d \omega_0}{c} \vec{1}_k \quad , \qquad (2.142)$$

$$\vec{k} = \frac{n_d}{c} [\omega_0 \pm \omega_\mu(\vec{q})] \vec{1}_k \quad , \qquad (2.143)$$

where n_i and n_d are the refractive indices for the polarization of the incident and scattered lights, respectively, and $\vec{1}_{k_0}$ is the unit vector in the direction of the incident-light wave vector $\vec{k}_0$.

Carrying out the same procedures as [*A*], we obtain the fluctuation of the electric displacement in the wurtzite-type crystals:

$$\delta\vec{D}^\mu(\vec{q}, t) = \delta\varepsilon^\mu(\vec{q}, t)\vec{E}_0 = \frac{\varepsilon_{11}^2}{i} u^\mu(\vec{q}, t)|\vec{q}||\vec{E}_0|\vec{\zeta}^\mu \quad , \qquad (2.144)$$

where

$$\vec{\zeta}^{\mu} = \frac{p_{44}}{\varepsilon_{11}^{2}} [\varepsilon_0 \vec{\pi}^{\mu} (\varepsilon_0 \vec{\pi}^{\mu} \cdot \vec{I}_E) + (\varepsilon_0 \vec{\pi}^{\mu} \cdot \vec{I}_E) \varepsilon_0 \vec{I}_q] - \frac{2p_{44}}{\varepsilon_{11}^{2}} \sum_{l} \varepsilon_{ll}^{2} (\vec{\pi}^{\mu})_l (\vec{I}_q)_l (\vec{I}_E)_l \vec{I}_l$$

$$+ \sum_{m} [\sum_{l} p_{ml} (\varepsilon_{mm}^{2} / \varepsilon_{11}^{2}) (\vec{\pi}^{\mu})_l (\vec{I}_q)_l] (\vec{I}_E)_l \vec{I}_m + (\frac{p_{11} - p_{12}}{2} - p_{44})$$

$$\times [(\vec{\pi}^{\mu})_1 (\vec{I}_q)_2 (\vec{I}_E)_2 \vec{I}_1 + (\vec{\pi}^{\mu})_2 (\vec{I}_q)_1 (\vec{I}_E)_1 \vec{I}_1 + (\vec{\pi}^{\mu})_2 (\vec{I}_q)_1 (\vec{I}_E)_1 \vec{I}_2$$

$$+ (\vec{\pi}^{\mu})_1 (\vec{I}_q)_2 (\vec{I}_E)_1 \vec{I}_2] \quad . \tag{2.145}$$

In Eqs. (2.144) and (2.145), the notations used are the same as those appeared in [*4*]. $\vec{I}_l$ [l = 1, 2, 3 (x, y, z)] and $\vec{I}_m$ [m = 1, 2, 3 (x, y, z)] are unit vectors along the cube axes OX_1, OX_2 and OX_3 defined in the text of Nye,[42] where OX_3 (*z*) *is parallel to the c-axis of the crystal.* ε_0 *is the dielectric* constant tensor in the absence of strain. The vector $\vec{\xi}^{\mu}$, which determines the polarization of the scattered light, is given by the same form as Eq. (2.118). We finally obtain the Brillouin-scattering cross section in the wurtzite-type crystals as

$$\sigma_B = \frac{\pi^2 \varepsilon_{11}^{4}}{\lambda_0^{4}} \sum_{\mu} \frac{\Phi^{\mu}}{2\rho v_{\mu}^{2}} |\vec{\xi}^{\mu}|^2 \frac{\cos\theta_d}{n_d \sqrt{n_d^{2} - \sin^2\theta_d}} \quad . \tag{2.146}$$

In the following, we evaluate the Brillouin-scattering cross sections in the wurtzite-type crystals for three special phonon modes (a) T1-mode acoustical phonons, (b) T2-mode acoustical phonons and (c) PL-mode acoustical phonons by the aid of the above results.

(a) T1-Mode Acoustical Phonons:

The T1-mode phonons propagate in the direction perpendicular to the *c*-axis

with shear polarization perpendicular to the c-axis. We adopt the configuration that the incident-light polarization is perpendicular to the c-axis and parallel to the shear polarization [see Fig. 3-4 (a)]. The vectors $\vec{\pi}$, $\vec{I}_q$ and $\vec{I}_E$, thus, become

$$\vec{\pi} = (0,\ 1,\ 0) \quad , \tag{2.147a}$$

$$\vec{I}_q = (1,\ 0,\ 0) \quad , \tag{2.147b}$$

$$\vec{I}_E = (0,\ 1,\ 0) \quad . \tag{2.147c}$$

Substituting Eq. (2.147) into Eqs. (2.145) and (2.118), one obtains $\vec{\xi}^{T1}$ as

$$\vec{\xi}^{T1} = \frac{1}{2}\,(p_{11} - p_{12})(\vec{I}_k)_3\vec{I}_{xz} \quad , \tag{2.148}$$

where $\vec{I}_{xz}$ is the unit vector lying in the OX_1-OX_3 plane. Thus,

$$\frac{|\vec{\xi}^{T1}|^2}{2\rho v_{T1}^{\ 2}} = \frac{(p_{11}-p_{12})^2}{2(C_{11}-C_{12})}\,(\vec{I}_k)_3^{\ 2}\ |\vec{I}_{xz}|^2 \quad , \tag{2.149}$$

where the sound velocity v_{T1} of this phonon mode is given by the same form as Eq. (2.129). The elastic stiffness tensor [C] has the similar form as Eq. (2.139). The Brillouin-scattering cross section can be obtained by substituting Eq. (2.149) into Eq. (2.146). It is clear from Eq. (2.148) that the scattered-light polarization is explicitly perpendicular to the incident-light polarization.

(b) T2-Mode Acoustical Phonons:

The T2-mode phonons propagate in the direction perpendicular to the c-axis with shear polarization parallel to the c-axis. We adopt the configuration that the incident-light polarization is parallel to the c-axis [see Fig. 3-4 (b)] The vectors $\vec{\pi}$, $\vec{I}_q$ and $\vec{I}_E$ are, thus, written as

$$\vec{\pi} = (0,\ 0,\ 1) \quad , \tag{2.150a}$$

$$\vec{I}_q = (0,\ 1,\ 0) \quad , \tag{2.150b}$$

$$\vec{I}_E = (0,\ 0,\ 1) \quad . \tag{2.150c}$$

It is clear from Eq. (2.150) that

$$\vec{\pi}\cdot\vec{I}_q = 0, \quad \vec{I}_q\cdot\vec{I}_E = 0 \quad \text{and} \quad (\vec{\pi}^{\mu})_l(\vec{I}_q)_l(\vec{I}_E)_l = 0 \quad , \tag{2.151}$$

so that Eq. (2.145) can be reduced to as

$$\vec{\zeta}^{T2} = p_{44}\left(\frac{\varepsilon_{33}}{\varepsilon_{11}}\right)^2 \vec{I}_q \quad . \tag{2.152}$$

Then, one obtains

$$\vec{\xi}^{T2} = p_{44}\left(\frac{\varepsilon_{33}}{\varepsilon_{11}}\right)^2 |\vec{I}_k \times \vec{I}_q|\, \vec{I}_{\perp c} \quad , \tag{2.153}$$

where $\vec{I}_{\perp c}$ is the unit vector perpendicular to the c-axis. It can be found from Eq. (2.153) that the scattered-light polarization is perpendicular to the incident-light polarization. One can finally obtain

$$\frac{|\vec{\xi}^{T2}|^2}{\rho v_{T2}^{\,2}} = \frac{p_{44}^{\,2}}{2C_{44}}\left(\frac{\varepsilon_{33}}{\varepsilon_{11}}\right)^4 |\vec{I}_k \times \vec{I}_q|^2\, |\vec{I}_{\perp c}|^2 \quad . \tag{2.154}$$

The sound velocity v_{T2} is given by the same form as Eq. (2.135). The Brillouin-scattering cross section can be obtained by substituting Eq. (2.154) into Eq. (2.146).

(c) PL-Mode Acoustical Phonons:

The PL-mode (pure longitudinal) phonons propagate in the direction perpendicular to the c-axis with acoustical polarization perpendicular to the c-axis. We adopt the configuration that the incident-light polarization is parallel to the c-axis [see Fig. 3-4 (c)]. The vectors $\vec{\pi}$, $\vec{I}_q$ and $\vec{I}_E$, thus, become

$$\vec{\pi} = (1,\ 0,\ 0) \quad , \tag{2.155a}$$

$$\vec{I}_q = (1,\ 0,\ 0) \quad , \tag{2.155b}$$

$$\vec{I}_E = (0,\ 0,\ 0) \quad . \tag{2.155c}$$

Thus, Eq. (2.145) can be reduced to as

$$\vec{\xi}^{PL} = p_{31} \left(\frac{\varepsilon_{33}}{\varepsilon_{11}} \right)^2 \vec{I}_{\parallel c} \quad , \tag{2.156}$$

where $I_{\parallel c}$ is the unit vector parallel to the c-axis. It can be seen from Eq. (2.156) that the polarization vector of the light does not change after being the Brillouin-scattering process. Finally, one obtains

$$\frac{|\vec{\xi}^{PL}|^2}{2\rho v_{PL}^2} = \frac{p_{31}}{2C_{11}} \left(\frac{\varepsilon_{33}}{\varepsilon_{11}} \right)^4 |\vec{I}_{\parallel c}|^2 \quad . \tag{2.157}$$

In Eq. (2.157), we used the following relation:

$$v_{PL} = (C_{11}/\rho)^{\frac{1}{2}} \quad . \tag{2.158}$$

The Brillouin-scattering cross section can also be obtained by substituting Eq. (2.157) into Eq. (2.146).

2.3 PIEZOBIREFRINGENCE THEORY

2.3.1 Dielectric Constant

In this subsection, we shall discuss theoretical expressions of the frequency-dependent dielectric constant. First, we cosider the dielectric theory from a classical point of view[84] in which the N atoms in a volume V are represented by N damped harmonic oscillators. We present an electron of mass m and charge (-e) from the valence band in the form of the classical oscillator, whose natural frequency ω_0 is equal to difference between the energies of the electron in the valence band and in the conduction band. The presence of an electromagnetic wave having electric field $E = E_0 \exp(-i\omega t)$, polarized in the x-direction, produces forced oscillations. The equation of motion of an oscillator is

$$m(\ddot{X} + \Gamma\dot{X} + \omega_0^2 X) = (-e)E_0 \exp(-i\omega t) \quad , \tag{2.159}$$

where the dots indicate time derivatives and X is the displacement of the charge from its equilibrium position. Γ is the phenomenological damping constant. The solution of Eq. (2.159) is given by

$$X = \frac{(-e)E_0 \exp(-i\omega t)}{m(\omega_0^2 - \omega^2 - i\Gamma\omega)} \quad . \tag{2.160}$$

The electric field $\vec{E}$ in a medium is described by the electric displacement vector $\vec{D}$. The relation between the electric field and electric displacement is given by

$$\vec{D} = \vec{E} + \vec{P} \quad , \tag{2.161}$$

where $\vec{P}$ is the polarization of the medium and is equal to the density of the electric dipoles induced by the electric field. The polarization can be assumed in the linear approximation as [see Eq. (2.99)]

$$\vec{P} = \alpha\vec{E} \quad , \tag{2.162}$$

where α is the polarizability (susceptibility) tensor. We can find from Eqs. (2.161) and (2.162) that

$$\vec{D} = (1 + \alpha)\vec{E} = \varepsilon\vec{E} \quad , \tag{2.163}$$

where ε is the second-rank dielectric constant tensor [see, *e.g.*, Eqs. (2.112) and (2.136)]. The polarization is equal to N(-e)X. Thus, the frequency-dependent dielectric constant can be written from Eq. (2.160) as

$$\varepsilon(\omega) = 1 + \frac{Ne^2}{m(\omega_0^2 - \omega^2 - i\Gamma\omega)} \quad . \tag{2.164}$$

The classical result (2.164) refers to a single atomic transition frequency. The polarizability of a solid of atoms having many excitation frequencies

ω_{0i} is calculated by dividing the N harmonic oscillators into fractions (N_i/N) which have frequency ω_{0i} and damping parameter Γ_i. The dielectric constant is, then, given by a sum of terms like those in Eq. (2.164), one for each group of oscillators,

$$\varepsilon(\omega) = 1 + \sum_i \frac{N_i e^2}{m(\omega_{0i}^2 - \omega^2 - i\Gamma_i\omega)} \quad , \tag{2.165}$$

where

$$\sum_i \left(\frac{N_i}{N} \right) = 1 \quad . \tag{2.166}$$

When ω is close to one of ω_i, the corresponding term in the summation is dominant, and the remaining contributions can often be neglected.

A quantum theory of the dielectric constant can be obtained by calculating the electric-dipole-moment operator form quantum-mechanical concepts. Consider a system described in the Schrödinger representation by a wave function $\Psi(t)$ which satisfies [time-dependent Schrödinger equation]

$$\mathcal{H}(t)\Psi(t) = i\hbar \frac{\partial\Psi(t)}{\partial t} \quad . \tag{2.167}$$

Here, $\mathcal{H}(t)$ is the total time-dependent Hamiltonian of the system, being given by

$$\mathcal{H}(t) = \mathcal{H}_0 + \mathcal{H}_{ED}(t) \quad . \tag{2.168}$$

$\mathcal{H}_0$ is the Hamiltonian of the system in the absence of the electromagnetic radiation, and $\mathcal{H}_{ED}(t)$ is the Hamiltonian of the electric-dipole interaction written as (dipole approximation)

$$\mathcal{H}_{ED}(t) = - \sum_j e\vec{r}_j \cdot \vec{E}(t) = M\vec{E}(t) \quad , \tag{2.169}$$

where

$$M = - \sum_j e\vec{r}_j \tag{2.170}$$

is the electric-dipole-moment operator. The summation is over all particles in a unit volume. The electric field is now given by

$$\vec{E} = \frac{1}{2}\vec{E}_0[\ \exp(i\omega t) + \exp(-i\omega t)\ ] \quad . \tag{2.171}$$

Thus, at time t, when the wave function is $\Psi(t)$, the electric dipole moment is

$$M(t) = \int \Psi^*(t) M \Psi(t) dV \tag{2.172a}$$

or equivalently

$$M(t) = \langle\Psi|M|\Psi\rangle \quad . \tag{2.172b}$$

Let us suppose that ω is close to a single transition of frequency ω_0 between two states ϕ_m and ϕ_n having energies $\hbar\omega_m$ and $\hbar\omega_n$. The remaining energy levels are ignored for the present, and the general form of the wave function is then

$$\Psi(t) = a_m(t)\phi_m \exp(-i\omega_m t) + a_n(t)\phi_n \exp(-i\omega_n t) \quad . \tag{2.173}$$

The time-dependent coefficients $a_m(t)$ and $a_n(t)$ must be obtained by solutions of the following equations:

$$a_m\langle\phi_m|H_{ED}|\phi_m\rangle + a_n\langle\phi_m|H_{ED}|\phi_n\rangle\exp(-i\omega_0 t) = i\hbar\dot{a}_m \tag{2.174}$$

and

$$a_m\langle\phi_n|H_{ED}|\phi_m\rangle\exp(i\omega_0 t) + a_n\langle\phi_n|H_{ED}|\phi_n\rangle = i\hbar\dot{a}_n \tag{2.175}$$

Substituting Eq. (2.173) into Eq. (2.172), we obtain

$$M(t) = a_m^* a_n\langle\phi_m|M|\phi_n\rangle\exp(-i\omega_0 t) + a_n^* a_m\langle\phi_n|M|\phi_m\rangle\exp(i\omega_0 t) \quad . \tag{2.176}$$

The electric dipole moment given by Eq. (2.176) is a real quantity as expected physically. The second derivative of Eq. (2.176) with respect to "t" gives

$$M(t) = -i\omega_0[(\dot{a}^*_m a_n + a^*_m \dot{a}_n - i\omega_0 a^*_m a_n)\langle\phi_m|M|\phi_n\rangle \exp(-i\omega_0 t)$$

$$- (\dot{a}^*_n a_m + a^*_n \dot{a}_m + i\omega_0 a^*_n a_m)\langle\phi_n|M|\phi_m\rangle \exp(i\omega_0 t)]$$

$$= (2\omega_0^2 |\langle\phi_m|M|\phi_n\rangle|^2 \cos\omega t)(|a_m|^2 - |a_n|^2) - \omega_0^2 M(t) \quad . \qquad (2.177)$$

The applied electric field is assumed to be sufficiently weak that the atomic populations suffer a negligible disturbance from their thermal equilibrium values, so that in Eq. (2.177) $|a_n|^2$ can be neglected and $|a_m|^2$ set equal to unity. Thus, we obtain

$$\ddot{M}(t) + \omega_0^2 M(t) = 2\omega_0^2 |\langle\phi_m|M|\phi_n\rangle|^2 \cos\omega t \quad . \qquad (2.178)$$

The quantity M(t) now represents the dipole moment per atom at time, and the macroscopical polarization of the solid is simply

$$P(t) = NM(t)/V \quad . \qquad (2.179)$$

The differential equation (2.178) is easily solved, and the resulting dielectric constant obtained from comparison of Eq. (2.179) with Eqs. (2.162) and (2.163) is

$$\varepsilon(\omega) = 1 + \frac{N|\langle\phi_m|M|\phi_n\rangle|^2}{V\varepsilon_0\hbar} \cdot \frac{2\omega_0}{\omega_0^2 - \omega^2} \quad . \qquad (2.180)$$

It is obvious from comparison of Eq. (2.180) with Eq. (2.164) that the quantum-mechanical expression is very similar to the classical one if the phenomenological damping parameter Γ is taken into account in Eq. (2.180). The quantum-mechanical expression for the dielectric constant of a solid having many transition frequencies ω_{0i} can also be obtained by a generalization of the method used for a single transition ω_0. The result is written as

$$\varepsilon(\omega) = 1 + \frac{N}{V\varepsilon_0\hbar} \sum_i \frac{2\omega_{0i} |\langle\phi_m|M|\phi_i\rangle|^2}{\omega_{0i}^2 - \omega^2} \quad . \tag{2.181}$$

In the following, we shall obtain the model dielectric constants in semiconductors based on simplified models of the interband transitions. First, we consider the contribution of the free electron-hole pairs or direct band-to-band transitions to the dielectric constant. It is a good approximation to assume that the band edge in semiconductors such as II-VI compounds is parabolic in $\vec{k}$-space, *e.g.*,

$$\hbar\omega_g(\vec{k}) = E_g(\vec{k}) + \frac{\hbar^2 k^2}{2\mu} \quad , \tag{2.182}$$

where μ is the reduced effective mass given in Eq. (2.26). We obtain the real part of the dielectric constant as an analogy to Eq. (2.164) or (2.180):

$$\varepsilon_1^F(\omega) - 1 = \frac{8\pi e^2}{3m^2\hbar} \sum_k \frac{|P(\vec{k})|^2}{[\omega_g(\vec{k})^2 - \omega^2 - i\Gamma\omega]\omega_g(\vec{k})} \quad , \tag{2.183}$$

where $P(\vec{k})$ is the $\vec{k}$-dependent momentum matrix element. Substituting Eq. (2.182) into Eq. (2.183) and converting the summation of k into an integral, we finally obtain

$$\varepsilon_1^F - 1 = C_0 \, f(x_0) \quad , \tag{2.184}$$

where

$$f(x_0) = x^{-2}[2 - (1 - x)^{\frac{1}{2}} - (1 + x)^{\frac{1}{2}}] \quad , \tag{2.185}$$

$$C_0 = \frac{2}{3} (3/2\,\mu)^{3/2} \, \omega_g^{-3/2} P^2 \quad , \tag{2.186}$$

$$x_0 = \omega/\,\omega_g \quad . \tag{2.187}$$

To obtain Eq. (2.184), we separated the real and imaginary parts and carried out the integration. Equation (2.184) is, thus, only valid in the region of

non absorption (i.e., $x < 1$). Moreover, for simplicity, we assumed that the matrix element P is $\vec{k}$-independent quantity.

It is well known that the contribution of the E_0 gap to the imaginary part of the dielectric constant can be written as

$$\varepsilon_2^F(\omega) = C_0 \frac{1}{\omega^2} (\omega - \omega_g)^{\frac{1}{2}} \quad , \tag{2.188}$$

where C_0 is given by Eq. (2.186). The real part of the dielectric constant can also be calculated from Eq. (2.188) by using the following Kramers-Kronig relations:

$$\varepsilon_1(\omega) = 1 + \frac{2}{\pi}\int_0^\infty \frac{\omega'\varepsilon_2(\omega')}{(\omega')^2 - \omega^2} d\omega' \quad , \tag{2.189a}$$

$$\varepsilon_2(\omega) = -\frac{2\omega}{\pi}\int_0^\infty \frac{\varepsilon_1(\omega')}{(\omega')^2 - \omega^2} d\omega' \quad . \tag{2.189b}$$

Substituting Eq. (2.188) into Eq. (2.189a), we obtain the same result as Eq. (2.185).[85-87] It is noting that the result (2.185) is based on the simple band model but not on the complex band structure connecting with overlapping of bands. If we consider crystals having the band structures given in Fig. 2-8, the contributions from the three valence bands must be included. In such a case, we obtain

$$\varepsilon_1^F(\omega) - 1 = \sum_{i=A,B,C} C_{0i} f(x_{0i}) \quad , \tag{2.190}$$

where

$$C_{0i} = \frac{2}{3} (3/2\mu)^{3/2} \omega_{gi}^{-3/2} |\langle c|P|i\rangle|^2 \quad , \tag{2.191}$$

$$x_{0i} = \omega/\omega_{gi} \quad . \tag{2.192}$$

In Eq. (2.191), $|\langle c|P|i\rangle|^2$ is the squared p-matrix element corresponding to the dipole transition between the i-valence band (i = A, B or C) and conduction

band, and ω_{gi} is the energy difference between the i-valence and conduction band (i.e., band-gap energy). For the zincblende-type crystals [see Fig. 2-8(b)], Eq. (2.190) becomes

$$\varepsilon_1^F(\omega) - 1 = C_{0z}\ [f(\frac{\omega}{\omega_0}) + \frac{1}{2}(\frac{\omega_0}{\omega_{os}})^{3/2} f(\frac{\omega}{\omega_{os}})] \quad , \qquad (2.193)$$

where

$$C_{0z} = \frac{4}{3}(3/2\ \mu)\ \omega_0^{-3/2}\ P^2 \quad , \qquad (2.194)$$

$$\hbar\omega_0 = E_0 \quad , \qquad (2.195a)$$

$$\hbar\omega_{os} = E_0 + \Delta_0 \quad . \qquad (2.195b)$$

In Eq. (2.193), we assumed that

$$|\langle c|P|i\rangle|^2 = P^2 \quad (i = A,\ B \text{ or } C) \quad . \qquad (2.196)$$

Next, we consider the contribution from the Wannier-Mott exciton transitions. For the discrete exciton transitions, the imaginary part of the dielectric constant is given by [68,88]

$$\varepsilon_2^D(E) = \sum_{i=A,B,C} \frac{f_i^D}{E^2} \sum_{i=1}^{\infty} |\phi_n(0)|^2 \delta(E_{ex}^n - E) \quad , \qquad (2.197)$$

where $\phi_n(0)$ is the envelope function of the n-th exciton state given by Eq. (2.49), E_{ex}^n is the n-th exciton energy given by Eq. (2.50), and f_i^D is the strength parameter proportional to the squared p-matrix element $|\langle c|P|i\rangle|^2$. The imaginary part of the dielectric constant is directly related to the absorption coefficient

$$\varepsilon_2(E) = \frac{\lambda n(E)}{2\pi}\alpha(E) \quad , \qquad (2.198)$$

where α is the absorption coefficient, λ is the wavelength of light, and n is the refractive index. The Kramers-Kronig transformation of Eq. (2.197) gives

$$\varepsilon_1^D(E) - 1 = \sum_{i=A,B,C} F_i^D \left\{ \sum_{n=1}^{\infty} \frac{1}{n^3[(E_{ex}^n)^2 - E^2]} \right\} , \qquad (2.199)$$

where, for simplicity, we replaced $2E_{ex}^n n^3 f_i^D |\phi_n(0)|^2 \pi^{-1}$ by F_i^D.

If there is a continuum of states, the imaginary part of the dielectric constant is written as[68,88]

$$\varepsilon_2^C(E) = \sum_{i=A,B,C} \frac{f_i^C}{E^2} \sum_k |\phi_k(0)|^2 \rho(E)\delta(E_{ex}^k - E) \; ; \; E > E_{gi} , \qquad (2.200)$$

where $\phi_k(0)$ is the envelope function of the continuum exciton state given by Eq. (2.51), E_{ex}^k is the energy of the continuum exciton state given by Eq. (2.53), f_i^D is the strength parameter proportional to the squared p-matrix element and $(E - E_{gi})^{-\frac{1}{2}}$, and $\rho(E)$ is the density-of-states function

$$\rho(E) = \frac{1}{2\pi^2} \left(\frac{2\mu}{\hbar^2} \right)^{\frac{1}{2}} (E - E_{gi})^{\frac{1}{2}} . \qquad (2.201)$$

The real part of the dielectric constant can be obtained by substituting Eq. (2.200) into Eq. (2.189). If the function of Eq. (2.51) is assumed to be

$$\frac{\pi\alpha\exp(\pi\alpha)}{\sinh(\pi\alpha)} = \frac{2\pi\alpha}{1 - \exp(-2\pi\alpha)} \simeq 2\pi\alpha , \qquad (2.202)$$

the Kramers-Kronig transformation gives[89]

$$\varepsilon_1^C(E) - 1 = \sum_{i=A,B,C} F_i^C \left(\frac{E_{i1}}{4G} \frac{1}{E^2} \ln \frac{E_{gi}^2}{E_{gi} - E^2} \right) , \qquad (2.203)$$

where F_i^C is thestrength-parameter constant having similar physical meanings as F_i^D of Eq. (2.199) and E_{i1} is the ground-state exciton energy. In the limit $G \to 0$, we also obtain

$$\varepsilon_1^C(\omega) - 1 = \sum_{i=A,B,C} \frac{F_i^C E_{i1}}{G^{3/2} E_{gi}^{1/2} \hbar^2} f(x_i) , \qquad (2.204)$$

where the dispersive term $f(x_i)$ has the same form as Eq. (2.190). This result reflects that if the exciton interaction is very small ($G \to 0$) the continuum exciton transitions behave like free electron-hole characteristics, as similar to the case discussed in Section 2.2.2.

Finally, we obtain the real part of the model dielectric constant of solids in the following form:

$$\varepsilon_1(E) = \varepsilon_1^F(E) + \varepsilon_1^D(E) + \varepsilon_1^C(E) + \varepsilon_{1\infty} \quad , \qquad (2.205)$$

where $\varepsilon_1^F(E)$, $\varepsilon_1^D(E)$ and $\varepsilon_1^C(E)$ are given by Eqs. (2.190), (2.199) and (2.203) [or (2.204)], respectively, and $\varepsilon_{1\infty}$ is the background dielectric constant arising from the higher-gap transitions such as the E_1, $E_1+\Delta_1$ and E_2 transitions. The strength parameters C_{0i}, F_i^D and F_i^C can be directly determined by fitting the expression (2.205) to the experimental data of refractive indices ($\varepsilon_1 = n^2$). The imaginary part of the dielectric constant is proportional to the absorption coefficient α according to the relation (2.198). This part is also related to reflectance R through the Kramers-Kronig transformation. Therefore, it is also possible to determine the strength parameters from the absorption or reflectance measurement.[69,90] It is noting that the discrete-exciton term ε_1^D shows sharp dispersion compared with the continuum exciton ε_1^C or the free electron-hole pair term ε_1^F. It is also clear from a comparison of Eq. (2.190) with Eq. (2.204) that the free electron-hole pair term is very similar to the continuum-exciton term. It is, thus, practical to include the free electron-hole pair term (or *vice versa* the continuum-exciton term) into the continuum-exciton term (the free electron-hole term) by introducing an extra parameter C in the strength constant, i.e.,

$$\varepsilon_1(E) = \varepsilon_1^D(E) + C\varepsilon_1^C(E) + \varepsilon_{1\infty} \quad . \qquad (2.206)$$

2.3.2 *Photoelastic Constant*

In Section 2.2.4, we showed from a macroscopical point of view that the Brillouin-scattering intensity can be expressed in terms of the corresponding photoelastic constant of the crystal. The numerical values of the photoelastic constants can be independently determined from the intrinsic-piezobirefringence measurements. The purpose of this subsection is to obtain the basic expression of the photoelastic constant from microscopical aspect. It is well known that uniaxial stress splits the degenerate valence band at $\vec{k} = 0$ of the zincblende-type crystal into two bands. The effect of such splitting could be investigated in suitable optical experiments. For example, Thomas[91] has measured the splitting of the exciton line in CdTe from the reflectance measurement. Such a measurement enables us to obtain information about the deformation potential because the splitting is strongly connected with this potential.[72] It is also obvious that the splitting of the valence band under the uniaxial stress would lead to the birefringence of the crystal. The piezo-birefringence, which is an old topic of crystal optics, could be described phenomenologically by the photoelastic constants or piezo-optical coefficients.[42] The sound wave propagating in a crystal, on the other hand, produces the dynamical elastic strain through the elastic displacements of compositional atoms [see Eq. (2.70)]. This strain produces the fluctuation in the dielectric constant of the crystal. The fluctuation in the dielectric constant is a linear function of the elastic strain connected with the photoelastic constant, as expressed by Eq. (2.111). Thus, the Brillouin-scattering phenomena are thought to be described by a phenomenological formalism analogous to that of the intrinsic piezobirefringence phenomena. In Fig. 2-9, we show a schematic of (a) the Brillouin-scattering and (b) intrinsic-piezobirefringence measurement. Note that the change in the dielectric constant is arising from the dynamical strain for the Brillouin-scattering experiment while this is arising from the

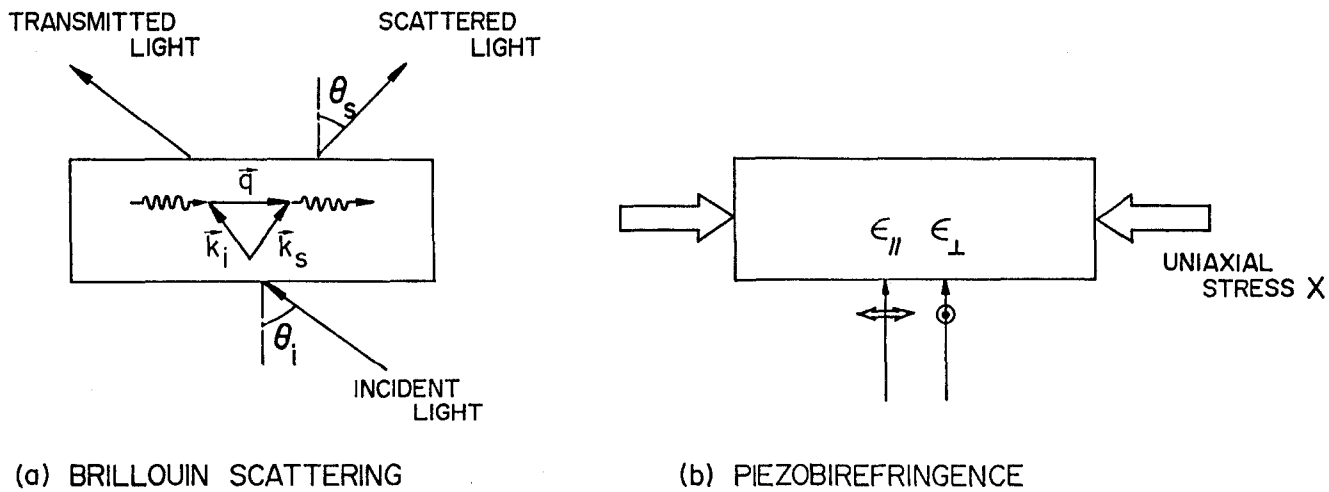

FIG. 2-9. Schematic representations of (a) Brillouin-scattering and (b) intrinsic-piezobirefringence measurement. The conservation of momentum (wavevector) is indicated in (a). θ_i and θ_s are the incident and scattering angles, respectively. ε is the dielectric constant of the crystal.

static strain produced by applying a uniaxial stress for the intrinsic-piezobirefringence experiment.

When a uniaxial stress is applied to a crystal having diamond or zincblende structure the crystal becomes birefringent. The intrinsic piezobirefringence is usually measured with linearly polarized light which propagates along a direction perpendicular to that of the applied stress.[64] Two linearly polarized waves with the amplitudes $E_{\parallel}$ (parallel to the stress direction) and $E_{\perp}$ (perpendicular to the stress direction) will propagate through the crystal. The components of the electric vectors of these waves, as a function of the position x in the crystal, can be written as

$$E_{\parallel}(x) = E_0 \exp[i(2\pi n_{\parallel} x/\lambda - \omega t)] \exp(-2\pi k_{\parallel} x/\lambda) \quad , \qquad (2.207a)$$

$$E_{\perp}(x) = E_0 \exp[i(2\pi n_{\perp} x/\lambda - \omega t)] \exp(-2\pi k_{\perp} x/\lambda) \quad , \qquad (2.207b)$$

where E_0 is the amplitude of the incident wave, and ω and λ are the angular frequency and wavelength in vacuum, respectively. $n^*_{\parallel} = n_{\parallel} + ik_{\parallel}$ ($n^*_{\perp} = n_{\perp} + ik_{\perp}$) is the complex refractive index for light polarized parallel (perpendicular) to the stress axis (n is the real refractive index and k is the attenuation index, also called the extinction coefficient). Equation (2.207) represents a wave traveling in x-direction with velocity c/n (c: light velocity in vacuum) which is attenuated by $\exp(-2\pi kx/\lambda)$. In the intrinsic-piezobirefringence experiments, one measures the phase difference between the components of the light polarized parallel and perpendicular to the stress axis. The phase difference per unit path length (d) is given by

$$\frac{\Delta}{d} = 2\pi(n_{\parallel} - n_{\perp}) / \lambda \quad . \qquad (2.208)$$

In a region where the absorption is small (i.e., $\varepsilon_2 \simeq 0$), the difference of the refractive indices ($n_{\parallel} - n_{\perp}$) can be written as

$$\Delta n \equiv (n_{\parallel} - n_{\perp}) = \frac{n_{\parallel}^{2} - n_{\perp}^{2}}{n_{\parallel} + n_{\perp}} = \frac{\varepsilon_1^{\parallel} - \varepsilon_1^{\perp}}{2n_0} \equiv \frac{\Delta\varepsilon_1}{2n_0} \quad , \tag{2.209}$$

where n_0 is the real refractive index in the absence of the applied stress. The photoelastic constant p_{ijkl} is defined by the equation:[42]

$$\Delta\left(\frac{1}{\varepsilon}\right)_{ij} = \frac{-\Delta\varepsilon_{ij}}{\varepsilon_{ii}\varepsilon_{jj}} = \sum_{kl} p_{ijkl} e_{kl} \quad , \tag{2.210}$$

where $\left(\frac{1}{\varepsilon}\right)_{ij}$ is the reciprocal of the dielectric constant tensor. The strain [e] and stress [X] tensors are related by a fourth-rank compliance tensor [S]:

$$e_{ij} = \sum_{kl} S_{ijkl} X_{kl} \quad , \tag{2.211}$$

where S has the same tensor form as Eq. (2.114) or (2.139). The piezo-optical constant π_{ijkl} is also defined by the following equation:

$$\Delta\left(\frac{1}{\varepsilon}\right)_{ij} = \frac{-\Delta\varepsilon_{ij}}{\varepsilon_{ii}\varepsilon_{jj}} = \sum_{kl} \pi_{ijkl} X_{kl} \quad . \tag{2.212}$$

The piezobirefringence coefficient α defined by Yu and Cardona[92] can now be given from Eq. (2.210) by

$$\alpha = \frac{\Delta\varepsilon_{ij}}{X} = -\sum_{mn} \varepsilon_{ii}\varepsilon_{jj} p_{ijkl} S_{klmn} \quad . \tag{2.213}$$

In Eqs. (2.210), (2.212) and (2.213), ε_{ij} is the real part of the component of dielectric constant tensor. If the piezobirefringence measurement is carried out in an opaque region (i.e., $\varepsilon_2 = 0$), we must take into account the contributions both from the real and imaginary parts of the dielectric constant. Details of such a case will be presented in Chapter VI.

Now, we show the effects of [001] and [110] stress for the zincblende-type crystal. For the [001] stress, the strain tensor is written from Eqs. (2.113) and (2.211) as

$$[e]_{001} = \begin{bmatrix} S_{12}X & 0 & 0 \\ 0 & S_{12}X & 0 \\ 0 & 0 & S_{11}X \end{bmatrix} \quad . \tag{2.214}$$

Substituting Eq. (2.214) into Eq. (2.210) or (2.212), we obtain

$$\Delta\varepsilon_{[001]} = - \varepsilon_{11}{}^{2}(p_{11} - p_{12})(S_{11} - S_{12})X \tag{2.215a}$$

or

$$\Delta\varepsilon_{[001]} = - \varepsilon_{11}{}^{2}(\pi_{11} - \pi_{12})X \quad . \tag{2.215b}$$

For the [110] stress, the strain tensor becomes

$$[e]_{110} = \begin{bmatrix} (S_{11}+S_{12})X/2 & S_{44}X/4 & 0 \\ S_{44}X/4 & (S_{11}+S_{12})X/2 & 0 \\ 0 & 0 & S_{12}X \end{bmatrix} \quad . \tag{2.216}$$

We can, thus, obtain

$$\Delta\varepsilon_{[110]} = - \varepsilon_{11}{}^{2}p_{44}S_{44}X \tag{2.217a}$$

or

$$\Delta\varepsilon_{[110]} = - \varepsilon_{11}{}^{2}\pi_{44}X \quad . \tag{2.217b}$$

Note that the result (2.217) is the same as for the [111] stress.[64]

For the wurtzite-type crystal, the analysis is identical to that for the zincblende-type crystal. However, it becomes more difficult compared with that for the zincblende-type crystal because of the optically anisotropic nature of this material. We now show a typical example of such analyses which corresponds to the geometric configuration for the determination of the photoelastic constant p_{66}. In this case, the uniaxial stress is applied in plane perpendicular to the c-axis. If we choose the coordinate system such that the x-axis is parallel to the direction of the applied stress, the strain

tensor becomes

$$[e]_{\perp c} = \begin{bmatrix} S_{11}X & 0 & 0 \\ 0 & S_{12}X & 0 \\ 0 & 0 & S_{31}X \end{bmatrix} . \tag{2.218}$$

From Eqs. (2.210) and (2.218), we finally obtain

$$\Delta\varepsilon_{\perp c} = - \varepsilon_{11}\varepsilon_{22}(p_{11} - p_{12})(S_{11} - S_{12})X = - \varepsilon_{11}{}^2 p_{66}S_{66}X , \tag{2.219}$$

where

$$p_{66} = \frac{1}{2} (p_{11} - p_{12}) \quad , \tag{2.220a}$$

$$S_{66} = 2 (S_{11} - S_{12}) \quad . \tag{2.220b}$$

To first order in stress, the change in $\varepsilon_1(\omega)$ can be expressed by[39]

$$[\Delta\varepsilon_1(\omega)] = \frac{\partial\varepsilon_1}{\partial X} X = \sum_{i=A,B,C} \left(\frac{\partial\varepsilon_1}{\partial M_i} \Delta M_i + \frac{\partial\varepsilon_1}{\partial\omega_{gi}} \Delta\omega_{gi} \right) , \tag{2.221}$$

where $M = |\langle|p|\rangle|^2$ is the squared p-matrix element and the summation indicates that contributions from the three valence bands must be included. The first and second terms on the right-hand side of Eq. (2.221) correspond to the contributions from the first-order change in the squared p-matrix elements and interband transition energies, respectively. To calculate the changes in M_i and ω_{gi}, we can use the orbital-strain Hamiltonian Eq. (2.66) or (2.85) as a Hamiltonian for the stress effect on the electronic band structure of the crystal.

By way of example, let us calculate the changes in ω_{gi} and M_i in the case of the zincblende-type crystal for the [001] stress direction. As already shown in Fig. 2-8, without spin-orbit splitting the valence band edge at $\vec{k} = 0$ in the zincblende-type crystal is a six-fold degenerate multiplet with orbital symmetry Γ_{15}. The spin-orbit interaction lifts this degeneracy into a four-fold multiplet (Γ_8) and a two-fold multiplet (Γ_7). The spin-orbit Hamiltonian

is[93]

$$H_{so} = \frac{\Delta_{so}}{3\hbar} L \cdot \sigma \quad , \tag{2.222}$$

where L is the orbital-angular momentum operator given by Eq. (2.67) and σ is the Pauli-spin matrices[78]

$$\sigma_x = \begin{bmatrix} 0 & 1 \\ 1 & 0 \end{bmatrix} , \quad \sigma_y = \begin{bmatrix} 0 & -i \\ i & 0 \end{bmatrix} , \quad \sigma_z = \begin{bmatrix} 1 & 0 \\ 0 & -1 \end{bmatrix} \quad . \tag{2.223}$$

The total Hamiltonian is, thus,

$$H = H_{ev} + H_{so} \quad . \tag{2.224}$$

Substituting Eq. (2.214) into Eq. (2.66), we obtain

$$H_{ev} = - \; E_H - \frac{3}{2} \delta E_{001} (L_z^{\,2} - \frac{1}{3} \mathbf{L}^2) \quad , \tag{2.225}$$

where

$$\delta E_H = a \; (S_{11} + 2S_{12}) X \quad , \tag{2.226a}$$

$$\delta E_{001} = 2b \; (S_{11} - S_{12}) X \quad . \tag{2.226b}$$

From Eqs. (2.224), (2.225) and (2.75), the Hamiltonian matrix for the valence bands becomes[75]

$$\| H \| = \begin{array}{c} \begin{array}{ccc} |B\rangle & |A\rangle & |C\rangle \end{array} \\ \left\| \begin{array}{ccc} \frac{1}{3}\Delta_{so} - \delta E_H - \frac{1}{2}\delta E_{001} & 0 & 0 \\ 0 & \frac{1}{3}\Delta_{so} - \delta E_H + \frac{1}{2}\delta E_{001} & \frac{\sqrt{2}}{2}\delta E_{001} \\ 0 & \frac{\sqrt{2}}{2}\delta E_{001} & -\frac{2}{3}\Delta_{so} - \delta E_H \end{array} \right\| \end{array} \quad . \tag{2.227}$$

The diagonalization of Eq. (2.227) gives

$$\| H \| = \begin{array}{c} \begin{array}{ccc} |B'\rangle & |A'\rangle & |C'\rangle \end{array} \\ \left\| \begin{array}{ccc} B & 0 & 0 \\ 0 & A & 0 \\ 0 & 0 & C \end{array} \right\| \end{array} \quad , \tag{2.228}$$

where the eigenvalues are

$$A = -\frac{1}{6}\Delta_{so} - \delta E_H + \frac{1}{4}\Delta E_{001} + \frac{1}{2}[\Delta_{so}^2 + \Delta_{so}\delta E_{001} + \frac{9}{4}(\delta E_{001})^2]^{\frac{1}{2}} \quad , \tag{2.229a}$$

$$B = -\frac{1}{3}\Delta_{so} - E_H - \frac{1}{2}\delta E_{001} \quad , \tag{2.229b}$$

$$C = -\frac{1}{6}\Delta_{so} - \delta E_H + \frac{1}{4}\delta E_{001} - \frac{1}{2}[\Delta_{so}^2 + \Delta_{so}\delta E_{001} + \frac{9}{4}(\delta E_{001})^2]^{\frac{1}{2}} \quad . \tag{2.229c}$$

Assuming $\delta E_{001} \ll \Delta_{so}$, the changes in the band-gap energies to first order in stress are given from Eq. (2.228) by

$$\Delta E_{gA} = -\frac{1}{3}\Delta_{so} + \delta E_H - \frac{1}{2}\delta E_{001} \quad , \tag{2.230a}$$

$$\Delta E_{gB} = -\frac{1}{3}\Delta_{so} + \delta E_H + \frac{1}{2}\delta E_{001} \quad , \tag{2.230b}$$

$$\Delta E_{gC} = \frac{2}{3}\Delta_{so} + \delta E_H \quad . \tag{2.230c}$$

The eigenvectors of Eq. (2.227) to first order in stress can be expressed as

$$|A'\rangle = |A\rangle + \frac{\delta E_{001}}{\sqrt{2}\Delta_{so}}|C\rangle \quad , \tag{2.231a}$$

$$|B'\rangle = |B\rangle \quad , \tag{2.231b}$$

$$|C'\rangle = |C\rangle + \frac{\delta E_{001}}{\sqrt{2}\Delta_{so}}|A\rangle \quad . \tag{2.231c}$$

The squared p-matrix element M is given by

$$M = |\langle c|\vec{e}\cdot\vec{p}|i\rangle|^2 \quad , \tag{2.232}$$

where $\vec{e}$ is the unit polarization vector of the electric field of the incident radiation and $\vec{p}$ is the linear momentum operator

$$\vec{p} \rightarrow \frac{\hbar}{i}\nabla \quad . \tag{2.233}$$

$|c\rangle$ is the conduction-band wave function which transforms as an atomic *s* function

under the operations of the group of the tetrahedron [see Eq. (2.62)]. The changes in the squared p-matrix elements can be obtained from Eq. (2.232) by replacing $|i\rangle$ by the perturbed wave function $|A'\rangle$, $|B'\rangle$ or $|C'\rangle$ of Eq. (2.231). The strain-dependent p-matrix elements are now written as

$$M_{\parallel A}(e) = |\langle c|p_{\parallel}|A'\rangle|^2 = |\langle c|\frac{\hbar\partial}{i\partial Z}|A'\rangle|^2 \simeq \frac{2}{3}P^2[1+(\delta E_{001}/\Delta_{so})], \quad (2.234a)$$

$$M_{\perp A}(e) = |\langle c|p_{\perp}|A'\rangle|^2 = |\langle c|\frac{\hbar\partial}{i\partial X}|A'\rangle|^2 \simeq \frac{1}{6}P^2[1-2(\delta E_{001}/\Delta_{so})], \quad (2.234b)$$

$$M_{\parallel B}(e) = |\langle c|p_{\parallel}|B'\rangle|^2 = |\langle c|\frac{\hbar\partial}{i\partial Z}|B'\rangle|^2 = 0 \quad , \quad (2.234c)$$

$$M_{\perp B}(e) = |\langle c|p_{\perp}|B'\rangle|^2 = |\langle c|\frac{\hbar\partial}{i\partial X}|B'\rangle|^2 = \frac{1}{2}P^2 \quad , \quad (2.234d)$$

$$M_{\parallel C}(e) = |\langle c|p_{\parallel}|C'\rangle|^2 = |\langle c|\frac{\hbar\partial}{i\partial Z}|C'\rangle|^2 \simeq \frac{1}{3}P^2[1-2(\delta E_{001}/\Delta_{so})], \quad (2.234e)$$

$$M_{\perp C}(e) = |\langle c|p_{\perp}|C'\rangle|^2 = |\langle c|\frac{\hbar\partial}{i\partial X}|C'\rangle|^2 \simeq \frac{1}{3}P^2[1+(\delta E_{001}/\Delta_{so})], \quad (2.234f)$$

where subscripts $\parallel$ and $\perp$ indicate light polarized parallel (z) and perpendicular (x) to the stress axis [001]. In Eq. (2.234), we used the following relation:

$$P^2 = |\langle c\uparrow|\frac{\hbar\partial}{i\partial X}|X\uparrow\rangle|^2 = |\langle c\uparrow|\frac{\hbar\partial}{i\partial Y}|Y\uparrow\rangle|^2 = |\langle c\uparrow|\frac{\hbar\partial}{i\partial Z}|Z\uparrow\rangle|^2 \quad (2.235)$$

with similar expressions for spin down. This relation has already been shown from symmetry considerations.[94] Using Eq. (2.63), the zero-strain p-matrix elements are also written from Eq. (2.232) as

$$M_{ZA}(0) = |\langle c|\frac{\hbar\partial}{i\partial Z}|A\rangle|^2 = \frac{2}{3}P^2 \quad , \quad (2.236a)$$

$$M_{XA}(0) = |\langle c|\frac{\hbar\partial}{i\partial X}|A\rangle|^2 = \frac{1}{6}P^2 \quad , \quad (2.236b)$$

$$M_{ZB}(0) = |\langle c|\frac{\hbar\partial}{i\partial Z}|B\rangle|^2 = 0 \quad , \quad (2.236c)$$

$$M_{XB}(0) = |\langle c|\frac{\hbar\partial}{i\partial X}|B\rangle|^2 = \frac{1}{2}P^2 \quad , \quad (2.236d)$$

$$M_{ZC}(0) = |\langle c|\frac{\hbar\partial}{i\partial Z}|C\rangle|^2 = \frac{1}{3}P^2 \quad , \quad (2.236e)$$

$$M_{XC}(0) = |\langle c| \frac{\hbar\partial}{i\partial X} |C\rangle|^2 = \frac{1}{3} P^2 \quad . \tag{2.236f}$$

From Eqs. (2.234) and (2.236), we obtain the stress-induced changes in the squared p-matrix elements as follows:

$$\Delta M_A = (\Delta M_{\parallel A} - \Delta M_{\perp A}) = P^2(\delta E_{001}/\Delta_{so}) \quad , \tag{2.237a}$$

$$\Delta M_B = (\Delta M_{\parallel B} - \Delta M_{\perp B}) = 0 \quad , \tag{2.237b}$$

$$\Delta M_C = (\Delta M_{\parallel C} - \Delta M_{\perp C}) = - P^2(\delta E_{001}/\Delta_{so}) \quad . \tag{2.237c}$$

The change in the real part of the dielectric constant can, thus, be obtained by substituting Eqs. (2.230) and (2.237) into Eq. (2.221). The photoelastic constant, $p_{11} - p_{12}$, can be expressed from Eq. (2.215a) in terms of the stress-induced change $\Delta\varepsilon_1$ as

$$p_{11} - p_{12} = \frac{- \Delta\varepsilon_{[001]}}{\varepsilon_{11}{}^2(S_{11} - S_{12})X} \quad . \tag{2.238}$$

For the [110] or [111] stress direction, the analysis is almost identical to that for the stress along [001]. The piezobirefringence analysis for the wurtzite-type crystal is also identical to that for the zincblende-type crystal. In Section 6.2, we will obtain concrete expressions of the photoelastic constants for both the zincblende- and wurtzite-type crystals in terms of the model dielectric constants presented in this Section.

CHAPTER III

EXPERIMENTAL PROCEDURE AND TECHNIQUE

3.1 INTRODUCTION

The objective of the present study is to measure the spectral dependence of the Brillouin-scattering cross sections in various semiconductors. During the past ten years inelastic-light-scattering spectroscopy has developed into one of the most powerful and most widely used optical techniques for the study of the properties of the elementary excitations in solids.[8] This has been, to some extent, a consequence of the availability of lasers as excitation sources and of improved spectrometers and associated electronics for recording weak light scattering signals. In piezoelectric semiconductors, where the interaction of phonons with free carriers is particularly strong, Hutson, McFee and White[12] demonstrated that acoustical waves could be amplified by carriers with drift velocity exceeding the sound velocity. When high drift fields are applied, intense packets of acoustical waves (domains) are observed to travel along the sample at the sound velocity. It is possible to amplify a selected group of such phonons by a factor of the order of 10^9 above their thermal equilibrium value.[18] Zucker and Zemon[15] were first to examine the spectrum of these phonon domains in CdS by means of the Brillouin-scattering technique. The acoustical-phonon domains have first been used by Garrod and Bray[25] to investigate resonance phenomena of Brillouin scattering in GaAs, where the intense acoustical-phonon domains provide strong scattering signals and thus

permit the use of a continuous light source monochromized by a conventional monochromator instead of a laser. This technique has also been extended by us to semiconductors with weak piezoelectricity such as ZnSe,[95] ZnTe[71] and $Zn_xCd_{1-x}Te$[96] by applying the acoustical-domain injection method.

In Section 3.2, we present some of the physical properties of the materials used in the present study and the sample-preparation method. Next, in Section 3.3, we discuss the details of the Brillouin-scattering technique. In this Section, we also review the theory of acoustoelectrical amplification and present the acoustical-domain injection technique. Moreover, we describe briefly the experimental arrangement used in the present study.

3.2 MATERIAL AND SAMPLE PREPARATION

3.2.1 Material

All measurements reported in the present study were carried out on bulk, single crystals, ZnSe, ZnTe, $Zn_xCd_{1-x}Te$, CdS, GaP, GaSe and GaS. The ZnSe crystals were provided from the Matsushita Electric Industrial Company.* The CdS crystals used were ultra-high purity (UHP) grade and purchased from the Eagle Picher Company. The GaP crystals were provided from the Sumitomo Electric Industries, Ltd.* The GaS crystals were provided from Tohoku University.* The ZnTe, $Zn_xCd_{1-x}Te$ and GaSe crystals were grown by the Bridgman method or the traveling heater method (THM)[97] in our laboratory. In Appendix, we will describe the method of THM used in the present study. In Table 3-1 are listed the crystal structure, conduction-band minima, growth method, electrical resistivity and conduction type for each material. Note that the layered structure of III-VI

---

*The author is grateful to Dr. M. Fukai for providing the ZnSe crystals, to Mr. K. Matsumoto and Dr. T. Suzuki for providing the GaP crystals, and to Dr. Y. Sasaki and Prof. Y. Nishina for providing the GaS crystals.

Table 3-1. Some physical and electrical properties of the materials used in the present study.

Material	Crystal Structure	Conduction-Band Structure	Crystal-Growth Method	Resistivity ($\Omega\cdot$cm)	Conduction Type	Remarks
ZnSe	zincblende	Γ (direct)	Melt Growth	$10^7 - 10^9$	*n*	as-grown
				~ 1	*n*	Zn-treat.
ZnTe	zincblende	Γ (direct)	Melt Growth	~ 20	*p*	
			THM	~ 50	*p*	
$Zn_xCd_{1-x}Te$	zincblende	Γ (direct)	THM	~ 50	*p*	$1.0 \geq x \geq 0.5$
CdS	wurtzite	Γ (direct)	Melt Growth	~ 30	*n*	
GaP	zincblende	X (indirect)	Czochralski			†
GaSe	layer type	M (indirect)	Bridgman	$3\times10^2 \sim 3\times10^3$	*p*	
GaS	layer type	M (indirect)	Bridgman			††

†Provided from the Sumitomo Electric Industries.

††Provided from Tohoku University.

compounds, GaSe and GaS, gives rise to a strong anisotropy in their physical properties due to the singularity of the crystal structure.[47] Such an anisotropic nature will be discussed in detail in Chapter X. In order to study some effects of the crystalline imperfections on the spectral dependence of the Brillouin-scattering cross sections, we have used two kinds of ZnTe and ZnSe single crystals. For ZnTe one is the single crystal grown by the conventional Bridgman method and the other is that grown by the THM. The THM belongs to the solution growth and is a suitable for the growth of perfect crystals. Two kinds of samples for ZnSe, on the other hand, were prepared; one is the as-grown sample grown by a melt-growth technique and the other is that purified in liquid Zn.[98] We made this purification at 1000°C for about 30 hours, where the crystals were sealed in evacuated quartz tube with Zn metal (6-N grade). The Zn-purification is known to be effective particularly in removing Zn vacancies and noble-metal impurities such as Cu and Ag.[98] The ability of this purification technique will be manifested from the photoluminescence measurements [see Chapter VII].

3.2.2 Sample Preparation

All the samples used were cut in the form of parallelepipeds with dimensions of about 0.6 × 1.5 × 5.0 mm. The crystal orientation of all the samples was determined by means of the X-ray Laue back-reflection method or from the cleavage properties of the crystals. They were mechanically polished, chemically etched at room temperature in a HCl : HNO_3 = 1 : 1 mixture (ZnSe, ZnTe, $Zn_xCd_{1-x}Te$ and GaP) and a dilute HCl (CdS), and polished breafly with Syton X30 (Monsanto). The optical-flat surfaces of the layer-type compounds GaSe and GaS were obtained by cleavage with a razor blade and used for the measurements without any additional surface treatment after this step, where the surfaces are perpendicular to the *c*-axis (i.e., *c*-planes).

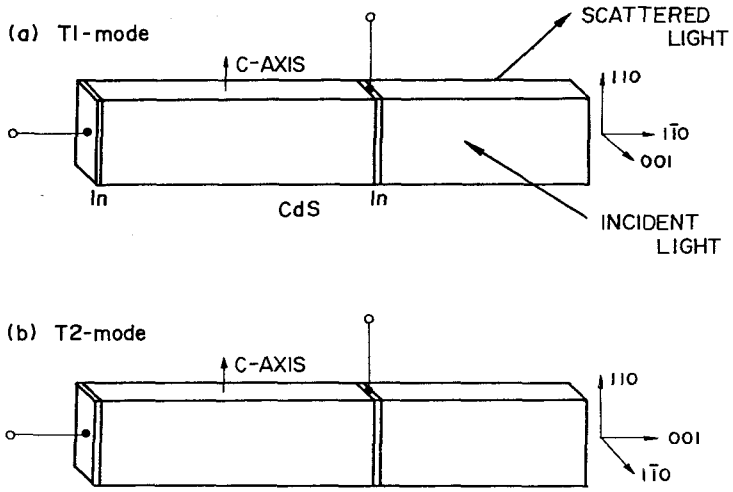

FIG. 3-1. Schematic drawing of the samples used for the acoustical-domain injection method (zincblende-type crystals). The acoustical-phonon domains can be produced by applying a pulse voltage across the CdS specimen.

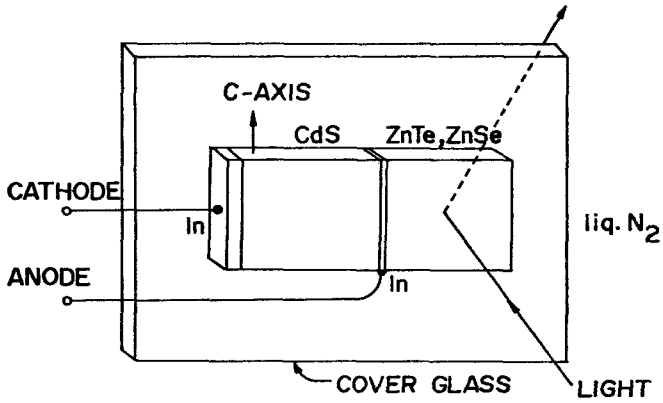

FIG. 3-2. Schematic drawing of the sample used for the Brillouin-scattering measurements at liquid-nitrogen temperature. The sample was mounted on a cover glass and immersed in liquid nitrogen contained in a glass Dewer.

The Brillouin-scattering measurements were carried out by using the acoustical-phonon domains amplified in the piezoelectric semiconductor CdS. Indium electrical contacts were made by vacuum evaporation onto the ends of the CdS samples. In order to obtain a strong phonon flux in semiconductors with weak piezoelectricity such as ZnSe, ZnTe and GaP, the acoustical-phonon domains amplified in CdS have been transmitted into such semiconductors through the end-bonded surfaces by making use of the acoustical-domain injection method.[33,34] Indium layers were deposited for this method by vacuum evaporation onto the end-surfaces of CdS and specimens, and they were bonded by heating the evaporated indium layers. Figure 3-1 shows a schematic drawing of the samples used for the acoustical-domain injection method (zincblende-type crystals). The intense acoustical-phonon domain was produced by applying a pulse voltage across the CdS specimen, where the rod axis of CdS was perpendicular to the c-axis, and the acoustical-phonon domain traveling along the rod axis was excited in CdS with atomic displacement parallel to the c-axis (T2-mode). The indium layer made in such a way provided a high-transmission efficiency of the acoustical-phonon domain from CdS into the specimens especially for lower-frequency phonon domains. By way of example, we obtained transmission efficiency up to 90 % for ZnSe at 0.2 GHz phonon frequency. Details of this technique will be presented in the following subsection [Section 3.3.4].

In order to clarify some temperature effects on the spectral dependence of the Brillouin-scattering cross sections, we have carried out the Brillouin-scattering experiments at room temperature and low temperature (77 K). For measurements at 77 K, a sample was mounted on a cover glass, as shown in Fig. 3-2, and was immersed in liquid nitrogen contained in a glass Dewer.

3.3 BRILLOUIN-SCATTERING TECHNIQUE

3.3.1 Experimental Arrangement

The experimental arrangement is divided into four blocks in the following and each examined in tern. Figure 3-3 shows a schematic diagram of the experimental arrangement used in the Brillouin-scattering experiments.

(1) Light Source and Monochromator

Resonant-light-scattering measurements taken with a few discrete laser lines may sometimes miss sharp structure between discrete points. This can be avoided by using a discrete laser line and tuning the band-gap energy with an external perturbation, *e.g.*, temperature and uniaxial stress. Using this method, Pine[11] has first reported resonance phenomena of the Brillouin-scattering cross sections in CdS, where the fundamental absorption edge of this material is thermally tuned through the incident radiation at 514.5 nm (Ar^+ laser). The intense acoustical-phonon domains, however, permit us the use of a continuous non-coherent light source instead of a laser. In the present study, we used a xenon flash lamp (SUNPAK, GT PRO 4011) as a light source instead of a tunable dye laser. This light source enabled us to measure resonant Brillouin scattering in the wide spectral range from infrared to ultraviolet region (1.0 — 4.0 eV). The monochromator was a JASCO, CT-50S, single pass instrument. This was calibrated with the emission lines from a mercury arc and He-Ne laser line (632.8 nm).

(2) Optical Table and Sample Holder

The sample was mounted on a goniometer stage fitted with a rotatable table (CHUO PRECISION INDUSTRY CO. LTD) which served to determine the angle of incidence of the light. A photomultiplier tube for detecting the scattered light was attached to a rotating arm which was used to select the desired scattering angle. The glass Dewer used for measurements at 77 K was also placed on the rotatable table, where the goniometer stage was removed from this table.

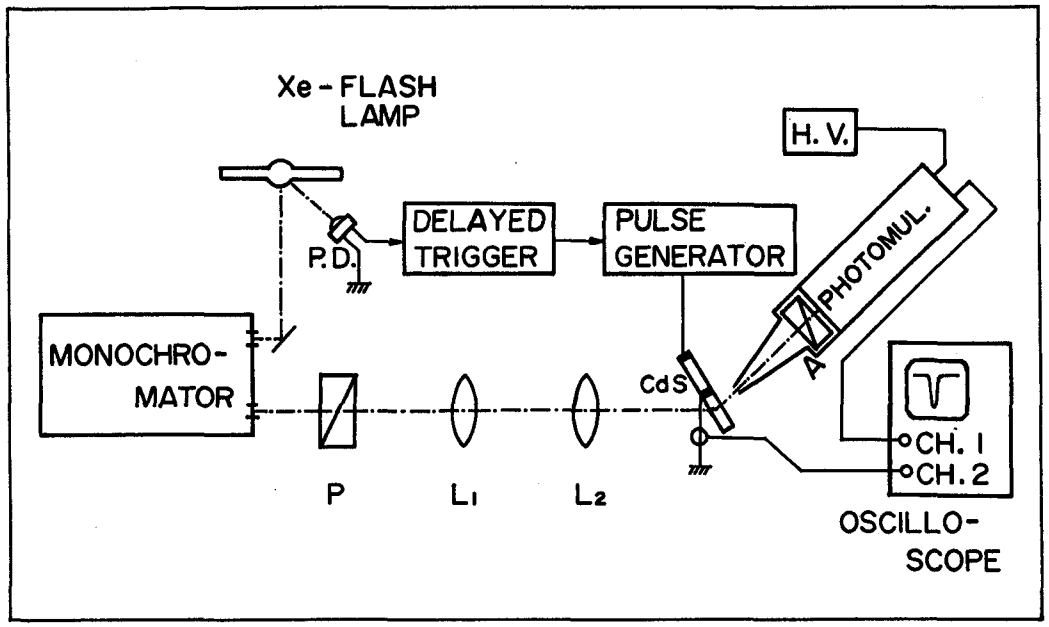

FIG. 3-3. Experimental arrangement used for the Brillouin-scattering measurements.

(3) Domain Generating System

Synchronization of optical and electronic pulses were necessary to measure scattering from the traveling domain when the pulsed light source was at its peak intensity. The domain was generated by the application to the CdS sample of a pulse of about 1000 V and several μsec duration depending on the sample length. The high-voltage pulses were obtained from a Velonex, Model 350, high-power pulse generator. A photo-diode and delayed trigger equipment in Fig. 3-3 were used for this synchronization system.

(4) Detector and Display

The incident light dispersed by the monochromator was focused by lenses, L_1 and L_2, and polarized by a Gran-Thompson prism. The size of light spot at the surface of the specimens was about 0.5 mm in diameter. The scattered light was detected by a photomultiplier tube (RCA 7265) with a Polaroid HN32 analyzer, and displayed on a strage oscilloscope (Tektronics 7623A). The intense acoustical-phonon domains provided strong Brillouin-scattering signals, and thus we measured these signals without the use of conventional photon counting or phase-sensitive detection system.

3.3.2 Growth Mechanism of Acoustical-Phonon Domain

In this subsection, we review the small-signal theory of acoustoelectrical amplification.[14] The increased interest in the physical phenomena due to interaction between free carriers and acoustical waves in solids was triggered off by the experimental results reported by Hutson, McFee and White (1961)[12] on acoustoelectrical amplificatiin in CdS. They observed substantial amplification of ultrasonic waves in photoconductive CdS, produced by applying a dc electric field in the direction of wave propagation. The amplification was found to be so large that sound waves could be amplified from thermal equilibrium amplitudes to values in the non-linear region within distance of

less than a centimeter. The large amplitude acoustical waves had a strong influence on the current-voltage characteristics of the crystals and gave rise to non-uniform electric field distributions, and in some cases to current instabilities. These non-linear effects were investigated by a number of different experimental methods such as field probing, microwave transmission and Brillouin-scattering techniques.[32] Such an acoustoelectrical effect has been found in many piezoelectric semiconductors such as CdS,[99-101] CdSe,[102,103] CdTe,[104,105] ZnO,[106,107] ZnS,[108] GaAs,[109,110] GaSb,[111] InSb,[112] Te[113] and Se.[114]

The linear theory of acoustoelectrical amplification in piezoelectric semiconductors[14] is in satisfactory agreement only for small signals. When a sound wave propagates in a piezoelectric crystal, it will be accompanied by a piezoelectric field which in tern acts on the mobile charge carriers that are present. Let us assume that the acoustical waves produce a piezoelectric potential U_0 in the absence of free carriers. If free carriers are present, U_0 is decreased due to screening effect. The degree of screening depends on the ratio between the wave vector $\vec{q}$ ($|\vec{q}| = q$) of the sound wave and Debye screening length

$$L_D = \left(\frac{\varepsilon k_B T}{e^2 n_0} \right)^{\frac{1}{2}} \quad , \tag{3.1}$$

where ε is the dielectric constant and n_0 is the free carrier concentration. The piezoelectric potential can now be given by

$$U = U_0 (qL_D)^2 / [1 + (qL_D)^2] \quad . \tag{3.2}$$

If $\lambda_s = 2\pi/q$ is long compared with L_D, the screening is strong while the free carrier effects become negligible when λ_s is small compared with L_D.

The small-signal expressions for the acoustical dispersion and amplification (attenuation) were first derived by White.[14] We assume that non-local transport effects can be neglected, i.e., that the following condition is satisfied:

$$q\ell \ll 1 \quad , \tag{3.3}$$

where ℓ is the free carrier mean free path. This condition enables us treatment of the electron-sound wave (acoustoelectrical) interaction from a classical point of view. The energy and momentum may be transferred from the mobile charge carriers to the sound waves when the drift velocity exceeds the sound velocity by the application of a sufficiently high electric field. The acousto-electrical interaction may, thus, be proportional to the drift parameter

$$\gamma = 1 - \frac{v_d}{v_s} \quad , \tag{3.4}$$

where $v_d = \mu E$ is the drift velocity [μ: carrier mobility, E: external electric field] and v_s is the sound velocity. The condition $q\ell \gg 1$, on the other hand, requires much complicated quantum-mechanical descriptions. The experimental data showed that in CdS, as in other piezoelectric semiconductors, the free carrier mean free path was normally very short. We can, therefore, safely consider that the condition (3.3) is satisfactorily fulfilled. Then, with the condition (3.3) one can use a classical macroscopical description. The basic equations of state describing a piezoelectric crystal are

$$T = CS - eE \quad , \tag{3.5a}$$

$$D = eS + \varepsilon E \quad , \tag{3.5b}$$

where C is the elastic stiffness constant at constant electric field, S is the strain [given by the same expression as Eq. (2.70)], e is the piezoelectric constant, E is the electric field, T is the stress and D is the electric displacement. Normally, the quantities in Eq. (3.5) are tensors, but they may be considered scaler if there is only one piezoelectric constant coupling an electric field in the x-direction to an sound wave traveling in the x-direction. Equation (3.5) is supplemented by the wave equation, Poisson's equation, charge-

continuity equation and expression for the current density (J):

$$\rho \frac{\partial^2 S}{\partial t^2} = \frac{\partial^2 T}{\partial x^2} \quad , \tag{3.6a}$$

$$\frac{\partial D}{\partial x} = -e(n - n_0) \quad , \tag{3.6b}$$

$$\frac{\partial J}{\partial x} = e \frac{\partial n}{\partial t} \quad , \tag{3.6c}$$

$$J = ne\mu E + eD \frac{\partial n}{\partial x} \quad , \tag{3.6d}$$

where ρ is the density of crystal, n is the total free carrier concentration, n_0 is the thermal equilibrium concentration and D is the diffusion constant. In the small signal theory, the electric field may be written as

$$E = E_0 + E_1 \exp[i(qx - \omega t)] \quad , \tag{3.7}$$

where E_0 is the field due to an applied dc voltage and E_1 is the sinusoidal field due to the sound wave traveling in a piezoelectric medium. The atomic displacement (u) of the sound wave is of the form [see Eq. (2.69)]:

$$u(x, t) = u \exp[i(qx - \omega t)] \quad . \tag{3.8}$$

Using Eq. (3.5a) for the stress, the wave equation in an elastic medium becomes

$$\rho \left(\frac{\partial^2 u}{\partial t^2} \right) = \frac{\partial T}{\partial x} = C \left(\frac{\partial^2 u}{\partial x^2} \right) - e \left(\frac{\partial E}{\partial x} \right) \quad . \tag{3.9}$$

From Eqs. (3.5) — (3.9), one can calculate the electronic dispersion and amplification (attenuation) of the sound waves. The final results for the sound velocity v_s and the amplification coefficient α due to the acoustoelectrical interaction can be written as

$$v_s = \left(\frac{c}{\rho}\right)^{\frac{1}{2}}\left\{1 + \frac{K^2}{2}\left[1 - \frac{\frac{\omega_c}{\omega}\left(\frac{\omega_c}{\omega} + \frac{\omega}{\omega_D}\right)}{\gamma^2 + \left(\frac{\omega_c}{\omega} + \frac{\omega}{\omega_D}\right)^2}\right]\right\} \tag{3.10}$$

and

$$\alpha = K^2 \frac{\omega_c \gamma}{\gamma^2 + \left(\frac{\omega_c}{\omega}\right)^2\left(1 + \frac{\omega^2}{\omega_c \omega_D}\right)^2} \quad , \tag{3.11}$$

where K^2 is the electromechanical coupling constant and ω_c and ω_D are the conductivity and diffusion frequencies, respectively, defined as

$$\omega_c \equiv \frac{\sigma}{\varepsilon} = \frac{n_0 e\mu}{\varepsilon} \tag{3.12}$$

and

$$\omega_D \equiv \left(\frac{c}{\rho}\right)\frac{1}{D} \quad . \tag{3.13}$$

In Eq. (3.12), σ is the electrical conductivity. The acoustoelectrical amplification occurs when the drift velocity v_d exceeds the sound velocity v_s while the attenuation accurs when v_d is slower than v_s. (When γ is negative, the attenuation is negative, that is, the traveling wave grows in amplitude instead of diminishing). The numerical value of α as a function of ω has a maximum at ω equal to

$$\omega_m = \left(\omega_c \omega_D\right)^{\frac{1}{2}} \quad . \tag{3.14}$$

The electromechanical coupling constant K^2 can be written as[32]

$$K^2 = \frac{e^2}{\varepsilon C} \quad . \tag{3.15}$$

In the case of the plane acoustical waves propagating in crystals of practical dimensions only the longitudinal piezoelectric fields are of importance for the

acoustoelectrical coupling. The waves having a non-zero longitudinal field component are termed "piezoelectrically active" waves. Examples of piezoelectrically active waves are longitudinal waves propagating along the *c*-axis in the wurtzite-type crystals [CdS, CdSe, ZnO, etc.] and shear waves propagating perpendicular to the *c*-axis in the wurtzite-type crystals with atomic displacement along the *c*-axis (i.e., T2-mode phonons).[32] The T2-mode phonons in the zincblende-type crystals are also piezoelectrically active waves (i.e., propagating in the [110] direction with shear polarization parallel to the [001] direction.[115] Since the quantities in Eq. (3.15) are normally tensors, K^2 depends strongly on the propagation direction of the sound waves (i.e., K^2 has strong inisotropy) and it has a maximum value in the direction of propagation of the piezoelectrically active waves. Table 3-2 shows the electromechanical coupling constants K^2 for the piezoelectrically active shear waves in various II-VI and III-V semiconductors. In this case, Eq. (3.15) can be written using the tensor components as

$$K_{T2}^2 = \frac{e_{15}}{\varepsilon_{11} C_{44}} \tag{3.16a}$$

for the wurtzite-type crystals, and

$$K_{T2}^2 = \frac{e_{14}}{\varepsilon_{11} C_{44}} \tag{3.16b}$$

for the zincblende-type crystals. The materials stated in Table 3-2 are classified into two categories; the strong piezoelectrics [II-VI compounds (wurtzite)] and weak piezoelectrics [II-VI compounds (zincblende) and III-V compounds (wurtzite)]. The stars (*) indicate the materials exhibiting the acoustoelectrical instabilities.

Next, we consider the build-up of acoustical-phonon domains from the thermal background in piezoelectric semiconductors as a result of the application of an external voltage pulse. It suffices here to consider only the piezo-

Table 3-2. Electromechanical coupling constants for various II-VI and III-V semiconductors.

Material	K_{T2}^2
CdS*	3.70×10^{-2} a,b
CdSe*	1.80×10^{-2} a,b
ZnO*	1.11×10^{-1} a,b
ZnSe	6.75×10^{-4} b
ZnTe	2.89×10^{-4} b
ZnS*	6.33×10^{-3} b
CdTe*	6.70×10^{-4} b
GaAs*	3.79×10^{-3} c
InSb*	1.01×10^{-3} c
InAs	4.62×10^{-4} c
GaSb *	3.55×10^{-3} c

[a]Calculated from Ref. 128.

[b]Calculated from Ref. 129.

[c]Calculated from Ref. 130.

*Materials exhibiting the acoustoelectrical instabilities.

electrically active shear waves in a narrow bandwidth near the frequency of maximum gain [see Eq. (3.14)], propagating with velocity v_s toward the anode (in n-type material). Upon application of a current, the energy density Φ in a coordinate system moving with the flux, grows at a rate

$$\frac{d\Phi}{dt} = \alpha_n \Phi + \alpha_0 \Phi_0 \quad , \tag{3.17}$$

where α_n is the net gain, i.e., the difference between the acoustoelectrical gain α and non-electronic attenuation coefficient $1/\tau_p$ and Φ_0 is the acoustical energy density at thermal equilibrium. From Eq. (3.11), the gain α is given by the following form:

$$\alpha = \alpha_{ac} \left(\frac{v_d}{v_s} - 1 \right) \quad . \tag{3.18}$$

The term $\alpha_0 \Phi_0$ is obtained from detailed balance arguments; for $\alpha_0 = \alpha_{ac} + \frac{1}{\tau_p}$, $d\Phi/dt = 0$ as required for $v_d = 0$ and $\Phi = \Phi_0$. Integrating Eq. (3.17), we obtain the amplified acoustical-energy density

$$\hat{\Phi}(t) \equiv \Phi(t) - \Phi_0 = \Phi_0 (1 + A)[\exp(\alpha_n t) - 1] \quad , \tag{3.19}$$

with

$$A = \frac{\alpha_0}{\alpha_n} = \left(\alpha_{ac} + \frac{1}{\tau_p} \right) / \alpha_n \quad . \tag{3.20}$$

Equation (3.19) represents that the acoustical flux grows exponentially from thermal background. The Brillouin-scattering studies of the acoustical-phonon domains showed that the amplified-phonon frequency distribution initially peaks near ω_m [Eq. (3.14)] and downshifts as the domain propagates through the crystals probably due to anharmonic parametric conversion.[18,116] Yamada *et al.*[18] reported that in CdS the growth rate and frequency dependence of the acoustical-phonon domains were all found to be consistent with the small-signal theory when the domain intensity was in the weak-flux regime (less than about

10^{-3} J/cm^3). In the subsequent stages of growth (i.e., in the strong-flux regime), however, many interesting non-linear effects were found by them in contrast to the small-signal theory. In the latter subsection (Section 3.3.4), we will present the data of attenuation coefficients of the acoustical-phonon domains as a function of phonon frequency. These data also reveal the presence of non-linear phonon-phonon interactions.

3.3.3 Incident and Scattering Angles

First, we consider the Brillouin-scattering process in an isotropic medium. The conservation of energy and momentum can be written as [see, *e.g.*, Eqs. (2.31) and (2.107)]

$$\omega_i - \omega_s = \pm \omega_q \quad , \tag{3.21}$$

$$\vec{k}_i - \vec{k}_s = \pm \vec{q} \quad , \tag{3.22}$$

where ω_q and $\vec{q}$ are the angular frequency and $\vec{k}$-vector of the acoustical phonon, respectively. The angular frequency and $\vec{k}$-vector can be connected by the following equations:

$$\omega_i = \frac{c}{n} |\vec{k}_i| \ , \qquad \omega_s = \frac{c}{n} |\vec{k}_s| \quad \text{and} \quad \omega_q = v_s |\vec{q}| \quad , \tag{3.23}$$

where n is the refractive index, c is the velocity of light and v_s is the sound velocity. Since the conditions $v_s \ll c$ and $c|\vec{k}_i| \gg v_s|\vec{q}|$ are normally fulfilled, one obtains

$$\omega_i \simeq \omega_s \quad \text{and} \quad |\vec{k}_i| \simeq |\vec{k}_s| \quad . \tag{3.24}$$

Equations (3.21) – (3.24) lead to the condition that

$$|\vec{k}_i| \sin \hat{\theta}_i = |\vec{q}|/2 \tag{3.25}$$

or

$$f = \frac{2nv_s}{\lambda_0} \sin \hat{\theta}_i \quad , \tag{3.26}$$

where $\hat{\theta}_i$ is the angle between the incident-optical beam and the normal to the acoustical $\vec{k}$-vector $\vec{q}$ (i.e., incident angle), $f = \omega_q/2\pi$ and λ_0 is the wavelength of light in vacuum. It is noting from Eq. (3.24) that the scattering angle $\hat{\theta}_s$ becomes equal to the incident angle $\hat{\theta}_i$ ($\hat{\theta}_s$ is the angle between the scattered-optical beam and the normal to the acoustical $\vec{k}$-vector $\vec{q}$). Note, additionally, that the angles $\hat{\theta}_i$ and $\hat{\theta}_s$ are the internal angles in the medium. Using Snell's law

$$\sin \theta_i = n \sin \hat{\theta}_i \quad , \tag{3.27}$$

one can rewrite Eq. (3.26) as

$$f = \frac{2v_s}{\lambda_0} \sin \theta_i \quad , \tag{3.28}$$

where θ_i is the incident angle outside the scattering medium [see Fig. 2-9 (a)]. Finally, from Eq. (3.28) one obtains the external incident angle θ_i and scattering angle θ_s as follows:

$$\theta_i = \theta_s = \sin^{-1} \left(\frac{f\lambda_0}{2v_s} \right) \quad . \tag{3.29}$$

Next, we consider the Brillouin-scattering process in an anisotropic medium.[63,117] In this case, we must take into account the dichroism of anisotropic material because the scattered and incident lights have usually different polarizations. Let us denote n_i and n_s as the refractive indices of the incident and scattered lights, respectively. In direct analogy to the case of the isotropic material, one write Eq. (3.23) as

$$|\vec{k}_i| = \frac{\omega_i}{c} n_i = \frac{2\pi n_i}{\lambda_0} \quad , \tag{3.30a}$$

$$|\vec{k}_s| = \frac{\omega_s}{c} n_s = \frac{\omega_i \pm \omega_q}{c} n_s \simeq \frac{\omega_i}{c} n_s = \frac{2\pi n_s}{\lambda_0} \quad . \tag{3.30b}$$

Considering the energy and momentum conservation, one finds

$$f = v_s \left[\frac{n_i}{\lambda_0} \sin \hat{\theta}_i + \frac{n_s}{\lambda_0} \sin \hat{\theta}_s \right] \quad , \tag{3.31a}$$

$$\frac{n_i}{\lambda_0} \cos \hat{\theta}_i = \frac{n_s}{\lambda_0} \cos \hat{\theta}_s \quad . \tag{3.31b}$$

From Eq. (3.31), we obtain

$$\sin \hat{\theta}_i = \frac{\lambda_0}{2n_i v_s} \left[f + \frac{v_s^2}{f\lambda_0^2} (n_i^2 - n_s^2) \right] \quad , \tag{3.32a}$$

$$\sin \hat{\theta}_d = \frac{\lambda_0}{2n_s v_s} \left[f - \frac{v_s^2}{f\lambda_0^2} (n_i^2 - n_s^2) \right] \quad , \tag{3.32b}$$

Using Snell's law

$$\sin \theta_i = n_i \sin \hat{\theta}_i \quad \text{and} \quad \sin \theta_s = n_s \sin \hat{\theta}_s \quad , \tag{3.33}$$

we finally obtain

$$\theta_i = \sin^{-1} \left\{ \frac{\lambda_0}{2v_s} \left[f + \frac{v_s^2}{f\lambda_0^2} (n_i^2 - n_s^2) \right] \right\} \quad , \tag{3.34a}$$

$$\theta_s = \sin^{-1} \left\{ \frac{\lambda_0}{2v_s} \left[f - \frac{v_s^2}{f\lambda_0^2} (n_i^2 - n_s^2) \right] \right\} \quad . \tag{3.34b}$$

Table 3-3 lists the experimental configurations for the Brillouin-scattering measurements carried out in the present study. The schematic diagrams of the Brillouin-scattering measurements for the wurtzite-type crystal CdS are shown in Fig. 3-4. The T2-mode acoustical-phonon domain [Fig. 3-4 (b)] is obtained by the acoustoelectrical amplification [see Section 3.3.3], while the T1-

Table 3-3. Experimental configurations for the Brillouin-scattering measurements used in the present study.

Material	Phonon Mode	Acoustical Propagation; $\vec{l}_q$	Acoustical Polarization; $\vec{\pi}$	Incident Light Polarization; $\vec{l}_E$	Scattered Light Polarization; $\vec{l}_k$	Domain
ZnSe	T1-mode	$\vec{l}_q \parallel [1\bar{1}0]$	$\vec{\pi} \parallel [110]$	$\vec{l}_E \parallel [110]$	$\vec{l}_k \perp \vec{l}_E$	I
	T2-mode	$\parallel [001]$	$\parallel [110]$	$\parallel [110]$	$\perp \vec{l}_E$	I
ZnTe	T1-mode	$\parallel [1\bar{1}0]$	$\parallel [110]$	$\parallel [110]$	$\perp \vec{l}_E$	I
	T2-mode	$\parallel [001]$	$\parallel [110]$	$\parallel [110]$	$\perp \vec{l}_E$	I
$Zn_xCd_{1-x}Te$	T2-mode	$\parallel [001]$	$\parallel [110]$	$\parallel [110]$	$\perp \vec{l}_E$	I
CdS	T1-mode	$\perp c$-axis	$\perp c$-axis	$\perp c$-axis	$\perp \vec{l}_E (\vec{l}_k \perp \vec{c})$	M
	T2-mode	$\perp c$-axis	$\parallel c$-axis	$\parallel c$-axis	$\perp \vec{l}_E (\vec{l}_k \perp \vec{c})$	A
	PL-mode	$\mid c$-axis	$\mid c$-axis	$\parallel c$-axis	$\parallel \vec{l}_E (\vec{l}_k \parallel \vec{c})$	M
GaP	T1-mode	$\parallel [1\bar{1}0]$	$\parallel [110]$	$\parallel [110]$	$\perp \vec{l}_E$	I
	T2-mode	$\parallel [001]$	$\parallel [110]$	$\parallel [110]$	$\perp \vec{l}_E$	I
GaSe	T1-mode	$\perp c$-axis	$\perp c$-axis	$\perp c$-axis	$\perp \vec{l}_E (\vec{l}_k \perp \vec{c})$	I
GaS	T1-mode	$\perp c$-axis	$\perp c$-axis	$\perp c$-axis	$\perp \vec{l}_E (\vec{l}_k \perp \vec{c})$	I

I: Injected domain

M: Mode-converted domain

A: Acoustoelectrically amplified domain

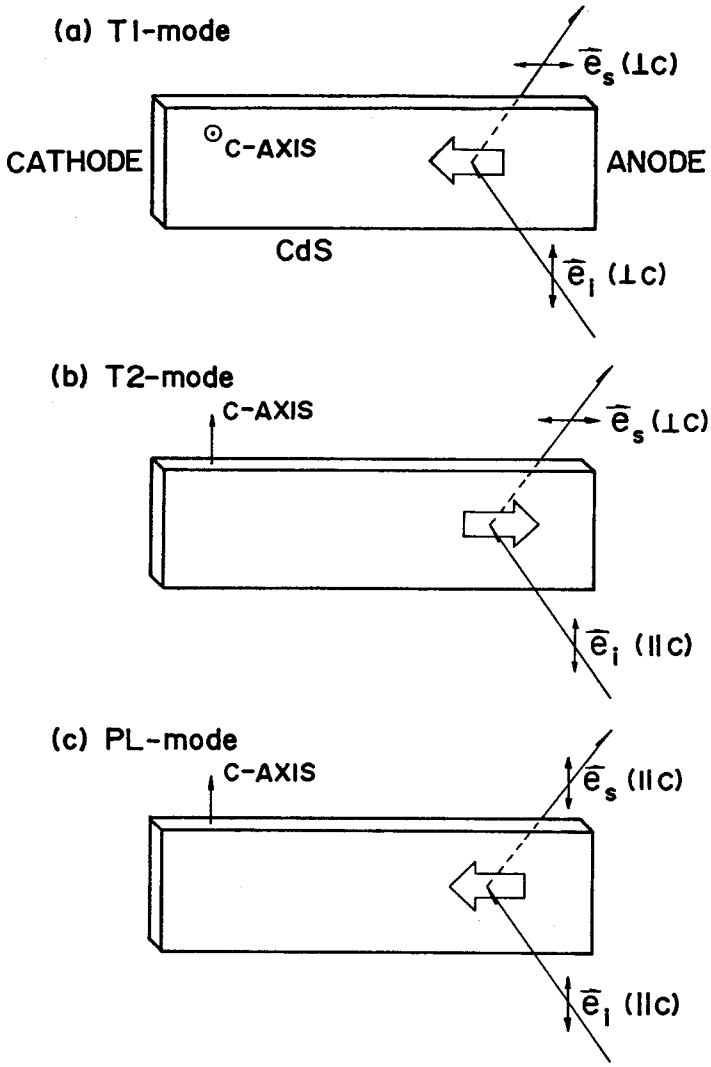

FIG. 3-4. Schematic diagrams of the Brillouin-scattering measurements for the wurtzite-type crystal CdS. (a) T1-mode phonon domain; (b) T2-mode phonon domain; (c) PL-mode phonon domain. $\vec{e}_i$ and $\vec{e}_s$ are the incident and scattered light polarizations, respectively.

[Fig. 3-4 (a)] and PL-mode phonon domain [Fig. 3-4 (c)] are obtained by mode conversion upon partial reflection of the T2-mode phonon domains. We can calculate the incident and scattering angles for the zincblende-type crystals from Eq. (3.29). While those for the wurtzite-type crystals may be calculated from Eq. (3.34). The scattered and incident lights have almost the same polarizations for the case of the Tl- and PL-mode phonons [see Table 3-3], i.e., $n_i \simeq n_s \simeq n_o$ for the Tl-mode phonons and $n_i = n_s = n_e$ for the PL-mode phonons (where n_o and n_e are the refractive indices for the ordinary and extraordinary rays, respectively). The calculated angles for the Tl- and PL-mode phonons, thus, accord well with those of derived by assuming an isotropic medium. This arises from the fact that if the scattering medium is almost isotropic, we have $n_i = n_s$ and in this case Eq. (3.34) can be reduced to the simple isotropic form (3.29). However, the incident and scattering angles for the T2-mode phonons must be calculated by exactly taking into account the anisotropic nature of the refractive indices (because $n_i = n_e$ and $n_s \simeq n_o$).

3.3.4 Acoustical-Domain Injection Method

In this subsection, we describe an outline of the acoustical-domain injection method.[33,34] Using this method, it is possible to extend studies of resonant Brillouin scattering in various semiconductors with weak piezoelectricity. This technique also enables us the investigation of the propagation behaviors such as lattice attenuation and phase velocity of the high-frequency phonons in many materials by means of Brillouin scattering. Ando *et al.*[118-120] have first demonstrated an availability of this method by injecting the acoustical-phonon domains from CdS into ZnSe. Subsequently, Yamabe *et al.*[33,34] have derived injection (transmission) efficiency from theoretical aspects and compared it with the experimental data. Good agreement between the calculation and experiment has been found in various systems such as CdS-ZnSe, CdS-ZnTe and CdS-GaP.

Acoustical wave propagating in an elastic medium can be written in terms of

the stress T_{ij} and strain S_{kl}. We start from the two basic equations [see Eqs. (2.70) and (3.9)]:

$$\rho \left(\frac{\partial^2 u_i}{\partial t^2} \right) = \frac{\partial}{\partial r_j} T_{ij} \quad , \tag{3.35}$$

$$T_{ij} = C_{ijkl} S_{kl} = C_{ijkl} \frac{\partial u_k}{\partial r_l} \quad , \tag{3.36}$$

where r_j is the j-component (j = x, y or z) of the orthogonal coordinates, u_i is the i-component (i = x, y or z) of atomic displacement and C_{ijkl} is the component of the elastic stiffness constant tensor. These equations can be written by introducing the atomic-displacement velocity as

$$\rho \frac{\partial v_i}{\partial t} = \frac{\partial}{\partial r_j} T_{ij} \quad , \tag{3.37}$$

$$\frac{\partial}{\partial t} T_{ij} = C_{ijkl} \frac{\partial v_k}{\partial r_l} \quad . \tag{3.38}$$

Now, we introduce the following complex acoustical Poynting vector:[121]

$$\vec{P}_{ac} = - \frac{1}{2} \sum_{ij} \vec{I}_i \, v_j^* \, T_{ij} \quad , \tag{3.39}$$

where $\vec{I}_i$ is the unit vector of the i-direction in the orthogonal coordinate system and v_j^* stands for the complex conjugate of v_j. The acoustical-power propagation can be estimated by solving Eqs. (3.37) — (3.39). Next, we consider the boundary condition of the acoustical waves at interface of the two different materials (i.e., at the bonded surface). If we assume that the interface is rigidly bonded so that there exists no slipping, the boundary condition can be given by

$$[v_i]_s = [v_i]_d \quad , \tag{3.40}$$

where the suffices s and d stand for the bonded two media. This equation means that the atomic-displacement velocity v_i is continuous across the boundary surface. If we also assume that the external traction force is continuous across the boundary surface, the boundary condition for the stress can be written as

$$[\ T_{kj}\ ]_s \cdot [\ n\ ] = [\ T_{ij}\ ]_d \cdot [\ n\ ] \quad , \tag{3.41}$$

where [n] is the unit vector normal to the boundary surface.

Yamabe *et al.*[33] proceeded numerical calculations to obtain the transmission efficiency in the following steps; (i) Equations (3.37) and (3.38) are solved by using the boundary conditions (3.40) and (3.41). (ii) The acoustical Poynting vector is evaluated from Eq. (3.39). (iii) The transmission efficiency is finally obtained by calculating the ratio of the transmitted and incident Poynting vectors.

In Fig. 3-5, we plotted theoretical transmission efficiencies of the quasi-transverse (T2-mode) phonons for the CdS-ZnSe and CdS-ZnTe systems as a function of propagation direction Θ. It is found from the figure that the transmission efficiency has appreciably high value for both the CdS-ZnSe and CdS-ZnTe systems. Figure 3-6 shows an example of the oscilloscope display of the Brillouin-scattering signal by the injected acoustical-phonon domain obtained from the CdS-ZnSe system (upper trace). The current waveform exhibiting the acoustoelectrical instability is also shown in the lower trace (CdS). The Brillouin-scattering signal P_1 is produced by the injected forward-traveling domain, while the signal P_2 is produced by the reflected backward-traveling domain at the end-surface of ZnSe. Experimentally, we obtained the transmission efficiency up to 90 % at lower-phonon frequency. It was found that the efficiency depends strongly on the acoustical-phonon frequency, i.e., it decreases with increasing acoustical-phonon frequency. It seems this is

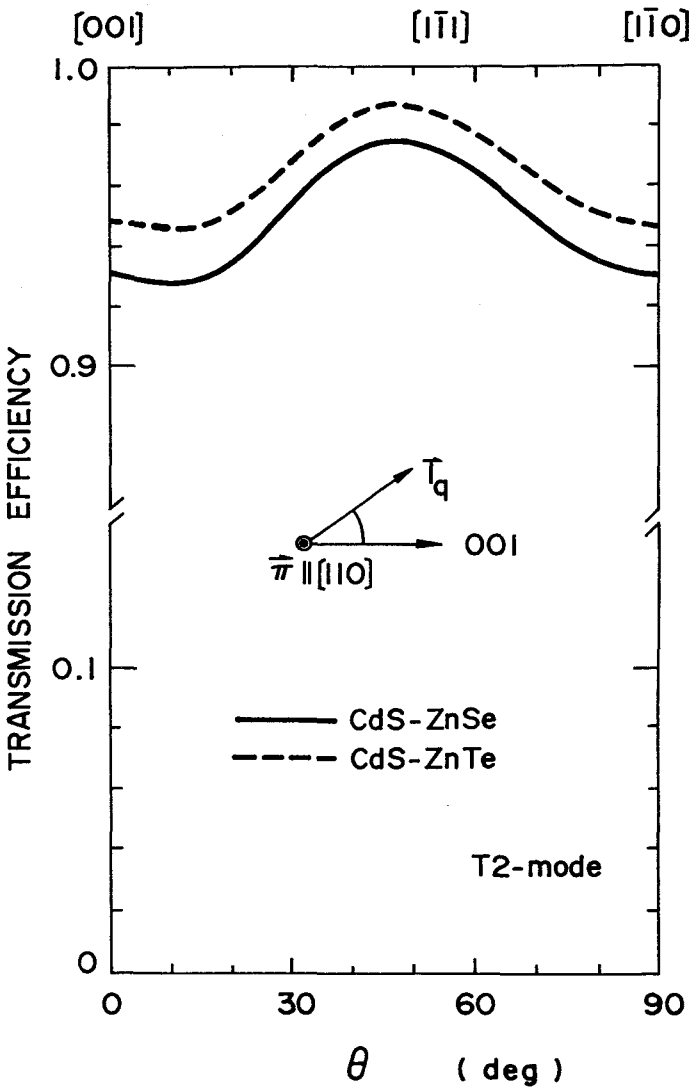

FIG. 3-5. Theoretical transmission efficiencies of the quasi-transverse (T2-mode) phonon domains for the CdS-ZnSe and CdS-ZnTe systems as a function of propagation direction θ.

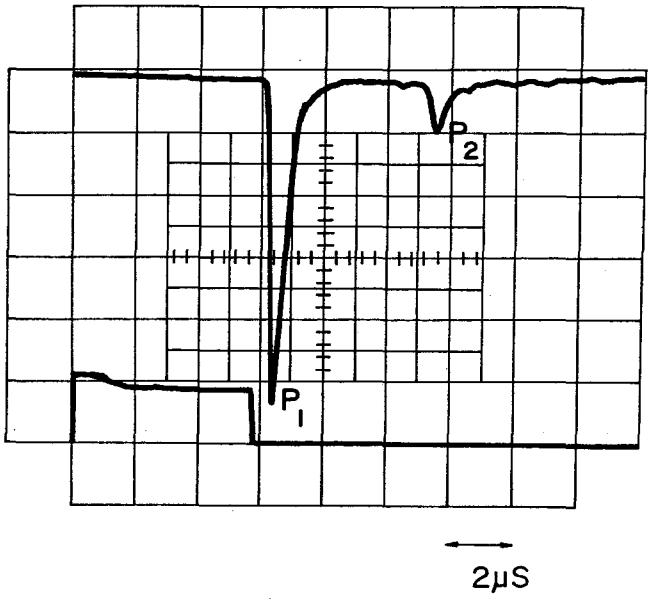

FIG. 3-6. Oscilloscope display of the Brillouin-scattering signal by the injected acoustical-phonon domain obtained from the CdS-ZnSe system (upper trace). The current waveform exhibiting the acoustoelectrical instability is also shown in the lower trace.

due to that the indium layer between the bonded materials acts like low-pass filter for the acoustical-phonon transmission [see Fig. 3-1]. Indeed, it is possible to consider that the phonon-domain transmission becomes difficult when the wavelength of the phonon domain beyonds the thickness of the indium layer (note that higher-frequency phonons have shorter wavelengths). Such an effect of the indium layer was not taken into account in the theoretical analysis for simplicity.

We have mentioned above that the intense acoustical-phonon domains produced in CdS can be injected into different materials by making use of the acoustical-domain injection method. As a typical example of the applications of this method, we present lattice-attenuation data obtained in the CdS-ZnSe and CdS-ZnTe systems. The lattice attenuation is an old topic of the crystal dynamics.[122,123] Zucker *et al.*[124] have first measured the lattice attenuation of amplified phonon domains in CdS by using the Brillouin-scattering technique.

The frequency dependence of the lattice loss α_L can be written simply as

$$\alpha_L \propto \omega \tag{3.42}$$

for Landau-Rumer loss ($\omega\tau_{th} \gg 1$), and

$$\alpha_L \propto \omega^2 \tag{3.43}$$

for Akhieser loss ($\omega\tau_{th} \ll 1$), where τ_{th} is the relaxation time of thermal phonons. Figure 3-7 shows the frequency dependence of the attenuation coefficient of the acoustical-phonon domains propagating in ZnSe in the [001] direction with shear polarization parallel to the [110] direction (T2-mode phonons).[34] The observed frequency dependence is of the form of $\alpha_L \propto f^{1.45}$. The frequency dependence of the attenuation coefficient for the T2-mode phonon domains in ZnTe is shown in Fig. 3-8.[125] The open and solid circles are the data in the weak- and strong-flux regimes, respectively. The experimental frequency dependence shows $f^{1.2}$ in the weak-flux regime and $f^{0.3}$ in the strong-

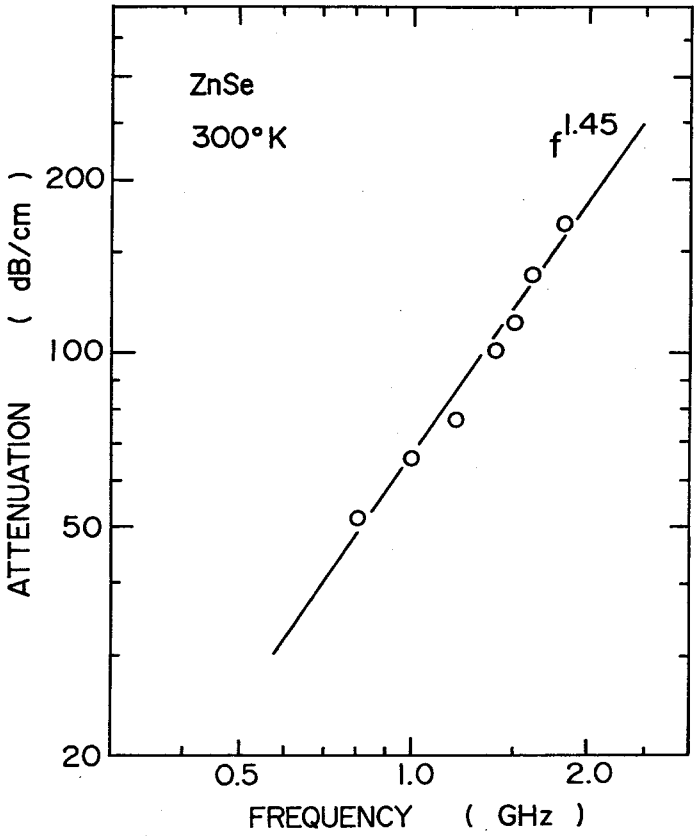

FIG. 3-7. Frequency dependence of the attenuation coefficient for the acoustical-phonon domains in ZnSe (T2-mode phonons).

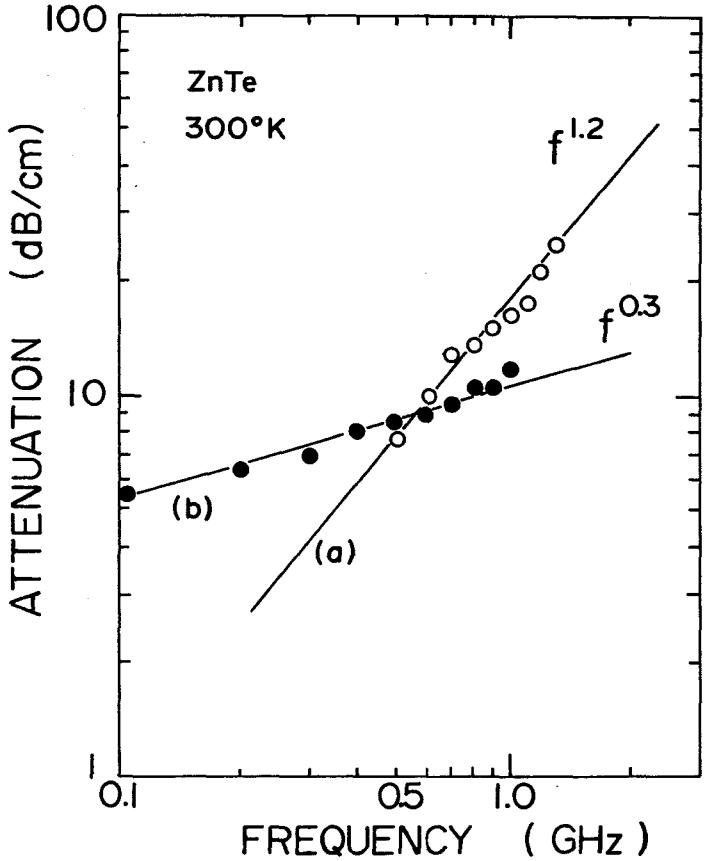

FIG. 3-8. Frequency dependence of the attenuation coefficient for the T2-mode phonon domains in ZnTe. The open and solid circles are the data in the weak- and strong-flux regimes, respectively.

flux regime. The present experimental conditions should satisfy the Akhieser-loss process (i.e., $\omega\tau_{th} \ll 1$). Our experimental data, however, depart from the Akhieser-loss process. The deviation from the Akhieser loss has also been reported in semiconductors such as CdS,[18,124,126] ZnSe[118,127] and GaAs.[16] Such deviations can be interpreted in terms of non-linear phonon-phonon interactions, as pointed out by Palik and Bray.[16] The difference of f^n in the weak- and strong-flux regimes supports the possibility of the non-linear phonon-phonon interactions in ZnTe.

CHAPTER IV

RESONANT BRILLOUIN SCATTERING IN ZnSe, ZnTe, $Zn_xCd_{1-x}Te$ AND CdS

4.1 INTRODUCTION

In recent years theoretical and experimental investigations on the subject of resonant light scattering in semiconductors have been carried out extensively by many workers.[8] The majority of the experimental studies have been concentrated on dispersion of the scattering cross sections when the incident-photon energy approaches dielectric singularities of the semiconductors. The acoustoelectrically amplified phonon domains have recently been used to investigate resonance phenomena of Brillouin scattering in piezoelectric semiconductors such as GaAs,[25] CdS,[26-30] ZnO[29,30] and CdSe,[31] where the intense acoustical-phonon domains provide strong scattering signals and thus permit us the use of a continuous light source monochromized by a conventional monochromator instead of a laser, as mentioned previously (Chapter III).

The spectral dependence of the Brillouin-scattering cross sections in such semiconductors has shown resonant enhancement and cancellation (anti-resonance) in the region near the fundamental absorption edge. The observed dispersion curves have been interpreted satisfactorily in terms of the resonant-light-scattering theory developed by Loudon.[35,36] However, resonance behaviors in the neighborhood of the excitonic structure of the absorption edge have not yet been discussed in detail because of the experimental difficulty due

to the strong absorption coefficients in that wavelength region.

In this Chapter, we investigate resonant Brillouin scattering in II-VI semiconductors (ZnSe,[95] ZnTe,[71] $Zn_xCd_{1-x}Te$[96,125,131] and CdS[39]) by using the acoustoelectrically amplified phonon domains with exciting light wavelengths including a region sufficiently close to the fundamental absorption edge to clarify resonance behaviors near the M_0 critical points. For instance, previous work by Ando *et al.*[120] is limited to the wavelength range of 475 — 620 nm (room temperature), and thus only a weak resonant enhancement is observed. We performed the Brillouin-scattering measurements in the wavelength ranges of 465 — 640 nm (room temperature) and 450 — 640 nm (77 K) which include a region sufficiently close to the fundamental absorption edge of ZnSe. We improved our experimental setup and used high-quality ZnSe, which enabled us to discuss the resonance behaviors at a region very close to the fundamental absorption edge.

In Section 4.2, we present some physical properties of the II-VI group of semiconductors ZnSe, ZnTe, CdTe and CdS, such as the electronic band structure and crystallographical properties of these materials. In Section 4.3, we present the experimental results and compare them with the theoretical model based upon Loudon's light-scattering theory. The obtained spectral dependence of the Brillouin-scattering cross sections shows a new maximum at a photon energy very close to the ground-state exciton energy (i.e., in the resonant enhancement region). We show for the first time that the Brillouin-scattering efficiency depends strongly on a lifetime-broadening effect of the intermediate electronic states. The importance of the lifetime-broadening effect on resonant light scattering has been pointed out by Loudon[36] but not yet discussed up to date from an experimental point of view. The observed maximum in the spectral dependence of the Brillouin-scattering cross sections is well interpreted by including this broadening effect.

4.2 PROPERTIES OF ZnSe, ZnTe, $Zn_xCd_{1-x}Te$ AND CdS

4.2.1 Crystal Structure

The crystallography of the II-VI compounds is somewhat complicated by their propensity to crystallize in a variety of polymorphic modifications.[132] The principal structure types are cubic zincblende (sphalerite) and hexagonal wurtzite in which the atoms are tetrahedrally bond in network arrangements related to those of the group IV semiconductors. All of the II-VI compounds, and in paticular ZnSe, ZnTe and CdTe, form crystals with the zincblende arrangement. The II-VI compounds, in paticular CdS, CdSe and ZnO, also crystallize in the wurtzite arrangement. Figure 4-1 shows the arrangements of group-II metal atoms (small solid circles) and group-VI non-metal atoms (large open circles) in (a) zincblende and (b) wurtzite form. The zincblende structure is based on the cubic space group $T_d^2 - F\bar{4}3m$. There are four molecules ($A^{II}B^{VI}$) in a unit cell. The wurtzite structure is based on the hexagonal space group $C_{6v}^4 - P6_3mc$ and there are two molecules in the hexagonal unit cell. The lattice parameters for the zincblende (ZnSe, ZnTe and CdTe) and wurtzite structure (CdS) are summarized in Table 4-1. The separation between layers along the hexagonal stacking axis is c/N, where N is the number of layers in the repeating unit.

An important aspect of the zincblende arrangement is the absence of a center of symmetry or inversion. The $A^{II} - B^{VI}$ layers have unique orientations along the <111> directions. As a result, the zincblende crystals are polar, and opposed (111) [A-face] and ($\bar{1}\bar{1}\bar{1}$) face [B-face] and opposed [111] and [$\bar{1}\bar{1}\bar{1}$] directions may have different physical and chemical properties. This is known to be the crystallographical polarity. The crystallographical polarity, *vice versa*, enables us to identify the (111) and ($\bar{1}\bar{1}\bar{1}$) faces by the simple chemical etching test.[133] The wurtzite arrangement does not have a center of symmetry and there is a polar axis parallel to [001] (*c*-axis).

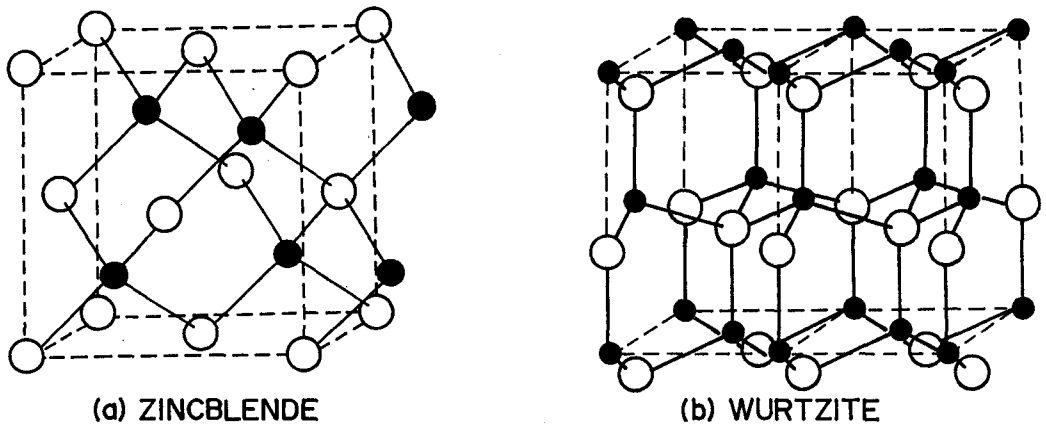

FIG. 4-1. Arrangements of group-II metal atoms (small solid circles) and group-VI non-metal atoms (large open circles) in (a) zincblende and (b) wurtzite form. The zincblende structure is based on the cubic space group $F\bar{4}3m$. The wurtzite structure is based on the hexagonal space group $P6_3mc$.

Table 4-1. Lattice parameters of $A^{II}B^{VI}$ compounds with the zincblende (ZnSe, ZnTe and CdTe) and wurtzite structure (CdS).

Material	a [Å]	c [Å]	d(A-A) [Å]	d(A-B) [Å]	c/N [Å]
ZnSe[(a)]	5.6687	———	4.01	2.45	———
ZnTe[(b)]	6.1037	———	4.32	2.64	———
CdTe[(c)]	6.481	———	4.58	2.80	———
CdS[(d)]	4.1367	6.7161	——	——	3.358

(a) Reference 180. (b) Reference 181.
(c) Reference 182. (d) Reference 183.

As in the zincblende, the A^{II} and B^{VI} ions of opposite polarity can be visualized as forming a network of permanent dipole moments. However, in the wurtzite the moments do not balance but create a single polar axis. Consequently, in addition to being piezoelectric, the wurtzite-type crystals are pyroelectric.

Crystals grown from combinations of II-VI compounds may be substitutional solid solutions or a mixture of zincblende and wurtzite modifications.[134-139] The relative concentration of the participants determines the band-gap energy [see, *e.g.*, Fig. 4-16], which plays a significant role in the Brillouin-scattering process through the intraband and interband electronic transitions.

4.2.2 Electronic Band Structure

The zincblende lattice has the translational symmetry of the face-centered cubic lattice [Fig. 4-1 (a)]. The Brillouin zone for the reciprocal lattice can be taken to be the truncated octahedron shown in Fig. 4-2. The points and lines of special symmetry are indicated in the figure with their conventional labels. The lattice of the wurtzite crystals consists of two interpenetrating

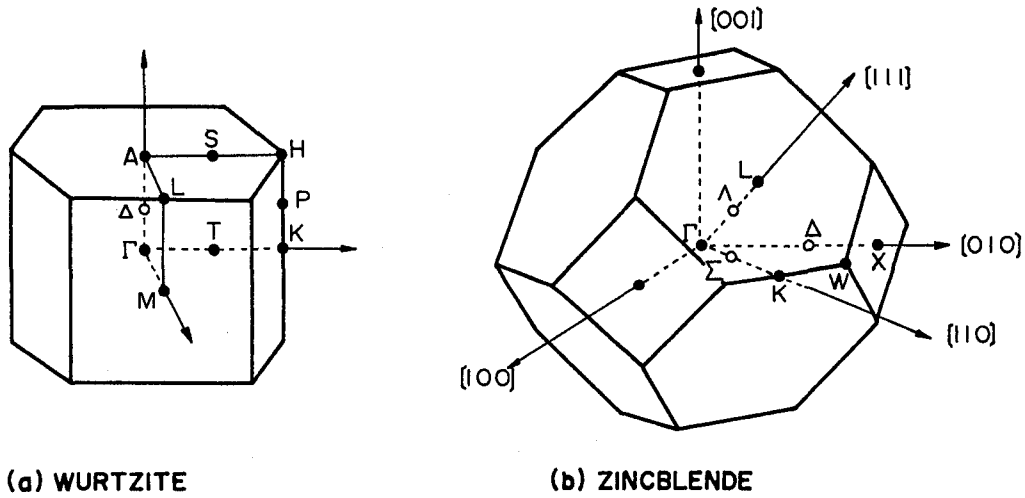

FIG. 4-2. The Brillouin zones for (a) wurtzite and (b) zincblende lattices with lines and points of special symmetry.

hexagonal close-packed lattices; one containing the cation (B^{VI}), the other anion (A^{II}) [Fig. 4-1 (b)]. The Brillouin zone for the reciprocal hexagonal lattice is shown in Fig. 4-2 along with lines and points of special symmetry. This Brillouin zone is the same as for the hexagonal close-packed lattice.

The lowest energy gap in II-VI compounds such as ZnSe and CdS is a direct and occurs in the center of the Brillouin zone, i.e., at $\vec{k} = 0$ (Γ point). The nature of energy transitions at different points in $\vec{k}$-space is reasonably well identified in most of the II-VI compounds.[140] However, the knowledge of band structure away from the principal symmetry points still tends to be more of a qualitative than a quantitative nature. The majority of the knowledge of electronic band structure in the II-VI compounds have been derived theoretically from the semi-empirical pseudopotential method.[141,142] This method has become an important tool both for the investigation of electronic band structures of solids and for understanding the behaviors of electrons in crystals. The semi-empirical pseudopotential studies of Cohen and Bergstresser [141,142] have included II-VI compounds with the zincblende and wurtzite structures. Figure 4-3 illustrates the band structures of ZnSe and ZnTe determined by Walter *et al.*[143] and of CdS by Bergstresser and Cohen.[142] These band structures are calculated using the semi-empirical potential method which involves adjusting pseudopotential form factors to achieve good agreement with experimental results for the principal optical transitions. The irreducible representations indicated are those for the double group (ZnSe and ZnTe) and for the single group (CdS).

4.2.3 Crystallographical Properties

As mentioned in Section 4.2.1, the II-VI compounds crystallizing in the tetrahedrally coordinated cubic zincblende and hexagonal wurtzite structures are the simplest crystals lacking a center of symmetry and, hence, capable of exhibiting piezoelectric and related effects depending on polar

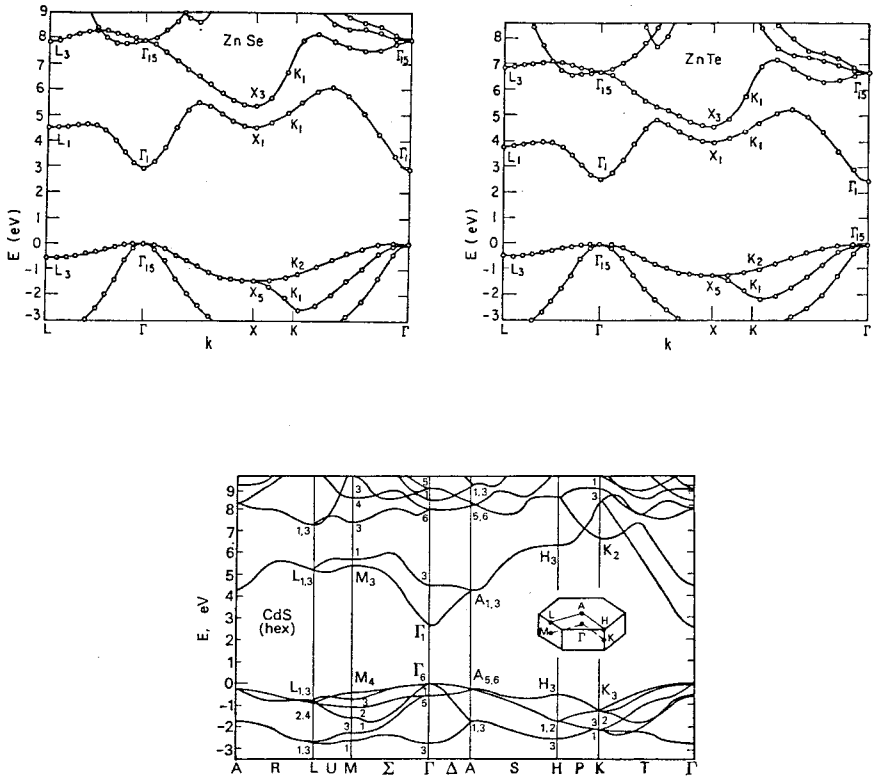

FIG. 4-3. Electronic band structures of ZnSe, ZnTe and CdS calculated from the semi-empirical potential method. (From Refs. 142 and 143).

symmetry. The elastic compliance, elastic stiffness, piezoelectric and static dielectric constants of the zincblende ZnSe, ZnTe and CdTe and wurtzite CdS are listed in Table 4-2. The crystal densities calculated using the lattice constants of Table 4-1 are also listed in this table. It has been found by Berlincourt *et al.*[129] that the piezoelectric constant for the wurtzite-type crystal CdS nearly satisfies the symmetry requirements of the cubic zincblende type, but has much higher magnitude. It seems that the stronger piezoelectricity and the preference for the wurtzite structure are both direct consequences of increasing ionicity of the bond. The temperature dependence of elastic constants together with the pressure dependence provide useful information in the study of the anharmonic effect of crystals. Lee[144,145] has measured the temperature and pressure dependence of the elastic constants of ZnSe and ZnTe by means of ultrasonic pulse-echo method, and found that the constants change almost linearly with temperature and pressure. The static dielectric constants have also been found to have linearly varying temperature dependence.[146] The calculated crystal densities agree well with those measured values [*e.g.*, 5.264 g/cm^3 for ZnSe and 5.633 g/cm^3 for ZnTe obtained by the weight-volume method[144]].

Figure 4-4 shows the phonon dispersion relations for (a) ZnSe and (b) ZnTe at room temperature taken from Refs. 147 and 148, respectively. Research on the dynamics of perfect lattices has aroused considerable interest especially in compounds having zincblende or diamond crystal structure. This development is the outcome of many experimental results, particularly neutron- and Raman-scattering data for phonon dispersion relations. In fact, the phonon dispersion relations for ZnSe and ZnTe given in Fig. 4-4 were obtained from the second-order Raman-scattering spectra and neutron-scattering data, respectively. The first-order Raman-scattering measurements give only information about phonon states with $\vec{k} \simeq 0$ (Γ). This severe limitation can

Table 4-2. Elastic, piezoelectric, dielectric constants and crystal density of the zincblende ZnSe, ZnTe and CdTe and wurtzite CdS at room temperature (25°C). S in 10^{-11} m^2/N; C in 10^{10} N/m^2; e in C/m^2; and g in g/cm^3.

	Material			
	ZnSe	ZnTe	CdTe	CdS
S_{11}	2.26[a]	2.40[a]	4.5[b]	2.069[a]
S_{12}	-0.85	-0.87	-1.5	-0.999
S_{44}	2.27	3.21	5.0	6.649
S_{33}	——	——	——	1.697
S_{13}	——	——	——	-0.581
S_{66}	——	——	——	6.136
C_{11}	8.10[a]	7.13[a]	5.351[b]	9.07[a]
C_{12}	4.88	4.07	3.681	5.81
C_{44}	4.41	3.12	1.994	1.50
C_{33}	——	——	——	9.38
C_{13}	——	——	——	5.10
C_{66}	——	——	——	1.63
e_{14}	0.049[a]	0.028[a]	0.0335[a]	——
e_{31}	——	——	——	-0.244[a]
e_{33}	——	——	——	(+)0.440
e_{15}	——	——	——	-0.210
$\varepsilon^S_{11}/\varepsilon_0$	9.25[c]	10.10[a]	11.00[c]	9.35[a]
$\varepsilon^S_{33}/\varepsilon_0$	——	——	——	10.33
g	5.262[d]	5.636[d]	5.849[d]	4.819[d]

(a) Reference 129.
(b) Reference 91.
(c) Reference 146.
(d) Calculated using the lattice constants listed in Table 4-1.

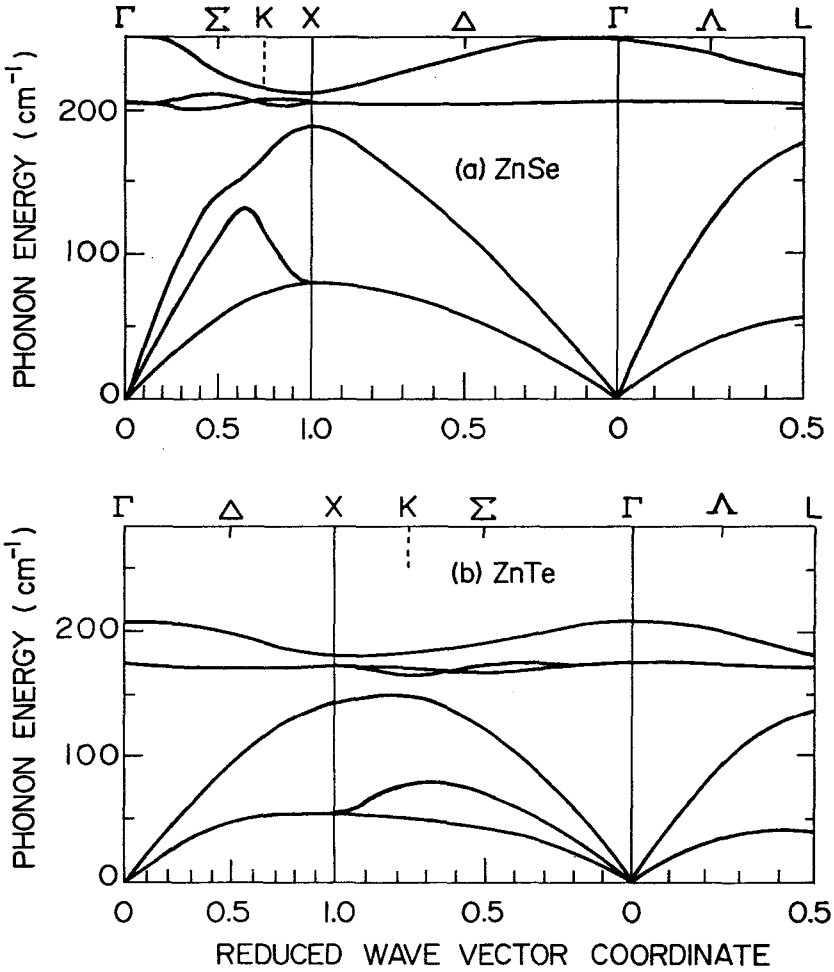

FIG. 4-4. Phonon dispersion relations for (a) ZnSe and (b) ZnTe at room temperature. (From Refs. 147 and 148).

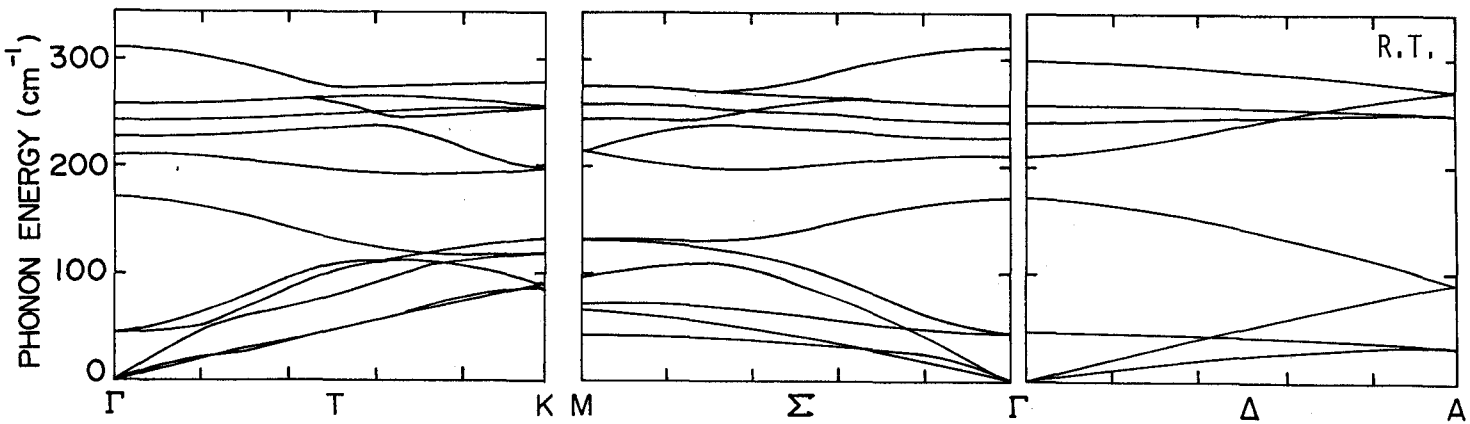

FIG. 4-5. Phonon dispersion relations for the wurtzite-type crystal CdS. (From Ref. 149).

be overcome by using the second-order Raman spectra; Two phonons with $\vec{k}_1 + \vec{k}_2 \simeq 0$ are then produced and the complete phonon spectrum becomes accessible. Figure 4-5 also shows the phonon dispersion relations for the wurtzite-type crystal CdS along directions Γ-K, Γ-M and Γ-A [see Fig. 4-2 (a)].[149] Such phonon dispersion curves, *vice versa*, enable us to identify the measured Raman- and Brillouin scattering spectra. The various components of the Raman (Brillouin) tensor can be calculated from the phonon dispersion data obtained with neutron scattering by the use of lattice dynamical models (shell model) which include nonlinear interactions. This procedure has been successfully used for the alkali halides[150] and for MgO.[151]

4.3 EXPERIMENTAL RESULTS AND DISCUSSION

4.3.1 ZnSe

The spectral dependence of the Brillouin-scattering cross sections for 0.2 GHz T1-mode phonon domains measured at room temperature is shown in Fig. 4-6. The measurements were carried out by making use of the acoustical-domain injection method. The vertical arrow in the figure indicates the position of the band gap E_g. The Brillouin-scattering cross section σ_B is deduced from the following equation:

$$\frac{I_s}{I_t} = \sigma_B \, b \, d\Omega_s \quad , \qquad (4.1)$$

where I_s and I_t are the scattered-light and transmitted-light intensities, respectively, b is the light-path length and $d\Omega_s$ is the solid angle in which the light is scattered. The Brillouin-scattering cross section shows a narrow and deep minimum at around 495 nm. Such an antiresonance behavior has also been found in GaAs,[25] CdS,[26-30] ZnO[29,30] and CdSe.[31] In addition, we can find a new maximum in the dispersion curve very close to the fundamental

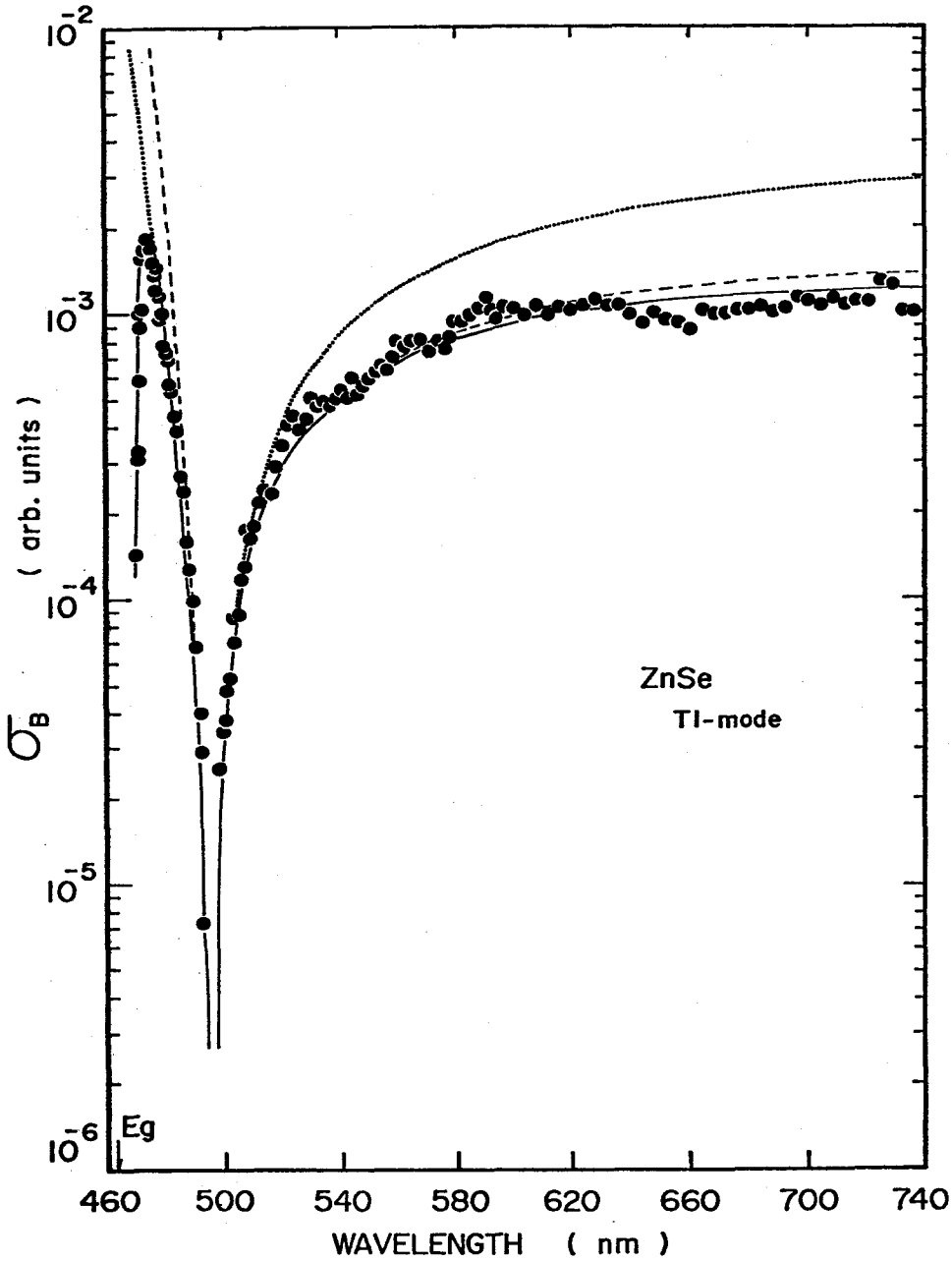

FIG. 4-6. Dispersion curve of the Brillouin-scattering cross sections in ZnSe [as-grown] for 0.2 GHz Tl-mode phonons at room temperature. The theoretical curves are obtained from Eq. (2.55) with Γ=0 meV (dashed line) and Γ=64 meV (solid line). The dotted line is obtained from Eq. (2.29). The vertical arrow indicates the position of the band gap E_g.

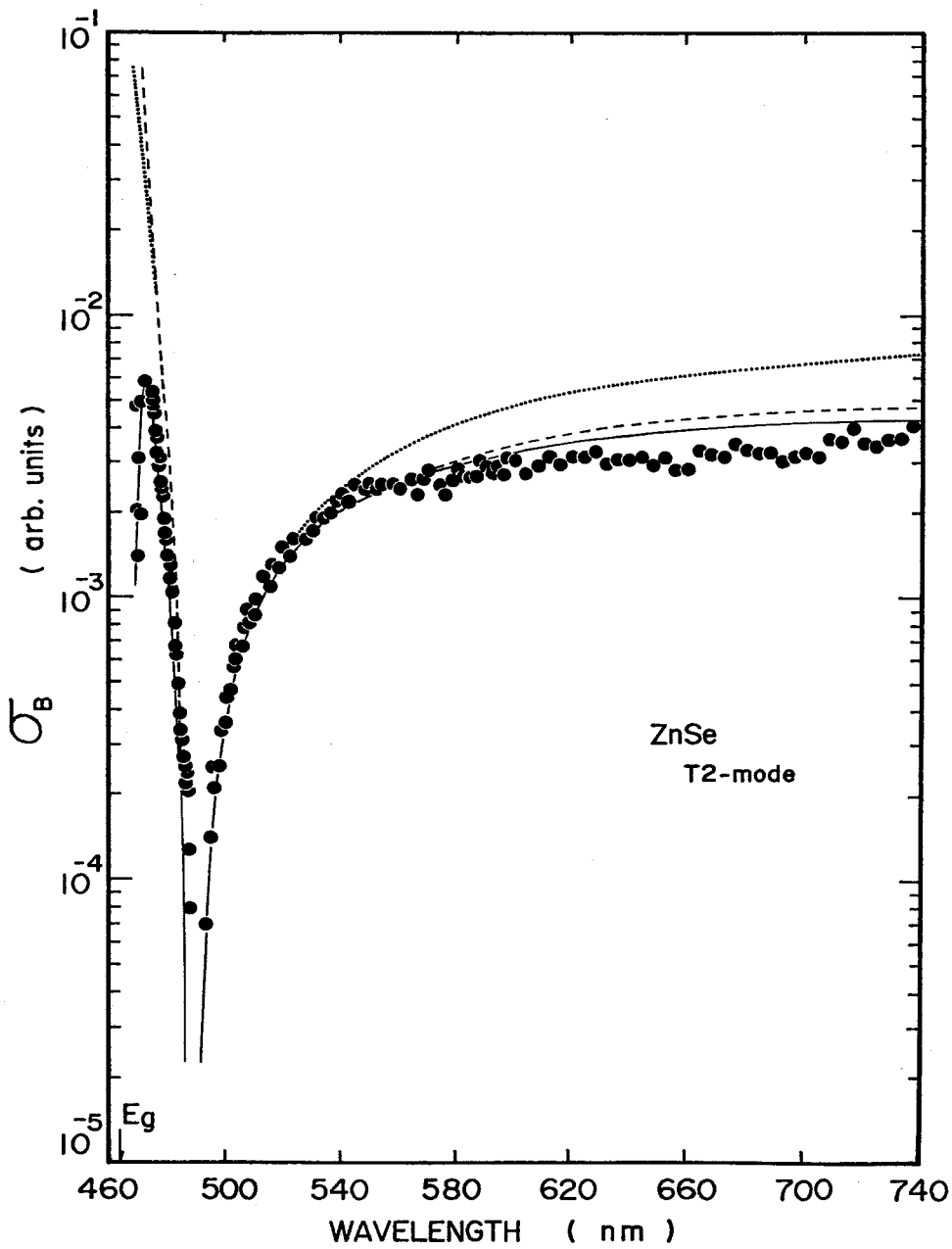

FIG. 4-7. Dispersion curve of the Brillouin-scattering cross sections in ZnSe [as-grown] for 0.2 GHz T2-mode phonons at room temperature. The theoretical curves are obtained from Eq. (2.55) with Γ=0 meV (dashed line) and Γ=56 meV (solid line). The dotted line is obtained from Eq. (2.29). The vertical arrow indicates the position of the band gap E_g.

absorption edge. Such a feature has not been clearly found in the previous work of Ando *et al.*[120]

The spectral dependence of the Brillouin-scattering cross sections for 0.2 GHz T2-mode phonon domains measured at room temperature is shown in Fig. 4-7. The resonance feature observed here is essentially the same as that for the case of the scattering by the T1-mode phonon domains, but the cancellation point shifts slightly and occurs at 490 nm. As will be mentioned in Chapter VI, the resonant cancellation can be interpreted macroscopically in terms of the appropriate photoelastic constant passing through zero (isotropic point) while undergoing a reversal in sign (here we have to note that the Brillouin-scattering cross section is proportional to the square of the photoelastic constant). We can find a good agreement between the cancellation points obtained from the Brillouin-scattering measurements and those predicted from the piezobirefringence data (isotropic points) of Yu and Cardona.[92]

The resonant cancellation can be explained by the following equation:[95]

$$\sigma_B \propto | R_{is} + R_0 |^2 \quad , \qquad (4.2)$$

where R_{is} is the resonant contribution given by Eq. (2.29) or (2.55), arising from the M_0 critical point, and R_0 is a nonresonant contribution arising from the other, far-off critical points in the band structure. The resonant contribution R_{is} is opposite in sign to the nonresonant contribution R_0 in the longer-wavelength region (apart from the fundamental absorption edge). The cancellation, therefore, occurs at a wavelength when $|R_{is} + R_0|$ becomes zero. As well shall see later, such a sign reversal relation does not hold in the region very close to the fundamental absorption edge when the lifetime-broadening effect is taken into account [see Figs. 4-10 and 4-11]. Kiefer *et al.*[57] have measured the resonance of Raman scattering in ZnSe by TO(Γ), TA + TO(X), 2TA(X) and 2LO(X) phonons in the vicinity of the E_0 gap, and

found that the spectral dependence shows clear resonant enhancement but non existence of resonant cancellation in the photon-energy region of 2.3 – 2.7 eV [see Fig. 4-12]. Such a considerably large difference in the experimental resonance data between Brillouin and Raman scattering can not be successfully understood at present.

Figures 4-8 and 4-9 show the spectral dependence of the Brillouin-scattering cross sections for 0.2 GHz T1- and T2-mode phonon domains measured at 77 K, respectively. The vertical arrows indicate the positions of the band gap E_g. It is clear from the figures that the experimental data taken at 77 K show the same resonance behaviors as those taken at room temperature, except a shift of the resonance curves toward shorter-wavelength side. The resonant cancellation, thus, occurs at about 480 and 474 nm for the T1- and T2-mode phonons, respectively.

The intermediate electronic states produced by the incident radiation interact with the acoustical phonons via a deformation potential, resulting in a change in their electronic states. The transitions of the intermediate states are determined by the symmetry properties of the electronic states and relevant phonon modes in crystals, as mentioned in Section 2.2.3. Such a selection rule of the deformation-potential scattering determines the electronic transition process (two- or three-band process) which plays a significant role in the Brillouin-scattering process. From Eqs. (2.76) and (2.77), the non-zero matrix element $\Xi_{\beta\alpha}$ can be given by

$$\Xi_{BA} = 3^{\frac{1}{2}}b = -2.08 \text{ eV} \quad , \qquad (4.3a)$$

$$\Xi_{CB} = 6^{\frac{1}{2}}b = -2.94 \text{ eV} \quad , \qquad (4.3b)$$

for the T1-mode phonons, and

$$\Xi_{BA} = d = -3.81 \text{ eV} \quad , \qquad (4.4a)$$

$$\Xi_{CB} = d/2^{\frac{1}{2}} = -2.69 \text{ eV} \quad , \qquad (4.4b)$$

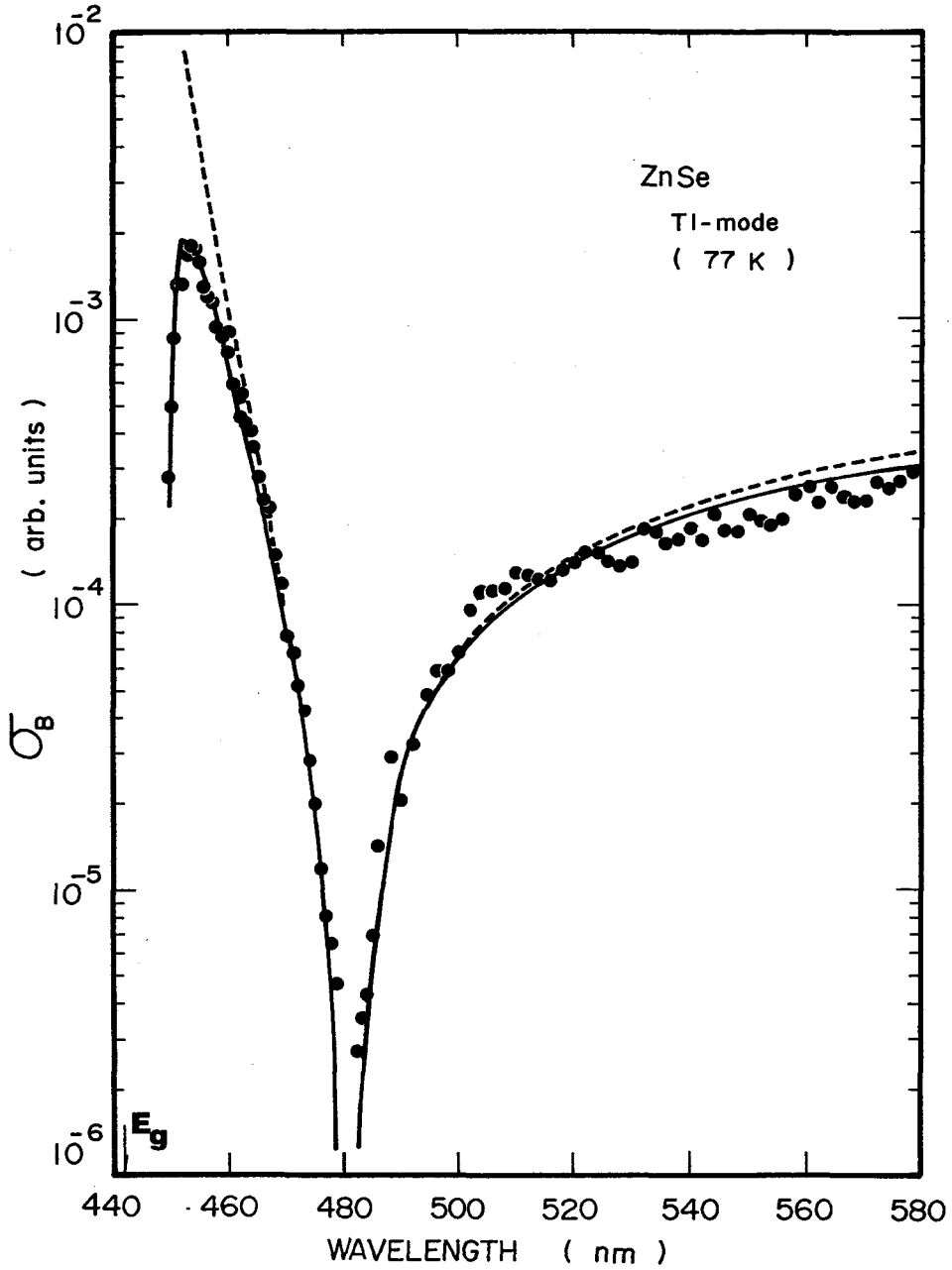

FIG. 4-8. Dispersion curve of the Brillouin-scattering cross sections in ZnSe [as-grown] for 0.2 GHz Tl-mode phonons measured at 77 K. The theoretical curves are obtained from Eq. (2.55) with Γ=0 meV (dashed line) and Γ=64 meV (solid line). The vertical arrow indicates the position of the band gap E_g.

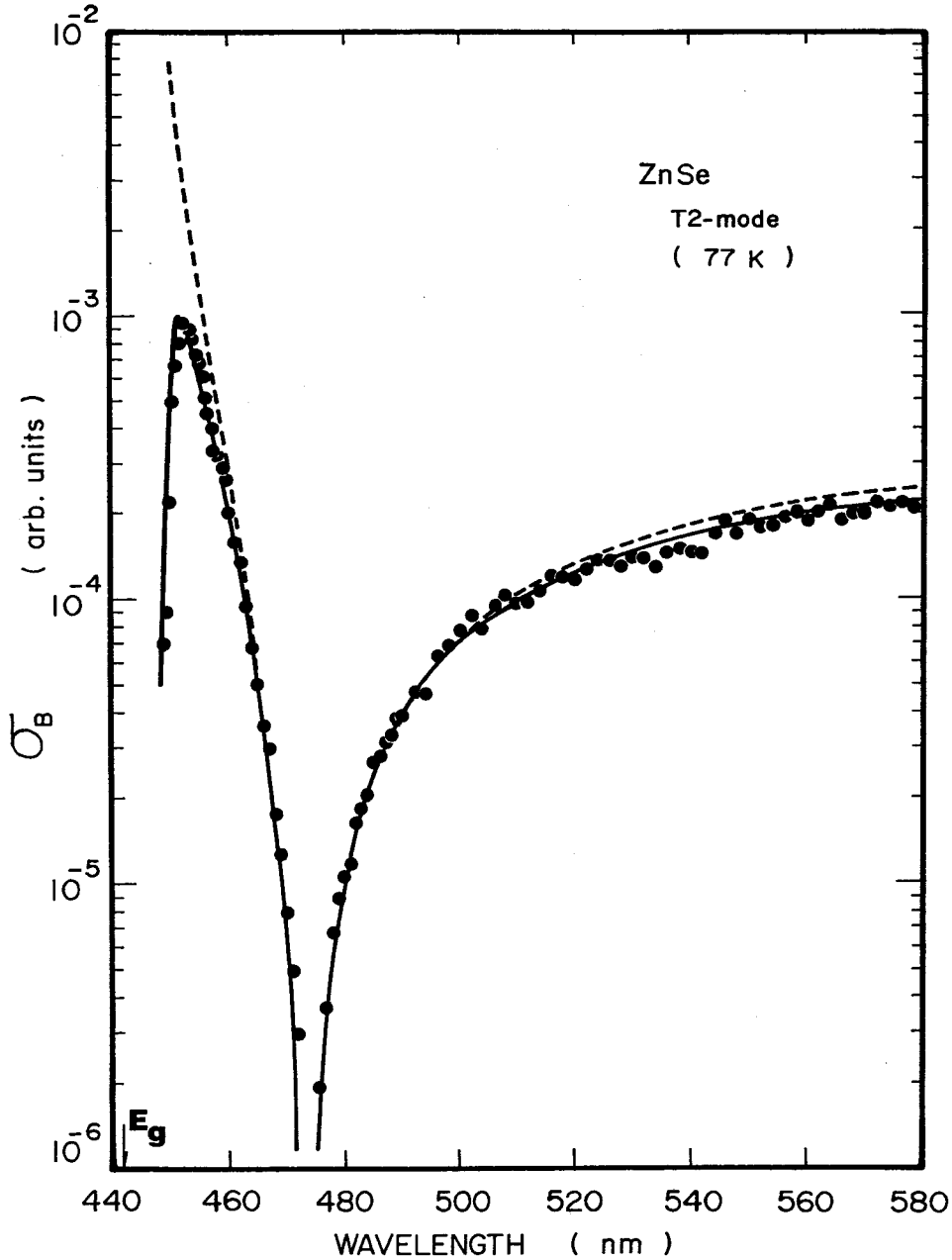

FIG. 4-9. Dispersion curve of the Brillouin-scattering cross sections in ZnSe [as-grown] for 0.2 GHz T2-mode phonons measured at 77 K. The theoretical curves are obtained from Eq. (2.55) with Γ=0 meV (dashed line) and Γ=56 meV (solid line). The vertical arrow indicates the position of the band gap E_g.

$$\Xi_{CA} = 6^{\frac{1}{2}}d/2 = -4.67 \text{ eV} \quad , \qquad (4.4c)$$

where the numerical values of the shear deformation potentials b and d are obtained from the data of Langer *et al.*[152]

The theoretical dispersion curves obtained from Loudon's theory [Eq. (2.29)] and Wannier-Mott exciton theory [Eq. (2.55)] are shown in Figs. 4-6 and 4-7 by dotted and dashed lines, respectively. The numerical values used in the calculations are listed in Table 4-3. The p-matrix elements are assumed to be $P_{\alpha 0} = P_{0\beta}$ since the detailed values are not yet well known at present. The curve calculated from Eq. (2.55) shows a better fit to the experimental data compared with that calculated from Eq. (2.29) except in the region very close to the exciton energy (band-edge region), where the theoretical dispersion shows a divergence at that region. To remove this disagreement, we consider in Eq. (2.55) the lifetime-broadening (damping) effect for the intermediate exciton states. It is well known that the excitonic transitions play an important role in the optical properties such as absorption and emission of photons in the band-edge region, because the Coulomb interaction is always present between the electrons and holes. They are affected strongly by the lifetime-broadening effect especially at higher temperatures caused by the relatively strong coupling to LO phonons (thermal broadening). When the lifetime-broadening effect is taken into account, the theoretical dispersion curve exhibits a peak near the band-edge region and thus the fit shows an excellent agreement with the experimental data as shown by the solid line (Figs. 4-6 and 4-7). The best-fitting values of the broadening energy are determined to be Γ = 64 and 56 meV for the T1- and T2-mode phonons, respectively, where they are the values in the assumption of Eq. (2.56). In Figs. 4-8 and 4-9, we show the theoretical curves calculated from Eq. (2.55) with $\Gamma = 0$ (dashed line) and $\Gamma \neq 0$ (solid line). The best-fitting values of the broadening energy at 77 K are determined to be Γ = 64

Table 4-3. Numerical values used to calculate the spectral dependence of the Brillouin-scattering cross sections.

	Material				
	ZnSe	ZnTe	$Zn_{0.8}Cd_{0.2}Te$	$Zn_{0.5}Cd_{0.5}Te$	CdS
$\hbar\omega_{gA}$ [eV]	2.68*a, 2.808**b	2.25*a, 2.379**c	2.10*d	1.80*d	2.452*e
$\hbar\omega_{gB}$ [eV]	2.68*a, 2.808**b	2.25*a, 2.379**c	2.10*d	1.80*d	2.466*e
$\hbar\omega_{gC}$ [eV]	3.09*a, 3.218**b	3.18*a, 3.309**c	——	——	2.525*e
$\hbar\Delta\omega_{gA}$ [eV]	5.0	4.5	4.2	3.6	
$\hbar\Delta\omega_{gB}$ [eV]	5.0	4.5	4.2	3.6	
$\hbar\Delta\omega_{gC}$ [eV]	5.0	4.5	——	——	
$\hbar R^*$ [meV]	19	10	10	10	28
a_0^* [Å]	51	45	45	45	28
μ	0.11	0.12	0.12	0.12	0.18

* Room temperature
** 77 K.

[a]Reference 184.
[b]Reference 185
[c]Reference 186.
[d]Estimated from Fig. 4-16.
[e]Reference 187.

and 56 meV for the T1- and T2-mode phonons (solid lines), respectively,

Figures 4-10 and 4-11 show the theoretical line shapes of the Brillouin-tensor term R_{is} for the T1- and T2-mode phonons, respectively, calculated from Eq. (2.55) in the vicinity of the excitonic structure with different broadening energies. The experimental data ($\sigma_B^{\frac{1}{2}} \propto |R_{is} + R_0|$) measured at room temperature and 77 K are plotted in the figures by taking into account the corresponding nondispersive terms R_0 which are also shown in the figures by dash-dotted lines. The vertical arrows in the figures indicate the positions of the lowest discrete-exciton state E_{x1}. When the exciton states have an infinite lifetime ($\Gamma = 0$), the theoretical curve (R_{is}) shows a divergence near the band-edge region. The broadening effect depresses the resonance feature, and the Brillouin-scattering efficiency decreases with increasing broadening energy Γ. Consequently, the peak of the Brillouin-scattering efficiency appears in the resonant-enhancement region. The broadening energies determined in the present work do not depend on the temperatures, as clearly seen in Figs. 4-10 and 4-11. In general, the broadening energy can be expressed by a sum[153]

$$\Gamma(T) = \Gamma_0 + \Gamma_T(T) \quad , \qquad (4.5)$$

where Γ_0 is independent of the temperature T, arising mainly from the impurity damping, and $\Gamma_T(T)$ is contributions from acoustical phonons, proportional to $[\exp(\hbar\omega_{LO}/k_BT) - 1]^{-1}$ (here $\hbar\omega_{LO}$ is a LO phonon energy). Thus, $\Gamma(T)$ decreases with decreasing T. In the present case, the amplified acoustical-phonon domains have an energy density a factor of the order of 10^9 above the thermal equilibrium value,[18] and thus the acoustical-phonon contribution has an appreciable value to contribute to the lifetime broadening. We can, therefore, expect specific effects of the high-density acoustical phonons on the lifetime broadening, as also suggested by Segall.[153] Details will be discussed in Chapter VII.

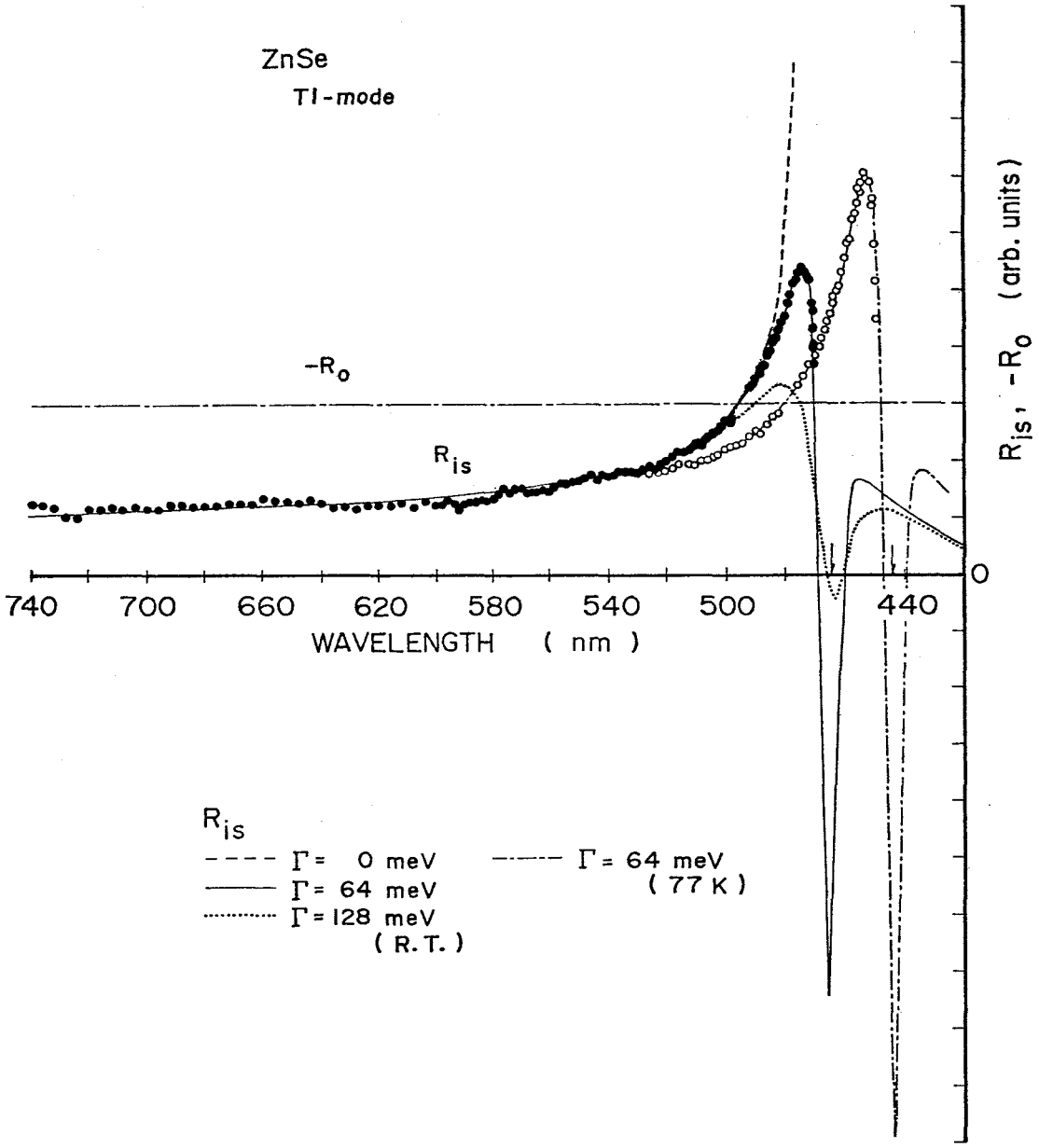

FIG. 4-10. Theoretical line shapes of R_{is} for the case of Tl-mode phonons obtained from Eq. (2.55) with three different broadening parameters in the neighborhood of the excitonic structure along with the experimental data measured at room temperature (solid circles) and 77 K (open circles). The vertical arrows indicate the positions of the lowest discrete-exciton state E_{x1}. The corresponding non-dispersive term ($-R_0$) is also shown in the figure.

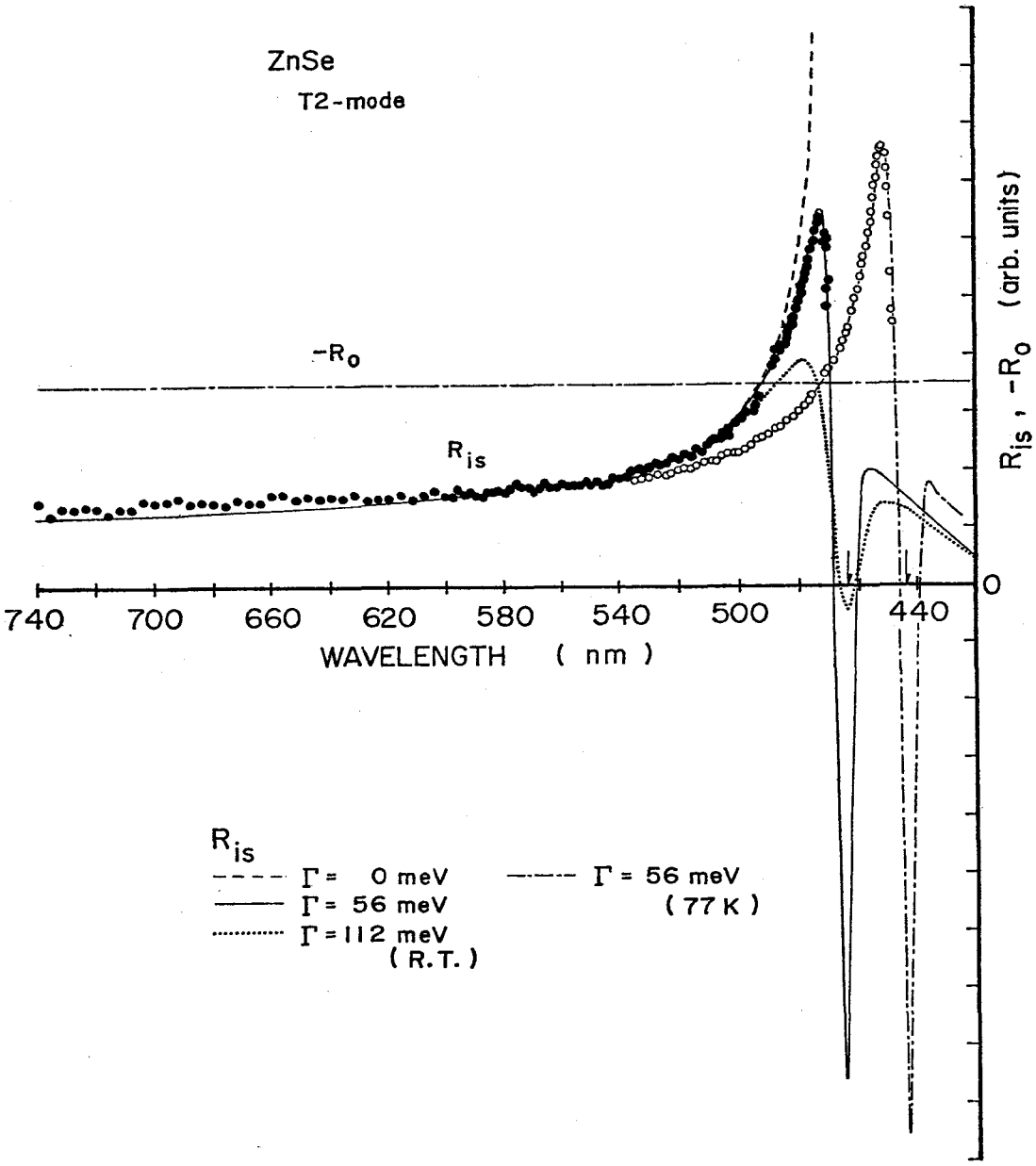

FIG. 4-11. Theoretical line shapes of R_{is} for the case of T2-mode phonons obtained from Eq. (2.55) with three different broadening parameters in the neighborhood of the excitonic structure along with the experimental data measured at room temperature (solid circles) and 77 K (open circles). The vertical arrows indicate the positions of the lowest discrete-exciton state E_{x1}. The corresponding non-dispersive term ($-R_0$) is also shown in the figure.

It should be noted here that the theoretical line shapes of R_{is} (solid lines) predict resonant cancellation at two different wavelengths [*e.g.*, at 495 and 470 nm for the T1-mode phonons (room temperature), see Fig. 4-10] according to the relation given by Eq. (4.2). Such a feature has been found clearly in the present experiments as shown in Figs. (4-6) — (4-9). The theoretical curve, further, predicts that a strong scattering signal should be observed at wavelengths near the ground-state exciton region (due to sharp peaks appeared in Figs. 4-10 and 4-11). We were, however, unable to find such a scattering signal because of the strong absorption coefficients in the exciton-energy region. In spite of such difficulty in experiments, we believe that measurements should be possible if sufficiently thin samples are prepared and a continuously tunable dye laser is used in the Brillouin-scattering measurements. When the incident-photon energy approaches the exciton resonance, we have to take into account the excitonic polariton states in the Brillouin-scattering process.[65,154,155] Brenig, Zeyer and Birman[66] have reported a theoretical analysis of resonant Brillouin scattering in crystals exhibiting spatial dispersion which included exciton polaritons as the intermediate states in the Brillouin-scattering process. Their result predicts a multiplet of the Brillouin spectrum near the exciton resonance with line separations and efficiencies, depending strongly on the incident-light energy because of the polariton dispersion. Recently, the first experimental observation of the effects predicted by Brenig *et al.*[66] has been reported by Winterling and Koteles in CdS.[158,159] Bruce and Cummins[160] have observed resonant dispersion of the Brillouin shift in CdS with a high-resolution triple-pass Fabry-Perot interferometer. Winterling *et al.*[161] have observed resonant Brillouin scattering by TA phonons near the A exciton of CdS in a usually forbidden backscattering configuration. Yu and Evangelisti[162,163] have also studied resonant Brillouin scattering by exciton polaritons in CdS

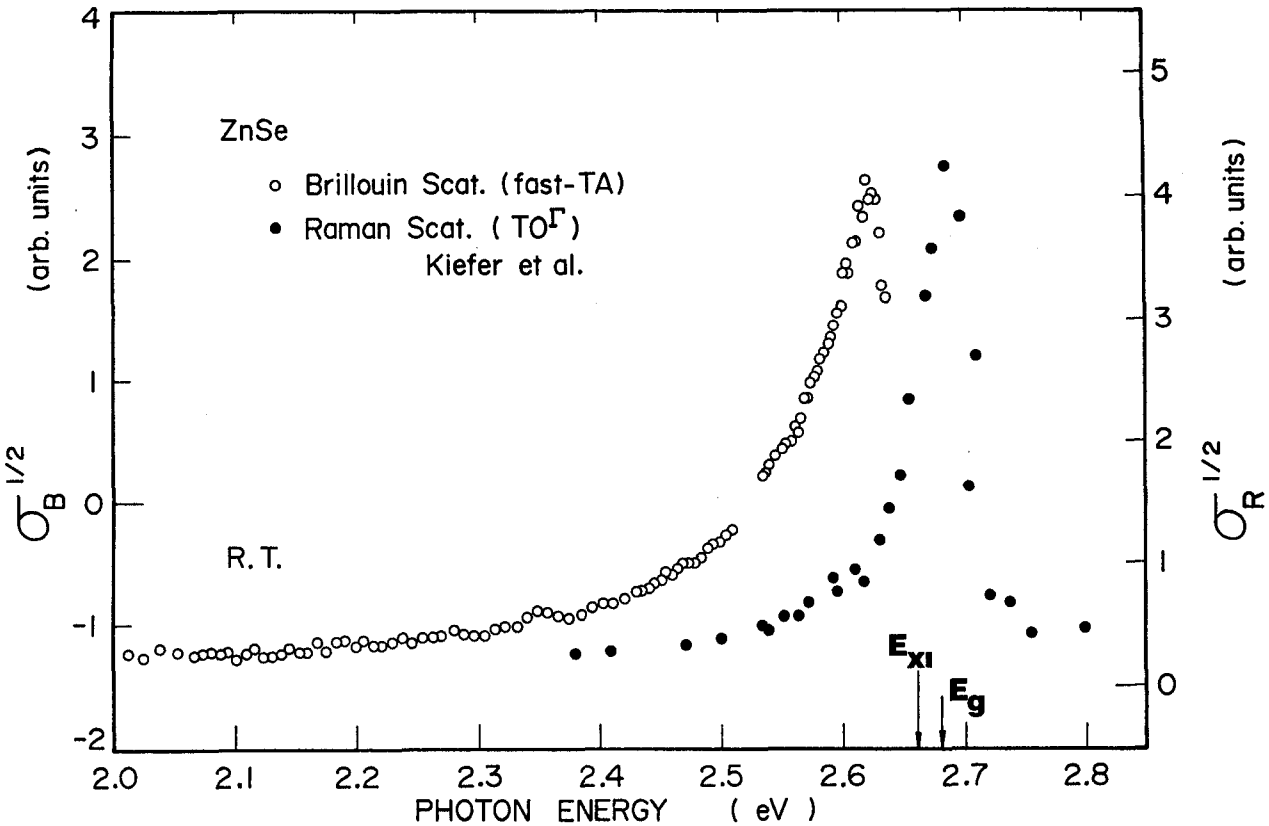

FIG. 4-12. Comparison of the resonance behavior of the Brillouin-scattering cross sections for fast-TA phonons (T2-mode phonons) with that of the Raman-scattering cross sections for TO(Γ) phonons in ZnSe obtained at room temperature. The Raman-scattering data are from Ref. 57.

and obtained a good agreement between theory and experiment. More recently, such Brillouin-scattering spectra of exciton polaritons have been measured in CdSe by Herman and Yu[164] and in ZnTe by Oka and Cardona.[165]

In Fig. 4-12, we show a comparison of the resonance behavior of the Brillouin-scattering cross sections for fast-TA (T2-mode) phonons with that of the Raman-scattering cross sections for TO(Γ) phonons in ZnSe obtained at room temperature. The Raman-scattering data are obtained from Kiefer *et al.*[57] The vertical arrows in the figure indicate the band-gap energy E_g and lowest discrete-exciton energy E_{x1}. It is noting that the spectral dependence of the Raman-scattering cross sections shows non existence of cancellation in the region below E_g, in contrast to the Brillouin-scattering data. The resonant cancellation of the Raman-scattering intensity is found in various wurtzite-type semiconductors such as CdS,[10,166] ZnO[58,167] and ZnS.[168,169] The Raman-scattering intensity shows a maximum near the band-gap energy, while the maximum in our Brillouin-scattering data appears below that of the Raman-scattering data. However, as mentioned above, our theoretical prediction indicates that maximum of the Brillouin-scattering intensity should be observed at the photon-energy region of E_{x1} (E_g), as similar to that of the Raman-scattering data. Such a expectation can be clearly seen in Fig. 2-6 in which the calculated Brillouin-scattering cross section shows a strong peak at the band edge in addition to the experimentally observed peak (below the band-gap energy).

4.3.2 ZnTe

The spectral dependence of the Brillouin-scattering cross sections for 0.2 GHz T1-mode phonon domains measured at room temperature is shown in Fig. 4-13. The Brillouin-scattering measurements were carried out by making use of the acoustical-domain injection method. We used here ZnTe single crystals grown by the traveling heater method (THM).[97] It is found from

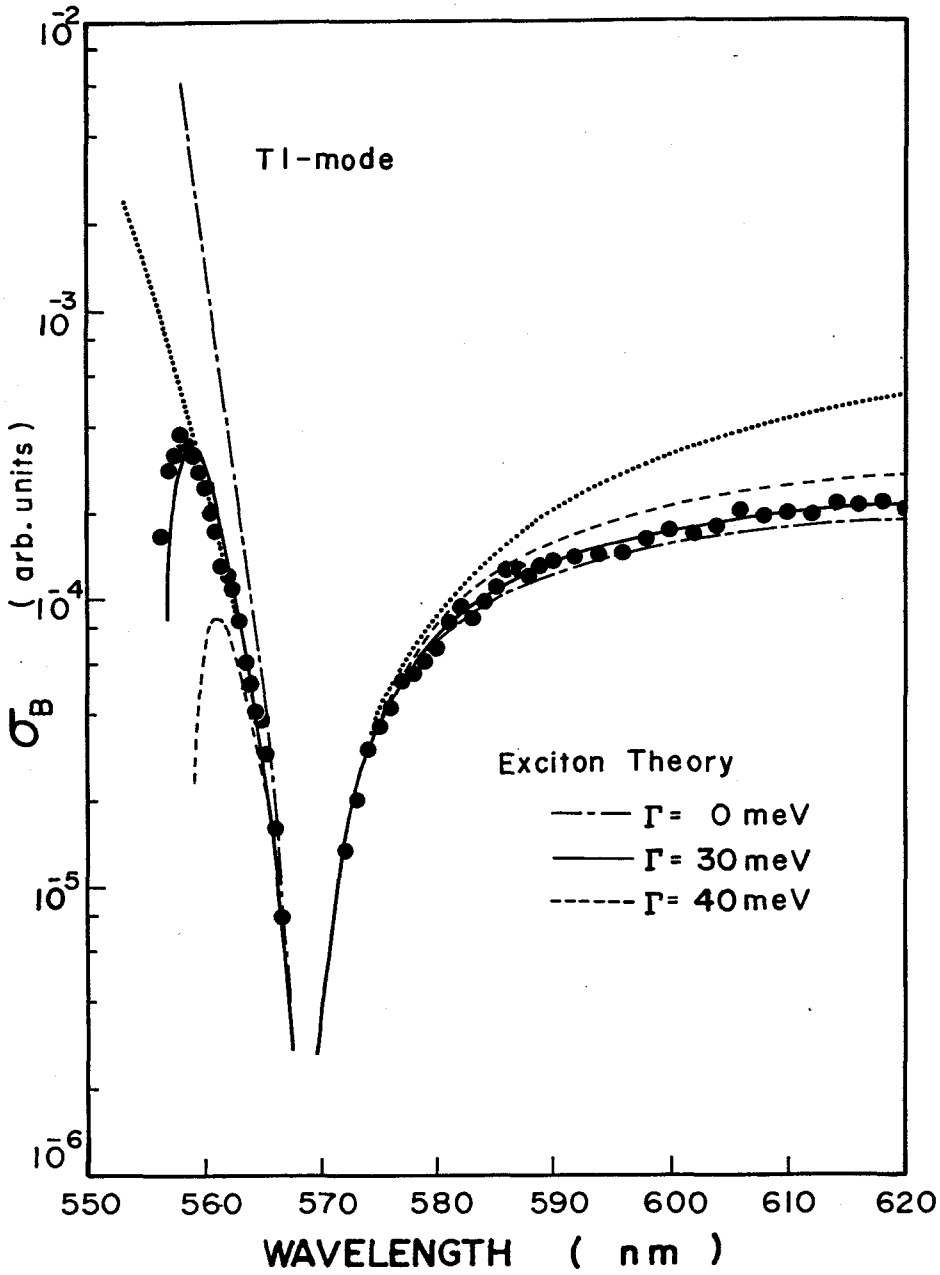

FIG. 4-13. Calculated dispersion curves of the Brillouin-scattering cross sections in ZnTe obtained from Eqs. (2.29) [dotted line] and (2.55) [exciton theory] along with the experimental data for 0.2 GHz Tl-mode phonons at room temperature.

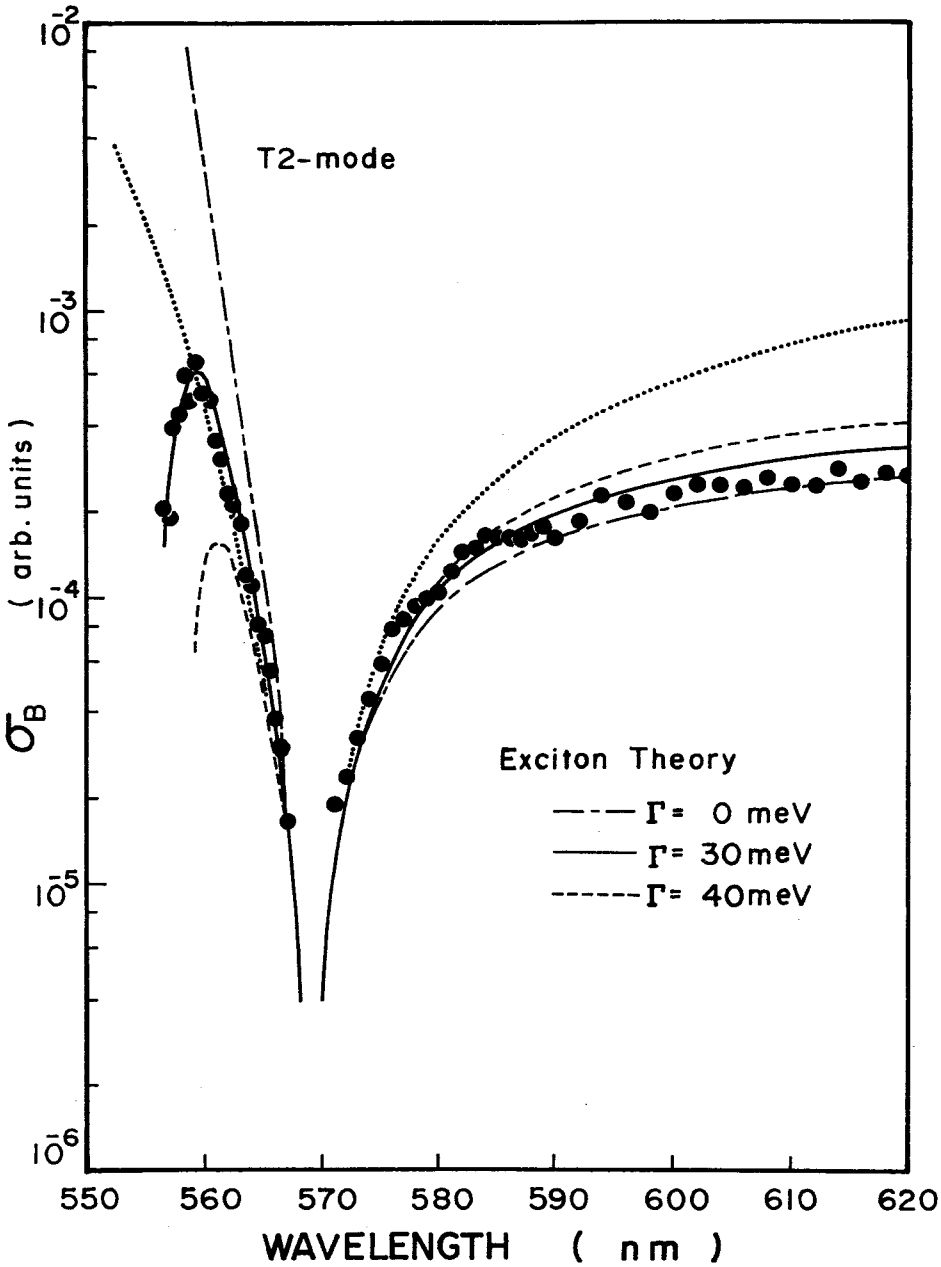

FIG. 4-14. Calculated dispersion curves of the Brillouin-scattering cross sections in ZnTe obtained from Eqs. (2.29) [dotted line] and (2.55) [exciton theory] along with the experimental data for 0.2 GHz T2-mode phonons at room temperature.

the figure that the Brillouin-scattering cross section shows clear resonant enhancement and cancellation as the incident-light wavelength approaches close to the fundamental absorption edge (≃ 551 nm). The cancellation point is found to be 568.5 nm. The spectral dependence of the Brillouin-scattering cross sections for 0.2 GHz T2-mode phonon domains measured at room temperature is shown in Fig. 4-14. The resonance features observed for the T2-mode phonons are found to be almost the same as that for the T1-mode phonons, where for this mode the resonant cancellation occurs at 569 nm. We also found that the experimental curves for both the T1- and T2-mode phonons are almost independent of their phonon frequencies, where the signals of specular phonon frequencies were picked up by varying incident and scattering angles according to Eq. (3.29). Similar features have also been found in GaAs[25] and CdS.[27] One of the most important features found here is that the Brillouin-scattering cross section exhibits a maximum at a photon energy very close to the band edge of ZnTe, as similar to that observed in ZnSe.

The theoretical dispersion curves obtained from Loudon's theory [Eq. (2.29)] are shown in Figs. 4-13 and 4-14 by dotted lines ($\Gamma = 0$). The curves obtained from the Wannier-Mott exciton theory [Eq. (2.55)] are also shown in the figures with three different broadening energies, $\Gamma = 0$ (dash-dotted lines); $\Gamma = 30$ meV (solid lines); and $\Gamma = 40$ meV (dashed lines). The numerical values used in the calculations are listed in Table 4-3. The non-zero matrix element $\Xi_{\beta\alpha}$ *for the deformation-potential scattering by the T1-mode phonons* can be obtained as [see Eq. (2.76)]

$$\Xi_{BA} = -3.08 \text{ eV} \quad \text{and} \quad \Xi_{CB} = -4.36 \text{ eV} \quad , \tag{4.6}$$

and by the T2-mode phonons as [see Eq. (2.77)]

$$\Xi_{BA} = -4.61 \text{ eV} \quad , \quad \Xi_{CB} = -3.26 \text{ eV} \quad \text{and} \quad \Xi_{CA} = -5.64 \text{ eV} \quad , \tag{4.7}$$

where the numerical values are estimated from the deformation potentials as

reported by Kaplyanskii and Suslina.[170] One finds that the Loudon's model shows a poor agreement with the experimental data at longer wavelength region for both the T1- and T2-mode phonons. The Wannier-Mott exciton model, on the other hand, shows a quite good agreement with the experimental data when we take into account the lifetime-broadening energy of Γ = 30 meV for both the T1- and T2-mode phonons (solid lines).

In Fig. 4-15, we show a comparison of the resonance behavior of the Brillouin-scattering cross sections for fast-TA (T2-mode) phonons with that of the Raman-scattering cross sections for TO(Γ) phonons in ZnTe obtained at room temperature. The vertical arrows indicate the band-gap energy E_g and lowest discrete-exciton energy E_{x1}. The Raman-scattering data are obtained from Schmidt *et al.*[56] They measured the resonance of the first- and second-order Raman-scattering spectra in ZnTe in the region of the E_0 edge using tunable cw dye lasers and ion lasers. The phonon frequencies assigned by them agree well with those of the phonon-dispersion data presented in Fig. 4-4 (b) [*e.g.*, 179 cm^{-1} for the TO(Γ) phonons]. In contrast to the Brillouin-scattering data, the Raman-scattering cross section does not show any evidence of resonant cancellation in the region below E_g, as similar to that for the case of ZnSe (Fig. 4-12). It can also be seen that the Raman-scattering intensity resonates at a photon-energy region higher than the Brillouin resonance, and consequently the resonance maximum occurs at a region beyond the band gap. When incident-photon energy is close to one of the resonance energies, i.e. [see, *e.g.*, Eq. (2.24)],

$$\omega_i \rightarrow \omega_{g\beta} + \omega_q \tag{4.8a}$$

$$\omega_i \rightarrow \omega_{g\alpha} \quad , \tag{4.8b}$$

the scattered light resonates strongly. This means that the resonance maximum occurs at an energy ω_q higher than the band-gap energy. The TA(Γ)

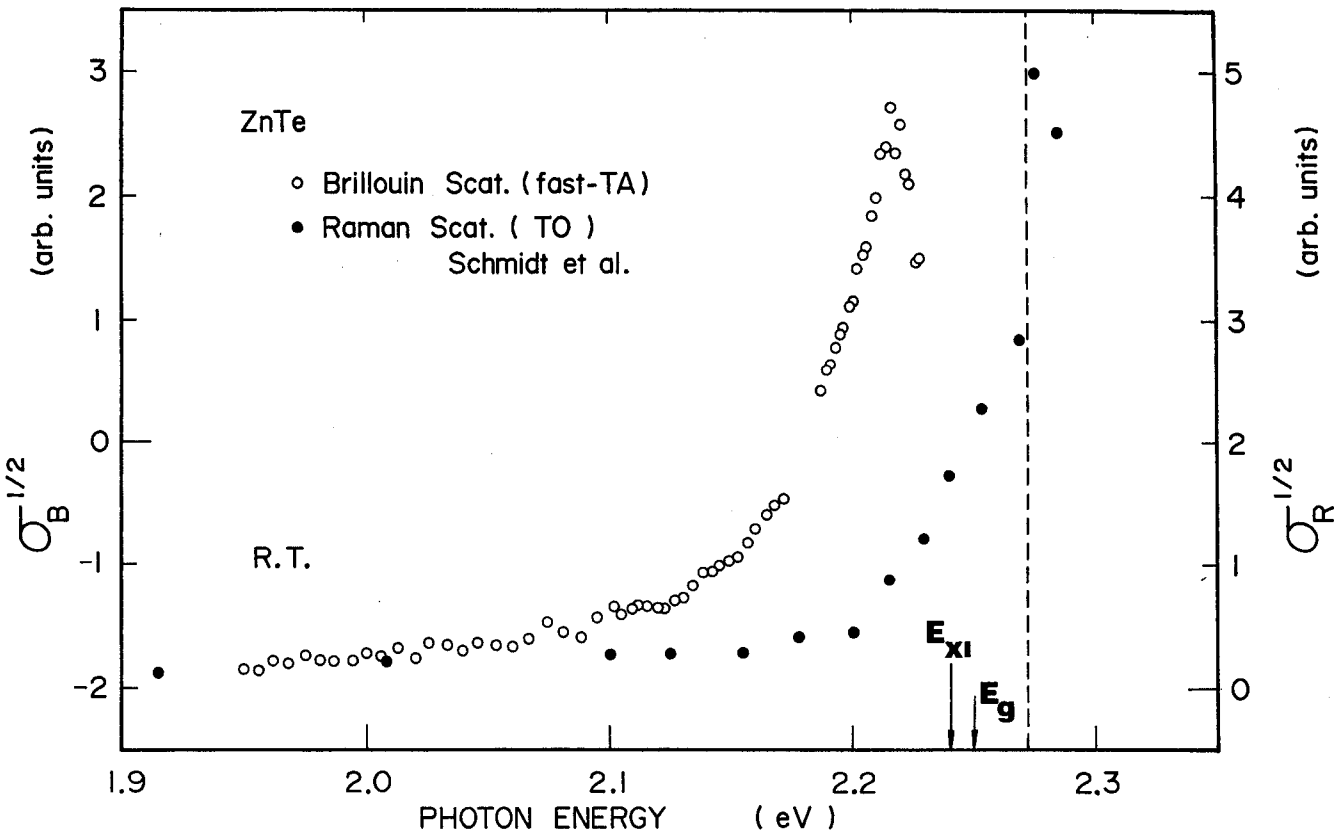

FIG. 4-15. Comparison of the resonance behavior of the Brillouin-scattering cross sections for fast-TA phonons (T2-mode phonons) with that of the Raman-scattering cross sections for TO(Γ) phonons in ZnTe obtained at room temperature. The Raman-scattering data are from Ref. 56.

and TO(Γ) phonon energies are estimated from Fig. 4-4 (b) to be 1.3×10^{-7} (0.2 GHz) and 0.022 eV (179 cm^{-1}), respectively. In Fig. 4-15, we show the position of the resonance energy represented by Eq. (4.8a) for the TO(Γ) phonons by the vertical dashed line. It is obvious from the figure that the resonance-energy shift for the Raman-scattering data agrees well with this simple estimation.

4.3.3 $Zn_xCd_{1-x}Te$

Resonance-Raman (Brillouin) effect has been intensively studied in several element and binary-compound semiconductors. There are, however, few reports on resonant light scattering in ternary compounds (solid solutions).[171-173] In solid solutions, the relative concentration of the participants determines the band-gap energy which usually falls within the range of the band-gap energies of the two pure compounds. The band-gap energy plays a significant role in resonance features through the intraband and interband electronic transitions. It is well known that the solid solutions can be divided into those having a one-mode type behavior and those having a two-mode type behavior in Raman scattering.[174] In the one-mode system, the $\vec{k} \simeq 0$ optical mode frequencies vary continuously with concentration from the frequency characteristic of one end member to that of the other end member. In the two-mode system, for each allowed optical mode two bands are observed with frequencies in the vicinity of those of the pure crystals. We report here the first observation of resonant Brillouin scattering in $Zn_xCd_{1-x}Te$ solid solutions investigated at room temperature by making use of the acoustical-domain injection method. The $Zn_xCd_{1-x}Te$ solid solutions used were grown by the traveling heater method (see Appendix).

The variation of the lowest gap E_0 with composition x for the $Zn_xCd_{1-x}Te$ solid solutions is expressed by a trinomial of the type[175]

$$E_0(x) = a + bx + cx^2 \quad , \qquad (4.9)$$

where the parameter c, which is the so-called bowing parameter, determines the deviation from linearity. This parameter is given by a sum of the intrinsic bowing c_i arising from the virtual crystal approximation and extrinsic bowing c_e originating in the aperiodicity of the crystal potential. The relation (4.9) is well known for the semiconductor-alloy systems. Several recent studies of the reflectance spectra of the ZnTe — CdTe system have revealed peaks such as E_0, $E_0+\Delta_0$, E_1, $E_1+\Delta_1$, e_1 and $e_1+\Delta_1$.[135,137,139] Such an analysis has also been recently performed by using the low-field electro-reflectance technique.[138] Figure 4-16 shows the lowest band gap E_0 as a function of x for the ZnTe — CdTe system. The spin-orbit splitting band $E_0+\Delta_0$ is also shown in the figure. We used the bowing parameter c = 0.33 eV to calculate the lowest band gap $E_0(x)$. This value is determined from the fit of reflectance data to Eq. (4.9).[137]

Figures 4-17 and 4-18 show the spectral dependence of the Brillouin-scattering cross sections for 0.2 GHz T2-mode phonons in $Zn_xCd_{1-x}Te$ solid solutions with x = 0.8 and 0.5, respectively. The phase velocity of the sound waves, $v_s = (C_{44}/\rho)^{\frac{1}{2}}$, which propagated in the [001] direction with shear polarization parallel to the [110] direction, was found to decrease as molar composition x decreases as follows: 2.50×10^5, 2.29×10^5 and 2.00×10^5 cm/sec for x = 1.0, 0.8 and 0.5, respectively. The spectral dependence shows clear resonance phenomena in the region near the band edge. They are found to be very similar to those of the pure binary compounds such as ZnSe and ZnTe. The data exhibit deep minima (cancellation) in the Brillouin-scattering efficiencies occuring at about 610 and 714 nm for x = 0.8 and 0.5, respectively.

The theoretical curves obtained from Eqs. (2.29) [free electron-hole pair model] and (2.55) [Wannier-Mott exciton model] are shown in the figures

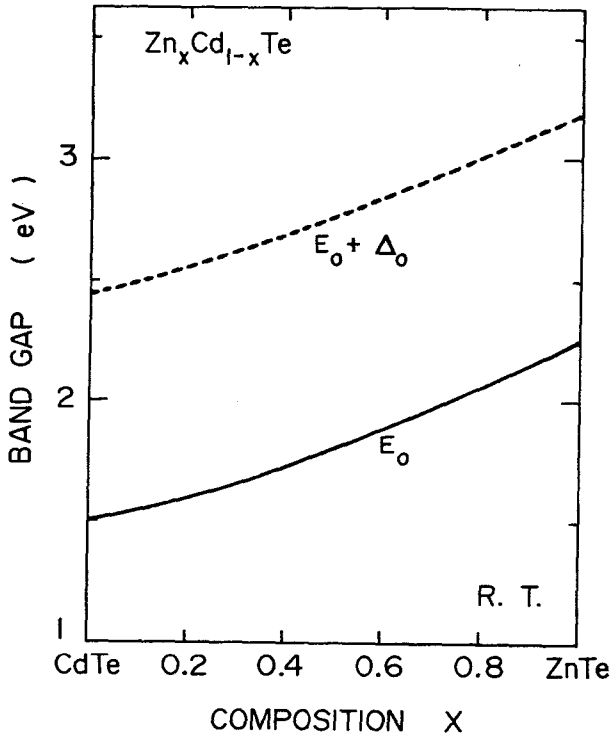

FIG. 4-16. Lowest band gap E_0 as a function of the molar composition x for $Zn_xCd_{1-x}Te$ solid solutions at room temperature. The spin-orbit splitting band $E_0+\Delta_0$ is also shown in the figure.

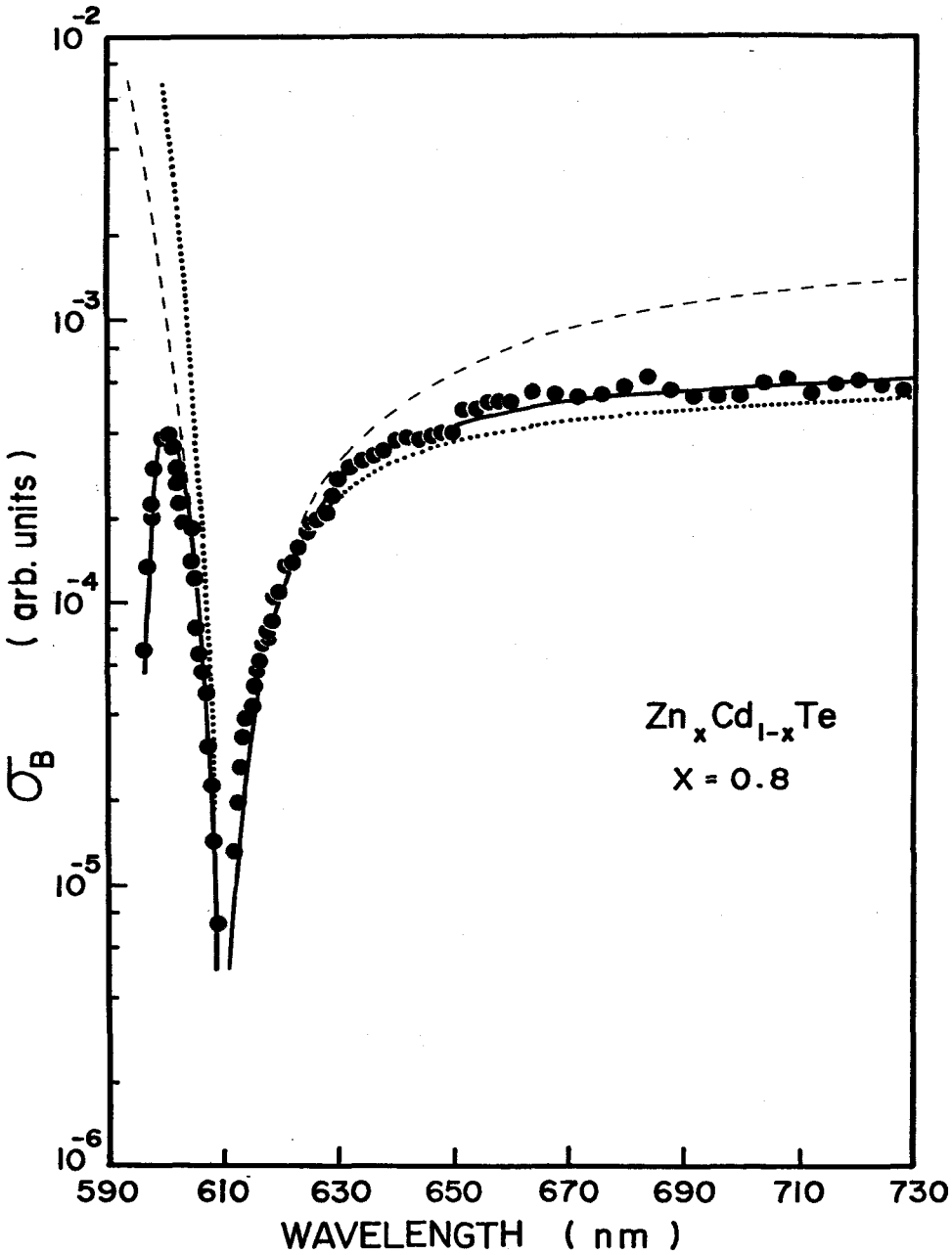

FIG. 4-17. Dispersion curve of the Brillouin-scattering cross sections in $Zn_{0.8}Cd_{0.2}Te$ for 0.2 GHz T2-mode phonons measured at room temperature. The theoretical curves are obtained from Eq. (2.55) with Γ=0 meV (dotted line) and Γ=34 meV (solid line) and from Eq. (2.29) with Γ=0 meV (dashed line).

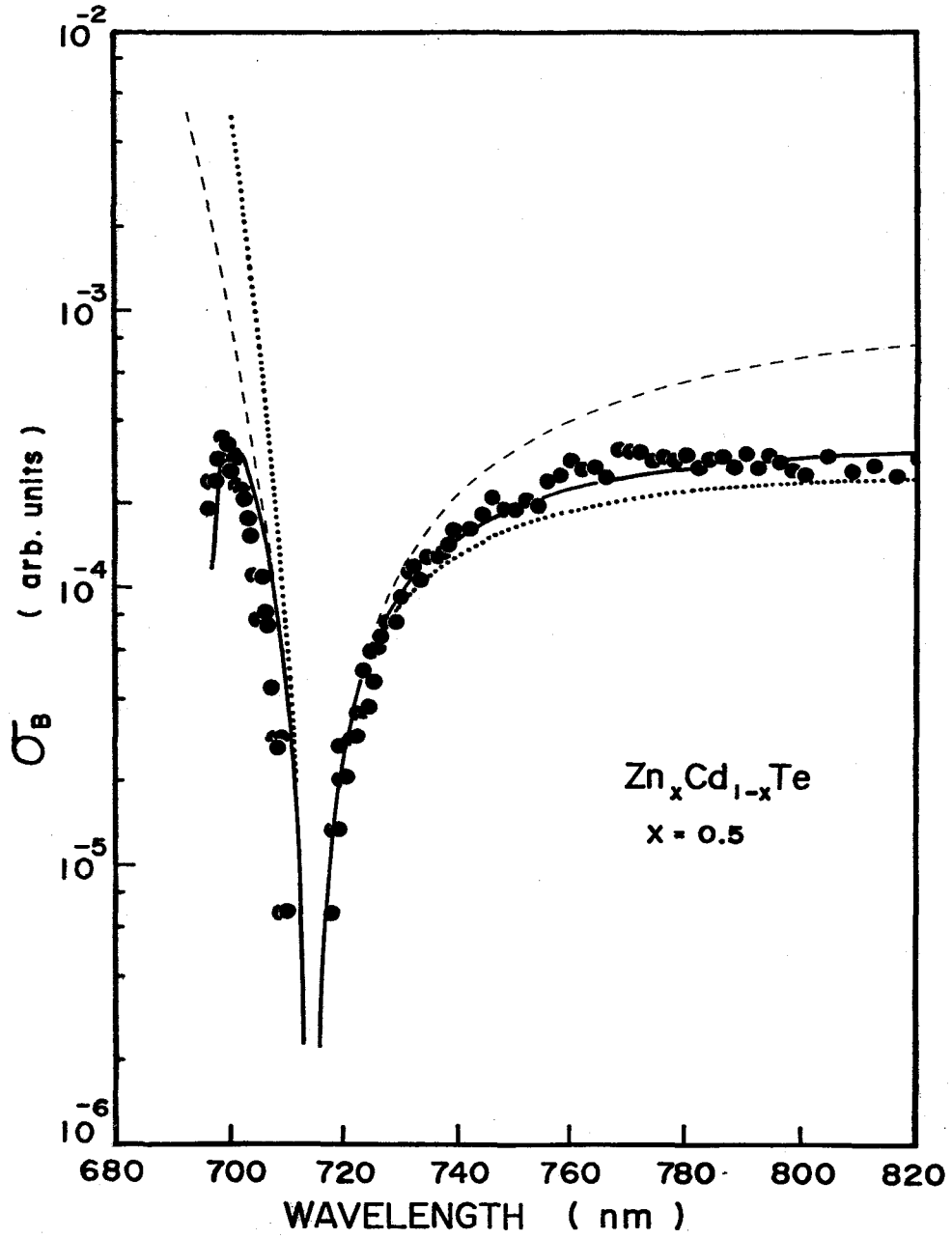

FIG. 4-18. Dispersion curve of the Brillouin-scattering cross sections in $Zn_{0.5}Cd_{0.5}Te$ for 0.2 GHz T2-mode phonons measured at room temperature. The theoretical curves are obtained from Eq. (2.55) with Γ=0 meV (dotted line) and Γ=29 meV (solid line) and from Eq. (2.29) with Γ=0 meV (dashed line).

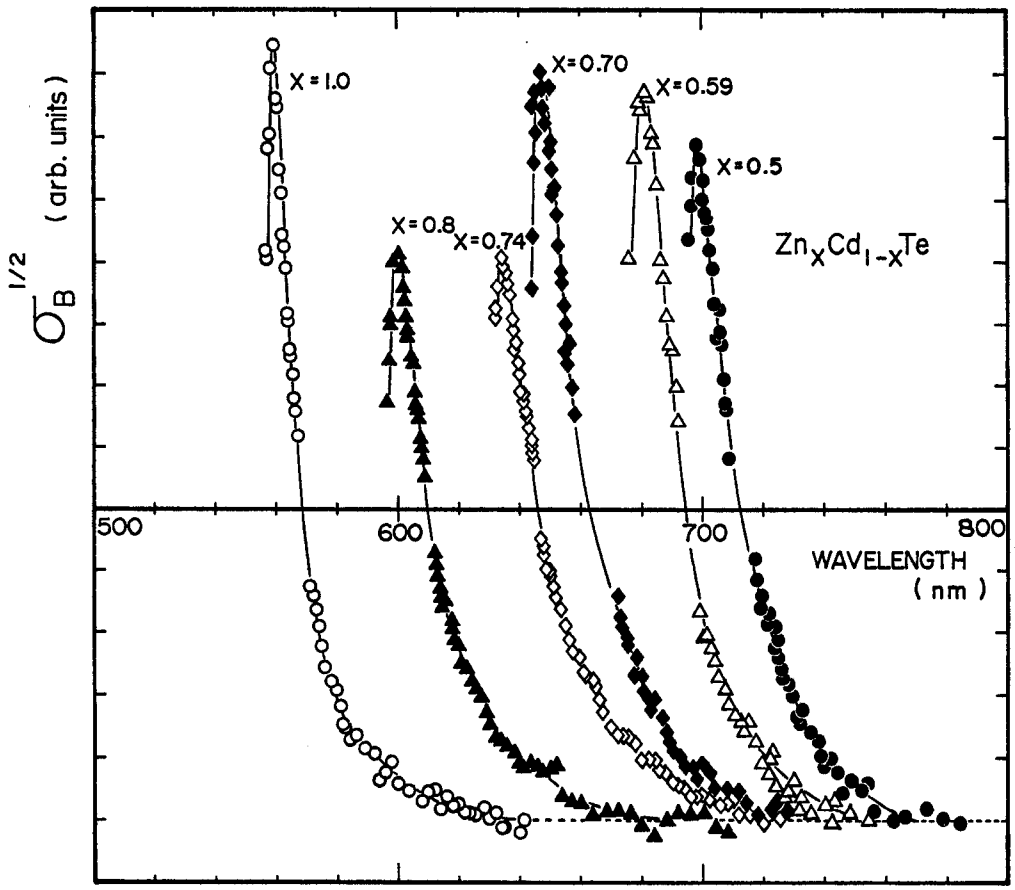

FIG. 4-19. $\sigma_B^{\frac{1}{2}}$ versus incident-light wavelength for several $Zn_xCd_{1-x}Te$ solid solutions with different molar composition x.

by dashed ($\Gamma = 0$) and dotted lines ($\Gamma = 0$), respectively. The theoretical curves obtained from Eq. (2.55) with taking into account the lifetime broadening effect are also shown in the figures by solid lines. The numerical values used in the calculations are listed in Table 4-3. We neglected contributions from the C valence band in the calculations because of the large value of Δ_{so} (spin-orbit splitting energy) in the full range of x [see Fig. 4-16]. The solid lines exhibit a good agreement with the experimental data, as shown in Figs. 4-17 and 4-18. The best-fitting broadening energies are determined to be $\Gamma = 34$ and 29 meV for x = 0.8 and 0.5, respectively.

Figure 4-19 shows $\sigma_B^{\frac{1}{2}}$ versus incident-light wavelength for several $Zn_xCd_{1-x}Te$ solid solutions with different composition x. As clearly seen in the figure, the resonance curve shifts toward longer-wavelength side as molar composition x decreases. This arises from the shift of the band-gap energies of $Zn_xCd_{1-x}Te$ solid solutions with the change of the molar composition x. It is most interesting to point out that all the measured specimens show scattering maxima near the fundamental absorption edges. The maxima are well interpreted in terms of the lifetime-broadening effect of the intermediate electronic states, as discussed before.

4.3.4 CdS

The amplified acoustical-phonon domains in CdS have an intensity a factor of the order of 10^9 above thermal equilibrium value, which are easily achieved in the frequency range from 0.1 to 6.0 GHz.[18] The phonon-frequency range is most suitable for the Brillouin-scattering measurements. The acoustical-phonon domains consist of transverse phonons (T2-mode), polarized along the *c*-axis and propagating in a narrow angle along the current direction ($\perp \vec{c}$). When the domain reaches the anode end of the specimen, part of the acoustical flux is reflected. The reflection is usually accompanied by mode conversion.[16] The piezoelectrically inactive TA-phonon (T1-mode phonon) and

pure-longitudinal (PL) phonon domains can, thus, be obtained by the mode conversion upon partial reflection of the T2-mode domains at the anode-end surface.

Figure 4-20 shows the spectral dependence of the Brillouin-scattering cross sections for 0.2 GHz T1-mode phonon domains measured at room temperature. The T1-mode domain was obtained by the mode conversion upon partial reflection of the T2-mode domains [see Fig. 3-4 (a)]. The identification of this domain was made by taking account of the selection rules of the light polarizations.[39] It should be noted that in anisotropic crystals such as CdS the absorption coefficient of the scattered light may be different from that of the incident light if the incident and scattered lights have different polarizations, *e.g.*, for the T2-mode phonons. In such a case, we have to take account of the dichroism correction for the scattering efficiency.[27] In the present case, the polarization of the scattered light is rotated by about 90° with respect to that of the incident light [see Table 3-3]. However, both the polarizations are almost perpendicular to the *c*-axis, and thus we need not take into account the dichroism correction for the scattering efficiency by the T1-mode phonon domains.[39] The Brillouin-scattering cross section can, thus, be deduced from the same equation as Eq. (4.1). As seen in Fig. 4-20, the experimental data show resonant cancellation and enhancement in the region near the fundamental absorption edge. The Brillouin-scattering efficiency exhibits a maximum in the resonant-enhancement region, i.e., at wavelength close to 522 nm. This maximum has an asymmetric shape with respect to the light wavelength.

The theoretical dispersion curves for the Brillouin-scattering efficiency were calculated using Eq. (2.55). The band parameters used are listed in Table 4-3. The values of the matrix element $\Xi_{\beta\alpha}$ for the deformation-potential scattering were calculated from Eq. (2.91). The results are listed in Table

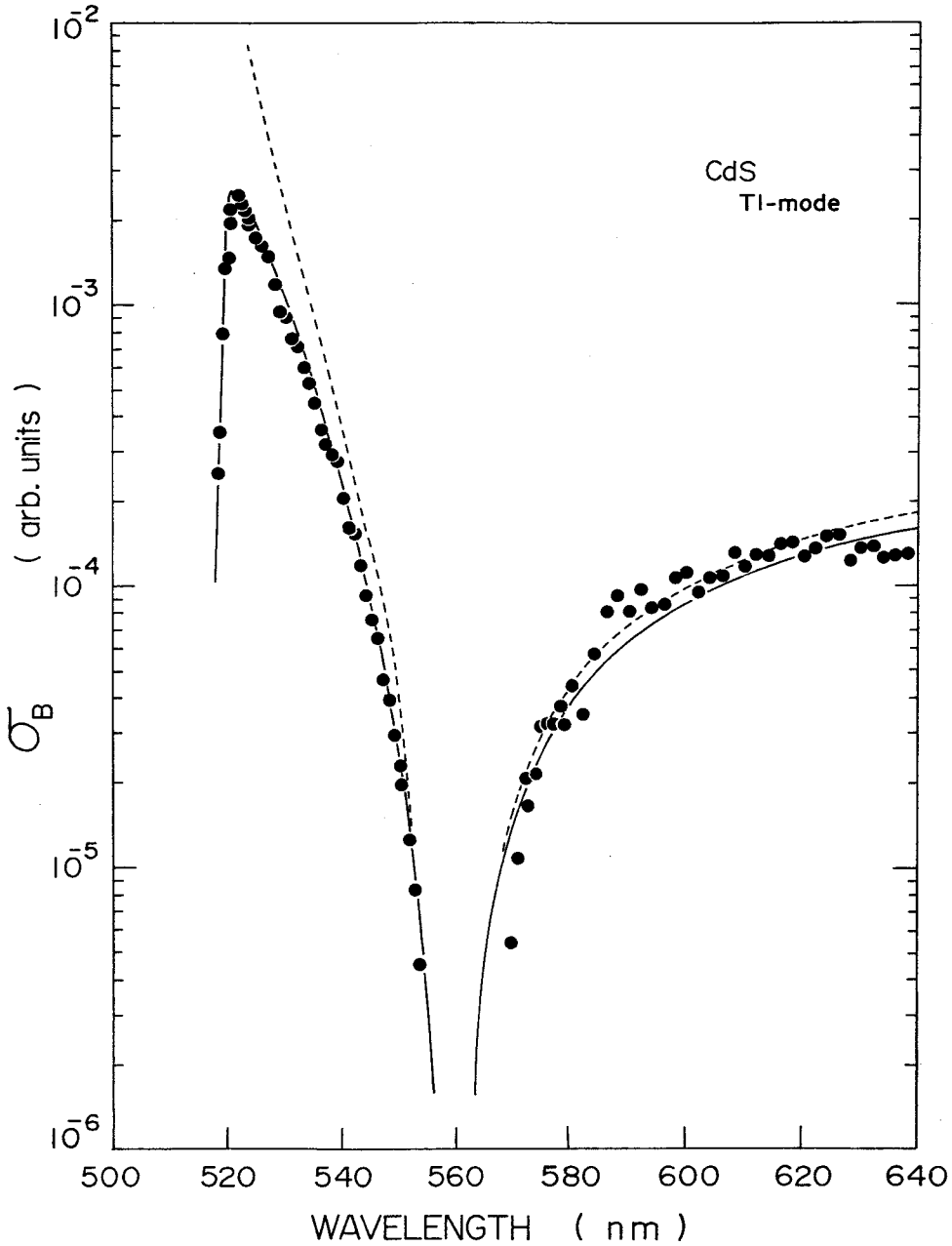

FIG. 4-20. Dispersion curve of the Brillouin-scattering cross sections in CdS for 0.2 GHz Tl-mode phonons measured at room temperature. The theoretical curves are obtained from Eq. (2.55) with Γ=0 meV (dashed line) and Γ=68 meV (solid line).

Table 4-4. Non-zero matrix elements $\Xi_{\beta\alpha}$ for the deformation-potential scattering of CdS (in eV). The numerical values are estimated from the deformation potentials as reported by Langer *et al.* (Ref. 152).

$\Xi_{\beta\alpha}$	CdS		
	T1-mode	T2-mode	PL-mode
Ξ_{BA}	-1.1	-0.8	1.6
Ξ_{CB}	——	-0.9	2.9
Ξ_{AC}	-1.0	-1.2	3.2
Ξ_{AA}	——	——	-1.1
Ξ_{BB}	——	——	-1.0
Ξ_{CC}	——	——	1.5

4-4 along with those for the cases of the T2-mode [Eq. (2.92)] and PL-mode phonons [Eq. (2.94)]. The admixture coefficients α_B (= 0.75) and α_C (=0.67) were calculated from Eq. (2.82). We used the values of the p-matrix elements reported by Thomas and Hopfield.[80] As mentioned previously, the theoretical curve with $\Gamma = 0$ (dashed line) shows a divergence at the fundamental absorption edge. It shows a poor fit with the experimental data especially in the resonant-enhancement region. The curve with $\Gamma = 68$ meV (solid line), on the other hand, shows an excellent agreement between the calculation and experimental data. Gutsche and Voigt[176] have measured lifetime-broadening energies for the excitonic transitions from the absorption spectra. The obtained values for the A, B and C excitons were $\Gamma = 37.1$, 30.3 and 73.5 meV ($\perp \vec{c}$), respectively. Bleil and Gay[177] have also measured lifetime-broadening energy for the A exciton emission as $\Gamma = 70$ meV which is very close to our value (68 meV). Therefore, we can conclude that the lifetime-broadening energy $\Gamma = 68$ meV determined here is thought

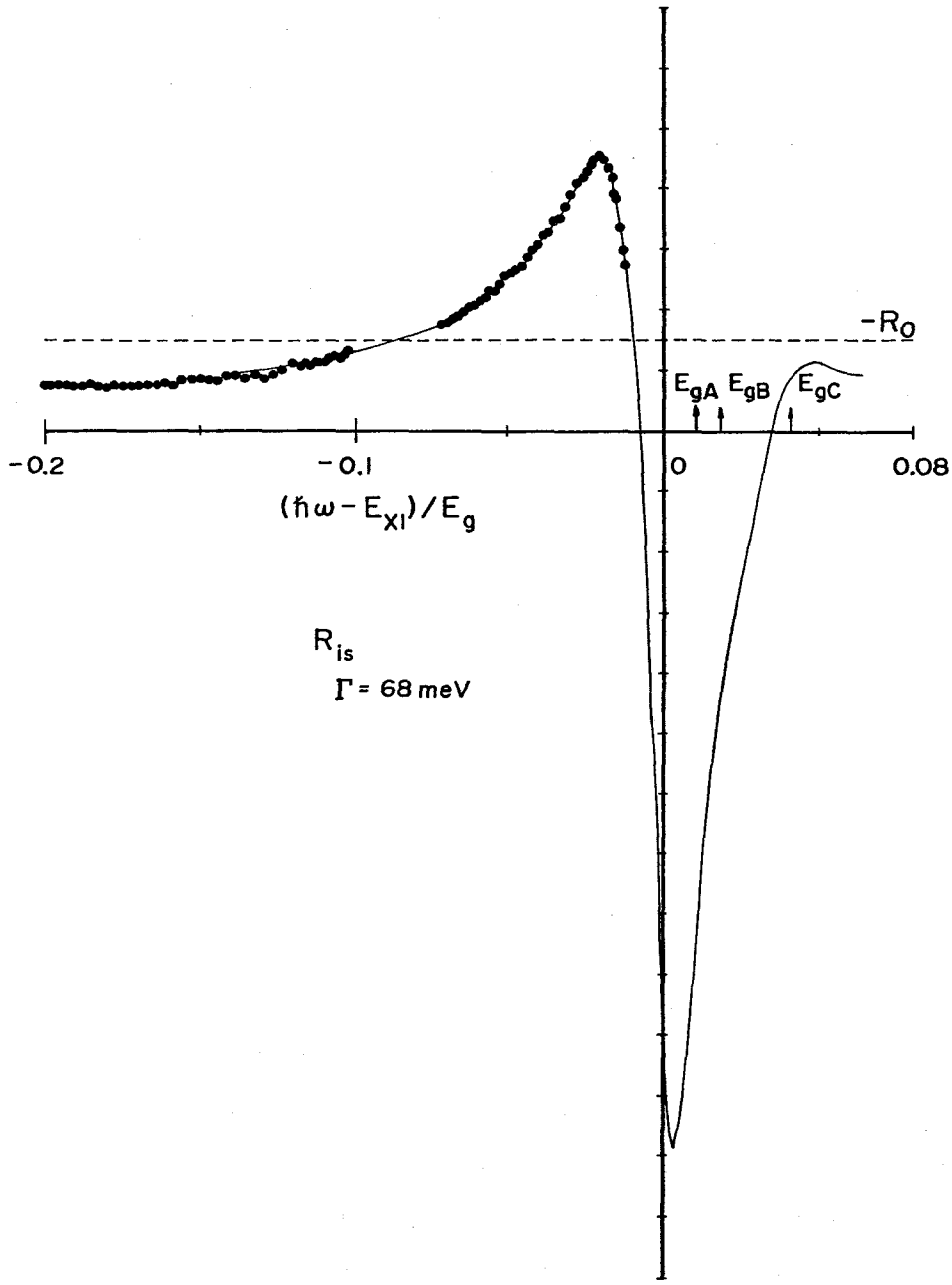

FIG. 4-21. Line shape of R_{is} [Eq. (2.55)] in the neighborhood of the excitonic structure along with the experimental data (CdS: Tl-mode). The corresponding nondispersive term ($-R_0$) is also shown by dashed line.

to be reasonable for the resonant-Brillouin-scattering process.

The line shape of the Brillouin-tensor term R_{is} calculated from Eq. (2.55) [Γ = 68 meV] in the vicinity of the excitonic structure along with the experimental data ($\sigma_B^{\frac{1}{2}}$) is shown in Fig. 4-21. The corresponding non-dispersive term R_0 is also shown in the figure by dashed line. The vertical arrows indicate the positions of the band-gap energies E_{gA}, E_{gB} and E_{gC}. The resonant cancellation can be well understood from the figure by the aid of the relation (4.2). Moreover, a good agreement between the exciton model Eq. (2.55) and experiment can be easily found in the figure. It should be noted here that the line shape of R_{is} is very similar to that of the first-derivative modulation spectroscopy such as thermoreflectance, piezoreflectance and wavelength-derivative modulation spectroscopy.[43,44] Indeed, we will analyze in Chapter VIII the resonant-Brillouin-scattering process as a form of the first-derivative modulation spectroscopy and find that they are very analogous to each other from a phenomenological point of view.

The spectral dependence of the Brillouin-scattering cross sections for the acoustoelectrically amplified T2-mode phonon domains in CdS measured at room temperature is shown in Fig. 4-22. The phonon frequency is selected to be 0.5 GHz. The incident and scattering angles related to the appropriate phonon frequency were obtained from Eq. (3.34) using the data of refractive indices reported in Ref. 178. In the case of the T2-mode phonons, the absorption coefficient of the scattered light is different from that of the incident light because the scattered and incident light have different polarizations ($\perp \vec{c}$ and $\parallel \vec{c}$, see Fig. 3-4). Hence, in order to deduce the Brillouin-scattering cross section, we have to take a dichroism correction of the absorption of light into account. This was first made by Ando and Hamaguchi.[27] They obtained the following relation near the fundamental absorption edge:

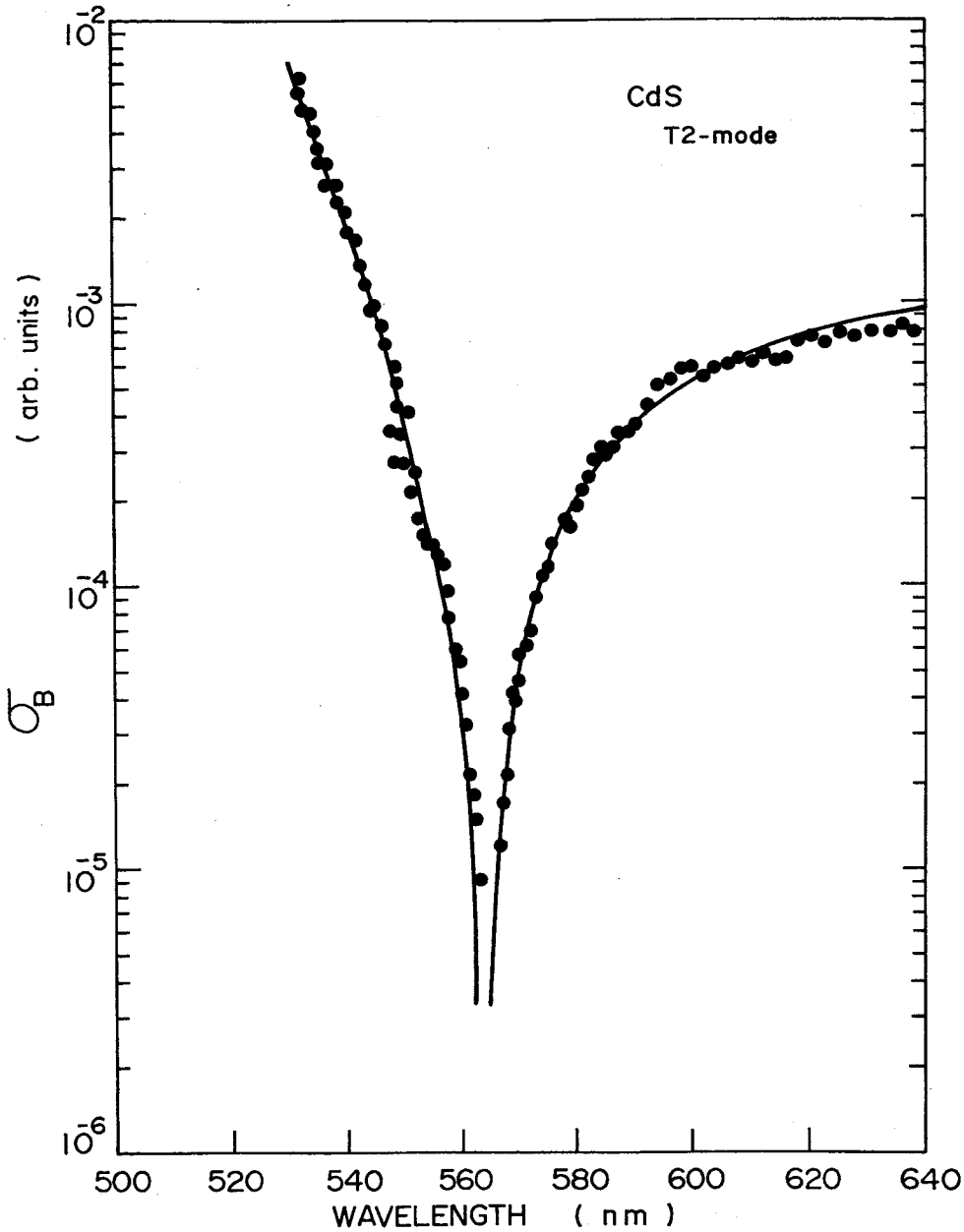

FIG. 4-22. Dispersion curve of the Brillouin-scattering cross sections in CdS for 0.5 GHz T2-mode phonons measured at room temperature. The theoretical curve is obtained from Eq. (2.55) with Γ=0 meV.

$$\frac{I_s}{I_o} = \frac{\sigma_B d\Omega_s}{\alpha_i - \alpha_s n_s/n_i} \exp\left(-\frac{\alpha_s b}{\cos\hat{\theta}_s}\right)$$

$$\times \left\{ 1 - \exp\left[-\left(\alpha_i - \alpha_s \frac{n_s}{n_i}\right) \frac{b}{\cos\hat{\theta}_i}\right]\right\} , \qquad (4.10)$$

where α_i and α_s are the absorption coefficients for the incident and scattered lights, respectively, and I_o is the incident-light intensity. n_i, n_s, $\hat{\theta}_i$ and $\hat{\theta}_s$ are defined in Section 3.3.3. The data shown in Fig. 4-22 are obtained from this dichroism correction using the absorption data of Dutton.[179]

The theoretical dispersion of the Brillouin-scattering efficiency was calculated using Eq. (2.55). The numerical values used are listed in Tables 4-3 and 4-4. We used the p-matrix elements reported by Thomas and Hopfield.[80] The matrix element Ξ_{BA} for the T2-mode phonons must be replaced by Ξ_{AB}, because for the $\vec{E} \parallel \vec{c}$ polarization of incident light the dipole transition between the A valence band and conduction band is forbidden but that between the B valence band and conduction band is allowed [see Fig. 2-8]. By this replacement the matrix elements of Eq. (2.55) become

$$P^s_{0B}\Xi_{BA}P^i_{A0} \rightarrow P^s_{0A}\Xi_{AB}P^i_{B0} \qquad , \qquad (4.11)$$

where the superscripts i and s of P indicate the components in the polarization directions of incident and scattered lights, respectively. It means that the intermediate electronic states produced by the incident radiation must be $|B\rangle$ states but not be $|A\rangle$ states. However, the numerical value of $\Xi_{\beta\alpha}$ is not affected by this replacement because of the symmetry property of this element [see Eq. (2.78)]. We were not able to find a maximum of the Brillouin-scattering efficiency in the experimental dispersion curve, because the dichroism correction introduced large ambiguity in the region very close to the fundamental absorption edge. We took into account in the calculation

the lifetime-broadening energy of Γ = 68 meV which was the same value as that determined for the T1-mode phonons. As seen in Fig. 4-22, the theoretical curve shows a good agreement with the experimental data. The cancellation point is found to be almost the same as that observed for the T1-mode phonons.

Figure 4-23 shows the spectral dependence of the Brillouin-scattering cross sections for 1.2 GHz PL-mode phonon domains measured at room temperature. The PL-mode domain was obtained by the mode conversion upon partial reflection of the T2-mode domains [see Fig. 3-4 (c)]. The identification of this domain was made by measuring the sound velocity; $v_{PL} = (C_{11}/\rho)^{\frac{1}{2}} \simeq 4.35\times10^5$ cm/sec. This velocity differs entirely from that of the reflected T2-mode domains [$v_{T2} = (C_{44}/\rho)^{\frac{1}{2}} \simeq 1.80\times10^5$ cm/sec]. The experimental data show clear resonant enhancement in the region near the fundamental absorption edge. However, one can not find an existence of resonant cancellation in the measured photon-energy range.

The theoretical curve obtained from Eq. (2.55) is shown in the figure by solid line. The numerical values used are listed in Tables 4-3 and 4-4. The matrix element Ξ_{BA} of Table 4-4 must be replaced by Ξ_{AB} because of the same reason as the case for the T2-mode phonons [see Eq. (4.11)]. Moreover, the resonant contribution from the intraband-scattering term [Ξ_{AA}] becomes zero, i.e.,

$$P^{s}_{0A}\Xi_{AA}P^{i}_{A0} = 0 \qquad . \qquad (4.12)$$

This arises from the fact that the dipole transitions are forbidden between the A valence band and conduction band for the $\vec{E} \parallel \vec{c}$ polarizations of the incident and scattered lights [see Table 3-3]. In order to calculate the theoretical curve, we took into account the lifetime-broadening energy of Γ = 68 meV. From the best-fit procedure using Eq. (4.2), we find cancellation point at wavelength of $\lambda \simeq 750$ nm. The same conclusion will be obtained from the quasi-static analysis, as presented in the next Chapter. The solid

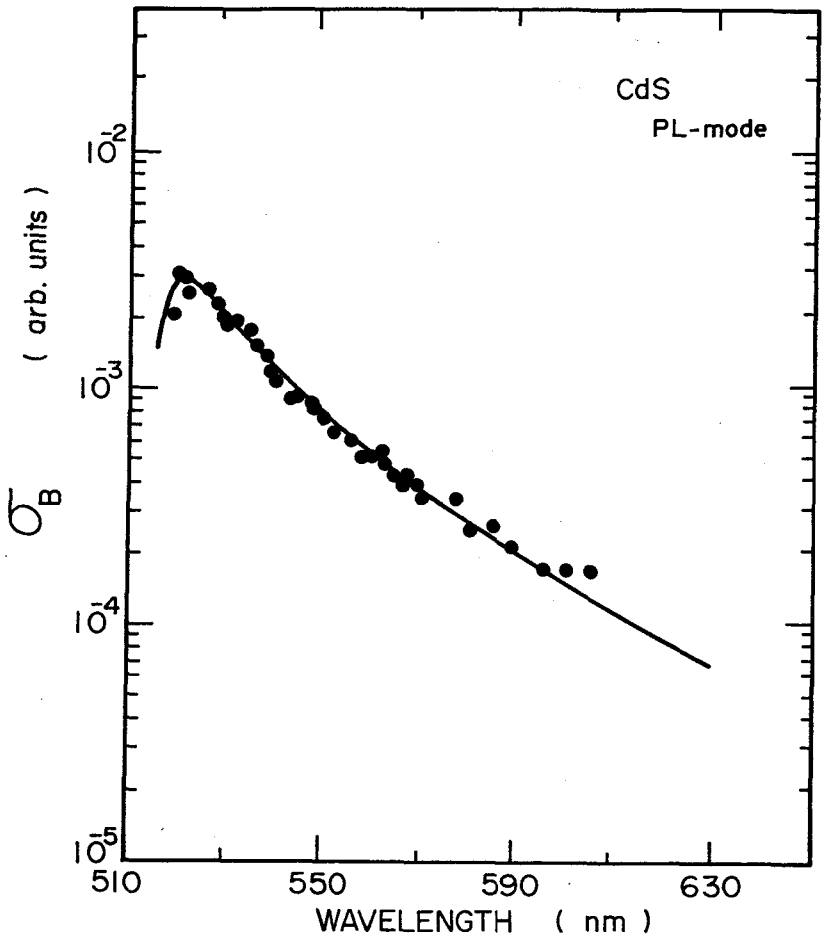

FIG. 4-23. Dispersion curve of the Brillouin-scattering cross sections in CdS for 1.2 GHz PL-mode phonons measured at room temperature. The theoretical curve is obtained from Eq. (2.55) with Γ=68 meV.

line in the figure is calculated by taking into account the nonresonant term [corresponding to the occurrence of the resonant cancellation at $\lambda \simeq 750$ nm]. It is clear from the figure that the calculation and experiment are in quite good agreement.

CHAPTER V

QUASI-STATIC ANALYSIS OF RESONANT BRILLOUIN SCATTERING IN ZnSe, ZnTe AND CdS

5.1 INTRODUCTION

Resonant light scattering in semiconductors has attracted increasing attention recently, since it has been found to be intimately related to the optical spectra of the crystals. It has been demonstrated that the qualitative features of resonant Raman scattering can be predicted from an expression based on the quasi-static approximation.[49-61] In this approximation, the phonons are assumed to act through the electron-phonon interactions like static perturbations of the electronic band structure of the crystal, which cause a change in the dielectric constant ε of the crystal. The dielectric theory of resonant light scattering shows that the two-band term of the first-order scattering efficiency (Raman tensor) is proportional to the first derivative of ε with respect to the band-gap energy. The experimental dispersion of resonant Raman scattering has been well explained by the derivative of a model description of ε.[49-54,56,57] Recent works[55,58-61] have also indicated that the dispersion of resonant Raman scattering shows a good agreement with the derivatives of ε obtained from optical measurements.

The conditions under which the quasi-static approximation is valid are found to be for the two-band process as[41]

$$| E_{g\alpha} - \hbar\omega_i | \gg \hbar\omega_q \quad , \qquad (5.1)$$

and for the three-band process as

$$| E_{g\alpha} - \hbar\omega_i | \gg \hbar\omega_q \quad , \tag{5.2a}$$

$$| E_{g\beta} - \hbar\omega_i | \gg \hbar\omega_q \quad . \tag{5.2b}$$

The Brillouin-scattering process usually satisfies this condition, since $\hbar\omega_q$ is sufficiently smaller than $\hbar\omega_i$.

In this Chapter, we analyze the Brillouin-scattering data [ZnSe(T1-, T2-mode), ZnTe(T1-, T2-mode) and CdS(T1-, T2-, PL-mode and forbidden Brillouin data)] from a view point of the quasi-static approximation.[188] Such an analysis has not yet been carried out until now in the field of resonant Brillouin scattering. The Brillouin-scattering cross section for the first-order allowed configuration can be shown to be proportional to the square of the first derivative of ε with respect to the band-gap energy or equivalently to the incident-photon energy. The dispersion in the dielectric constant of Ge and III-V compounds[64] can be well interpreted with the parabolic band model (band-to-band contribution). In a polar crystals such as II-VI compounds, an additional excitonic contribution has to be considered.[56] This excitonic contribution may be taken into account automatically when we use the experimentally obtained ε for the calculations of the quasi-static approximation.

In Section 5.2, we review the quasi-static approximation for the first-order allowed and forbidden Brillouin scattering to analyze the experimental data. In Section 5.3, we report the analyses of the Brillouin-scattering data for the allowed configuration based on the quasi-static approximation. The first derivatives of the experimentally obtained ε with respect to the photon energy are calculated by numerical differentiation, and compared it with the Brillouin-scattering data. Moreover, resonant forbidden Brillouin scattering by the TA-phonon domains in CdS are observed for the first time

in the region near the fundamental absorption edge.[189,190] The results are interpreted with a dielectric theory (quasi-static approximation) based on the second derivative of the dielectric constant.

5.2 QUASI-STATIC APPROXIMATION

5.2.1 Allowed Brillouin scattering

The dielectric theory of light scattering enables us to expand the dielectric constant $\varepsilon(\omega,u)$ with respect to the displacements u_1, u_2,·····, in the following form:

$$\varepsilon(\omega,u) = \varepsilon(\omega,0) + \frac{\partial\varepsilon}{\partial u_1} u_1 + \frac{1}{2}\frac{\partial^2\varepsilon}{\partial u_1 \partial u_2} u_1 u_2 + \cdots\cdots \quad . \tag{5.3}$$

The various derivatives in Eq. (5.3) define the first- and second-order Raman tensor. The first-order Raman (Brillouin) intensity I can now be given by

$$I \sim \omega^4 \left| \frac{\partial\varepsilon}{\partial u_1} \right|^2 \langle u_1^2 \rangle \quad , \tag{5.4}$$

where $\langle u_1^2 \rangle^{\frac{1}{2}}$ is the zero-point vibration amplitude of the phonon under consideration. Equation (5.4) indicate that Brillouin scattering may be induced by the modulation of the dielectric constant in the mediam. In the quasi-static approximation, the phonons are assumed to act as static perturbations of the electronic band structure of the crystal. The perturbation causes the following change in the dielectric constant *via* the changes in the interband transition energy $E_{g\alpha}$ and oscillator strength F^{α}_{mn} (first-order changes):

$$\Delta\varepsilon_{mn}(E) = \sum_{\alpha} \left[\frac{\partial\varepsilon^{\alpha}_{mn}(E)}{\partial E_{g\alpha}} \Delta E_{g\alpha} + \frac{\partial\varepsilon^{\alpha}_{mn}(E)}{\partial F^{\alpha}_{mn}} \Delta F^{\alpha}_{mn} \right] \quad , \tag{5.5}$$

where the subscripts m and n are the directions of the incident and scattering

fields, respectively, and $E = \hbar\omega$ is the incident-photon energy. The summation indicates that contributions from all the possible interband transitions should be included. From a relation[188]

$$\frac{\partial\varepsilon^{\alpha}_{mn}}{\partial u_1} = \frac{\partial\varepsilon^{\alpha}_{mn}}{\partial E_{g\alpha}}\frac{\partial E_{g\alpha}}{\partial u_1} + \frac{\partial\varepsilon^{\alpha}_{mn}}{\partial F^{\alpha}_{mn}}\frac{\partial F^{\alpha}_{mn}}{\partial u_1} \quad , \tag{5.6}$$

we find that the Brillouin-scattering intensity is proportional to the square of the change in the dielectric constant ($\Delta\varepsilon$). Generally, the contribution from the change in $E_{g\alpha}$ is much more dispersive than that from the change in F^{α}_{mn}.[58] In addition, the contribution from the change in F^{α}_{mn} is a negligible quantity compared with that from the change in $E_{g\alpha}$. We can, therefore, write Eq. (5.5) in good approximation by the following form:

$$\Delta\varepsilon_{mn}(E) \simeq \sum_{\alpha} \frac{\partial\varepsilon^{\alpha}_{mn}(E)}{\partial E_{g\alpha}} \Delta E_{g\alpha} \simeq -\left(\sum_{\alpha} \frac{\partial\varepsilon^{\alpha}_{mn}(E)}{\partial E} \Delta E_{g\alpha} \right) . \tag{5.7}$$

The quantity $\Delta E_{g\alpha}$ is referred to as a deformation potential, and the replacement of $\partial\varepsilon^{\alpha}_{mn}/\partial E_{g\alpha}$ by $-(\partial\varepsilon^{\alpha}_{mn}/\partial E)$ in Eq. (5.7), strictly speaking, requires the addition of a less dispersive term which is omitted since it can be lumped into a background contribution [see Eq. (5.10)].

The above result is valid only for the two-band process in light scattering The usual type of three-band term, due to coupling across a spin-orbit sprit gap (cubic crystal), is proportional to the difference $\varepsilon^{+} - \varepsilon^{-}$, where ε^{+} and ε^{-} are the contributions of the spin-orbit split $E_0/E_0+\Delta_0$ or $E_1/E_1+\Delta_1$ band transitions to ε [see Section 2.3.1]. The Raman-tensor component can, thus, be written as[60]

$$R^{0}_{is} = \frac{\sqrt{3}}{4\pi} \left(- \frac{\partial\varepsilon^{+}}{\partial E_0} + 2\,\frac{\varepsilon^{+}-\varepsilon^{-}}{\Delta_0} \right) d_0 \frac{u_0}{a_0}$$

$$\simeq \frac{\sqrt{3}}{4\pi} \left(\frac{\partial\varepsilon^+}{\partial E} + 2\,\frac{\varepsilon^+-\varepsilon^-}{\Delta_0} \right) d_0\,\frac{u_0}{a_0} \quad , \tag{5.8}$$

for the $E_0/E_0+\Delta_0$ gap resonance, and

$$R^1_{is} = \frac{1}{4\pi} \left(-\frac{1}{2\sqrt{3}}\,\frac{\partial\varepsilon^+}{\partial E_1}\,d^5_{1,0} + \frac{2\sqrt{2}}{\sqrt{3}}\,\frac{\varepsilon^+-\varepsilon^-}{\Delta_1}\,d^5_{3,0} \right) \frac{u_0}{a_0}$$

$$\simeq \frac{1}{4\pi} \left(\frac{1}{2\sqrt{3}}\,\frac{\partial\varepsilon^+}{\partial E}\,d^5_{1,0} + \frac{2\sqrt{2}}{\sqrt{3}}\,\frac{\varepsilon^+-\varepsilon^-}{\Delta_1}\,d^5_{3,0} \right) \frac{u_0}{a_0} \quad , \tag{5.9}$$

for the $E_1/E_1+\Delta_1$ gap resonance. In Eqs. (5.8) and (5.9), a_0 is the cubic lattice constant, u_0 is the zero-point vibrational amplitude of the corresponding phonons. The deformation potentials d_0, $d^5_{1,0}$ and $d^5_{3,0}$ are defined in Refs. 53 and 191. The first and second terms in the brackets of Eqs. (5.8) and (5.9) correspond to the contributions from the two- and three-band processes, respectively. In Section 5.3, we try to fit the experimental data of the Brillouin-scattering cross sections in ZnSe, ZnTe and CdS with the calculated curves from the quasi-static approximation by using the experimental data of the dielectric constants. It is difficult to separate the experimental dielectric constant ε into two different components ε^+ and ε^-. Therefore, for simplicity, we use the following expression as the quasi-static analysis [E_0 (M_0) gap resonance]:[188]

$$\sigma_B = A \left(\frac{d\varepsilon_{mn}}{dE} + B \right)^2 \quad , \tag{5.10}$$

where A is a constant proportional to the deformation potential and occupation number of the corresponding phonons. The constant B represents a nonresonant contribution arising from the higher-gap transitions such as the E_1, $E_1+\Delta_1$ and E_2 transitions. This expression assumes that only one type of E_0 (M_0) gap resonance, i.e. only the two-band contribution, is taken into account for the Brillouin-scattering process. The resonance line shapes can, thus,

be predicted from Eq. (5.10) if the spectral dependence of the dielectric constant ε_{mn} is known.

5.2.2 *Forbidden Brillouin Scattering*

There have been a number of resonant-Raman-scattering experiments in solids by LO phonons in a forbidden scattering configuration.[52,53,58,60,167,192-196] Only $\vec{e}_i \parallel \vec{e}_s$ (parallel-parallel configuration) is characteristic of this forbidden scattering (intraband Fröhlich interaction), where $\vec{e}_i$ and $\vec{e}_s$ are the incident and scattered photon polarizations, respectively. Recently, resonant forbidden Brillouin scattering has been reported by slow-TA (T2-mode) phonons in CdS.[161,162,189] Winterling *et al.*[161] have pointed out that resonant forbidden TA scattering in analogy to the forbidden LO scattering should take place in piezoelectric semiconductors such as CdS, since the piezoelectrically active TA phonon also has a longitudinal electric field. Impurity states or surface electric fields also modify the selection rules because they break the translational and point symmetry (which should lead to broad structure of scattering line since the phonon momentum is not fixed).[8]

The Hamiltonian for the intraband Fröhlich interaction has the following form [see Eq. (2.64)]:[76]

$$H_F = \frac{C_F}{|\vec{q}|} e^{i\vec{q}\vec{r}} \quad , \tag{5.11}$$

with

$$C_F = i\omega_{LO} \left(\frac{1}{2m^* \omega_{LO}} \right)^{1/4} \left(\frac{4\pi\alpha}{V} \right)^{1/2} \quad , \tag{5.12}$$

$$\alpha = \left(\frac{1}{\varepsilon_\infty} - \frac{1}{\varepsilon_0} \right) \left(\frac{m^*}{2\omega_{LO}} \right)^{1/2} \quad , \tag{5.13}$$

where C_F is the Fröhlich coupling constant and α is the polaron constant. The Raman-resonance behavior for the Fröhlich coupling mechanism near a

three-dimensional critical point has been theoretically treated by Zeyher *et al.*[155] For isotropic bands near the Γ point, the Raman tensor is diagonal so that a contribution of this coupling mechanism to Raman scattering is observed only for the parallel-parallel configuration. By the aid of third-order perturbation calculation, Zeyher *et al.* arrive to a result for the diagonal component of the Raman tensor which can be written as follows:

$$R_F = \frac{qC_F}{12\pi\omega^2}\frac{P^2}{3}(S_e-S_h)(\omega_{LO})^{-3/2}(2m^*)^{\frac{1}{2}}$$

$$\times\left[\left(\frac{\omega_0-\omega}{\omega_{LO}}\right)^{\frac{1}{2}}-\left(\frac{\omega_0-\omega+\omega_{LO}}{\omega_{LO}}\right)^{\frac{1}{2}}\right]^3 \qquad (5.14)$$

with

$$S_e = m_e^*/(m_e^*+m_h^*), \qquad S_h = m_h^*/(m_e^*+m_h^*) \quad , \qquad (5.15)$$

where $\hbar\omega_0$ is the E_0-gap energy and m_e^* and m_h^* are the electron and hole effective mass. The square bracket of Eq. (5.14) can now be written by using the dielectric theory as

$$\left[\left(\frac{\omega_0-\omega}{\omega_{LO}}\right)^{\frac{1}{2}}-\left(\frac{\omega_0-\omega+\omega_{LO}}{\omega_{LO}}\right)^{\frac{1}{2}}\right]^3 = \left[\omega^2\frac{3}{P^2}(2m^*)^{-3/2}(\omega_{LO})^{\frac{1}{2}}\right]^3\left(\frac{d\varepsilon}{d\omega}\right)^3 . \qquad (5.16)$$

The derivative of Eq. (5.16) can also be written in good approximation as

$$\left[8\pi\omega^2(2m^*)^{-3/2}\frac{3}{P^2}\right]^2\frac{1}{(4\pi)^2}\frac{1}{2}\left(\frac{d\varepsilon}{d\omega}\right)^3 = \frac{1}{\omega^2}(2m^*)^{3/2}\frac{P^2}{3}\frac{1}{4}(\omega_0-\omega)^{-3/2}$$

$$\simeq \frac{d^2\varepsilon}{d\omega^2} \quad . \qquad (5.17)$$

Using Eq. (5.17), we finally obtain the Raman tensor as

$$R_F = \frac{1}{48\pi}\frac{qC_F}{m^*}(S_e-S_h)\frac{d^2\varepsilon}{d\omega^2} \quad . \qquad (5.18)$$

Thus, within the spirit of the dielectric theory the Fröhlich-interaction-induced LO (and TA) strengths, as forbidden effects, should be proportional to the square of the second derivative of ε with respect to the incident-photon energy.

5.3 ANALYSIS AND DISCUSSION

5.3.1 ZnSe

Figure 5-1 shows the dispersion of the Brillouin-scattering cross sections for ZnSe obtained at room temperature by 0.2 GHz T1-mode (slow TA) phonons [same as Fig. 4-6], i.e., the transverse acoustical phonons propagating in the $[1\bar{1}0]$ direction with shear polarization parallel to the [110] direction. The solid line is calculated from Eq. (5.10) by differentiating the data of refractive indices reported in Refs. 197 and 198. The best-fitting value of B (in eV^{-1}) is given in Table 5-1. The corresponding cancellation point is also given in the table. We are not able to determine the value of A because the absolute scattering intensities were not measured in our experiments. The calculated curve is, thus, fitted to the experimental data at the corresponding cancellation point by adjusting multiplicative constants (vertical shifts in the log-plot of this figure). The resonant cancellation can be explained by the sign-opposite relation between the first-derivative term $\frac{d\varepsilon}{dE}$ and constant term B [i.e., $(\frac{d\varepsilon}{dE} + B) = 0$].

Figure 5-2 shows the dispersion of the Brillouin-scattering cross sections for ZnSe obtained at room temperature by 0.2 GHz T2-mode (fast TA) phonons [same as Fig. 4-7], i.e., the transverse acoustical phonons propagating in the [001] direction with shear polarization parallel to the [110] direction. In this case, the resonant cancellation shifts slightly to higher photon-energy side and occurs at 2.531 eV [see Table 5-1]. It is clear that the calculated curve shows a good agreement with the experimental data. The measurements

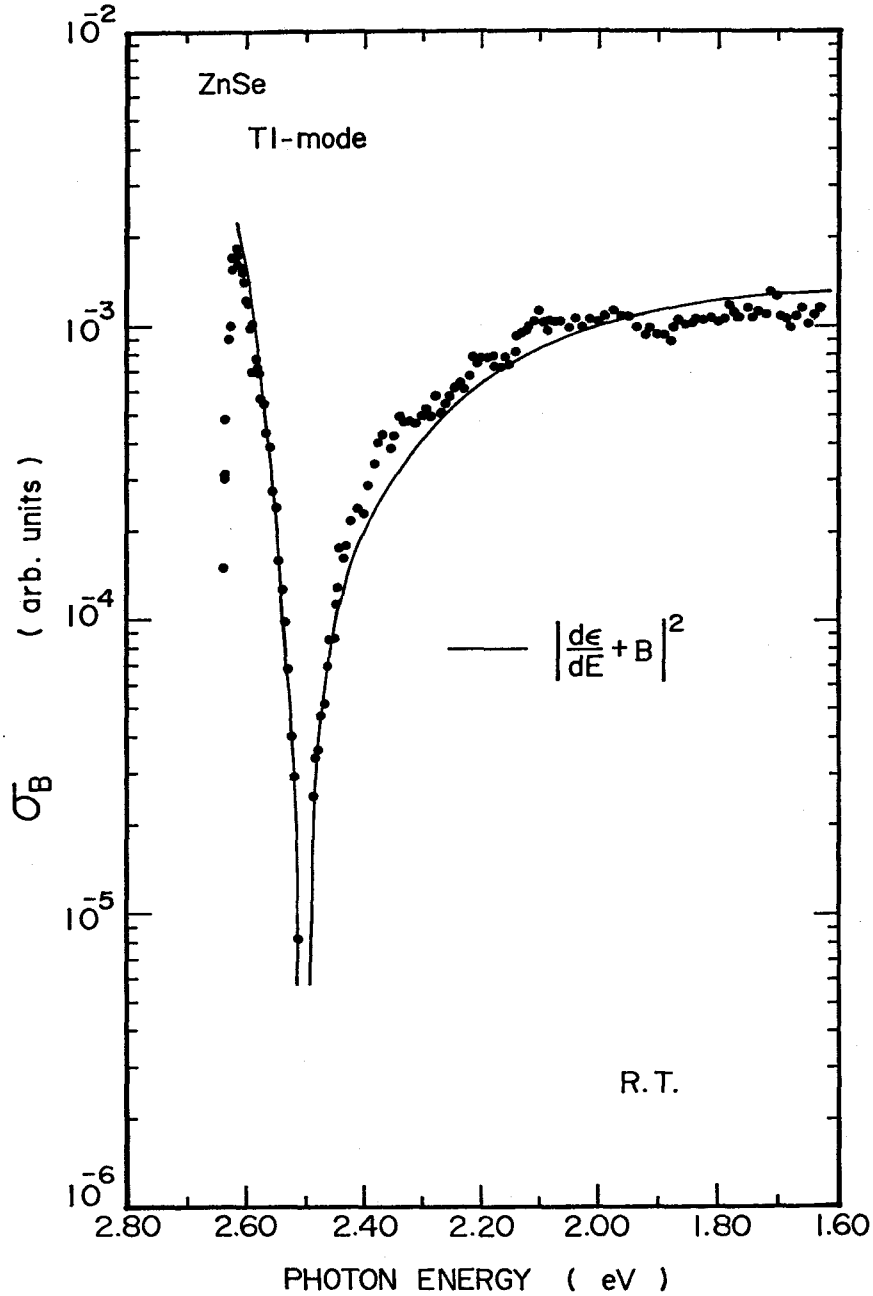

FIG. 5-1. Dispersion curve of the Brillouin-scattering cross sections for ZnSe [as-grown] measured at room temperature by 0.2 GHz Tl-mode phonons. The solid line is calculated from Eq. (5.10) by dirrerentiating the data of refractive indices reported in Refs. 197 and 198.

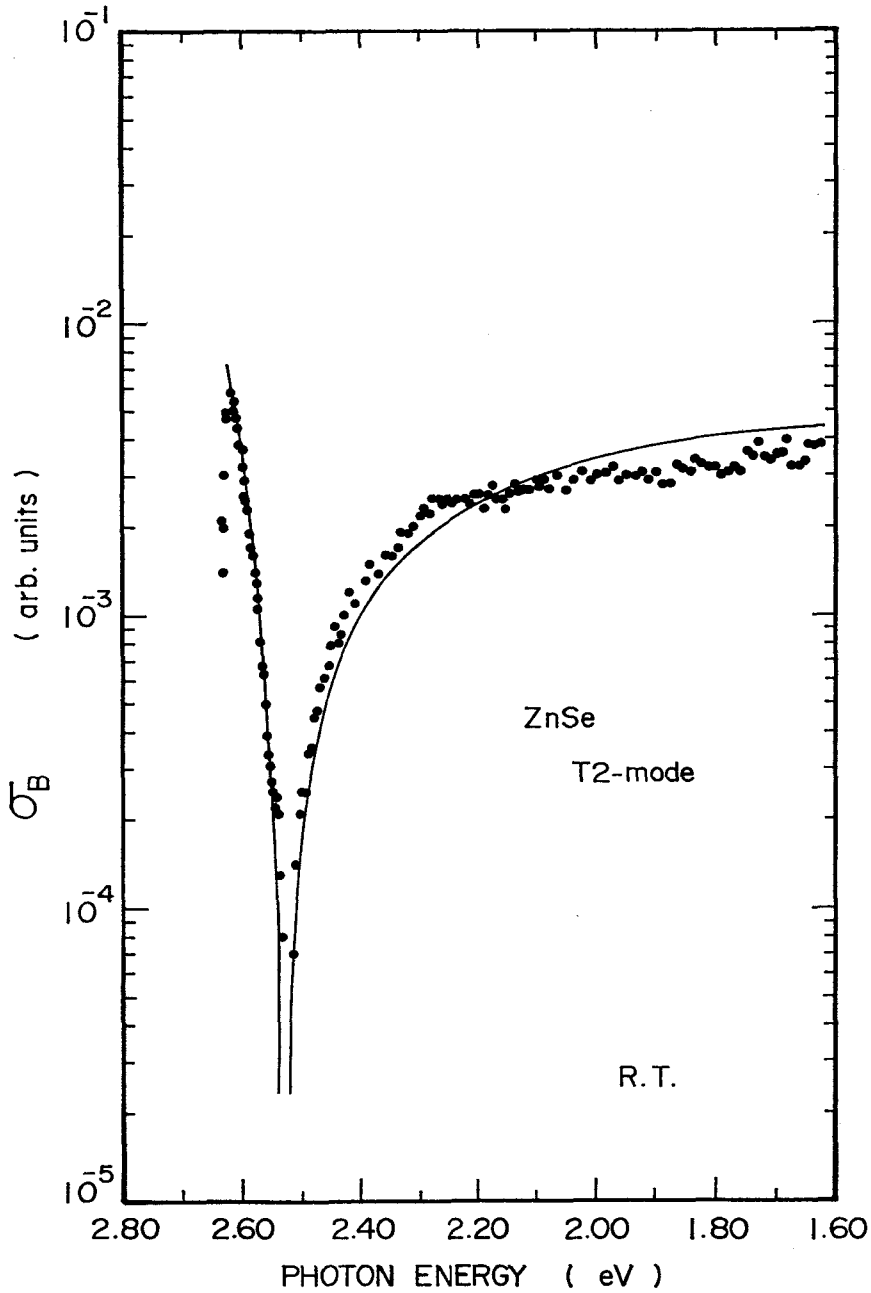

FIG. 5-2. Dispersion curve of the Brillouin-scattering cross sections for ZnSe [as-grown] measured at room temperature by 0.2 GHz T2-mode phonons. The solid line is calculated from Eq. (5.10) by differentiating the data of refractive indices reported in Refs. 197 and 198.

Table 5-1. Constant B resulting from the fit to the experimental Billouin-scattering cross sections with Eq. (5.10). The corresponding cancellation points are also shown in this table.

	ZnSe		ZnTe		CdS		
Mode	T1	T2	T1	T2	T1	T2	PL
B [eV^{-1}]	-2.82	-3.20	-5.65	-5.58	-2.75	-2.53*	-0.9
Cancellation Point [eV]	2.505	2.531	2.181	2.179	2.210	2.195	1.65**

*Obtained from the dielectric constant for the ordinary ray.
**Estimated from the fit of Eq. (5.10) to the experimental data.

made at 77 K for both the T1- and T2-mode phonons also showed essentially similar resonance behaviors to those at room temperature except the shift of resonance curves to higher photon-energy region due to the shift of the band-gap energy [see Figs. 4-8 and 4-9].

5.3.2 ZnTe

Figures 5-3 and 5-4 show the dispersion of the Brillouin-scattering cross sections for ZnTe obtained at room temperature by 0.2 GHz T1- and T2-mode phonons, respectively [same as Figs. 4-13 and 4-14]. The solid lines in the figures are calculated from Eq. (5.10) by differentiating the data of refractive indices reported in Refs. 197, 199 and 200. Our data indicate that the resonant cancellation for the T1- and T2-mode phonons occurs at almost the same photon energy ($\sim$ 2.18 eV), and thus the nondispersive background contribution B is almost equal for both the phonon modes [see Table 5-1]. It is obvious from Figs. 5-3 and 5-4 that the cancellation based on the quasi-static approximation shows a quite good agreement with the experimental data. Schmidt *et al.*[56] have studied first- and second-order Raman scattering in ZnTe and also analyzed with a model based on the quasi-static approximation by using the model dielectric constant (which includes not only the band-to-band contribution but also the excitonic contribution). They have obtained a good agreement between the calculation and experiment.

5.3.3 CdS

[A] Allowed Brillouin Scattering

Figure 5-5 shows the photon-energy derivatives of the dielectric constants for the ordinary (solid line) and extraordinary ray (dashed line) of CdS (in eV^{-1}). The calculated curves have been obtained by differentiating the data of Ref. 178. The photon-energy derivative of the dielectric constant for the ordinary ray shows steep increase as the photon energy approaches

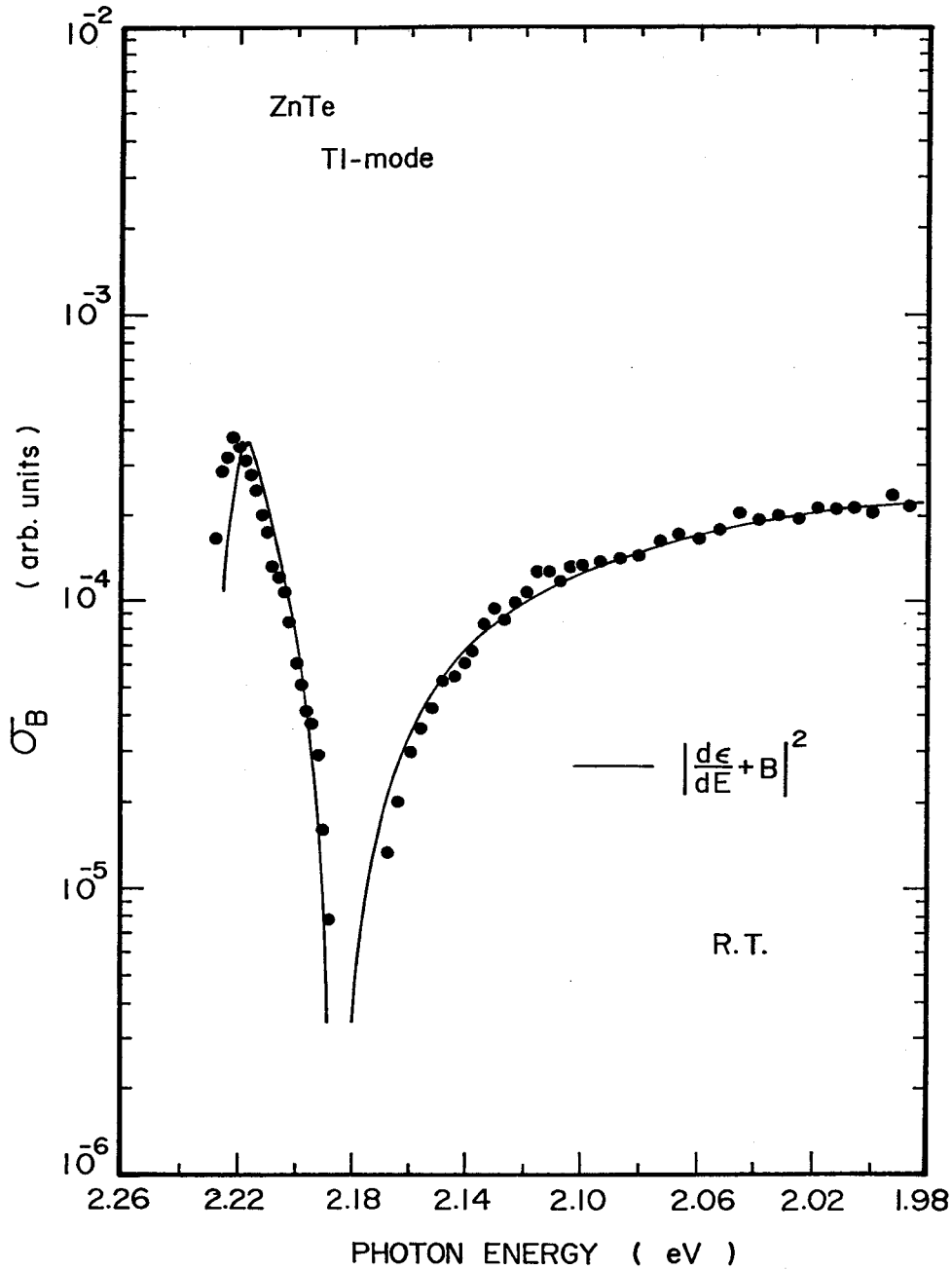

FIG. 5-3. Dispersion curve of the Brillouin-scattering cross sections for ZnTe measured at room temperature by 0.2 GHz Tl-mode phonons. The solid line is calculated from Eq. (5.10) by differentiating the data of refractive indices reported in Refs. 197, 199 and 200.

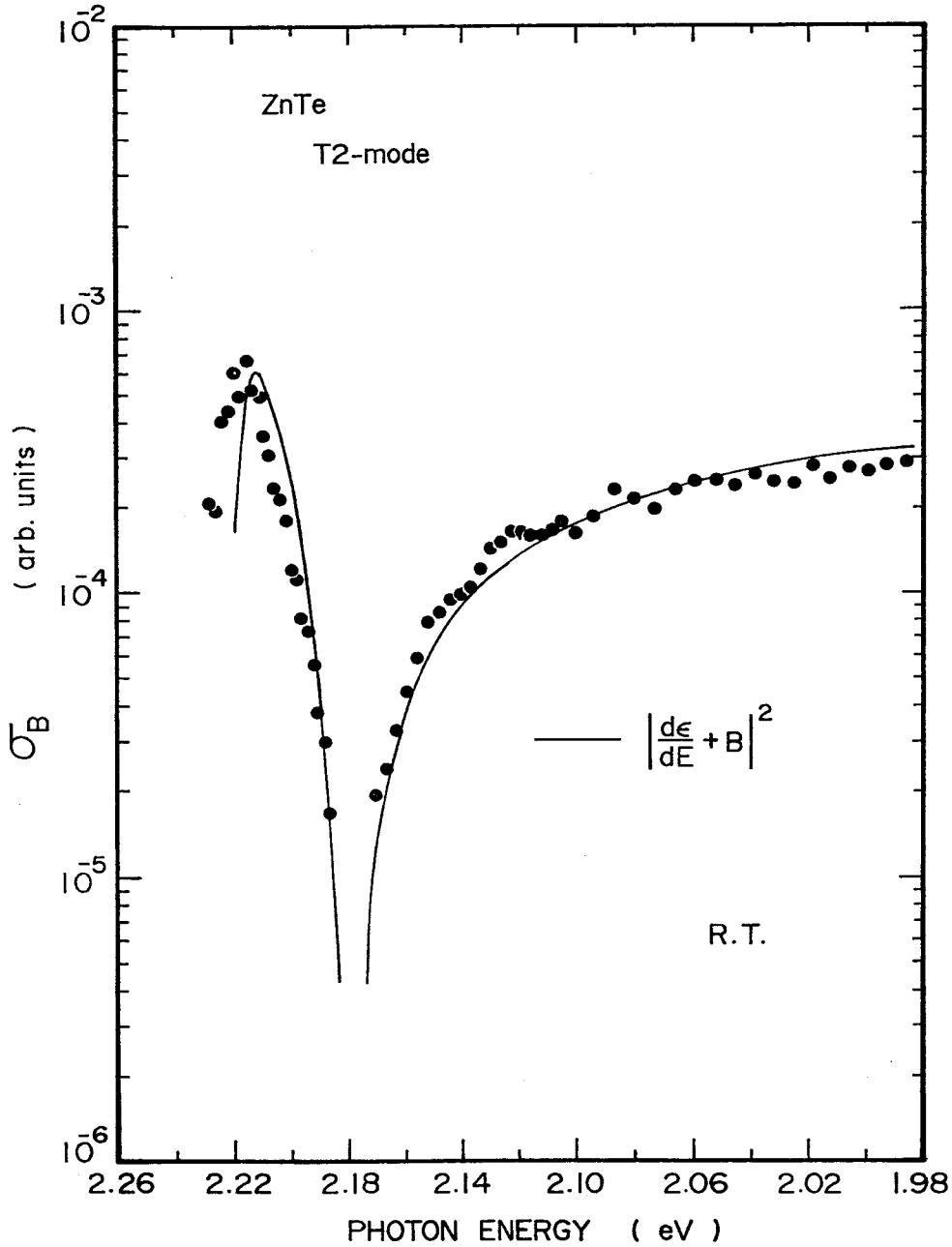

FIG. 5-4. Dispersion curve of the Brillouin-scattering cross sections for ZnTe measured at room temperature by 0.2 GHz T2-mode phonons. The solid line is calculated from Eq. (5.10) by differentiating the data of refractive indices reported in Refs. 197, 199 and 200.

the fundamental absorption edge, compared with that for the extraordinary ray. This is due to the fact that the lowest direct-gap transition (E_{gA}) is forbidden for the $\vec{E} \parallel \vec{c}$ polarization, and the dielectric constant for the $\vec{E} \perp \vec{c}$ polarization, thus, increases steeply as the photon energy approaches the lowest direct-gap energy (E_{gA}=2.452 eV).

Figure 5-6 shows the dispersion of the Brillouin-scattering cross sections for CdS obtained at room temperature by 0.2 GHz T1-mode (fast TA) phonons [same as Fig. 4-20], i.e., the transverse acoustical phonons propagating in the direction perpendicular to the c-axis. The solid line is calculated from Eq. (5.10) by differentiating the data of refractive indices reported in Ref. 178 [see Fig. 5-5]. The dielectric constant for the ordinary ray ($\vec{E} \perp \vec{c}$) has been used in the calculation because the Brillouin-scattering configurations for the T1-mode phonons are $\vec{e}_i \perp \vec{c}$ and $\vec{e}_s \perp \vec{c}$ [see Fig. 3-4 (a)], where $\vec{e}_i$ and $\vec{e}_s$ are the unit vectors in polarization directions of the incident and scattered light, respectively. It is found from Fig. 5-6 that our experimental dispersion is in a quite good agreement with the expression of Eq. (5.10).

The dispersion of the Brillouin-scattering cross sections for the acoustoelectrically amplified T2-mode (slow TA) phonons in CdS obtained at room temperature is shown in Fig. 5-7. The T2-mode phonon domains propagate in the direction perpendicular to the c-axis with shear polarization parallel to the c- axis (piezoelectrically active phonons). In this case, we can not exactly calculate the theoretical dispersion curve from Eq. (5.10) by using one of the dielectric constants (i.e., ordinary or extraordinary ray), since the incident and scattered light have different polarizations ($\vec{e}_i \parallel \vec{c}$ and $\vec{e}_s \perp \vec{c}$). For the purpose of comparison, the solid and dashed lines have been calculated by using the dielectric constants for the ordinary and extraordinary rays, respectively. As clearly seen in the figure, both the calculated curves show a reasonable fit in the whole region investigated, but we find a poor

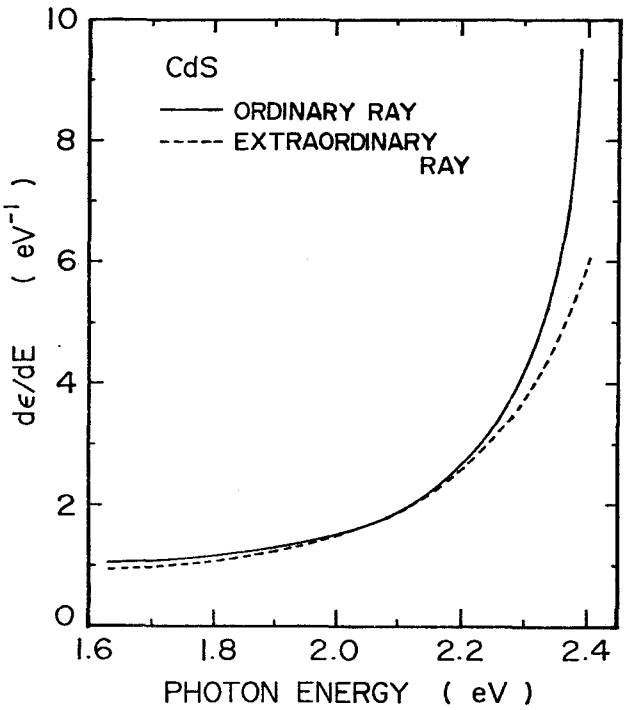

FIG. 5-5. Photon-energy derivatives of the dielectric constants for the ordinary (solid line) and extraordinary ray (dashed line) of CdS (in eV^{-1}). The calculated curves are obtained by differentiating the data of dielectric constants reported in Ref. 178.

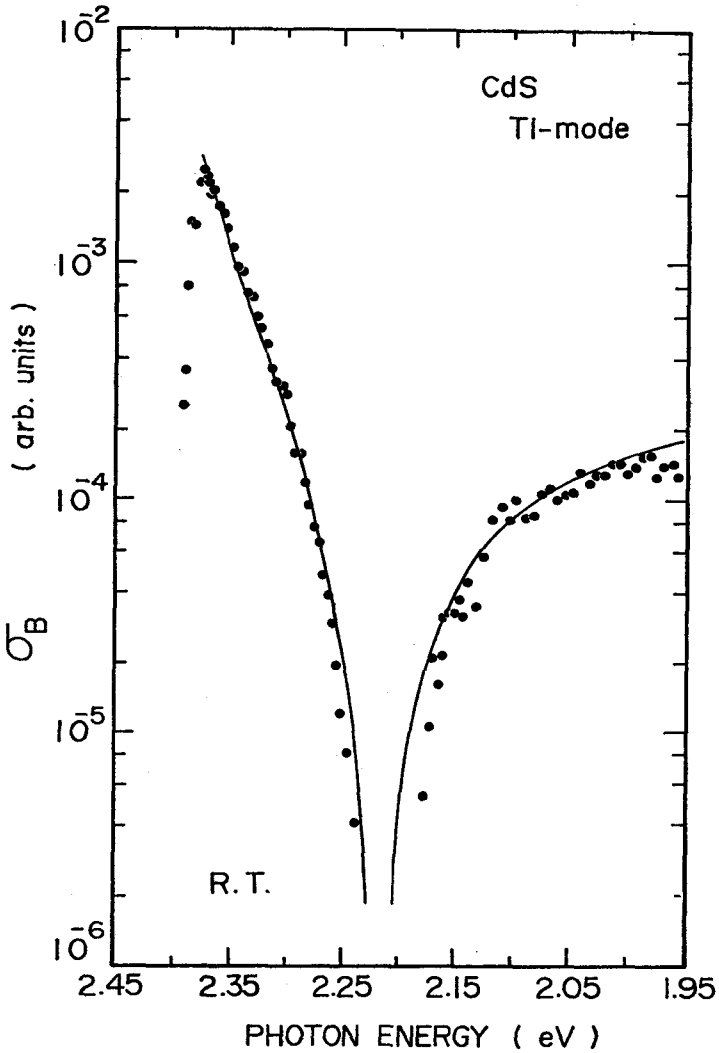

FIG. 5-6. Dispersion curve of the Brillouin-scattering cross sections for CdS measured at room temperature by 0.2 GHz Tl-mode phonons. The solid line is calculated from Eq. (5.10) by differentiating the data of refractive indices (ordinary ray) reported in Ref. 178.

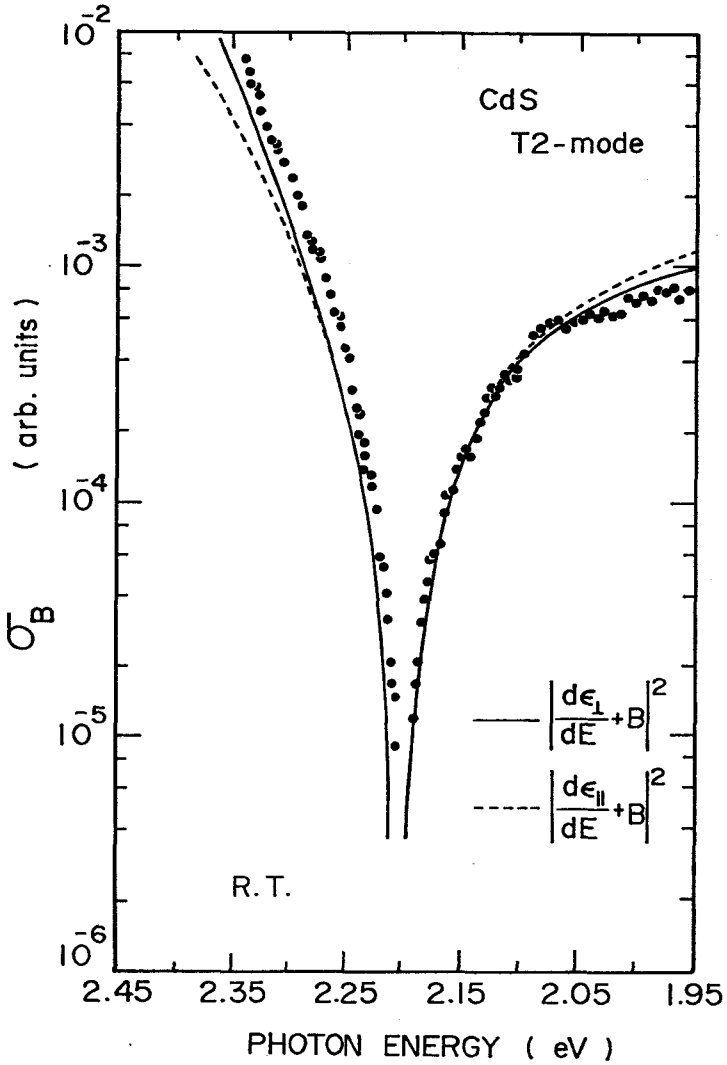

FIG. 5-7. Dispersion curve of the Brillouin-scattering cross sections for CdS measured at room temperature by 0.5 GHz T2-mode phonons. The solid and dashed lines are calculated from Eq. (5.10) by diffentiating the data of refractive indices for the ordinary and extraordinary rays [Ref. 178], respectively.

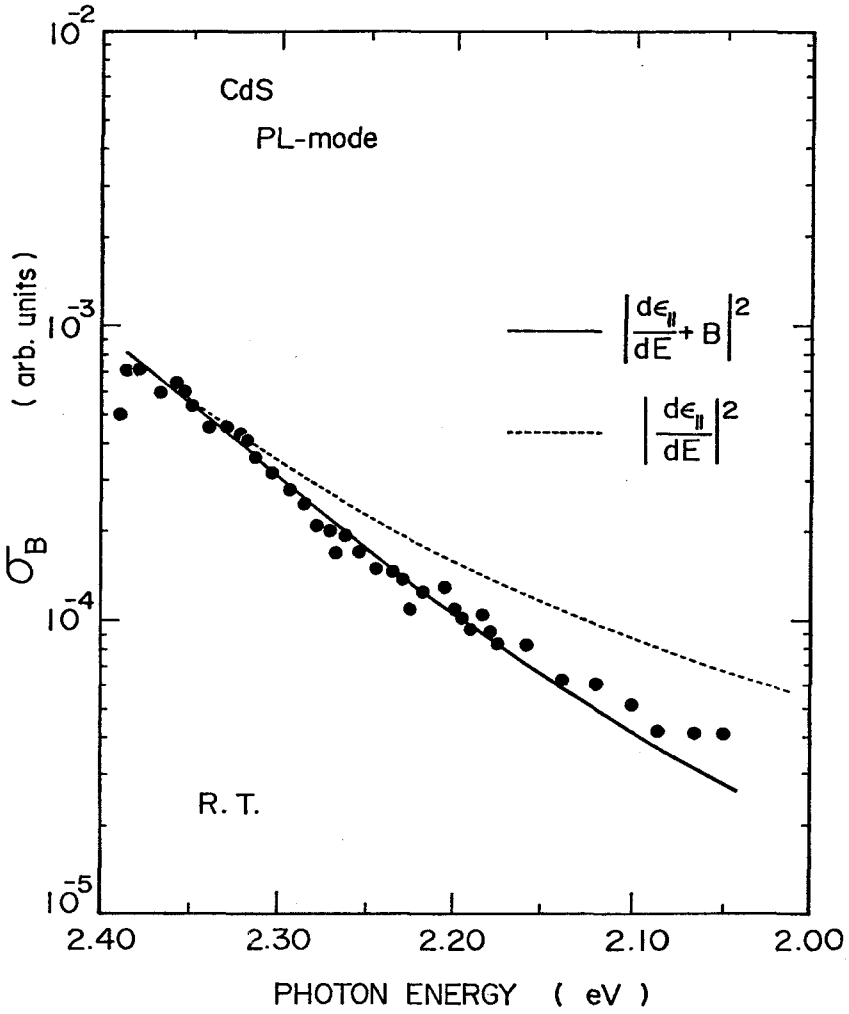

FIG. 5-8. Dispersion curve of the Brillouin-scattering cross sections for CdS measured at room temperature by 1.2 GHz PL-mode phonons. The solid and dashed lines are calculated from Eq. (5.10) by differentiating the data of refractive indices (extraordinary ray) reported in Ref. 178.

agreement in the region near the fundamental absorption edge.

Figure 5-8 shows the dispersion of the Brillouin-scattering cross sections for CdS obtained at room temperature by 1.2 GHz PL-mode (pure LA) phonons [same as Fig. 4-23], i.e., the pure-longitudinal acoustical phonons propagating in the direction perpendicular to the c-axis. The PL-mode phonon domains were obtained by the mode conversion upon partial reflection of the T2-mode phonon domains at the end-surface, as in the case for the T1-mode phonon domains. One can find that our data indicate an absence of the apparent cancellation in the measured photon-energy region 2.05 – 2.39 eV. We were not able to observe any scattering signal in the photon energy below 2.05 eV because of weak scattering intensities in this region. However, the solid line, which is best fitted to our data with Eq. (5.10), predicts an existence of the cancellation point at $\sim$ 1.65 eV [see Table 5-1]. In the calculation, we have used the dielectric constant for the extraordinary ray according to the experimental scattering configurations ($\vec{e}_i \parallel \vec{c}$ and $\vec{e}_s \parallel \vec{c}$). The dashed line is also calculated with B = 0 (i.e., an assumption of the absence of anti-resonance) which is in poor agreement with our data compared with the solid line ($B \neq 0$). Therefore, we can expect the presence of weak resonant cancellation at $\sim$ 1.65 eV, though it has not yet been verified by the measurements at present.

[*B*] *Forbidden Brillouin Scattering*

We present here experimental results of resonant forbidden Brillouin scattering in CdS by the acoustoelectrically amplified phonon domains (slow TA phonons) in several scattering configurations (parallel-parallel and parallel-perpendicular configurations). The experimental data show a resonance feature only in the region near the fundamental absorption edge, which is found to fit to the second derivative of ε with respect to the incident-photon

energy, in direct contrast to the first derivative of ε for the allowed Brillouin scattering.

When the $\vec{q}$-dependent Fröhlich interaction is assumed to be the forbidden Brillouin-scattering mechanism, the following expression has been found to hold for the free electron-hole pairs as the intermediate electronic states [see Eq. (5.18)]:

$$\sigma_B = A' q^2 \left| \langle n+1 \mid E_F \mid n \rangle \right|^2 \left(\frac{d^2\varepsilon}{dE^2} \right)^2 , \qquad (5.19)$$

where A' is a constant, q and n are the wave vector and occupation number of the slow-TA phonons, respectively, E_F is the longitudinal electric field associated with the slow-TA phonons, and E is the incident-photon energy. The above equation has been used by Winterling *et al.*[161] to explain the resonant-Brillouin-scattering date by TA phonons near the A exciton of CdS in the forbidden configuration. They have considered that this effect is attributed to electron-phonon piezoelectric coupling[201] and is equivalent to the Fröhlich-interaction-induced forbidden LO scattering [Eq. (5.18)]. It should be noted that Eq. (5.19) remains approximately valid for excitonic transitions, provided that one uses for ε the experimental data which includes exciton effects. In addition, the longitudinal electric field E_F in the acoustical phonon domain was estimated to be approximately 3×10^6 V/cm.[202]

Figure 5-9 shows the first and second derivatives of the dielectric constant for the ordinary ray of CdS with respect to the photon energy. The curves have been obtained by numerically differentiating the data of Ref. 178. It is clear from the figure that the second derivative (solid line) gives stronger dispersion than the first derivative (dashed line) especially in the region near the band edge.

The resonance behavior of forbidden scattering by the slow-TA phonon domains measured at room temperature is shown in Fig. 5-10. The allowed TA

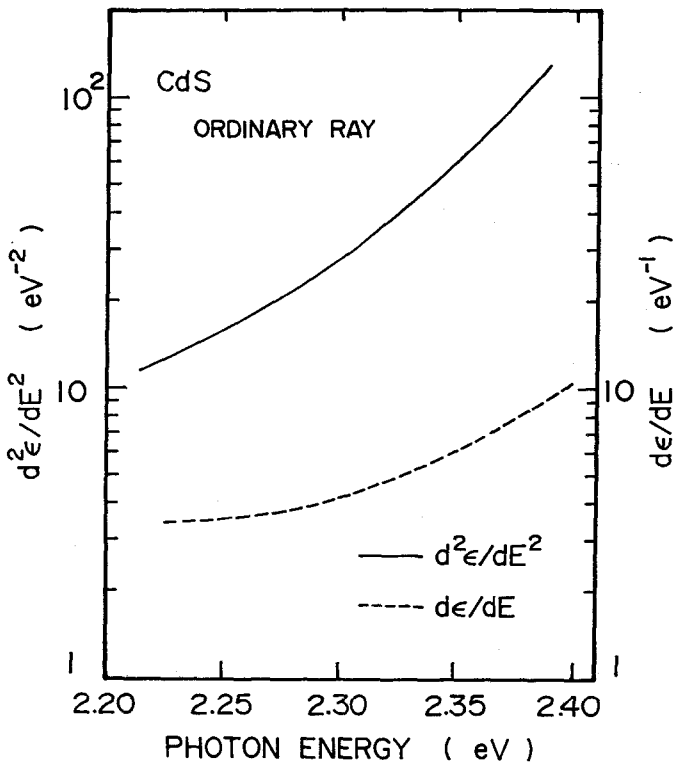

FIG. 5-9. First (dashed line) and second derivative (solid line) of the dielectric constant for the ordinary ray of CdS with respect to the photon energy. The calculated curves are obtained by differentiating the data of dielectric constants reported in Ref. 178.

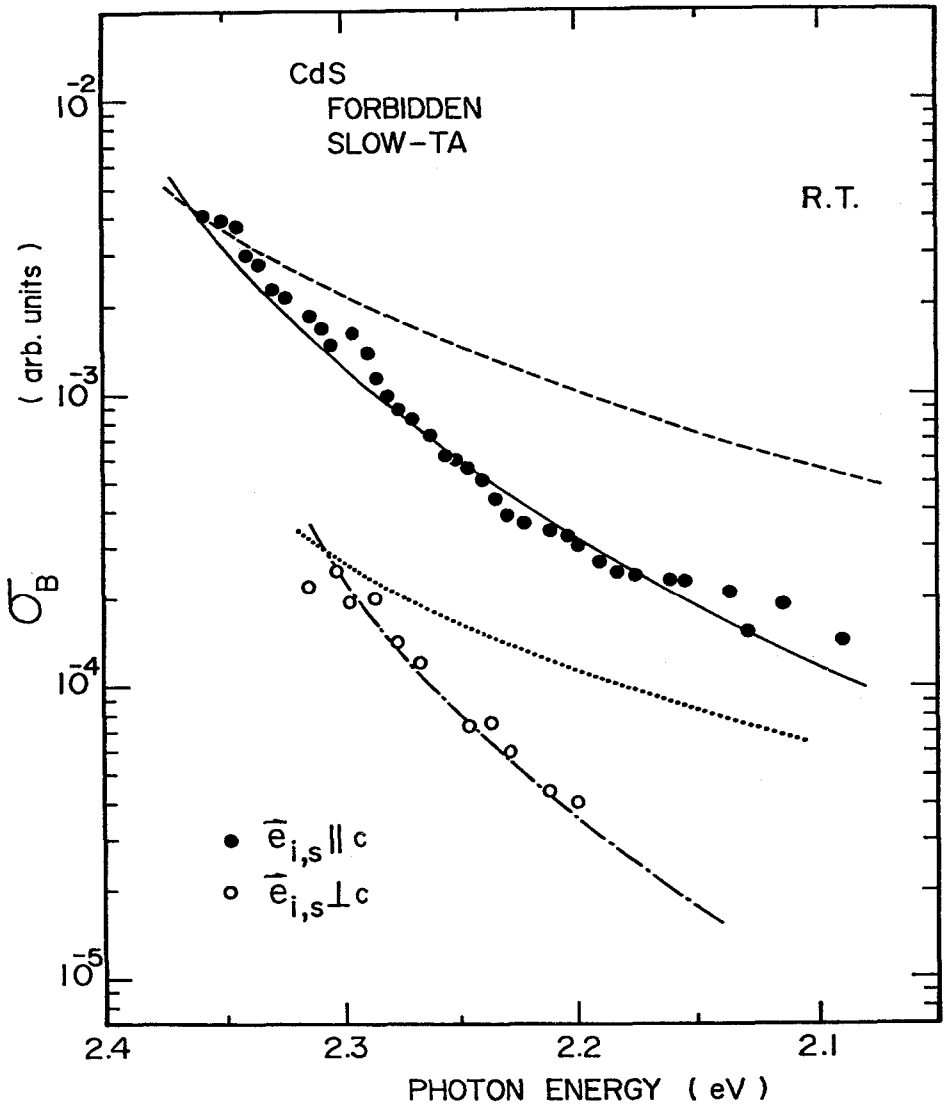

FIG. 5-10. Resonance behavior of the parallel-parallel (forbidden) scattering by the slow-TA (T2-mode) phonon domains in CdS measured at room temperature (see text).

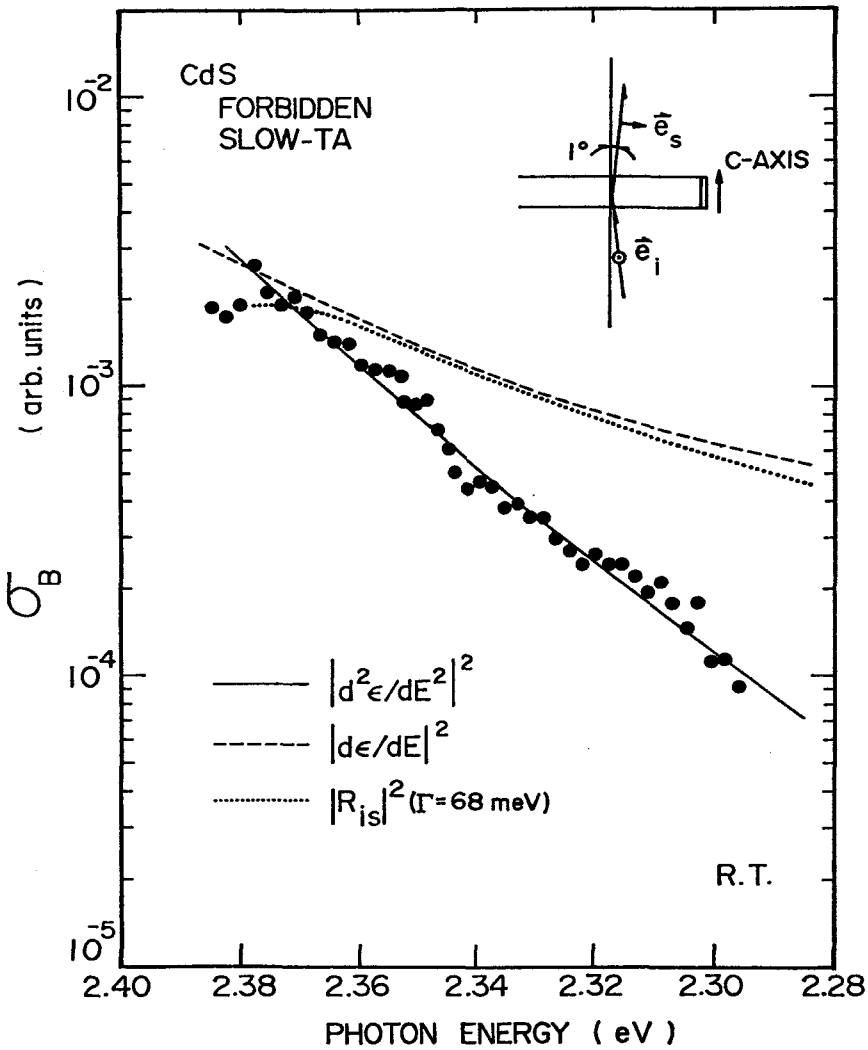

FIG. 5-11. Resonance behavior of the parallel-perpendicular (forbidden) scattering by the slow-TA (T2-mode) phonon domains in CdS measured at room temperature. The inset indicates the experimental configurations (see text).

scattering is only observable for $\vec{e}_i \perp \vec{e}_s$ (parallel-perpendicular configuration, see Section 2.2.4). The solid and open circles were taken in parallel-parallel configuration with $\vec{e}_i(\vec{e}_s) \parallel \vec{c}$ and $\vec{e}_i(\vec{e}_s) \perp \vec{c}$, respectively. In contrast to the data for the allowed TA scattering (Fig. 5-7), the forbidden signal was not observed in the photon-energy region far from the fundamental absorption edge. The solid and dash-dotted lines are obtained from Eq. (5.19) [Eq. (5.18)] by differentiating the dielectric constants for the extraordinary and ordinary rays, respectively. The theoretical curves obtained from the first derivatives $d\varepsilon_{\parallel}/dE$ ($d\varepsilon_{33}/dE$) and $d\varepsilon_{\perp}/dE$ ($d\varepsilon_{11}/dE$) are also shown in this figure by dashed and dotted lines, respectively. These curves correspond to the allowed Brillouin-scattering mechanism induced by the strain associated with the acoustical phonons. As clearly seen in Fig. 5-10, the second derivative shows a quite good agreement with the experimental data.

Figure 5-11 shows the resonance behavior of parallel-perpendicular (forbidden) scattering by the slow-TA phonon domains measured at room temperature. The inset indicates the experimental configurations. The allowed scattering component is involved in this configuration, but it is small enough to be neglected because of the small scattering angles ($\sim 1°$). The solid and dashed lines are obtained by differentiating the dielectric constant for the ordinary ray according to the experimental configurations ($\vec{e}_i \perp \vec{c}$ and $\vec{e}_s$ is almost perpendicular to the c-axis). For the purpose of comparison, we also show in the figure the line shape of the Brillouin-tensor term R_{is} obtained in Section 4.3.4. One can easily find in Fig. 5-11 that the second derivative shows a quite good agreement with the experimental data.

Forbidden Raman scattering by LO phonons for a parallel-perpendicular configuration has also been found in ZnTe by Schmidt *et al.*[56] They have explained this effect in terms of depolarization induced by internal strain. Although the forbidden-scattering mechanism observed here has not yet been

completely explained, it may be pointed out that the strong longitudinal field associated with the slow-TA phonon domain is one of the causes. A full understanding of our results will require further experimental and theoretical work to be done in this area.

5.3.4 *Comparison of Brillouin Tensor R_{is} with Photon-Energy Derivative of the Dielectric Constant*

Next, we compare the Brillouin-tensor term R_{is} with the photon-energy derivative of the dielectric constant. In the above, we obtained the photon-energy derivatives by numerically differentiating the experimental data of the dielectric constants. It is well known that the photon-energy derivative of the dielectric constant can be obtained directly from the modulation spectroscopy such as electroreflectance, electroabsorption, thermoreflectance, piezoreflectance and wavelength-derivative spectroscopy.[43,44] Indeed, in a technique of the thermoreflectance spectroscopy the effect of a temperature change on the optical properties of materials comes from a shift of the band-gap energy (and a change of the broadening parameter). This band-gap shift produces a change of the dielectric constant through the expression of Eq. (5.7). Thus, resonant Brillouin scattering is very analogous phenomenologically to the modulation spectroscopy. From this fact, the spectral dependence of the Brillouin-scattering cross sectios can be considered to contain information about the (first-derivative) modulation spectrum, which is verified by the following analyses.

Figure 5-12 (a) shows the dielectric constant ε_1 for ZnSe as a function of photon energy at room temperature taken from the data of Ref. 185. The first derivative of ε_1 with respect to the photon energy, obtained by numerical differentiation, is shown in Fig. 5-12 (b). Figure 5-12 (c) shows the theoretical line shapes of the Brillouin-tensor term R_{is} (solid and dashed lines) and corresponding dispersionless term R_0 (dashed line) along with the

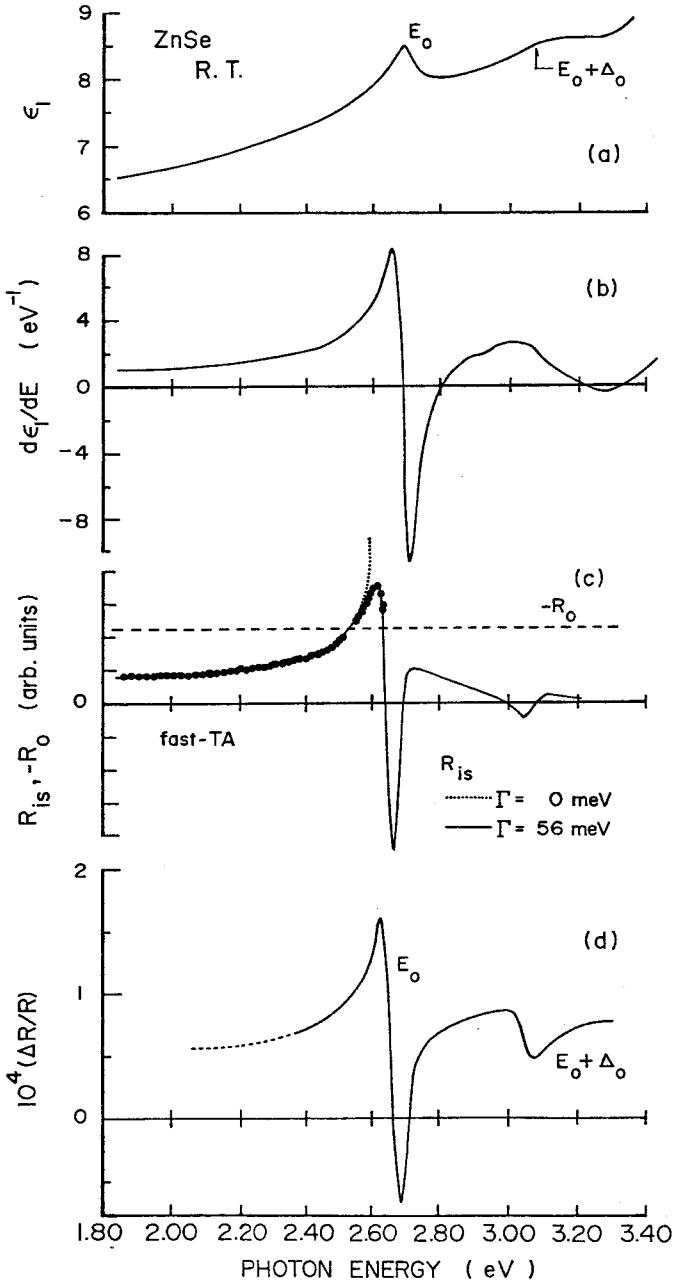

FIG. 5-12. Comparison of the dispersion of the Brillouin-scattering cross sections with the first-derivative spectra for ZnSe. (a) ε_1 (from Ref. 185); (b) $d\varepsilon_1/dE$, in eV^{-1}; (c) dispersion of the resonant term R_{is} (solid and dotted lines) and corresponding dispersionless term R_0 (dashed line) along with the experimental data (T2-mode); (d) thermoreflectance spectrum (from Ref. 184).

experimental data [Fig. 4-11]. The resonant term R_{is} is calculated from Eq. (2.55) with the lifetime-broadening energies of $\Gamma = 0$ (dotted line) and 56 meV (solid line). We can recognize that the line shape of the Brillouin-tensor term R_{is} (solid line) is similar to that of Fig. 5-12 (b). The thermoreflectance spectrum of ZnSe at room temperature[184] is shown in Fig. 5-12 (d). The significant feature found is that the thermoreflectance spectrum is very similar to the line shape of R_{is} especially near the E_0 and $E_0+\Delta_0$ transition regions.

Figures 5-13 (a) and (b) show the dielectric constant $\varepsilon_\perp$ ($\vec{E} \perp \vec{c}$) for CdS at room temperature and its first derivative with respect to the photon energy, respectively. The dielectric constant is obtained from Ref. 203. Figure 5-13 (c) shows the theoretical line shapes of the Brillouin-tensor term R_{is} (solid and dotted lines) and corresponding dispersionless term R_0 (dashed line) along with the experimental data [Fig. 4-20]. The resonant term R_{is} is calculated from Eq. (2.55) with the lifetime-broadening energies of $\Gamma = 0$ (dotted line) and 68 meV (solid line). The experimental data shows a quite good agreement with the theoretical line shape of R_{is} when the lifetime-broadening effect is taken into account in the calculation. The thermoreflectance spectrum of CdS ($\vec{E} \perp \vec{c}$) at room temperature[204] is shown in Fig. 5-13 (d). The peaks in the spectrum denoted by A, B and C can not be distinguished in the line shape of R_{is} [Fig. 5-13 (c)], where only the shoulder arising from the B and C excitons can be recognized in the figure. In the calculation of R_{is}, we took into account the lifetime-broadening energy of $\Gamma = 68$ meV to fit it to the experimental data. This energy is larger than the splitting energies of the three valence bands between the A — B (14 meV) and B — C bands (59 meV). Therefore, such a structureless feature appeared in the line shape of R_{is} is the result of broadening of the resonance energies (A, B and C excitons). Figure 5-13 clearly indicates that the spectra strongly

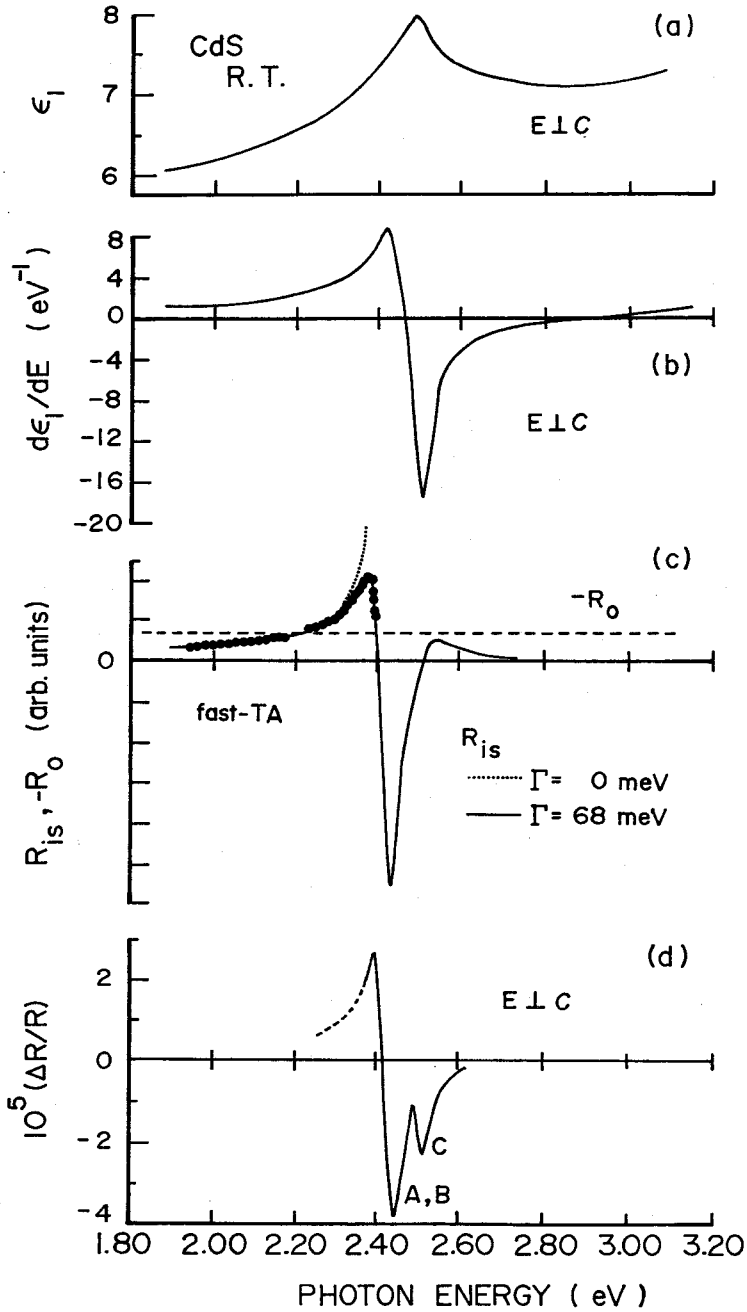

FIG. 5-13. Comparison of the dispersion of the Brillouin-scattering cross sections with the first-derivative spectra for CdS. (a) ε_1 ($\vec{E}\perp\vec{c}$, from Ref. 203); (b) $d\varepsilon_1/dE$, in eV^{-1}; (c) dispersion of the resonant term R_{is} (solid and dotted lines) and corresponding dispersionless term R_0 (dashed line) along with the experimental data (Tl-mode); (d) thermoreflectance spectrum (from Ref. 204).

resemble line shapes obtained in the first derivative of ε_1, resonant term R_{is} and thermoreflectance. We can, therefore, conclude from the analyses of the quasi-static approximation that the Brillouin-scattering spectroscopy is quite equivalent to the first-derivative modulation spectroscopy.

CHAPTER VI

DETERMINATION OF PHOTOELASTIC CONSTANT IN ZnSe, ZnTe AND CdS

6.1 INTRODUCTION

In this Chapter, we shall obtain the spectral dependence of the photoelastic constants in ZnSe, ZnTe and CdS from the Brillouin-scattering data by introducing the intrinsic-piezobirefringence analysis. From a macroscopical point of view, the Brillouin-scattering cross section is known to be proportional to the square of the corresponding photoelastic constant [see Section 2.2.4]. Such constant can be obtained independently from the stress-induced birefringence (piezobirefringence) measurement. The investigation of the piezobirefringence in solids is an old topic of crystal optics.[42] The application of a uniaxial stress to a solid produces a change in its crystal symmetry and lattice parameters which results in significant changes in its properties. An optically isotropic semiconductor usually becomes birefringent under the action of a uniaxial stress.

The piezobirefringence data have been reported in a variety of crystals such as Ge,[75] Si,[75] GaAs,[75,205] GaP,[206,207] AlSb,[208] GaSb,[209] InAs,[209] InSb,[209] InP,[207] ZnS,[210] ZnSe,[92,211] ZnTe,[92] CdTe,[92,212] CuCl,[213] CuBr,[213] CuI,[213] CdSe,[214] CdS,[30,92] ZnO[30] and diamond.[215] These data have been obtained accurately only in the region of transparency because of experimental reasons (i.e., transmission of light). Materials whose lowest gap is direct, or with a direct gap only slightly above the lowest one (*e.g.*, Ge), have a strong

dispersion of the photoelastic constants in the region near this gap. The dispersion near an indirect gap far removed from a direct gap (*e.g.*, Si and GaP) is found to be very weak. The sign of the photoelastic constant is, in materials with the lowest direct gaps larger than $\sim$ 0.7 eV, negative for long wavelengths and reverses sign when approaching the direct edge. Materials with small direct gaps (*e.g.*, InSb), on the other hand, do not exhibit this sign reversal. The sign of the photoelastic constants in such materials is positive at long wavelengths and also near the direct edge. The cancellation in the Brillouin-scattering cross section arises from the sign reversal of the photoelastic constant (i.e., occurs at an isotropic point). The isotropic point is known to be independent on the applied stress.

A usual technique employed consists of transmitting a beam of monochromized light through the sample perpendicular to the stress direction. The plane of polarization of the light is at 45° to the stress direction, and the ratio of the intensities of transmitted light polarized parallel and perpendicular to the incident beam is related to the stress-induced phase difference and therefore to the corresponding photoelastic constant [see Eq. (2.208)]. Another method to measure the photoelastic constants employs the diffraction of light traversing the sample by ultrasonic waves (Dixon-Cohen method).[216] Both methods are basically limited to the transparency region of the material, and can be used with success only below or near the fundamental absorption edge.

Recently, Chandrasekhar *et. al.*[217] have developed a new method to measure stress-induced birefringence in an opaque region of the material which employs the Raman-scattering technique as a probe. Using this new method, they have measured the magnitudes of the piezo-optical (photoelastic) constants in Si (0.5 – 3.38 eV)[218] and GaP (1.0 – 2.6 eV)[207] above the fundamental absorption edges.

In Section 6.2, we obtain theoretical expression of the photoelastic constants by using the model dielectric constants. A comparison of the theoretical expression with the experimental data is presented in Section 6.3. In Section 6.4, we present a new method to analyze the piezobirefringence effect in a opaque region of the material, where the stress-induced changes in both the real and imaginary parts of the dielectric constant are properly taken into account by introducing new fractional coefficients.[219] The piezobirefringence data reported up to date were analyzed by considering only the stress-induced change in the real part of the dielectric constant. Using the present method, it should be possible to extend the piezobirefringence analysis in a large number of opaque materials.

6.2 THEORETICAL EXPRESSION

6.2.1 Zincblende-Type Crystal

In Section 2.3, we have obtained the basic expression of the photoelastic constants. Using this results, we shall obtain here the concrete expression of the photoelastic constants in terms of the model dielectric constants.

The spectral dependence of the dielectric constants in Ge and III-V compounds can be well interpreted with the parabolic band model.[64] In this model, the real part of the dielectric constant below the fundamental absorption edge is the sum of the contribution of the $E_0/E_0+\Delta_0$ edge plus a constant term ε_∞ which corresponds to the effect of the average gap (i.e., contribution from the higher gaps such as the E_1, $E_1+\Delta_1$ and E_2 gaps). Under the assumption of parabolic bands, the model dielectric constant can be written from Eqs. (2.193) and (2.206) as

$$\varepsilon_1(\omega) = C_{0z} \left[f\left(\frac{\omega}{\omega_0}\right) + \frac{1}{2}\left(\frac{\omega_0}{\omega_{os}}\right)^{3/2} f\left(\frac{\omega}{\omega_{os}}\right) \right] + \varepsilon_\infty . \qquad (6.1)$$

Figure 6-1 compares the result of our model (6.1) to the experimental data of ZnTe. The experimental data are taken from Sliker and Jost.[191] The solid line is a fit of Eq. (6.1) to the data. The numerical values used are as follows: $\hbar\omega_0 = 2.25$ eV, $\hbar\omega_{os} = 3.18$ eV, $C_{0z} = 13.20$ and $\varepsilon_\infty = 3.05$. It is clear from the figure that the calculation shows a considerably good agreement with the experimental data. It seems that our model should be in much better agreement with the experimental data if the exciton modification of the interband absorption edge is taken into account. However, it is difficult to evaluate this effect from the fit procedure between the model dielectric constant and experimental data. A differential effect of the piezobirefringence, as we shall see below, is much more dispersive than ε_1 near the E_0 edge, and a separation of the excitonic and interband contributions becomes to be possible. If we include the contribution of the ground state of the E_0 exciton [see Eq. (2.199)]:

$$\frac{F_A^D}{E_{ex}^2 - E^2} = \frac{F_A^D}{\hbar^2} \frac{1}{\omega_{x1}^2 - \omega^2} \quad , \tag{6.2}$$

we can write the real part of ε below E_0 as:

$$\varepsilon_1(\omega) = C_{0z} \left[f\left(\frac{\omega}{\omega_0}\right) + \frac{1}{2}\left(\frac{\omega_0}{\omega_{os}}\right)^{3/2} f\left(\frac{\omega}{\omega_{os}}\right) \right] + \frac{F_A^D}{\hbar^2} \frac{1}{\omega_{x1}^2 - \omega^2} + \varepsilon_\infty \quad , \tag{6.3}$$

where $E_{x1} = \hbar\omega_{x1}$ is the ground-state energy of the E_0 exciton.

Substituting Eqs. (2.230) and(2.237) into Eq. (2.221) and using the model dielectric constant of Eq. (6.3), we obtain the expression of the photoelastic constant $p_{11} - p_{12}$ in the following form:[71]

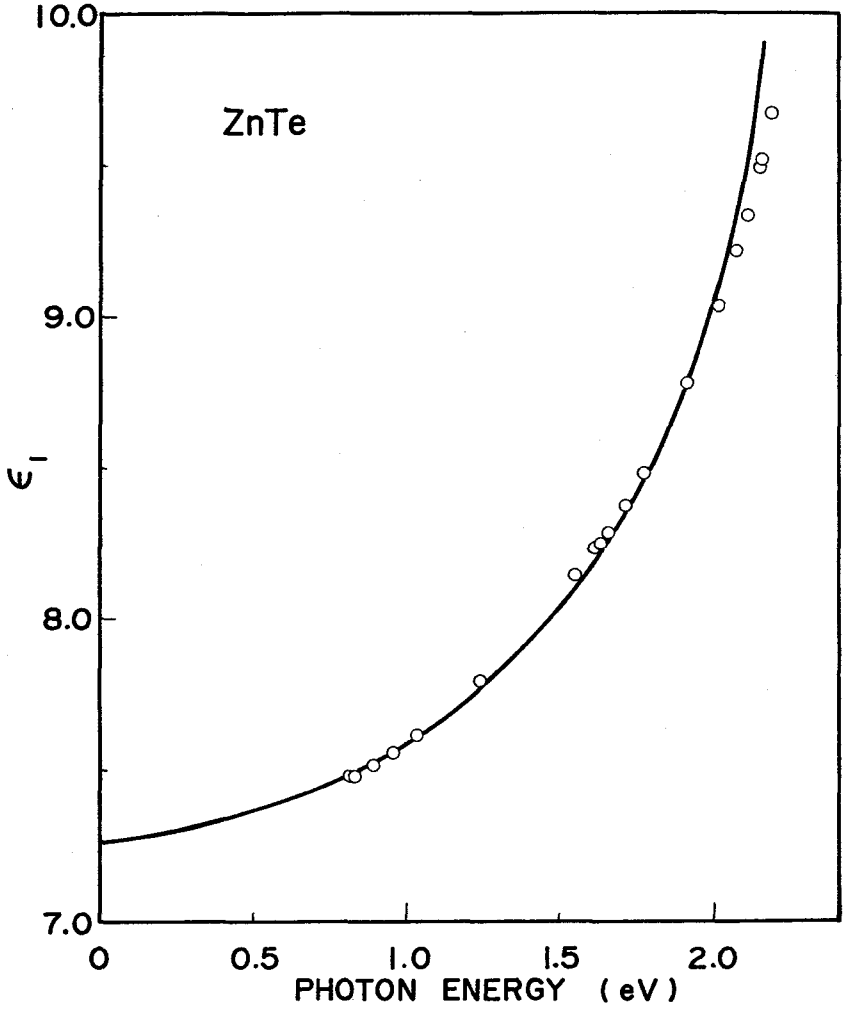

FIG. 6-1. Dielectric constant of ZnTe at room temperature in the region of transparency (from Ref. 191). The solid line is a fit of Eq. (6.1) to the data.

$$p_{11}-p_{12}=\frac{C}{\varepsilon_{11}^{2}}\{-g(\frac{\omega}{\omega_0})+4\frac{E_0}{\Delta_{so}}[f(\frac{\omega}{\omega_0})-(\frac{\omega_0}{\omega_{os}})^{3/2}f(\frac{\omega}{\omega_{os}})]\}$$

$$+\frac{C_{ex}}{\varepsilon_{11}^{2}}\{\frac{3-\chi_{ex}^{2}}{(1-\chi_{ex}^{2})^{2}}+\frac{E_{x1}}{\Delta_{so}}[\frac{1}{1-\chi_{ex}^{2}}-(\frac{E_{x1}}{E_{x1}+\Delta_{so}})^{3}\frac{1}{1-\chi_{exs}^{2}}]\}$$

$$+D \quad , \tag{6.4}$$

where

$$g(x) = [\ 2 - (1+x)^{-\frac{1}{2}} - (1-x)^{-\frac{1}{2}}\ ]/x^2 \quad , \tag{6.5}$$

$$C = -\ (\frac{3}{2}m_e^*)^{3/2}P^2 b\omega_0^{-5/2} \quad , \tag{6.6a}$$

$$C_{ex} = -\ 3F_A^D b/E_{x1}^{3} \quad . \tag{6.6b}$$

In Eqs. (6.4) — (6.6), b is the shear deformation potential of Pikus and Bir [see Section 2.3.2)], and

$$\chi_{ex} = \hbar\omega/E_{x1} \quad , \qquad \chi_{exs} = \hbar\omega/(E_{x1} + \Delta_{so}) \quad . \tag{6.7}$$

The strength parameter F_A^D can be replaced by $(4\pi N f_1)$, where N and f_1 are the number of molecules per unit volume and the oscillator strength per molecule of the excitons, respectively. The first and second terms inEq. (6.4) correspond to the contributions from the band-to-band and ground-state $E_0/E_0+\Delta_0$ exciton transitions, respectively. Since the contributions of the higher gaps (E_1, $E_1+\Delta_1$ and E_2) are generally less dispersive than those of the E_0 and $E_0+\Delta_0$ gaps, we include such contributions in Eq. (6.4) as a nondispersive term D.

The photoelastic constant p_{44} can also be obtained by proceeding the analysis almost identical to the case of $p_{11} - p_{12}$. The orbital-strain Hamiltonian matrix can be given by the same form as Eq. (2.227) if we replace the energy shift δE_{001} [Eq. (2.226b)] by

$$\delta E_{110} = (d/\sqrt{3})S_{44}X \quad , \tag{6.8}$$

where d is the shear deformation potential. The stress-induced changes in energy gaps and squared-p matrix elements, required for the evaluation of Eq. (2.221), are then given by the same equations as Eqs. (2.230) and (2.237), respectively, except a replacement of δE_{001} by δE_{110} in the equations. Finally, we obtain the photoelastic constant p_{44} which has the same form as Eq. (6.4) but the following changes of Eq. (6.6) must be required:

$$C = -\frac{1}{4}\left(\frac{3}{2} m_e^*\right)^{3/2} P^2 d\omega_0^{-5/2} \quad , \qquad (6.9a)$$

$$C_{ex} = -3F_A^D d/4E_{x1}^3 \quad . \qquad (6.9b)$$

The sign reversal of the piezobirefringence may be understood in terms of cancellation between the $E_0/E_0+\Delta_0$ gap contributions and contributions from the higher gaps. The contributions from the higher-lying gaps have been treated quite successfully by Yu *et al.*[209] with the Penn model (a simple model of an insulator in which an average isotropic gap at the edge of a spherical Brillouin zone is assumed). It is known that for the zincblende-type materials the imaginary part of ε has a strong peak (E_2 transition) in the neighborhood of which most of the optical density of states is concentrated. In order to explain this effect, Penn[220] suggested the model of the non-physical spherical Brillouin zone with an isotropic gap (Penn gap) at its boundaries. The usual complex energy bands of the material are then replaced by those of a free electron with the Penn gap ω_g at the boundary of the spherical Brillouin zone. This gap should occur in the vicinity of the E_2 (M_2) optical structure. In the Penn model, the long-wavelength dielectric constant $\varepsilon(0)$ of a solid is given by

$$\varepsilon(0) = 1 + D_v\left(\frac{\omega_p}{\omega_g}\right)^2 \simeq 1 + \left(\frac{\omega_p}{\omega_g}\right)^2 \quad , \qquad (6.10)$$

where ω_p is the plasma frequency of the valence electrons and D_v is a parameter introduced by Van Vechten[221] to take into account the effect of *d*-like core electrons. Equation (6.10) yields two contributions to the change in $\varepsilon(0)$

due to the stress X; one arises from the change in plasma frequency and the other from the change in the Penn gap, i.e.,

$$\frac{1}{\varepsilon(0)}\frac{d\varepsilon(0)}{dX} = \frac{1}{\varepsilon(0)}\frac{d\varepsilon(0)}{dV}\frac{dV}{dX} = 2\left(\frac{d\ln\omega_p}{dV}\frac{dV}{dX} - \frac{d\ln\omega_g}{dV}\frac{dV}{dX}\right) , \qquad (6.11)$$

where V is the volume of a crystal. The first term in the bracket of Eq. (6.11) should not exist for a pure shear stress. Yu *et al.*[209] obtained the following Penn-gap change contribution in tensor form:

$$\frac{1}{\varepsilon(0)}\Delta\overleftrightarrow{\varepsilon}(0) = 5\overleftrightarrow{e} \qquad , \qquad (6.12)$$

where $\overleftrightarrow{\varepsilon}$ and $\overleftrightarrow{e}$ are the dielectric and strain tensors, respectively. Using Eq. (6.12), we obtain the nondispersive component of the photoelastic constant:

$$D = \frac{1}{\varepsilon_{11}^2}\, 5\, \varepsilon(0) \qquad \text{for } p_{11}-p_{12} \qquad (6.13)$$

$$D = \frac{1}{\varepsilon_{11}^2}\, \frac{5}{2}\, \varepsilon(0) \qquad \text{for } p_{44} \quad . \qquad (6.14)$$

Figure 6-2 shows a typical example of the theoretical line shapes of the photoelastic constant calculated from Eq. (6.4) with three different broadening parameters; $\Gamma = 0$ (dashed line), $0.02E_0$ (solid line) and $0.03E_0$ (dotted line). The lifetime-broadening effect has been introduced in Eq. (6.4) in a phenomenological manner by replacing ω by $\omega+i\Gamma/2\hbar$. When the electronic states have an infinite lifetime ($\Gamma = 0$), the calculated line shape shows a divergence at the band-edge region. The lifetime broadening suppresses this divergent feature and as a result a complex structure appears in the vicinity of the band edge E_0. It is clear that this structure is very similar to that for the Brillouin-tensor term R_{is} [see, *e.g.*, Fig. 4-10].

6.2.2 Wurtzite-Type Crystal

The piezobirefringence analysis for the wurtzite-type crystal is almost

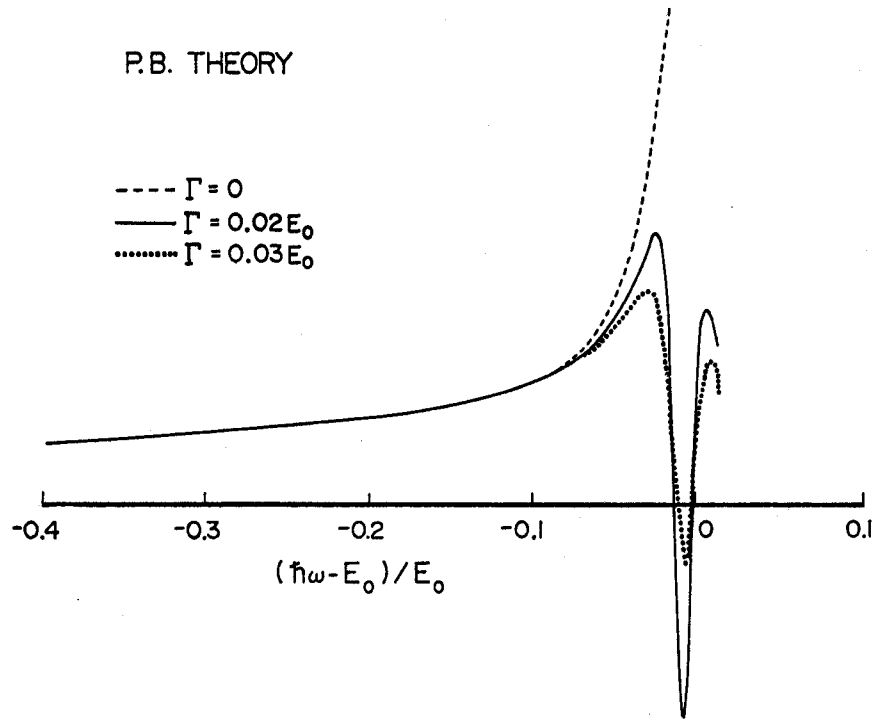

FIG. 6-2. Typical example of the theoretical line shapes of the photoelastic constant calculated from Eq. (6.4) with three different broadening parameters.

identical to that for the zincblende-type crystal. The stress-induced changes in the band-gap energies and squared-p matrix elements can be obtained by solving the eigenvalue problems as similar to those discussed in Section 2.3.2. Since the wurtzite-type crystal is already birefringent before stress is applied, it is only possible to observe accurately the birefringence induced by the stress along parallel and perpendicular to the *c*-axis. The linear combinations of the photoelastic constants may, of course, be determined from the piezo-birefringence experiment by properly selecting the experimental coordinate systems.[92] We now express the component of dielectric tensor by taking into account the exciton effect in the following form:

$$\varepsilon_{ij}(E) = \sum_{\alpha} \varepsilon_{ij}^{\alpha}(E) + \varepsilon_{ij\infty} \quad , \tag{6.15}$$

where

$$\varepsilon_{ij}^{\alpha}(E) = F_{ij}^{\alpha}\left[\sum_{n=1}^{\infty} \frac{1}{n^3[(E_{g\alpha}-G/n^2)^2-E^2]} + C_{ij}\frac{E_{x1}}{4G}\frac{1}{E^2}\ln\frac{E_{g\alpha}^2}{E_{g\alpha}^2-E^2}\right] \quad . \tag{6.16}$$

Here α labels the three valence bands A, B and C, F_{ij}^{α} is the strength parameter related to the squared-p matrix element, and G is the exciton Rydberg constant. C_{ij} and $\varepsilon_{ij\infty}$ are adjustable parameters which can be determined by fitting the experimental data of refractive indices with Eq. (6.15). The first and second terms in the right-hand side of Eq. (6.16) correspond to the contributions from the discrete excitons and the unbound continuum excitons plus band-to-band transitions, respectively. The expression (6.16) has been used by Berkowicz[89] to explain his piezobirefringence data of CdS and ZnO. It should be noted that the second term of Eq. (6.16) has very similar spectral dependence to that of the band-to-band contribution, i.e., to that appeared in Eq. (6.1) [see Section 2.3.1]. The parameter C_{ij} is

then introduced in Eq. (6.16) in order to account for both the continuum excitons and band-to-band transitions by the common expression, i.e., by the second term of Eq. (6.16).

One can obtain the orbital-strain Hamiltonian matrix from Eqs. (2.80) and (2.85). The stress-induced change in the band-gap energies may be calculated by diagonalizing this Hamiltonian matrix. The stress-induced change in the strength parameters may also be calculated in a manner mentioned in Section 2.3.2 by using the perturbed wave functions. The piezobirefringence can only be measured accurately when the axes of the stress-induced change in the dielectric tensor coincide with those of the dielectric constant at zero stress (natural birefringence), i.e., when the stress is applied along a principal axis. We shall, therefore, consider first the case corresponding to the photoelastic constant p_{66}. As mentioned in Section 2.3.2, the experimental coordinate system for the determination of p_{66} satisfies this requirement (the x-axis is parallel to the direction of the applied stress). In this case, we can use the orbital-strain Hamiltonian of Eq. (2.88b) instead of Eq. (2.85). Using the quasi-cubic model for the unperturbed bands, the stress-induced changes in the band-gap energies and strength parameters are obtained as follows (first order in stress):

$$\Delta E_{gA} = [\, E_{gA}(X) - E_{gA}(0) \,] = 0 \quad , \tag{6.17a}$$

$$\Delta E_{gB} = [\, E_{gB}(X) - E_{gB}(0) \,] = 0 \quad , \tag{6.17b}$$

$$\Delta E_{gC} = [\, E_{gC}(X) - E_{gC}(0) \,] = 0 \quad , \tag{6.17c}$$

and

$$\Delta F^A_{xy}/F^A_{xx}(0) = [\Delta F^A_{xx} - \Delta F^A_{yy}]/F^A_{xx}(0) = 4\left(\frac{\alpha_B^2}{E_{BA}} + \frac{\alpha_C^2}{E_{CA}}\right)C_5(S_{11}-S_{12})X \ , \tag{6.18a}$$

$$\Delta F^B_{xy}/F^B_{xx}(0) = [\Delta F^B_{xx} - \Delta F^B_{yy}]/F^B_{xx}(0) = -\frac{4}{E_{BA}}\, C_5(S_{11}-S_{12})X \ , \tag{6.18b}$$

$$\Delta F^C_{xy}/F^C_{xx}(0) = [\Delta F^C_{xx} - \Delta F^C_{yy}]/F^C_{xx}(0) = -\frac{4}{E_{CA}} C_5(S_{11}-S_{12})X \ , \tag{6.18c}$$

where C_5 is the shear deformation potential, $\Delta F^\alpha_{ii}=F^\alpha_{ii}(X)-F^\alpha_{ii}(0)$ and E_{BA} and E_{CA} are given by Eq. (2.79). The photoelastic constant can be written from Eq. (2.210) as

$$p_{mn} = -\frac{1}{\varepsilon_{ii}\varepsilon_{jj}} \frac{\partial\varepsilon_{ij}}{\partial e_{kl}} \frac{1+\delta_{kl}}{2} \quad . \tag{6.19}$$

The factor $(1 + \delta_{kl})/2$ appears because the off-diagonal components of the strain tensor contribute twice to the sum (2.210). Substituting Eqs. (6.17) and (6.18) into Eq. (2.221), we finally obtain the expression of the photoelastic constant p_{66} in the following form:[39]

$$p_{66} = \frac{1}{\varepsilon_{11}^2} (D_{66} + C_5F_{66}) \quad , \tag{6.20}$$

where

$$F_{66} = 2 [\frac{\alpha_B^2\varepsilon^A_{xx} - \varepsilon^B_{xx}}{E_{BA}} + \frac{\alpha_C^2\varepsilon^A_{xx} - \varepsilon^C_{xx}}{E_{CA}}] \quad . \tag{6.21}$$

In Eq. (6.20), D_{66} is the nondispersive contribution arising from the higher-lying gap transitions. In accordance with the previous discussion, we can introduce the lifetime-broadening effect in the calculation of the photoelastic constant by replacing E of Eq. (6.16) by $E + i(\Gamma/2)$.

We next proceed to calculate the photoelastic constant p_{44} in a similar way. From experimental aspect, this constant can not be measured accurately because the axes of the stress-induced change in the dielectric tensor do not coincide with those of the dielectric constant at zero stress, in contrast to the case of p_{66}. Yu and Cardona[92] have determined the spectral dependence of p_{66} and the linear combinations of the photoelastic constants. Recently, however, Berkowicz and Skettrup[30] have obtained the spectral dependence of both p_{44} and p_{66}. In the case of p_{44}, they have used the coordinate system

with the stress direction forming an angle 45° with the c-axis to yield the shear strain component e_{xz}. We can now use the orbital-strain Hamiltonian of Eq. (2.89b) instead of Eq. (2.85). From this Hamiltonian, we obtain the following stress-induced changes in the band-gap energies and strength parameters (first order in stress):

$$E_{gA} = [\ E_{gA}(X) - E_{gA}(0)\ ] = 0 \quad , \tag{6.22a}$$

$$E_{gB} = [\ E_{gB}(X) - E_{gB}(0)\ ] = 0 \quad , \tag{6.22b}$$

$$E_{gC} = [\ E_{gC}(X) - E_{gC}(0)\ ] = 0 \quad , \tag{6.22c}$$

and

$$\Delta F^A_{xz}/F^A_{xx}(0) = \frac{1}{\sqrt{2}}\, C_6\, T\, \left(\frac{\alpha_C^{\,2}}{E_{BA}} + \frac{\alpha_B^{\,2}}{E_{CA}} \right) \quad , \tag{6.23a}$$

$$\Delta F^B_{xz}/F^B_{xx}(0) = -\frac{1}{\sqrt{2}}\, C_6 \frac{T}{\alpha_B^{\,2}} \left(\frac{\alpha_C^{\,2}}{E_{BA}} - \frac{1}{E_{CB}} \right) \quad , \tag{6.23b}$$

$$\Delta F^C_{xz}/F^C_{xx}(0) = -\frac{1}{\sqrt{2}}\, C_6 \frac{T}{\alpha_C^{\,2}} \left(\frac{\alpha_B^{\,2}}{E_{CA}} + \frac{1}{E_{CB}} \right) \quad , \tag{6.23c}$$

where C_6 is the shear deformation potential, and

$$T = \left[\frac{\alpha_B^{\,2} F^B_{zz}(0)}{2\alpha_C^{\,2} F^B_{xx}(0)} \right]^{\frac{1}{2}} = \left[\frac{\alpha_C^{\,2} F^C_{zz}(0)}{2\alpha_B^{\,2} F^C_{xx}(0)} \right]^{\frac{1}{2}} \quad . \tag{6.24}$$

Substituting Eqs. (6.22) and (6.23) into Eq. (2.221), we obtain

$$P_{44} = \frac{1}{\varepsilon_{11}\varepsilon_{33}} \left(D_{44} + C_6 F_{44} \right) \quad , \tag{6.25}$$

where

$$F_{44} = \frac{T}{2\sqrt{2}} \left[\frac{\alpha_C^{\,2}}{E_{BA}} \left(\varepsilon^A_{xx} - \frac{\varepsilon^B_{xx}}{\alpha_B^{\,2}} \right) + \frac{\alpha_B^{\,2}}{E_{CA}} \left(\varepsilon^A_{xx} - \frac{\varepsilon^C_{xx}}{\alpha_C^{\,2}} \right) + \frac{1}{E_{CB}} \left(\frac{\varepsilon^B_{xx}}{\alpha_B^{\,2}} - \frac{\varepsilon^C_{xx}}{\alpha_C^{\,2}} \right) \right] . \tag{6.26}$$

In Eq. (6.25), D_{44} is the nondispersive contribution arising from the higher-lying gap transitions.

The photoelastic constant p_{31} may also be derived in the same way as was done to the case of p_{66} and p_{44}. However, this constant can not be determined from the piezobirefringence experiment because of the limitation of the experimental coordinate system. The Brillouin-scattering technique enables us to determine the photoelastic constant p_{31} from the intensity measurements of corresponding Brillouin component.[222] The macroscopical theory of Brillouin scattering gives intensity of the PL-mode phonon component in terms of p_{31} [see Section 2.2.4]. As already mentioned in Section 2.2.3, the PL-mode phonon produces the non-vanishing strain component e_{xx}. Therefore, we can use the orbital-strain Hamiltonians of Eqs. (2.93a) and (2.93b) instead of Eqs. (2.84) and (2.85). From these Hamiltonian matrices, the stress-induced changes in the band-gap energies and strength parameters become to first order in the stress:

$$\Delta E_{gA} = [\ (C_2 - d_2) + C_4\ ]\ e_{xx} \quad , \qquad (6.27a)$$

$$\Delta E_{gB} = [\ (C_2 - d_2) + \alpha_B^2 C_4\ ]\ e_{xx} \quad , \qquad (6.27b)$$

$$\Delta E_{gC} = [\ (C_2 - d_2) + \alpha_C^2 C_4\ ]\ e_{xx} \quad , \qquad (6.27c)$$

and

$$\Delta F^A_{zz}/F^A_{zz}(0) = 0 \quad , \qquad (6.28a)$$

$$\Delta F^B_{zz}/F^B_{zz}(0) = -\ 2\ C_4 \frac{\alpha_B^2}{E_{CB}} \quad , \qquad (6.28b)$$

$$\Delta F^C_{zz}/F^C_{zz}(0) = +\ 2\ C_4 \frac{\alpha_C^2}{E_{CB}} \quad . \qquad (6.28c)$$

Substituting Eqs. (6.27) and (6.28) into Eq. (2.221), we obtain the expression of the photoelastic constant p_{31} in the following form:

$$p_{31} = \frac{1}{\varepsilon_{33}^{2}} [D_{31} + C_4 F_{31}^{(A)} + (C_2 - d_2) F_{31}^{(B)}] \quad , \tag{6.29}$$

where

$$F_{31}^{(A)} = -2[\frac{\alpha_B^2 \varepsilon_{zz}^B - \alpha_C^2 \varepsilon_{zz}^C}{E_{CB}}] + [\frac{\partial \varepsilon_{zz}^A}{\partial E_{gA}} + \alpha_B^2 \frac{\partial \varepsilon_{zz}^B}{\partial E_{gB}} + \alpha_C^2 \frac{\partial \varepsilon_{zz}^C}{\partial E_{gC}}] \ , \tag{6.30}$$

$$F_{31}^{(B)} = (\frac{\partial \varepsilon_{zz}^A}{\partial E_{gA}} + \frac{\partial \varepsilon_{zz}^B}{\partial E_{gB}} + \frac{\partial \varepsilon_{zz}^C}{\partial E_{gC}}) \quad . \tag{6.31}$$

In Eq. (6.28), D_{31} is the nondispersive contribution arising from the higher-lying gap transitions.

6.3 COMPARISON OF THEORY WITH EXPERIMENTAL DATA

The macroscopical theory of Brillouin scattering presented in Section 2.2.4 gives intensities of the Brillouin-scattering cross sections in terms of the photoelastic constants:

$$\sigma_B(T1) \propto (p_{11} - p_{12})^2 \quad , \tag{6.32a}$$

$$\sigma_B(T2) \propto p_{44}^2 \quad , \tag{6.32b}$$

for the zincblende-type crystals, and

$$\sigma_B(T1) \propto p_{66}^2 \quad , \tag{6.33a}$$

$$\sigma_B(T2) \propto p_{44}^2 \quad , \tag{6.33b}$$

$$\sigma_B(PL) \propto p_{31}^2 \quad , \tag{6.33c}$$

for the wurtzite-type crystals. We shall obtain here the spectral dependence of the photoelastic constants from the present data by introducing the intrinsic-piezobirefringence analyses.

6.3.1 ZnSe

Figures 6-3 and 6-4 show the spectral dependence of the photoelastic

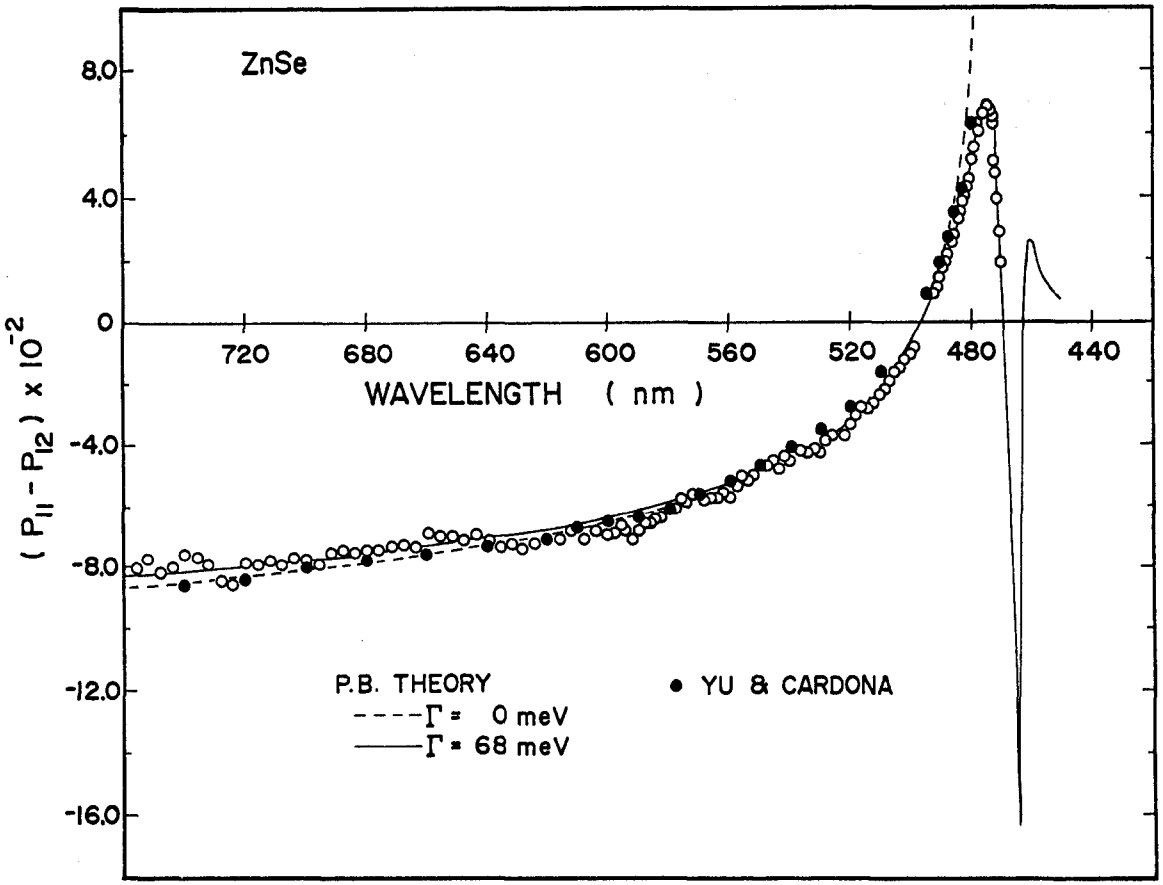

FIG. 6-3. Dispersion of the photoelastic constant $p_{11} - p_{12}$ in ZnSe (room temperature). The theoretical curves are obtained from Eq. (6.4) with Γ=0 meV (dashed line) and Γ=68 meV (solid line). The piezobirefringence data of Yu and Cardona (Ref. 92) are also shown by solid circles.

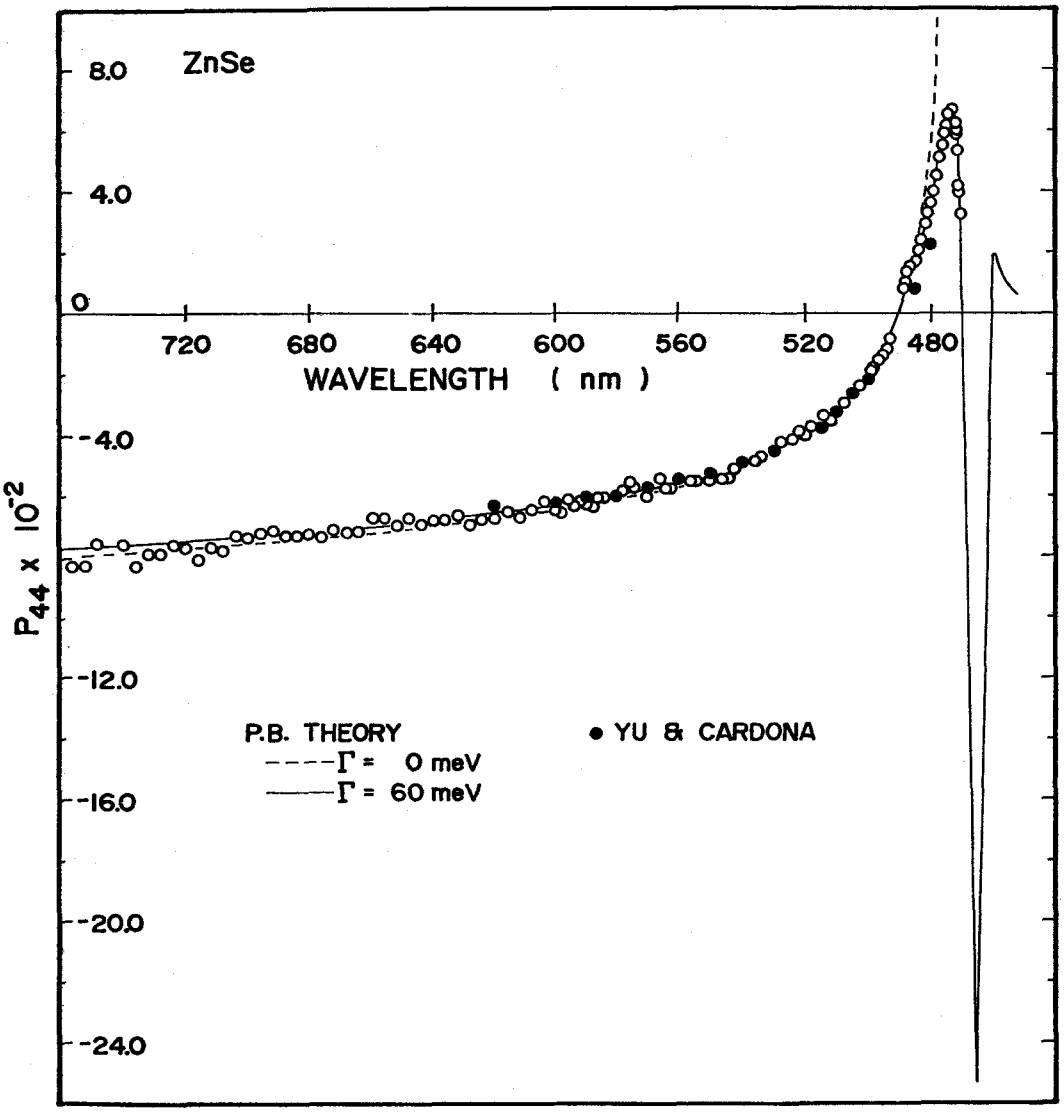

FIG. 6-4. Dispersion of the photoelastic constant p_{44} in ZnSe (room temperature). The theoretical curves are obtained from Eq. (6.4) with Γ=0 meV (dashed line) and Γ=60 meV (solid line). The piezo-birefringence data of Yu and Cardona (Ref. 92) are also shown by solid circles.

constants $p_{11} - p_{12}$ and p_{44} for ZnSe, respectively, obtained at room temperature. The theoretical curves have been calculated from Eq. (6.4) with $\Gamma = 0$ (dashed line) and $\Gamma \neq 0$ (solid line). The numerical values used are listed in Table 6-1. The constants C and C_{ex} are deduced from the experimental data of the intrinsic-piezobirefringence measurements reported by Yu and Cardona.[92] The piezobirefringence data of Yu and Cardona are also shown in the figures by the filled circles. As clearly seen in the figures, the data obtained from the Brillouin-scattering measurements show a quite good agreement with the piezobirefringence data. The theoretical curve ($\Gamma = 0$) shows a poor fit with the experimental data in the region near the fundamental absorption edge. Such a feature is improved by taking into account the lifetime-broadening effect. This effect has not yet been considered in the previous piezobirefringence analyses because of the experimental difficulty in the region of the photon energies sufficiently close to the fundamental absorption edge (where there exists strong absorption of light in thick samples used to avoid a destruction with the applied uniaxial stress). The best-fitting values of the broadening energy are determined to be $\Gamma = 68$ and 60 meV for $p_{11} - p_{12}$ and p_{44}, respectively. These values agree reasonably with those derived in the analysis of the Brillouin-scattering cross sections [see Section 4.3]. The piezobirefringence coefficients of ZnSe have been measured at liquid nitrogen temperature by Dubenskii *et al.*[211] Cooling the samples make it possible to study piezobirefringence close to the absorption edge since the edge becomes sharper at 77 K. Comparing their data with ours, we found that the long-wavelength photoelastic constants do not vary much with temperatures.

6.3.2 ZnTe

Figures 6-5 and 6-6 show the spectral dependence of the photoelastic constants $p_{11} - p_{12}$ and p_{44} for ZnTe, respectively, obtained at room temperature. The theoretical curves have been calculated from Eq. (6.4) with $\Gamma = 0$ (dashed

Table 6-1. Numerical values used to calculate spectral dependence of the photoelastic constants $p_{11} - p_{12}$ and p_{44} for ZnSe and ZnTe.

	ZnSe		ZnTe	
	$p_{11} - p_{12}$	p_{44}	$p_{11} - p_{12}$	p_{44}
$C^{(a)}$	1.42	9.15×10^{-1}	1.02	1.29×10^{-1}
$C_{ex}^{(a)}$	3.94×10^{-3}	5.26×10^{-3}	2.27×10^{-3}	5.59×10^{-3}
$D^{(b)}$	-1.49×10^{-1}	-1.35×10^{-1}	-8.65×10^{-2}	-3.70×10^{-2}
$\varepsilon_{11}(\omega)$	Reference 189		Reference 189	
E_0 [eV]	2.68		2.25	
Δ_{so} [eV]	0.41		0.93	

(a) Reference 92.

(b) Estimated from our experimental data.

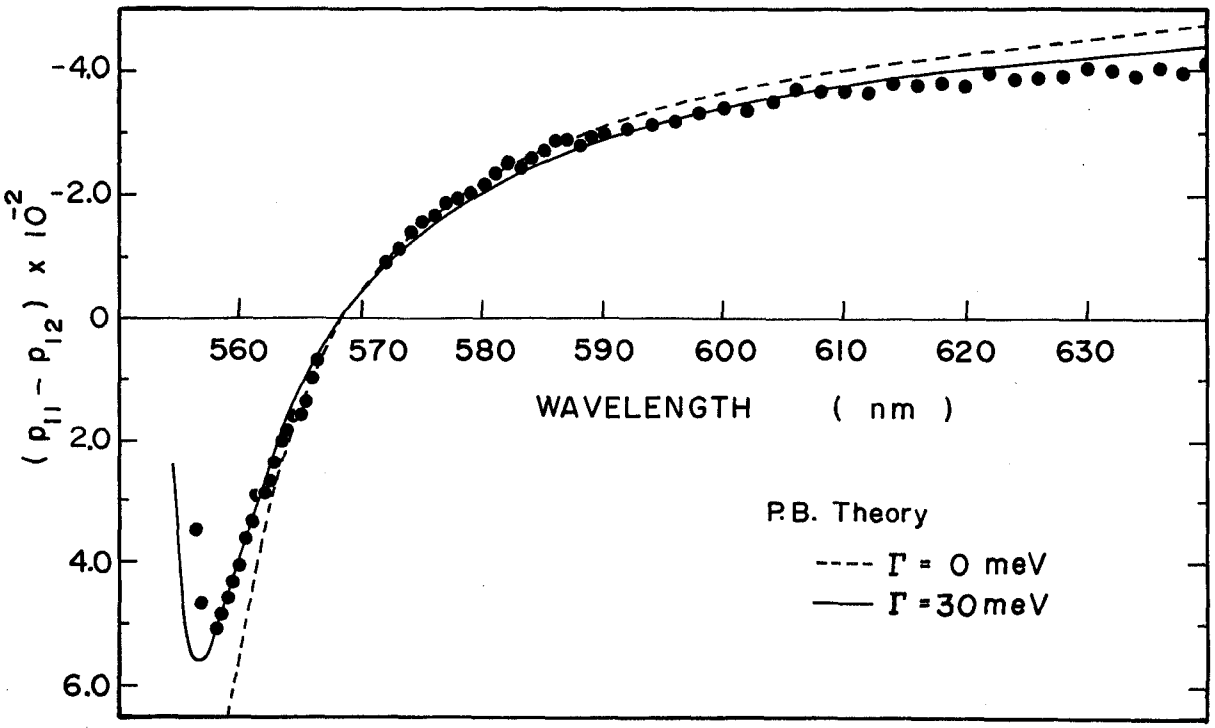

FIG. 6-5. Dispersion of the photoelastic constant $p_{11} - p_{12}$ in ZnTe (room temperature). The theoretical curves are obtained from Eq. (6.4) with Γ=0 meV (dashed line) and Γ=30 meV (solid line).

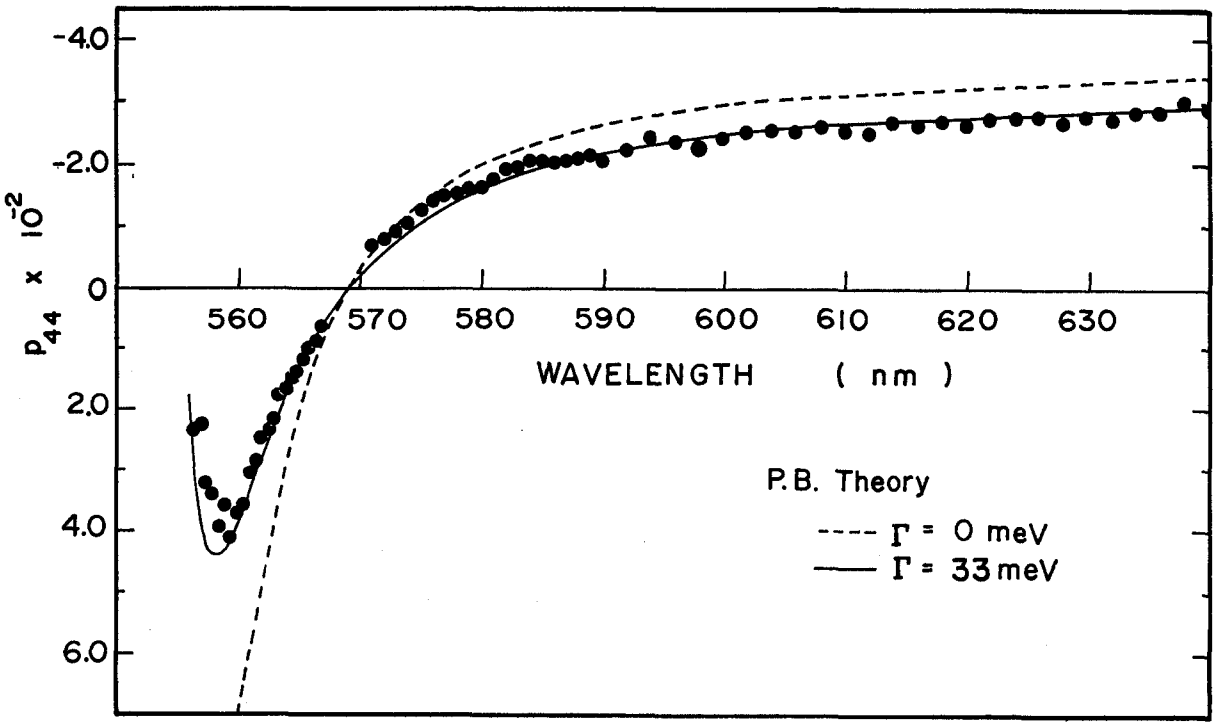

FIG. 6-6. Dispersion of the photoelastic constant p_{44} in ZnTe (room temperature). The theoretical curves are obtained from Eq. (6.4) with Γ=0 meV (dashed line) and Γ=33 meV (solid line).

line) and $\Gamma \neq 0$ (solid line). The numerical values used are listed in Table 6-1. The theoretical curve (solid line) shows a quite good agreement with the experimental data especially near the fundamental absorption edge when we take into account the lifetime-broadening energy of $\Gamma = 30 \sim 33$ meV. This value agrees exactly with those derived in the analysis of the Brillouin-scattering cross sections. The sign of $p_{11} - p_{12}$ and p_{44} is negative in the region far from the band edge and becomes positive when the wavelength approaches the band gap. Yu and Cardona[92] have reported the spectral dependence of the photoelastic constants $p_{11} - p_{12}$ and p_{44} from the piezobirefringence measurements. However, they have not measured the value of p_{44} in the positive-sign region (i.e., near the band-edge region). Our experimental data, on the other hand, clearly indicates an existence of that p_{44} passes through zero while undergoing a reversal in sign.

6.3.3 CdS

The spectral dependence of the photoelastic constant p_{66} obtained at room temperature is shown in Fig. 6-7. The theoretical curves have been calculated from Eq. (6.20) with $\Gamma = 0$ (dashed line) and $\Gamma \neq 0$ (solid line). The numerical values used are listed in Table 6-2. The piezobirefringence data of Yu and Cardona[92] and Berkowicz and Skettrup[30] are also shown in the figure by filled and open triangles, respectively. The best-fitting broadening energy is determined to be $\Gamma = 68$ meV as shown by solid line. This energy agrees well with that taken into account in the Brillouin-scattering analysis. It is clear from the figure that our data show a quite good agreement with the piezobirefringence data.

Figure 6-8 shows the spectral dependence of the photoelastic constant p_{44} obtained at room temperature. The solid line has been calculated from Eq. (6.25) by taking into account the lifetime-broadening energy of $\Gamma = 68$ meV.

The numerical values used are listed in Table 6-2. The piezobirefringence

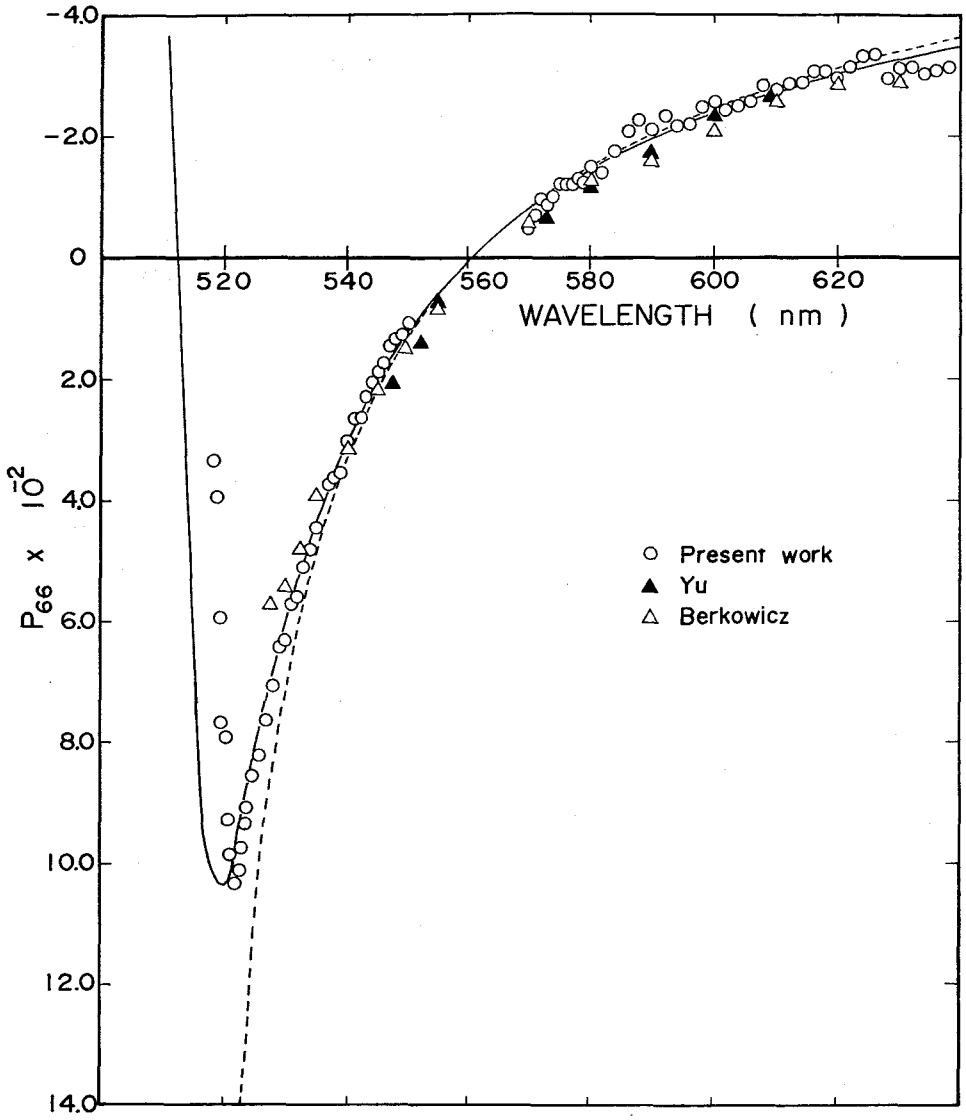

FIG. 6-7. Dispersion of the photoelastic constant p_{66} in CdS (room temperature). The theoretical curves are obtained from Eq. (6.20) with Γ=0 meV (dashed line) and Γ=68 meV (solid line). The piezo-birefringence data of Yu and Cardona (Ref. 92) and Berkowicz and Skettrup (Ref. 30) are also shown by solid and open triangles, respectively.

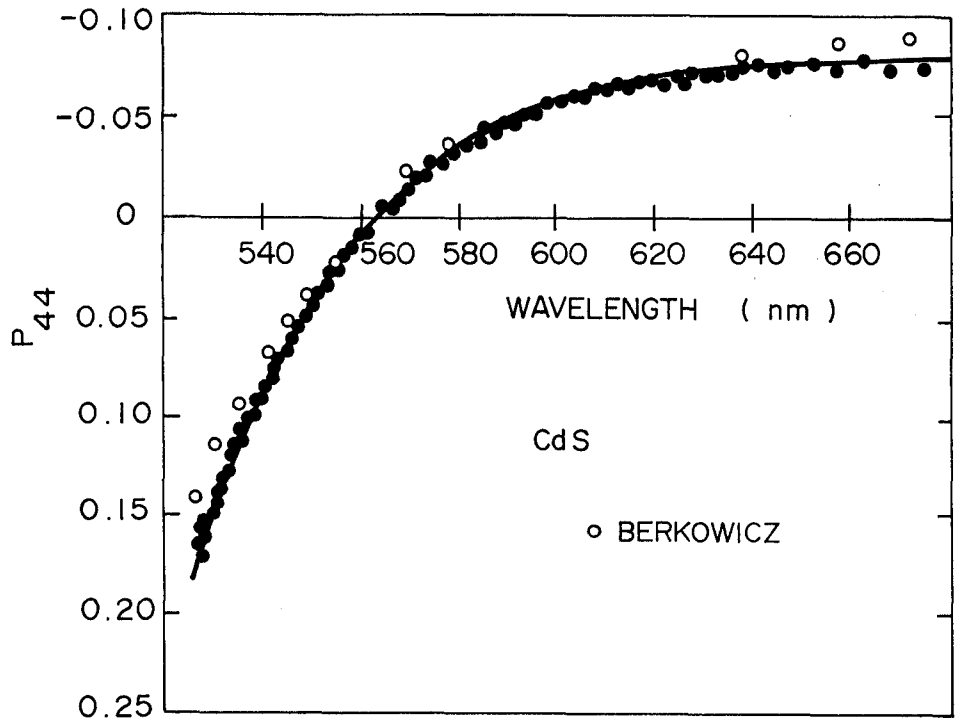

FIG. 6-8. Dispersion of the photoelastic constant p_{44} in CdS (room temperature). The theoretical curve is obtained from Eq. (6.25) by taking into account the lifetime-broadening energy of Γ=68 meV. The piezobirefringence data of Berkowicz and Skettrup (Ref. 30) are also shown by open circles.

Table 6-2. Numerical values used to calculate spectral dependence of the photoelastic constants p_{66}, p_{44} and p_{31} for CdS.

Symbol	Numerical value
E_{gA} (a)	2.452 eV
E_{gB} (a)	2.466 eV
E_{gC} (a)	2.525 eV
F^A_{xx}, F^A_{zz} (b)	0.0131, 0
F^B_{xx}, F^B_{zz} (b)	0.0073, 0.0083
F^C_{xx}, F^C_{zz} (b)	0.0041, 0.0087
G (b)	28 meV
C_2 (c)	-4.5 eV
C_4 (c)	2.9 eV
C_5 (c)	-1.5 eV
C_6 (c)	-2.4 eV

(a) Reference 187.

(b) Reference 80.

(c) Reference 152.

data of Berkowicz and Skettrup[30] are also shown in the figure by open circles. It is well known that the piezoelectrically active (T2-mode) phonon domains produce high longitudinal electric field. This electric field may induce the electro-optic effect of crystals. In such a case, the photoelastic constant [Eq. (6.33b)] is given by [223]

$$p_{44} = p^*_{44} + (p_{44})_{ind} \quad , \qquad (6.34)$$

where p^*_{44} is the Pockels photoelastic constant arising from the elasto-optic effect and $(p_{44})_{ind}$ is the indirect photoelastic constant arising from the electro-optic effect. $(p_{44})_{ind}$ is given by

$$(p_{44})ind = -\frac{e_{15}r_{51}}{\varepsilon_{11}} \quad , \qquad (6.35)$$

where e_{15}, r_{51} and ε_{11} are the piezoelectric, Pockels electro-optic and dielectric constants, respectively. Hamaguchi *et al.*[223] have estimated that the value of $(p_{44})_{ind}$ in CdS is about 18 % of the Pockels photoelastic constant p^*_{44}. In Fig. 6-8, we find a quite good agreement between the present data and piezobirefringence data. This fact suggests that Brillouin scattering is mainly governed by the elasto-optic effect, i.e., it means that in Eq. (6.34) $p_{44} \simeq p^*_{44}$. It is obvious from Figs. 6-7 and 6-8 that the isotropic point occurs at the same wavelengths for both p_{66} and p_{44} within the experimental accuracy. There is nothing in theory which indicates that the isotropic point should be positioned at the same wavelengths for both p_{44} and p_{66}. However, one can expect such a fact on the basis of the quasi-cubic model.[30] When the crystal-field parameter $\Delta_c = 0$ and $(p_{44})_{ind} = 0$, then $p_{66} = p_{44}$. The crystal-field parameter Δ_c for CdS is about 0.027 eV which is thought to be considerably small. From this fact, one should expect the isotropic points to be nearly common to p_{44} and p_{66}.

The spectral dependence of the photoelastic constant p_{31} obtained at

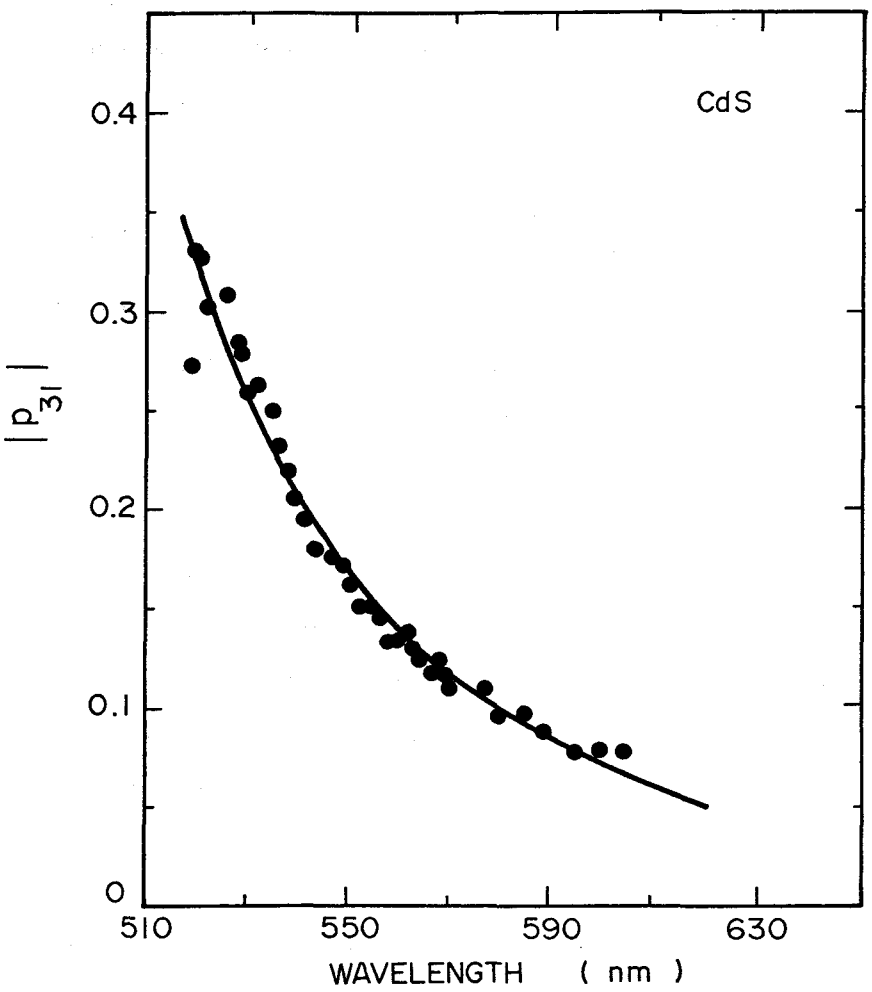

FIG. 6-9. Dispersion of the photoelastic constant p_{31} in CdS (room temperature). The theoretical curve is obtained from Eq. (6.29) by taking into account the lifetime-broadening energy of Γ=68 meV.

room temperature is shown in Fig. 6-9. The solid line has been calculated from Eq. (6.29) by taking into account the lifetime-broadening energy of Γ = 68 meV. Note that the energy derivative term of $\partial\varepsilon^{A}_{zz}/\partial E_{gA}$ does not contribute to p_{31}, because $F^{A}_{zz} = 0$ [see Table 6-2]. Absolute values of this constant are given in the figure; they were determined by normalizing our data to the absolute one measured by Dixon (Dixon-Cohen method)[46] at a light wavelength of 632.8 nm ($|p_{31}| = 0.041$ at this wavelength). Tell *et al.*[222] have also determined the spectral dependence of the off-diagonal photoelastic components p_{12} and p_{31} in the wavelength range of 530 — 630 nm by means of the Raman-Nath method. We found that our data show a quite good agreement with the data of Tell *et al.*

6.4 PIEZOBIREFRINGENCE IN AN OPAQUE REGION

In the previous subsection, we have presented the spectral dependence of the photoelastic constants in various semiconductors in the region below the lowest direct gap determined from the Brillouin-scattering data by introducing the intrinsic-piezobirefringence analysis. We have, however, disregarded the contribution from the imaginary part of the dielectric constant to the photoelastic constant assuming that the contribution is negligibly small compared with that from the real part of the dielectric constant in the photon-energy region of transparency. Recently, Chandrasekhar *et al.*[207] have developed a new method to measure the stress-induced birefringence in an opaque region which employs the Raman-scattering technique as a probe. Using this new method, they have measured the magnitudes of the piezo-optical (photoelastic) constants in Si (0.5 — 3.38 eV)[218] and GaP (1.0 — 2.6 eV)[207] above the fundamental absorption edge. In their analysis, the contribution from the imaginary part of the dielectric constant has also been neglected,

although they have pointed out that its contribution should be taken into account in order to discuss the spectral dependence of the piezo-optical constants in the region above 3.0 eV in Si.

Let us now present here a new method to analyze the piezobirefringence effect in the opaque region of solids, where the stress-induced changes in both the real and imaginary parts of the dielectric constant are properly taken into account by introducing new fractional coefficients.[219] We will apply the present model to the analysis of the experimental data of Si[218] and ZnSe (present work).

6.4.1 Model

The photoelastic constant or piezo-optical constant is exactly related to the difference of refractive indices $(n_{\parallel} - n_{\perp})$ through [see Eqs. (2.208) and (2.209)]

$$\Delta n = n_{\parallel} - n_{\perp} = -\frac{1}{2} n_0^3 (S_{11} - S_{12})(p_{11} - p_{12})X \quad , \qquad (6.36a)$$

$$\Delta n = n_{\parallel} - n_{\perp} = -\frac{1}{2} n_0^3 (\pi_{11} - \pi_{12})X \quad , \qquad (6.36b)$$

for the [001] stress direction, and

$$\Delta n = n_{\parallel} - n_{\perp} = -\frac{1}{2} n_0^3 S_{44} p_{44} X \quad , \qquad (6.37a)$$

$$\Delta n = n_{\parallel} - n_{\perp} = -\frac{1}{2} n_0^3 \pi_{44} X \quad , \qquad (6.37b)$$

for the [110] stress direction. We note here that Eqs. (2.215) and (2.217) are only valid when the optical absorption is small, i.e., $\varepsilon_2 \simeq 0$. The optical constants n and k of Eq. (2.207) are real and positive numbers and can be determined by optical measurements. They are related to the dielectric constant $(\varepsilon = \varepsilon_1 + i\varepsilon_2)$ by the following equations:

$$\varepsilon_1 = n^2 - k^2 \quad , \qquad (6.38a)$$

$$\varepsilon_2 = 2nk \quad . \qquad (6.38b)$$

Resolving these equations in n and k, we obtain

$$n = \left[\frac{(\varepsilon_1^2 + \varepsilon_2^2)^{\frac{1}{2}} + \varepsilon_1}{2} \right]^{\frac{1}{2}} , \qquad (6.39a)$$

$$k = \left[\frac{(\varepsilon_1^2 + \varepsilon_2^2)^{\frac{1}{2}} - \varepsilon_1}{2} \right]^{\frac{1}{2}} . \qquad (6.39b)$$

The change in the refractive index Δn can now be given by (first order in stress)

$$\Delta n = \frac{\partial n}{\partial X} X = \alpha_r(\varepsilon_1, \varepsilon_2) \frac{\partial \varepsilon_1}{\partial X} X + \beta_i(\varepsilon_1, \varepsilon_2) \frac{\partial \varepsilon_2}{\partial X} X$$

$$= \alpha_r(\varepsilon_1, \varepsilon_2) \Delta\varepsilon_1 + \beta_i(\varepsilon_1, \varepsilon_2) \Delta\varepsilon_2 , \qquad (6.40)$$

with

$$\alpha_r = \frac{\partial n}{\partial \varepsilon_1} = \frac{1}{4} \left[\frac{\varepsilon_1 + (\varepsilon_1^2 + \varepsilon_2^2)^{\frac{1}{2}}}{2} \right]^{-\frac{1}{2}} [1 + (\varepsilon_1^2 + \varepsilon_2^2)^{-\frac{1}{2}}\varepsilon_1] , \qquad (6.41a)$$

$$\beta_i = \frac{\partial n}{\partial \varepsilon_2} = \frac{1}{4} \left[\frac{\varepsilon_1 + (\varepsilon_1^2 + \varepsilon_2^2)^{\frac{1}{2}}}{2} \right]^{-\frac{1}{2}} [(\varepsilon_1^2 + \varepsilon_2^2)^{-\frac{1}{2}}\varepsilon_2] . \qquad (6.41b)$$

The first and second terms of Eq. (6.40) are contributions from the stress-induced changes in the real and imaginary parts of the dielectric constant, respectively. The coefficients α_r and β_i are functions of photon energy, and their sign and relative magnitude determine the fractional contributions of $\Delta\varepsilon_1$ and $\Delta\varepsilon_2$ to the piezobirefringence effect.

The change in the real part of the dielectric constant with the applied stress can be given by the expression (2.221). The stress-induced change in the imaginary part of the dielectric constant $\Delta\varepsilon_2$ is also give by replacing ε_1 of Eq. (2.221) by ε_2, i.e.,

$$[\Delta\varepsilon_2(\omega)] = \frac{\partial \varepsilon_2}{\partial X} X = \sum_{i=A,B,C} \left(\frac{\partial \varepsilon_2}{\partial M_i} \Delta M_i + \frac{\partial \varepsilon_2}{\partial \omega_{gi}} \Delta\omega_{gi} \right) . \qquad (6.42)$$

The photoelastic (piezo-optic) constant can be obtained by substituting Eq.

(6.40) into Eq. (6.36) [Eq. (6.37)].

6.4.2 Results and Analysis

First, we consider the contribution from the imaginary part of the dielectric constant to the piezo-optical constant of Si in the region of the E_1 transition ($\sim$ 3.3 eV) where the sample is opaque. Figure 6-10 shows the spectral dependence of the fractional coefficients α_r and β_i for Si, calculated from experimental values of the optical constants reported by Philipp and Ehrenreich.[224] A low-energy region (below 3.0 eV), which contains the fundamental absorption edge, is dominated by α_r. The α_r dominance in this region makes it easy to analyze the piezobirefringence effect using a conventional technique which employs transmission of light through the sample.[64] The fractional coefficient β_i increases at the photon energies above 3.0 eV, and rising β_i and falling α_r produce a crossover at about 4.1 eV. In this region, the piezobirefringence analysis becomes very difficult, because the fractions of the contributions from $\Delta\varepsilon_1$ and $\Delta\varepsilon_2$ should be exactly taken into account. Figure 6-11 shows the changes in the dielectric constants $\Delta\varepsilon_1$ and $\Delta\varepsilon_2$ as a function of photon energy. In order to calculate $\Delta\varepsilon_1$ and $\Delta\varepsilon_2$, we have used the following approximations:

$$\Delta\varepsilon_1 = \frac{\partial\varepsilon_1}{\partial X} X \simeq \frac{\partial\varepsilon_1}{\partial E_g} \Delta E_g \simeq - \frac{\partial\varepsilon_1}{\partial E} \Delta E_g \quad , \qquad (6.43a)$$

$$\Delta\varepsilon_2 = \frac{\partial\varepsilon_2}{\partial X} X \simeq \frac{\partial\varepsilon_2}{\partial E_g} \Delta E_g \simeq - \frac{\partial\varepsilon_2}{\partial E} \Delta E_g \quad , \qquad (6.43b)$$

where E_g is the E_1-gap energy and E is the photon energy. We have calculated $\Delta\varepsilon_1$ and $\Delta\varepsilon_2$ by numerically differentiating the experimental data of Philipp and Ehrenreich.[224] The obtained results are shown in Fig. 6-11 by solid ($\Delta\varepsilon_1$) and dashed line ($\Delta\varepsilon_2$). The changes in the dielectric properties under strain have also been calculated by Tsay *et al.*[225] in terms of a full band-structure approach to estimate the Brillouin-scattering efficiencies of Ge and Si.

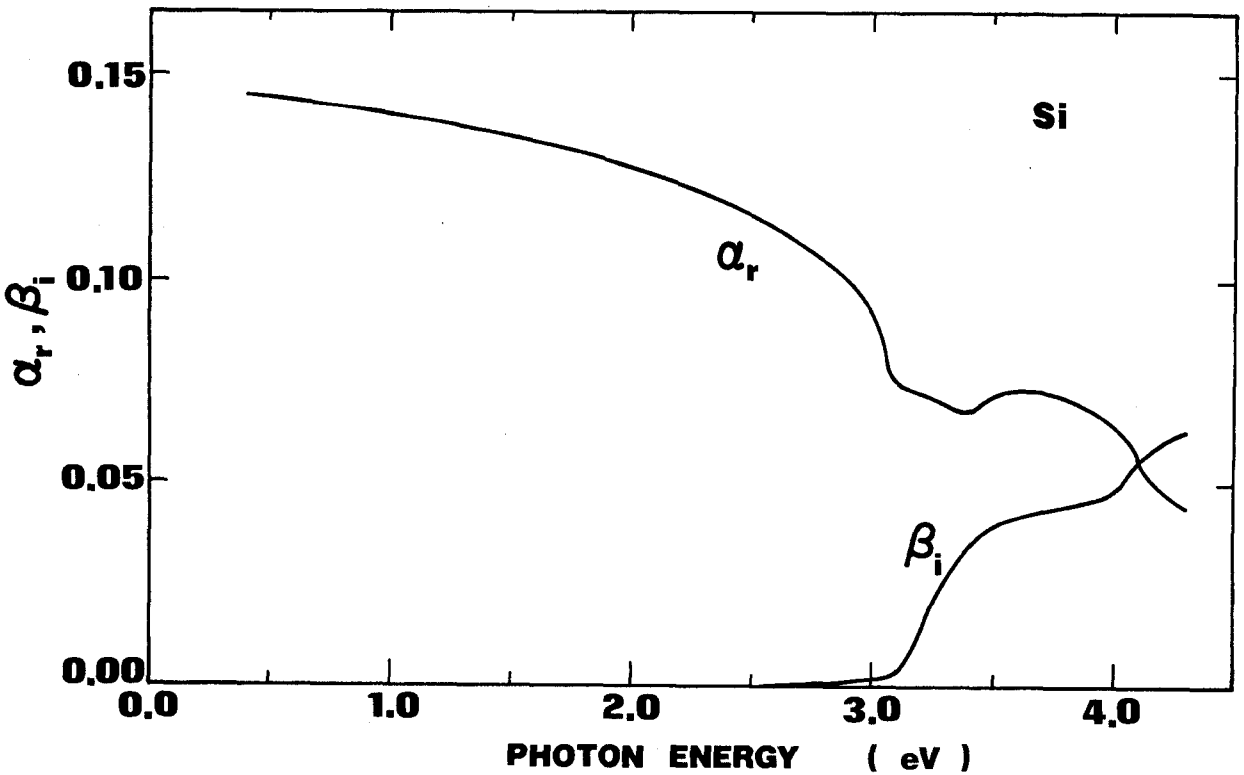

FIG.6-10. Fractional coefficients α_r and β_i in Eq. (6.40) for Si.

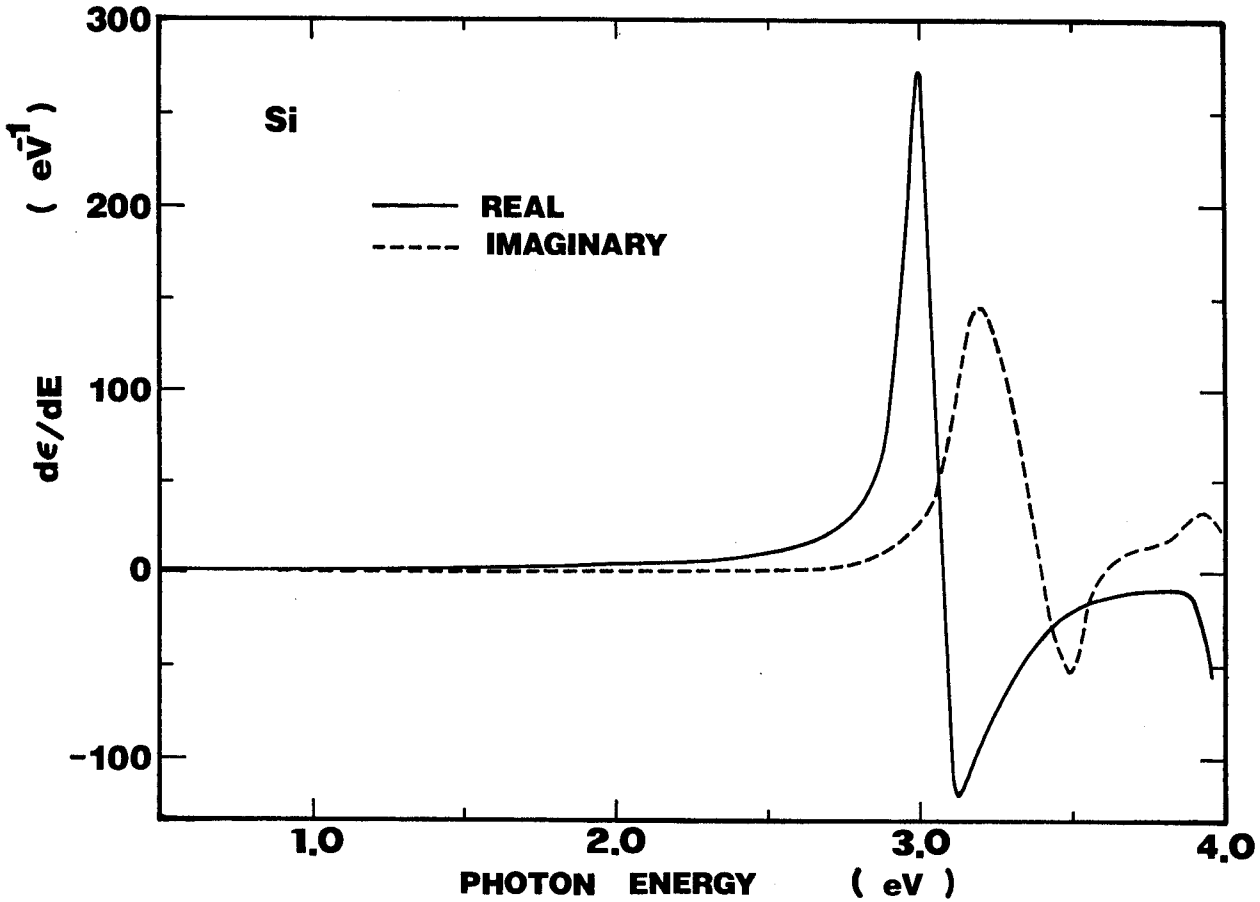

FIG. 6-11. Stress-induced changes in the real $\Delta\varepsilon_1$ (solid line) and imaginary part $\Delta\varepsilon_2$ (dashed line) of the dielectric constant for Si. The curves are obtained by numerically differentiating the experimental data of Philipp and Ehrenreich (Ref. 224).

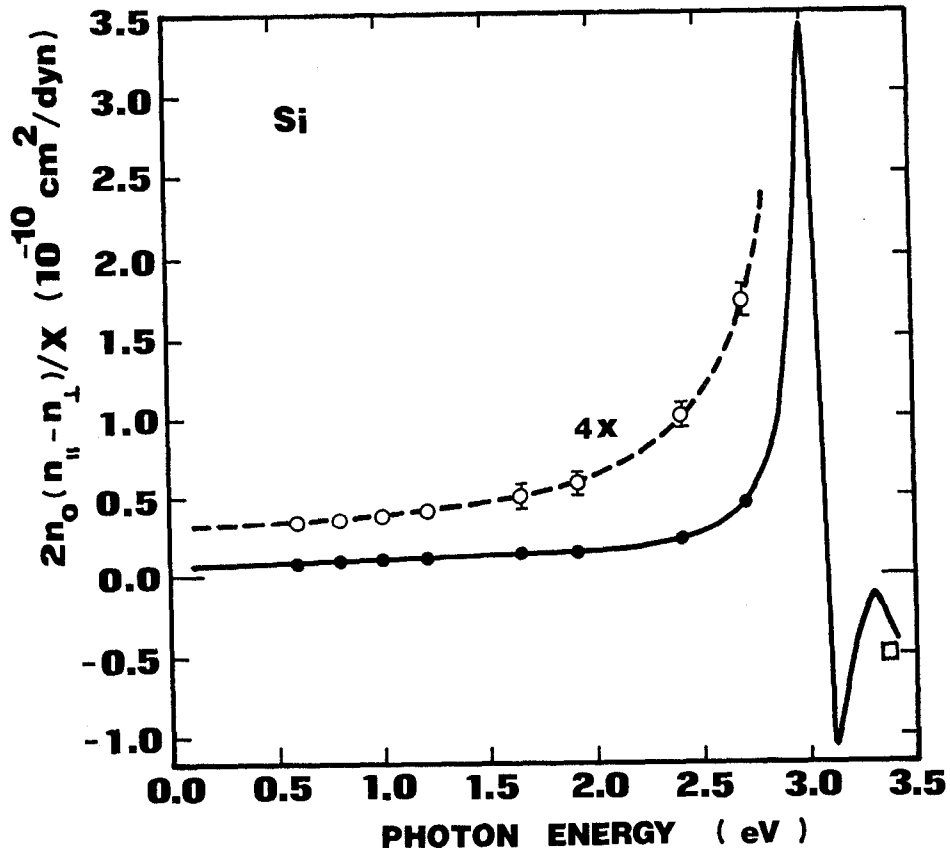

FIG. 6-12. Theoretical dispersion of the piezo-optical constant for Si calculated from Eq. (6.40). The experimental data are obtained from Ref. 218. The filled (solid) circles are plotted on the scale incicated in the figure, while the open circles are replots of the same values on an expanded (4×) scale and the open square is plot of the data at E=3.38 eV on a reduced (1/10 ×) scale.

Now, we compare our theoretical model with the data of S_i.[218] Figure 6-12 shows the theoretical curve calculated from Eq. (6.40) along with the experimental data [Fig. 7 of Ref. 218]. The filled circles are plotted on the scale indicated in the figure, while the open circles are replots of the same values on an expanded scale (4×). The theoretical curve was calculated using the fractional coefficients and the changes in the dielectric constant given in Figs. 6-10 and 6-11, respectively. The data below 1.5 eV are obtained from Ref. 64 (conventional method) and those above 1.5 eV from Ref. 218 (new method). It is evident from Fig. 6-12 that the experiment and calculation are in quite good agreement.

Chandrasekhar *et al.*[218] have also reported the experimental value at E = 3.38 eV, where it is plotted on a reduced scale ($\frac{1}{10}$×). Due to the lack of points at intermediate photon energies they have not been able to infer the sign of the effect at E = 3.38 eV. They have suggested that in the photon-energy region close to the critical point real transitions occur and the exact linewidth, including the imaginary part of the stress-induced dielectric constant, is required for an accurate description of the piezo-birefringence phenomena. By virtue of the present model, we can estimate the sign of the data at E = 3.38 eV to be negative because the signs of α_r and β_i are positive in this photon-energy region but those of $\Delta\varepsilon_1$ and $\Delta\varepsilon_2$ are negative.

Next, we consider the contribution from the imaginary part of the dielectric constant to the piezobirefringence coefficient in ZnSe determined from the Brillouin-scattering measurements. Figure 6-13 shows the spectral dependence of the fractional coefficients α_r and β_i for ZnSe, calculated from experimental values of the optical constants reported by Aven *et al.*[190] The stress-induced changes in the dielectric constant $\Delta\varepsilon_1$ and $\Delta\varepsilon_2$ as a function of wavelength for the case of the [001] stress direction are shown in Fig. 6-14 by solid ($\Delta\varepsilon_1$)

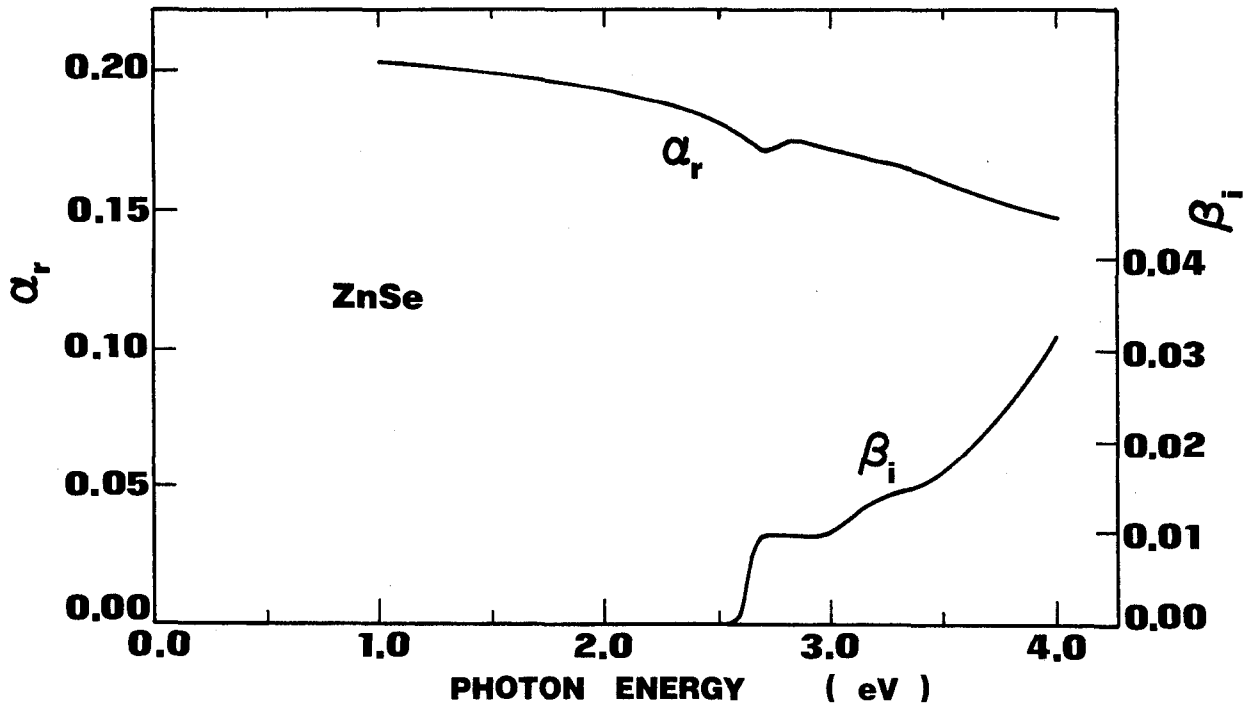

FIG. 6-13. Fractional coefficients α_r and β_i in Eq. (6.40) for ZnSe.

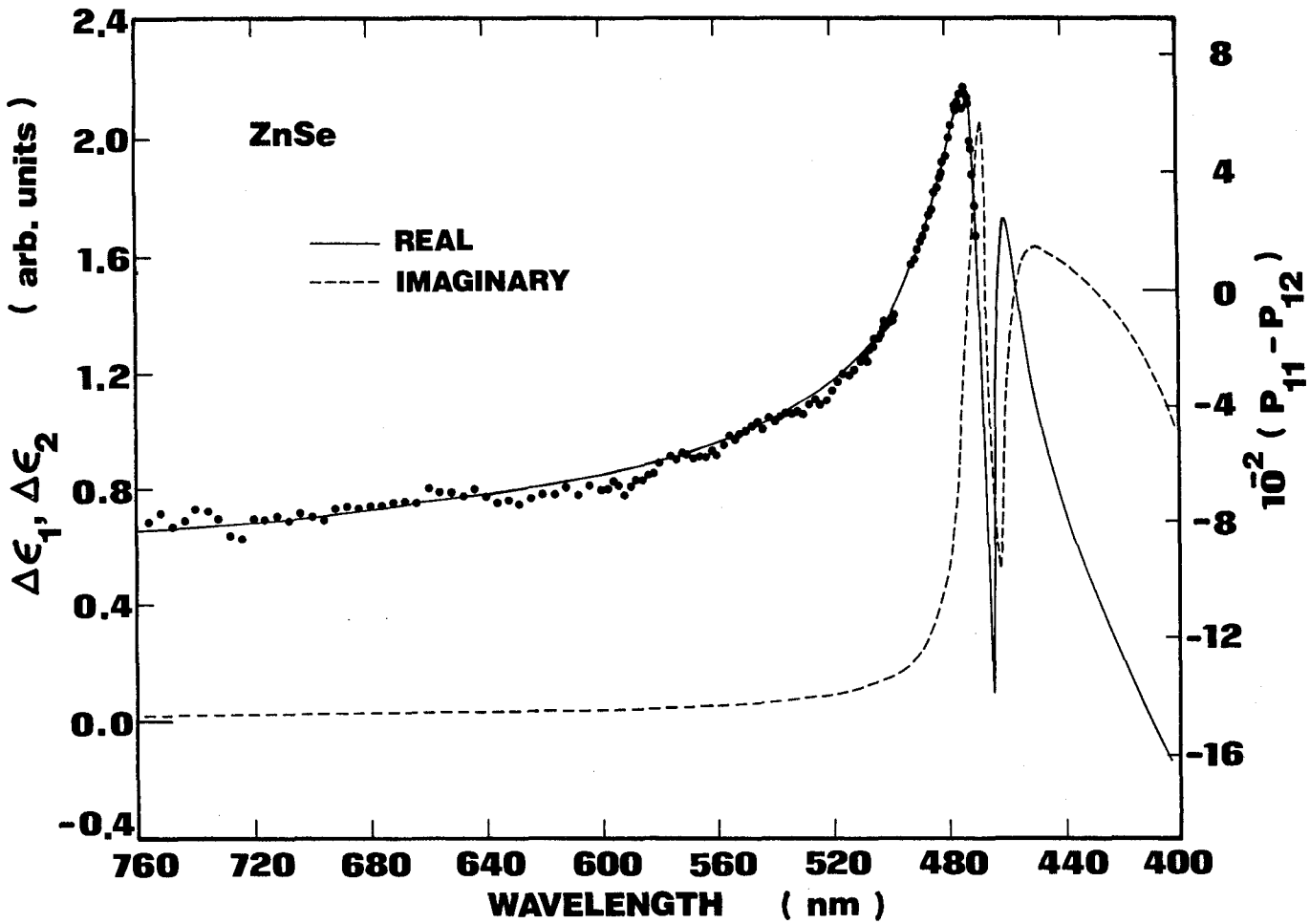

FIG. 6-14. Stress-induced changes in the real $\Delta\varepsilon_1$ (solid line) and imaginary part $\Delta\varepsilon_2$ (dashed line) of the dielectric constant for ZnSe along with the experimental data of the photoelastic constant $p_{11} - p_{12}$ (see text).

and dashed line ($\Delta\varepsilon_2$). In the calculations, we have replaced ω of Eq. (2.221) by $\omega + i(\Gamma/\hbar)$ and calculated real and imaginary parts of this equation. It is important to point out that the change in the imaginary part ($\Delta\varepsilon_2$) has considerably large value in the region very close to the fundamental absorption edge (2.68 eV ≃ 463 nm). However, the fractional coefficient β_i is very small, compared with α_r, in the photon-energy region. It is clear from this fact that the contribution from the imaginary part of the dielectric constant to the piezobirefringence effect is much smaller than that from the real part of the dielectric constant, and therefore we can disregard the imaginary-part contribution in the region below and near the lowest direct gap in a good approximation. From these considerations, the photoelastic constant $p_{11} - p_{12}$ becomes proportional to $\alpha_r \Delta\varepsilon_1$ [see Eqs. (6.36a) and (6.40)]. We have, therefore, fitted our experimental data of $p_{11} - p_{12}$ to the calculated curve (solid line) by taking into account the constant term which arises from the higher-gap contributions (E_1, $E_1+\Delta_1$ and E_2 transitions), where we have assumed that α_r is nondispersive in the measured wavelength region [see Fig. 6-13]. It is clear from the figure that the calculated curve shows an excellent agreement with the experimental data. From these discussions, we conclude that the photoelastic constants in the region of transparency can be safely determined only by the stress-induced change in the real part of the dielectric constant, and therefore our previous results (Section 6.3) can be used without any modification.

It can be found from Figs. 6-10 and 6-13 that the spectral dependence of the fractional coefficients α_r and β_i is very similar to that of the modulation spectroscopy proposed by Seraphin and Bottka (Seraphin coefficients).[226] The Seraphin coefficients, which are obtained by differentiating Frenel's formula, are functions of photon energy, and their sign and relative magnitude determine the fractional contributions of $\Delta\varepsilon_1$ and $\Delta\varepsilon_2$ to the modulation spectro-

scopy. In Chapter VIII, we will survey a relation between resonant Brillouin scattering (piezobirefringence) and the first-derivative modulation spectroscopy such as thermoreflectance, piezoreflectance and wavelength-derivative spectroscopy, and will compare the experimental Brillouin spectra with the first-derivative modulation spectra obtained in some semiconductors. The results will clearly suggest a close relationship between them.

Finally, we have obtained a generalized expression of the piezobirefringence effect by taking into account both the stress-induced changes in the real ($\Delta\varepsilon_1$) and imaginary part ($\Delta\varepsilon_2$) of the dielectric constant. The coefficients α_r and β_i, which are functions of photon energy, have been calculated from an analytical point of view. Such coefficients determine the fractional contributions of $\Delta\varepsilon_1$ and $\Delta\varepsilon_2$ to the piezobirefringence response. The present model has been demonstrated for Si and ZnSe in the photon-energy regions of opaque (E_1 edge) and of transparency (E_0 edge), respectively. Good agreement between the experiment and calculation has been found. When the present method is adopted, it is possible to extend the piezobirefringence analysis in a large number of opaque materials.

CHAPTER VII

EFFECT OF LIFETIME BROADENING ON RESONANT BRILLOUIN SCATTERING IN ZnSe AND ZnTe

7.1 INTRODUCTION

The purpose of this Chapter is to report some effects of the lifetime broadening on resonant Brillouin scattering. It is well known from the earlier work that the excitons play an important role on the optical properties, at least at low temperatures, in the spectral region of the fundamental absorption edge.[69] The investigations were mainly concerned with the energy states of the excitons which were found to be of the Wannier-Mott type [see Section 2.2.2]. From numerous investigations, it is known that in semiconductors the optical spectra near the fundamental absorption edge are strongly influenced by exciton-phonon or electron-phonon interactions. Below the edge, this interaction determines the line shape of the exciton spectrum. Furthermore, the interaction of electrons and excitons with phonons may cause additional structures near the edge. Toyozawa[227] suggested that when the exciton-phonon coupling is weak and the exciton effective mass is small, the exciton absorption band is of a Lorentzian shape, provided that the temperature T is not too high. The half-value width (broadening) was given by the level broadening of the optically produced exciton due to phonon scattering, so that it was proportional to T except at low temperatures. He also obtained that if the coupling is strong, or the exciton effective

mass is large, or the temperature is very high, the absorption band is expected to be of a Gaussian shape and the half-value width is proportional to $T^{\frac{1}{2}}$. The optical properties of various interacting exciton-phonon systems have been explained within the framework of the Toyozawa's theory.

In this Chapter, we report on a study of the lifetime-broadening (referred to as *damping* hereafter) effect of the intermediate electronic states on resonant Brillouin scattering in ZnTe and ZnSe. The light-scattering efficiency derived by Loudon[35] contains various band parameters. The optical absorption spectra are also specified by these parameters. Indeed, Pine[11] has discussed a relationship between the Brillouin-scattering cross section and absorption, and tried to explain the resonant-Brillouin data (Brillouin scattering by thermal LA phonons in CdS) from this aspect. The optical-absorption data reveal that samples of ZnSe, as in other II-VI compounds,[185,228] should be selected and prepared carefully in order to minimize extrinsic absorption arising from native or foreign defects. It is well known that optical spectra in semiconductors are affected strongly by the damping (*e.g.*, absorption, reflection and emission of the exciton lines).[43,44,153,176,177] Such a damping can be represented by a sum of the temperature dependent and independent parts;[153] the former arises from the thermal vibrations of the lattice and the later from the crystalline imperfections. From the analyses of the optical spectra,[153,176,177] it was found that the value of the damping energy increases with increasing the lattice temperature. This fact easily suggests an importance of the temperature-dependent part (i.e., the damping induced by lattice vibrations) in the damping process. From these facts, it is expected that the Brillouin-scattering cross section is also affected by the damping effect of the intermediate electronic states. This is the motivation of the present study.

In order to investigate the temperature dependence of the damping energy,

we have measured resonant Brillouin scattering at room temperature and low temperature (77 K). Moreover, we have used two kinds of ZnTe and ZnSe single crystals to study some effects of the crystalline imperfections on the spectral dependence of the Brillouin-scattering cross sections.[229] For ZnTe, one is the single crystal grown by the conventional melt-grown method and the other is that grown by the traveling heater method (THM, see Appendix). ZnTe has a high melting point (∿ 1298°C),[230] and is usually prepared from non-stoichiometric melts or by vapor phase transport method. The high-temperature growth from non-stoichiometric melt is, in general, suffered from a contamination from silica. The crystals grown from the vapor phase, on the other hand, often contain numerous dislocations and inclusions. In contrast to the above methods, the THM belongs to the solution growth and is suitable for the growth of perfect crystals.[231,232] Two kinds of samples for ZnSe were prepared; one is the as-grown sample grown by a melt-growth technique and the other is that purified in liquid Zn.[98] We made this purification at 1000°C for about 30 hours, where the crystals were sealed in evaquated quartz tube with Zn metal (6N grade). The Zn-purification is known to be efffective particularly in removing Zn vacancies and noble-metal impurities such as Cu and Ag. The ability of this purification technique was already manifested from optical and electrical properties of the purified crystals.[98,185,233-235]

The results obtained here have shown that the damping of the intermediate electronic states does not depend on the temperatures but strongly on the crystalline imperfections. The damping energy of high-quality ZnTe (ZnSe) determined from resonant Brillouin scattering is Γ = 26 meV (44 meV) at 77 K, which is very large compared with the value of $\Gamma \simeq 2$ meV (3 meV) obtained from reflectance spectrum.[236] We propose here for the explanation of this difference the domain-induced damping of the intermediate electronic states arising from an interaction of the states with the high-intensity acoustical

phonon domains.

7.2 LIFETIME-BROADENING EFFECT

When the frequency of radiation approaches one of the resonance frequencies of a solid, we must take into account the finite lifetime of the excited states. The finite lifetime of the states is a consequence of the spontaneous transition of the quantum system from higher states to lower ones. A calculation of the optical process, *e.g.* electric susceptivility, based on a fully quantum-mechanical theory may automatically include spontaneous-transition effects. However, a good approximation to the rigorous result can be obtained in a comparatively simple way by a phenomenological inclusion of spontaneous-transition damping in the theory, i.e., by replacing

$$\omega \rightarrow \omega + i\frac{\Gamma}{2\hbar} \quad , \tag{7.1}$$

where ω is the frequency of radiation and Γ is the phenomenological damping energy [see, *e.g.*, Eq. (2.55)]. The probability that the quantum system at the time t is still in the excited state is given by

$$W(t) = [\exp -(\Gamma t/\hbar)] \quad . \tag{7.2}$$

The quantity $T_0 = \hbar\Gamma^{-1}$ is called the lifetime of the excited state. This quantity determines the broadening of the resonance energy according to the well known uncertainty relation:

$$\Delta E \cdot T_0 \simeq \hbar \quad . \tag{7.3}$$

Equation (7.3) follows that the resonance energy is broadened by an amount $\Delta E \simeq \frac{\hbar}{T_0} = \Gamma$.

At very low temperatures, the line shape of absorption and emission of the excitons results from interactions with acoustical phonons. But, because of the relatively strong coupling to the LO phonons, one would expect this

coupling to influence the exciton line width at moderately low temperatures.[237] The thermal-broadening mechanism is represented schematically in Fig. 7-1. The discrete-exciton bands are depicted by the solid parabolas and the hatched area is for the continuum-exciton bands. The dotted curves represent the dispersion curves for the low-lying polariton modes. The lifetime broadening is a consequence of the scattering of an exciton (excited electronic state) associated with the annihilation of a phonon of wave vector $\vec{q}$ and energy $\hbar\omega_q$. All energetically accessible states are permissible final states.

In general, the damping energy can be expressed by a sum of three independent contributions:[153]

$$\Gamma(T) = \Gamma_0 + \Gamma_{ac}(T) + \Gamma_{LO}(T) \quad . \tag{7.4}$$

In Eq. (7.4), Γ_0 is an independent part of temperature T arising from the foreign and/or native defects, $\Gamma_{ac}(T)$ is a contribution from acoustical phonons, proportional to the occupation number of acoustical phonons (proportional to T for the thermal phonons), and $\Gamma_{LO}(T)$ is a contribution from LO phonons given gy

$$\Gamma_{LO}(T) = \frac{A}{[\ \exp\ (\hbar\omega_{LO}/k_B T) - 1\ ]} \quad , \tag{7.5}$$

where A is a constant taken to be independent of temperature and $\hbar\omega_{LO}$ is the LO phonon energy. The damping energy $\Gamma(T)$, thus, always decreases as the temperature is lowered because of the temperature-dependent parts of $\Gamma_{ac}(T)$ and $\Gamma_{LO}(T)$. An information about the shape of the exciton peak can be obtained by emission, absorption and reflectance measurements. A series of such studies has been carried out on ZnSe,[236] ZnTe,[236] CdTe[236] and CdS[176] for temperatures from about 2 K up to those where the exciton induced structure disappears. Figure 7-2 shows the experimentally determined widths of the ground-state (n = 1) exciton lines for ZnTe and

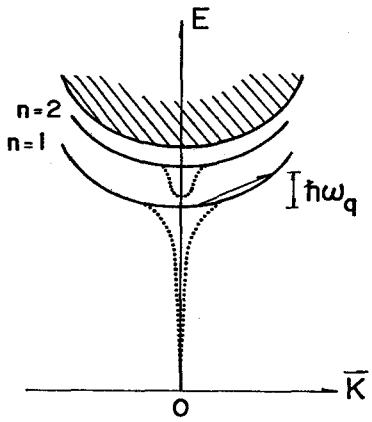

FIG. 7-1. Thermal-broadening mechanism. The discrete-exciton bands are depicted by the solid parabolas and the hatched area is for the continuum-exciton bands. The dotted curves represent the dispersion curves for the low-lying polariton modes. The lifetime broadening is a consequence of the scattering of an exciton associated with the annihilation of a phonon of energy $\hbar\omega_q$.

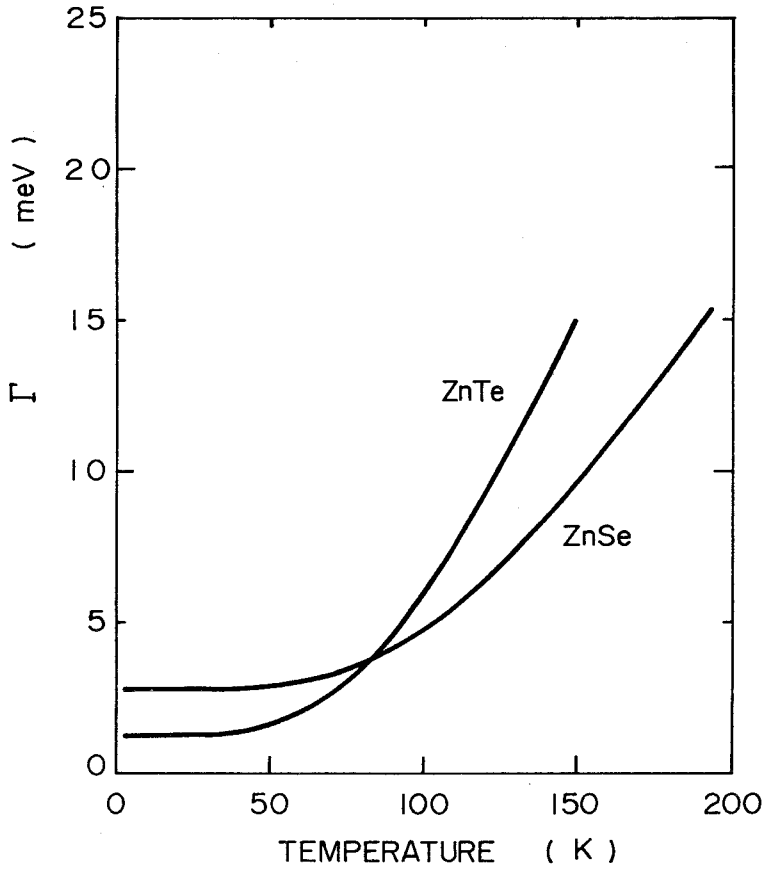

FIG. 7-2. Damping (lifetime-broadening) energy of the ground-state (n = 1) exciton lines for ZnTe and ZnSe as a function of temperature.

ZnSe as a function of temperature T.[236] The line widths are obtained from the reflectance data by introducing the Kramers-Kronig analysis for a range of temperatures. The widths of these curves as a function of temperature exhibit the same behavior, namely a relatively constant value (Γ_0) from low T up to T ≃ 60 K (ZnTe) or to 80 K (ZnSe) at which temperature the contribution $\Gamma_{LO}(T)$ becomes discernable. Gutsche and Voigt[176] have also obtained a similar result regarding the width for the n = 1 peak of the B exciton of CdS on the basis of direct absorption measurements on thin as-grown platelets.

7.3 EXPERIMENTAL RESULTS AND DISCUSSION

7.3.1 Heat-Treatment Effect

Aven and Woodbury[98] have reported a method of the purification of II-VI compounds by firing treatment in molten group-II metals, and obtained segregation coefficients by a radioactive tracer technique using isotopes Cu^{64} and Ag^{110}. Since then, this method has been frequently used in order to eliminate impurities and to reduce resistivities of the semiconductors.[238-241] This method consists in heating the crystals to be purified in contact with a molten metal in which the particular impurity to be extracted is readily soluble: the logical choice for the solvent metal being Zn for ZnSe, ZnTe and ZnS, and Cd for CdS.

It is the purpose of this subject to clarify purification effects in ZnSe by the heat treatment in molten Zn by using the photoluminescence technique.[242] ZnSe single crystals used were grown by the melt-growth technique. They were not intentionally doped with impurities, but contained copper residue impurity of less than 10 ppm. Prior to the heat treatment in molten Zn, ZnSe single crystals were mechanically and chemically polished

along the (110) crystal plane and etched at room temperature in a mixture of 1 part HCl and 1 part HNO_3. The heat-treated samples were once more polished and etched slightly in the same manner mentioned above. A Hg lamp with a Toshiba UV-D1A filter was used as a exciting light source for the photoluminescence measurements. The emission spectra were obtained with a modified Shimazu UV-200 monochromator and a Hamamatsu TV R-136 photomultiplier tube.

Figure 7-3 shows the photoluminescence spectra of the as-grown sample (dashed line) and the same sample heat-treated in molten Zn (solid line) measured at 77 K. The as-grown sample shows a broad emission band and a weak edge emission. The broad emission band is thought to be a result of the overlapping of three individual characteristic emission bands; Cu-G, Cu-R and SAL. Stringfellow and Bube[243] described the copper emission bands by a multivalent-copper-impurity model in which Cu^{+2} and Cu^{+} ions substituting for Zn site in ZnSe were responsible for the green and red emission bands. The Cu-G (green) and Cu-R (red) emission bands correspond to these copper-multivalent-luminescence bands.[244-246] The heat-treated sample gives a strong edge emission and a yellow-orange emission band known to as the self activated luminescence (SAL)[247-249] peaking at about 590 nm. The SAL center is essentially an associated center of an impurity-vacancy pair which consists of a Zn vacancy and a halogen atom substituting for an adjacent Se site. The nature of the SAL center has been successfully explained in terms of a localized molecular model and the one-dimensional configurational coordinate model.[247] It is interesting to point out that the Cu-G and Cu-R emission bands disappear by the heat treatment of ZnSe in molten Zn. The disappearance of these emission bands is thought to be caused by the effect of the Zn-extraction. Recently, Yamaguchi and Shigematsu [235] have carried out similar measurements to clarify effects of the copper

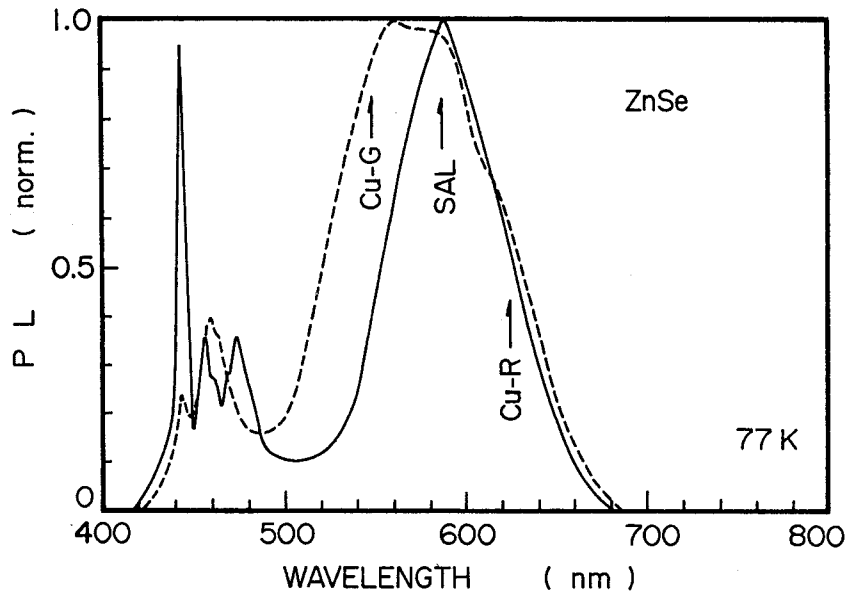

FIG. 7-3. Photoluminescence spectra of the as-grown ZnSe (dashed line) and the same sample heat-treated in molten Zn (solid line) measured at 77 K.

residual impurity from luminescence properties of ZnSe, and to clarify purification effect of this material by the heat treatment in molten Zn. They have concluded that the heat treatment in molten Zn can effectively remove the copper residual impurity from ZnSe.

Figure 7-4 shows the edge emission spectrum of the heat-treated ZnSe at 77 K. It is well known that the noble-metal impurities such as Cu and Ag suppress near-band-edge emission. In fact, our as-grown sample does not show any clear edge-emission structure, as shown in Fig. 7-3. The near-edge emission spectrum of Fig. 7-4 exhibits the series of 5 lines located just to the long-wavelength side of the absorption edge (441.6 nm);

I : 444 nm (2.793 eV)

A_0 : 458 nm (2.707 eV)

A_1 : 463 nm (2.678 eV)

A_2 : 469 nm (2.644 eV)

B : 476 nm (2.605 eV) .

The sharp emission line I is located at 2.793 eV (444 nm). This value is close to that determined by Hite *et al.*[185] from reflectance measurements and therefore corresponds to the annihiration of the discrete exciton (n = 1).[250] The A series and B line are thought to be due to free electron-acceptor (or donor-acceptor) pair transitions. The separation energy between A-series lines is approximately 0.03 eV which is in good agreement with the LO phonon energy reported in the literature.[251,252] The A-series lines, thus, result from the LO phonon interactions (LO-phonon replica).

In addition, we have fabricated light-emitting MS (metal-semiconductor) diodes from the heat-treated ZnSe single crystals with gold-Schottky and indium-ohmic contacts. The as-grown ZnSe crystals usually show very high resistivity — normally $10^7 \sim 10^9$ Ω-cm at room temperature — probably due to residual-impurity defects and Zn vacancies produced during crystal growth.

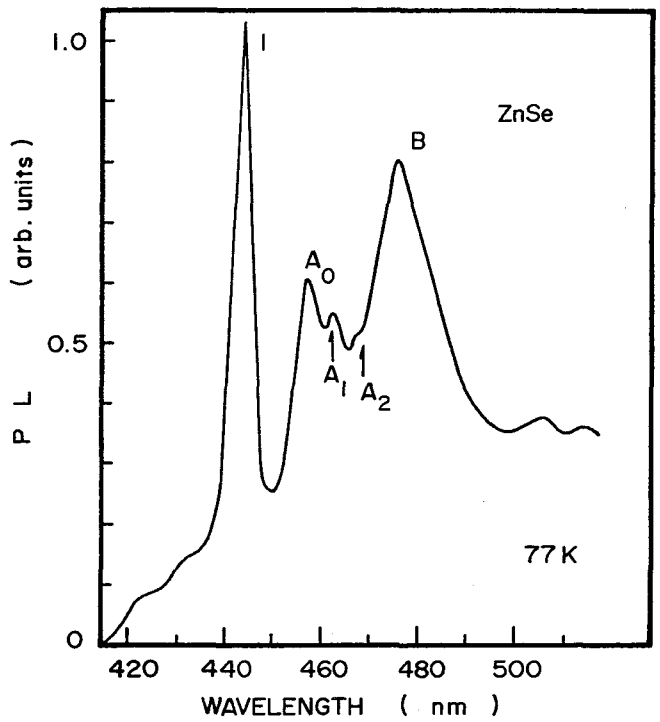

FIG. 7-4. Edge emission spectrum of the heat-treated ZnSe measured at 77 K.

The Zn-extraction allows us this semiconductor with about 1 Ω-cm n-type resistivity and a room temperature electron mobility of about 500 $cm^2/V\cdot sec$ which is believed to be close to the intrinsic mobility for this semiconductor. Figure 7-5 shows the electroluminescence (EL) spectra from the forward and reverse biased MS diodes at 77 K. In the forward bias (solid line), the diode exhibits an EL spectrum very similar to the photoluminescence spectrum shown in Fig. 7-3. The spectrum clearly exhibits a blue emission band consisting of two peaks at 444 and 458 nm and a deep emission band SAL peaking at about 590 nm. In the reverse bias (dashed line), on the other hand, the diode exhibits only a broad emission band. This notable difference in the emission spectra suggests that the emission mechanism in the forward bias is thought to be due to a minority carrier (hole) injection from gold contact into ZnSe substrate,[253,254] and that in the reverse bias is thought to be due to an impact-ionization excitation. The threshold voltages for the EL emission are found to be about 2.0 and 20 eV in the forward and reverse biases, respectively. This fact satisfactorily supports the emission mechanisms stated above. A similar difference in the emission mechanisms between forward- and reverse-biased gold-ZnSe diodes has also been reported by Bouley *et al.*[254] They have observed a blue emission (462 nm) similar to that seen in their photoluminescence spectrum from a forward-biased diode, while observed a broad emission band from a reverse-biased diode which differs quitely from the photoluminescence spectrum.

It is concluded from such drastic changes in the optical and electrical properties of the heat-treated samples that the treatment in molten Zn can effectively remove a wide spectrum of metallic impurities and lattice defects such as Zn vacancies from this semiconductor. The high purity of ZnSe crystals can, thus, be obtained by treating the Zn-extraction technique.

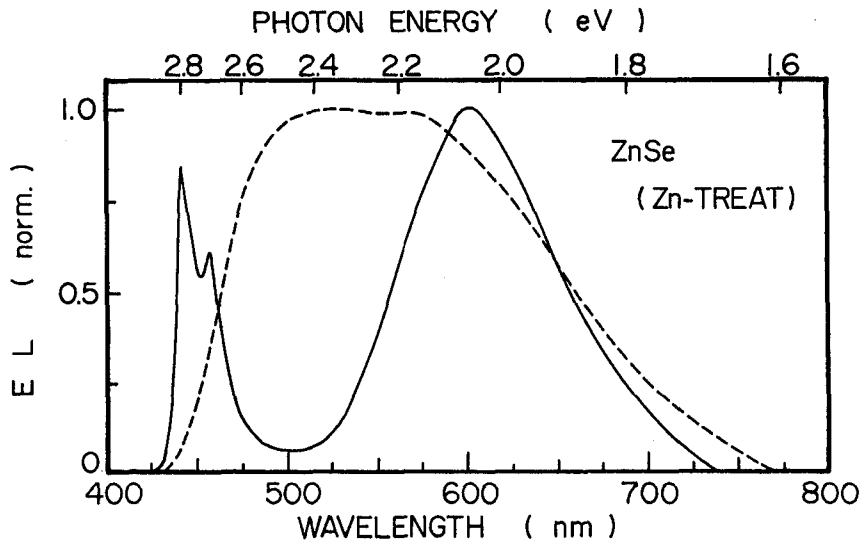

FIG. 7-5. Electroluminescence spectra from the forward and reverse biased MS diodes [heat-treated ZnSe] measured at 77 K. Forward bias: solid line; reverse bias: dashed line.

7.3.2 *Resonant Brillouin Scattering*

Next, we discuss some effects of the crystalline imperfections and temperatures on the spectral dependence of the Brillouin-scattering cross sections. Figure 7-6 shows resonance behaviors of the Brillouin-scattering cross sections in ZnTe for 0.2 GHz fast-TA (T2-mode) phonon domains measured at room temperature [filled triangles (melt-grown crystal) and open circles (THM crystals)] and 77 K [filled circles (THM crystals)]. The vertical arrows in the figure indicate the positions of wavelength corresponding to the band-gap energies (E_g at room temperature and 77 K). The resonant cancellation observed here occurs at 569 and 545 nm at room temperature and 77 K, respectively. One finds in Fig. 7-6 that the resonant enhancement for the crystal grown by the THM is stronger than that for the crystal grown from the melt. In addition, one finds that the resonant enhancement for the THM crystal increases with decreasing the temperature from room temperature to 77 K, which seems to be coincide with that the intrinsic absorption edge becomes sharper at lower temperatures.

The theoretical curves of the Brillouin-scattering cross sections, calculated from Eqs. (2.25) and (2.55) by taking into account the various damping energies, are shown in Fig. 7-6. They are fitted to the experimental data at the corresponding cancellation points by adjusting multiplicative constants (i.e., vertical shifts in the log-plot of this figure). The numerical values used to calculate the resonant-Brillouin term R_{is} are listed in Table 4-3. The best-fitting values of the damping energy are determined to be Γ = 60 meV for the melt-grown crystal (room temperature), Γ = 30 meV for the THM crystal (room temperature) and Γ = 26 meV for the THM crystal (77 K).

In order to make these resonance features clear, we show in Fig. 7-7 the line shapes of the resonant-Brillouin term R_{is} in the region near the fundamental absorption edge along with the experimental data. The data points

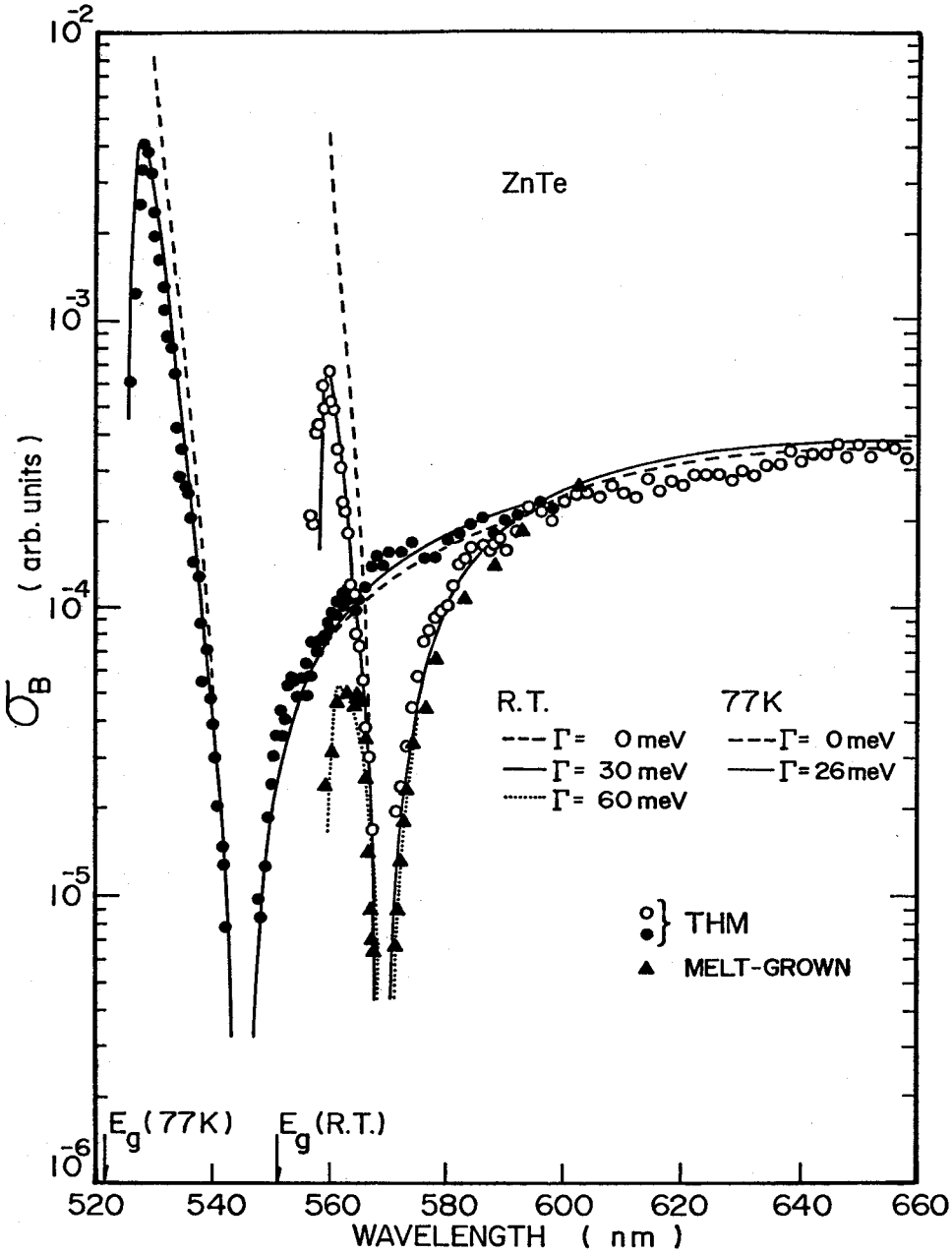

FIG. 7-6. Dispersion of the Brillouin-scattering cross sections in ZnTe by 0.2 GHz fast-TA phonon domains measured at room temperature [filled triangles (melt-grown crystal) and open circles (THM crystal)] and at 77 K [filled circles (THM crystal)]. The theoretical curves are calculated from Eq. (2.55) with Γ=0 meV (dashed lines: room temperature and 77 K), Γ=30 meV (solid line: room temperature), Γ=60 meV (dotted line: room temperature) and Γ=26 meV (solid line: 77 K). The vertical arrows indicate the position of wavelengths corresponding to the band-gap energies at room temperature and 77 K.

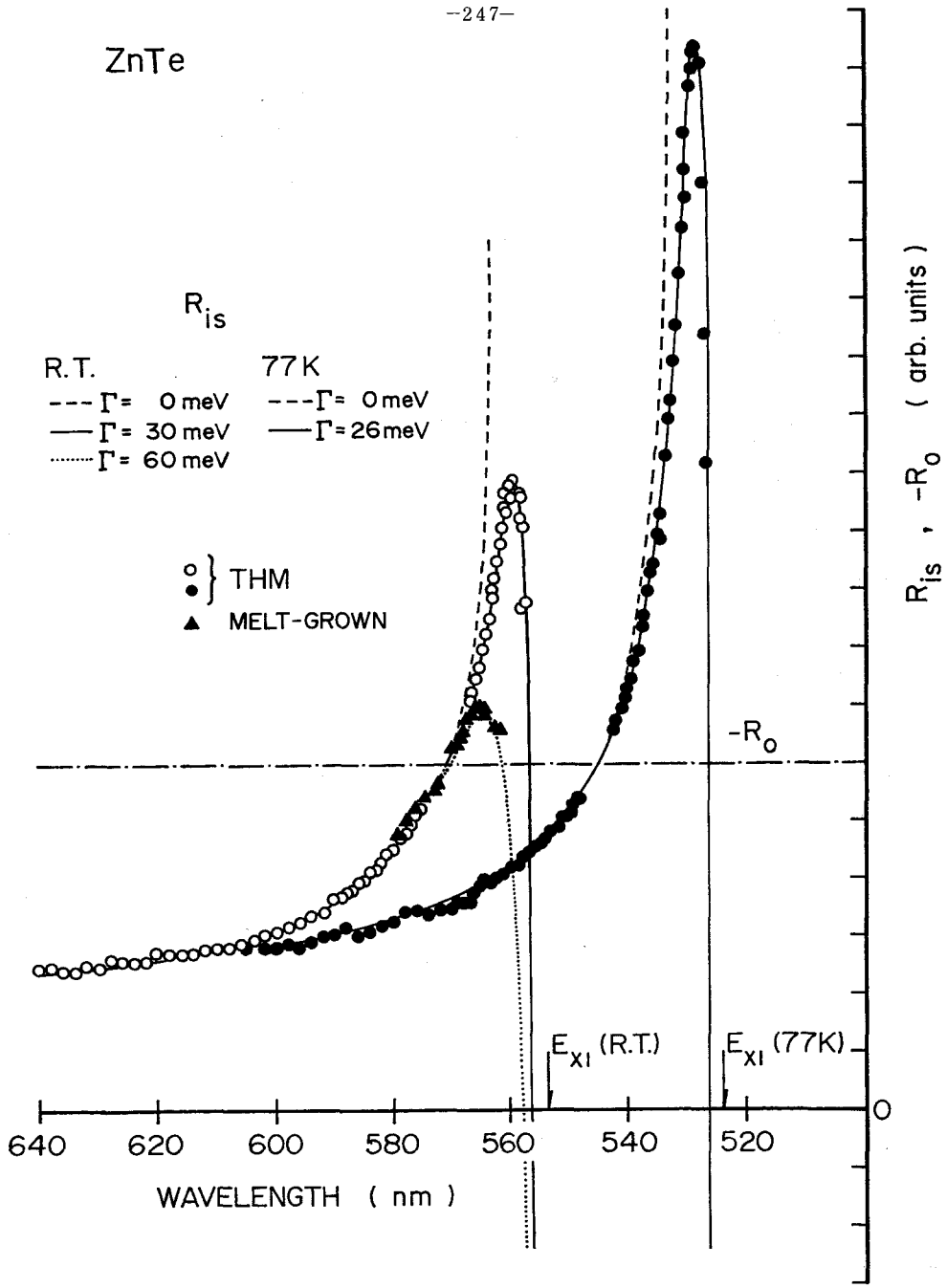

FIG. 7-7. Theoretical line shapes of the resonant term R_{is} for ZnTe in the region near the n = 1 exciton states along with the experimental data measured at room temperature [filled triangles (melt-grown crystal) and open circles (THM crystal)] and at 77 K [filled circles (THM crystal)]. The corresponding nondispersive term R_0 is also shown by dash-dotted line. The vertical arrows indicate the position of wavelengths corresponding to the n = 1 exciton states (E_{x1}) at room temperature and 77 K.

shown in the figure are obtained by calculating the square roots of σ_B (Fig. 7-6), and they are plotted to fit to R_{is} by taking account of the corresponding nondispersive term R_0 ($\sigma_B^{\frac{1}{2}} \propto |R_{is} + R_0|$). The vertical arrows in the figure indicate the positions of wavelength corresponding to the n = 1 exciton states (E_{x1}). It is apparent from Fig. 7-7 that the damping energies do not depend strongly on the temperatures but on the kinds of the crystals. The contribution $\Gamma_{ac}(T)$ of Eq. (7.4) is usually smaller than $\Gamma_{LO}(T)$ especially in the temperature region higher than about 60 K. In the present case, the amplified acoustical-phonon domains have an energy density a factor of the order of 10^9 above the thermal equilibrium value,[18] and thus $\Gamma_{ac}(T)$ has an appreciable value to contribute to the damping of the intermediate electronic states. Therefore, we can expect specific effects of the high-intensity phonon domains on the damping of the intermediate electronic states, as also suggested by Segall.[153] We found that the Brillouin-scattering intensities obtained at room temperature and 77 K are almost same at the wavelength of He-Ne laser (632.8 nm). This means that the densities of the acoustical-phonon domains are almost same at the two different temperatures. Considering this fact, $\Gamma_{ac}(T)$ becomes independent of temperatures in the range from 77 K to room temperature. The obtained value of Γ = 26 meV for the THM crystal at 77 K is much larger than that determined from reflectance measurements of ZnTe at 77 K ($\Gamma \simeq 2$ meV, see Fig. 7-2). Because of the temperature-independent nature of Γ, we suspect that the damping energy determined here arises mainly from the Γ_{ac} contribution induced by the intense acoustical-phonon domains.

In Figs. 7-8 and 7-9, we present the line shapes of the resonant-Brillouin term R_{is} for ZnSe along with the experimental data taken at room temperature and 77 K (fast-TA phonon domains), respectively. The corresponding nonresonant term R_0 is also shown in the figures by dash-dotted lines. The open and filled

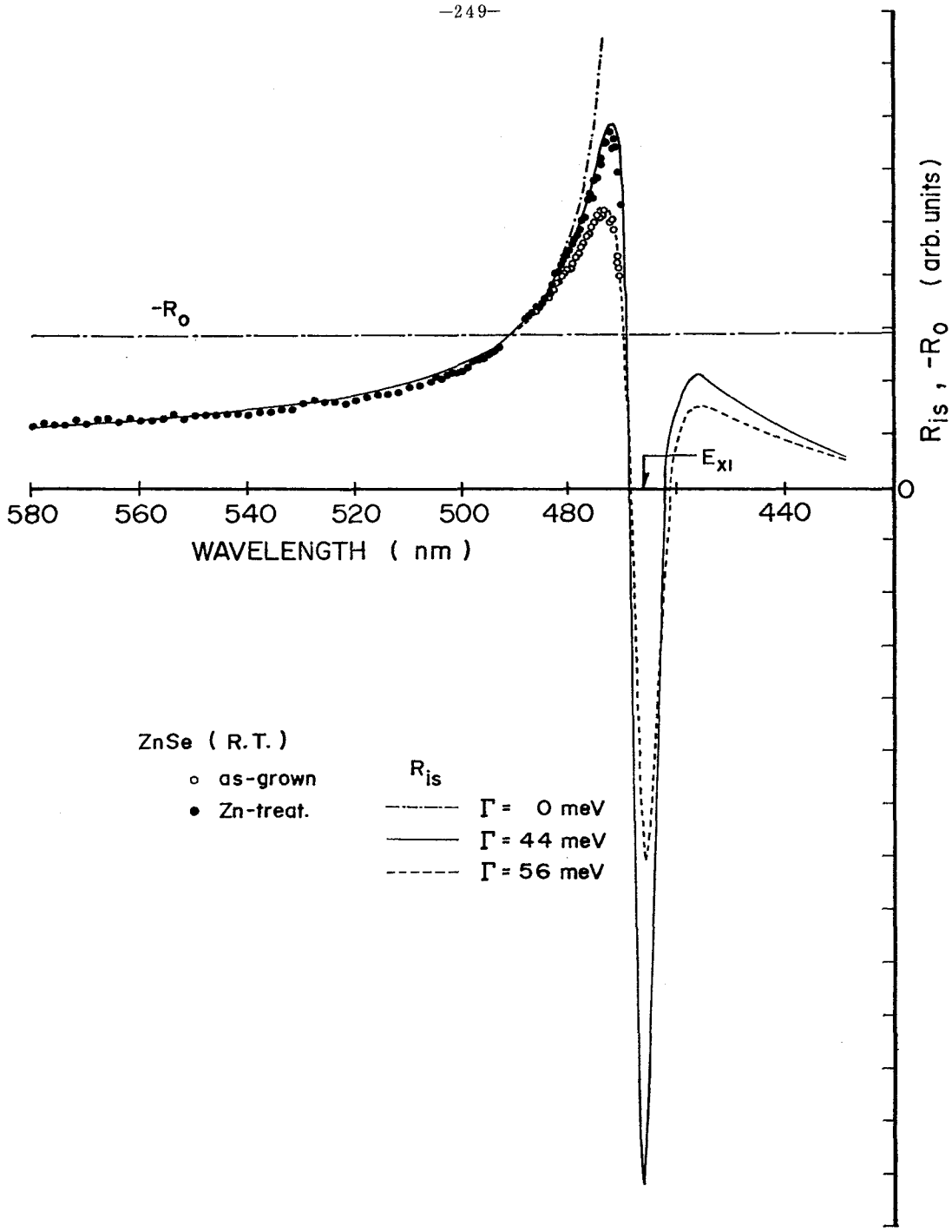

FIG. 7-8. Theoretical line shapes of the resonant term R_{is} for ZnSe in the neighborhood of the fundamental absorption edge along with the experimental data [as-grown (open circles) and Zn-purified ZnSe (filled circles)] taken at room temperature. The corresponding nondispersive term R_0 is also shown by dash-dotted line.

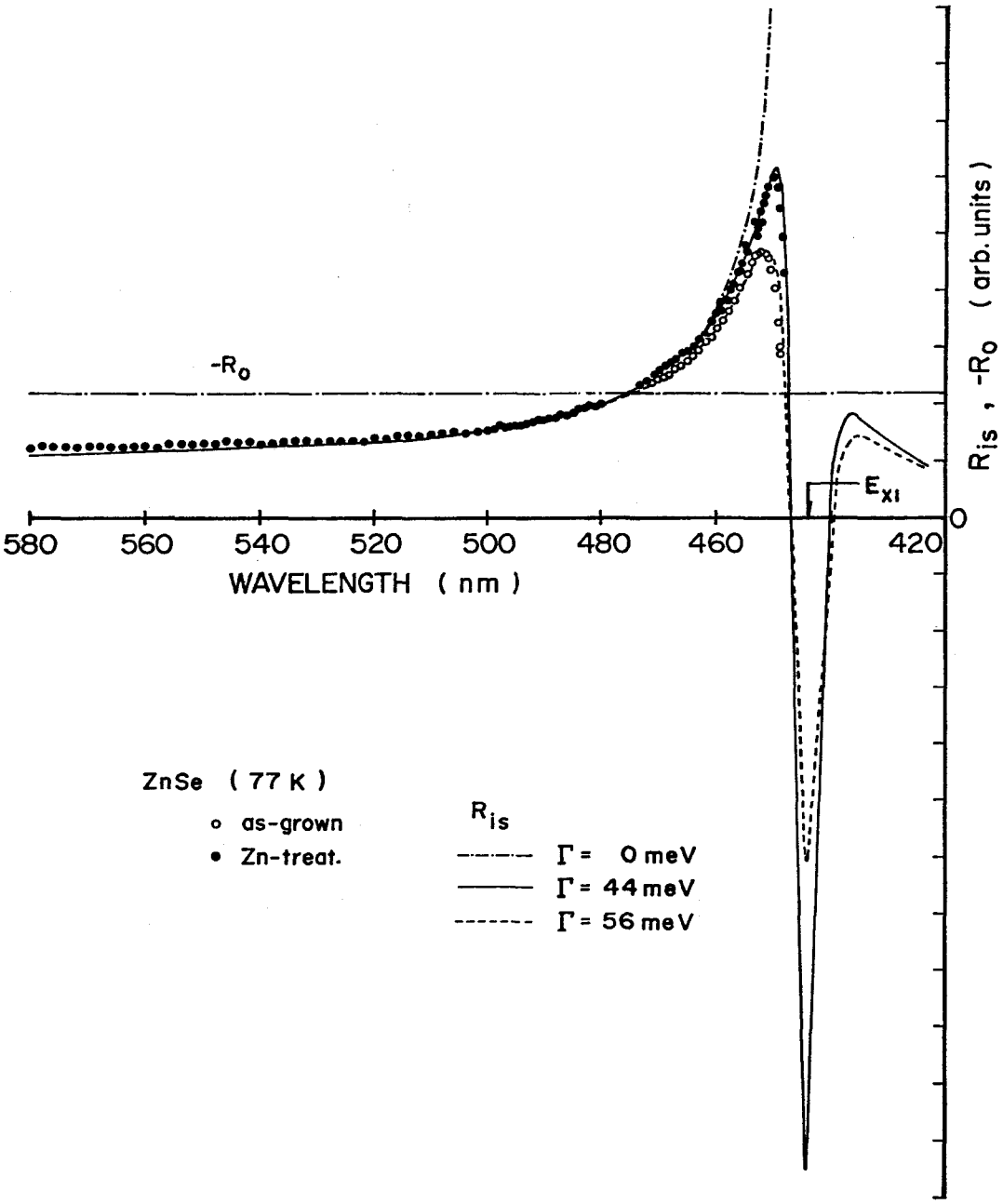

FIG. 7-9. Theoretical line shapes of the resonant term R_{is} for ZnSe in the neighborhood of the fundamental absorption edge along with the experimental data [as-grown (open circles) and Zn-purified ZnSe (filled circles)] taken at 77 K. The corresponding nondispersive term R_0 is also shown by dash-dotted line.

circles are taken for crystals from the as-grown and heat-treated ZnSe, respectively. The numerical values used to calculate the resonant-Brillouin term R_{is} are listed in Table 4-3. The vertical arrows in the figures indicate the positions of wavelength corresponding to the n = 1 exciton states. THe data taken at liquid-nitrogen temperature shows the same resonance behaviors as that taken at room temperature, except a shift of the resonance curve in wavelength due to the shift of resonance energy followed by the shift of the band-gap energy. It is clearly seen from the figures that the resonant enhancement for the heat-treated ZnSe (filled circles) in much stronger than that for the as-grown ZnSe (open circles) both at room temperature and 77 K. The experimental dispersion shows a good agreement with the theoretical curves with Γ = 56 meV (as-grown ZnSe) and 44 meV (heat-treated ZnSe) [room temperature and also 77 K], indicating that the damping energy does not depend on the temperatures but on the kinds of the crystals. The value of Γ = 44 meV for the heat-treated ZnSe is much larger than that obtained from reflectance measurements of ZnSe at 77 K ($\Gamma \simeq$ 3 meV, see Fig. 7-2). Such a result agrees with that obtained for ZnTe as mentioned above. Thus, we consider that the main contribution to the damping process comes from an interaction of the intermediate electronic states with the intense acoustical-phonon domains.

Since little attention has been payed on the effect of damping on resonant light scattering, it is difficult for us to discuss extensively concerning this problem by comparing with other published works so far. Recently, Klochikhin *et al.*[172] have studied resonant Raman scattering in $Zn_xCd_{1-x}Te$ solid solutions by LO phonons near E_0 gap. They obtained the temperature dependence of the Raman-scattering cross sections in the range 77 — 300 K, and found that the resonance curves depend on the damping of the intermediate electronic (exciton) states. The data of the temperature dependence of the exciton lifetime deduced from the Raman-scattering spectra were compared with

those obtained from reflectance measurements. The comparison showed a good agreement with each other, and the temperature dependence wea explained by the same expression as Eq. (7.4). More recently, Trommer and Cardona[60] have studied resonant Raman scattering in GaAs in the vicinity of $E_0/E_0+\Delta_0$ and $E_1/E_1+\Delta_1$ critical points. They found that Raman scattering taken at 80 K by LO phonons near $E_0+\Delta_0$ critical point required a damping of $\Gamma = 0.3\hbar\omega_{LO}$ ($\hbar\omega_{LO}$: LO phonon energy). Measurements taken at liquid-helium temperature showed exactly the same resonance behaviors as that taken at 80 K. On the other hand, the resonance curve at room temperature required a fit with a damping of $\Gamma = 0.45\hbar\omega_{LO}$. These data suggest that $\Gamma(T)$ is almost constant in the temperature range from low T to about 80 K, while at temperatures higher than 80 K the Γ_{LO} contribution becomes discernible. It is evident for the above two studies that the Γ_{ac} contribution is negligibly small [because the occupation number of thermal acoustical phonons is very small compared with the intense acoustical-phonon domains].

In summary, we have determined the damping energies of the intermediate electronic states for ZnTe and ZnSe from the Brillouin-scattering measurements, and found that it does not depend strongly on the temperatures but on the kinds of the crystals. We consider that the damping of the intermediate electronic states arises mainly from the contribution due to the high-intensity acoustical-phonon domains (i.e., from an interaction of the intermediate electronic states with the intense acoustical-phonon domains). It is well known that the intense acoustical-phonon domains can produce an exponential broadening on the intrinsic absorption edge of semiconductors.[255] We believe that the effects of the intense phonon domains on the damping of the electronic states should be revealed by measuring optical spectra such as reflection, absorption and emission of the exciton lines during the presence of the intence phonon domains (i.e., by measuring the destruction of the exciton spectrum during the presence of the intense phonon domains).

CHAPTER VIII

RESONANT BRILLOUIN SCATTERING AS A FORM OF MODULATION SPECTROSCOPY

8.1 INTRODUCTION

The attention of many researchers has recently been drawn to the study on optical properties of solids by means of reflectance and absorption modulation.[43,44] The common feature of all modulation techniques of optical spectroscopy is the measurement of the derivative of some optical properties with respect to some parameters such as electric field, temperature, stress, wavelength and magnetic field. The various modulation parameters define a whole family of (reflectance) modulation techniques such as electroreflectance thermoreflectance, piezoreflectance, wavelength-derivative spectroscopy and magnetoreflectance. The modulated reflectance techniques better define the spectral contrast of structure than do static reflectance techniques. A rather featureless reflectance spectrum is replaced by a modulation trace rich in structure compressed into narrow regions of photon energy. The modulation-spectroscopy techniques have, therefore, been widely adopted in precision investigations of the optical properties of solids. The main task in the first investigations of the modulation spectroscopy has been to determine more accurately the energies of electronic transitions at critical points of the band structure. Structure in the real and imaginary parts of the dielectric constant is well known to be intimately related to the presence

of critical points in the optical energy versus k-vector relation. These critical points have played a mojor role on studies of the band structure. The modulation spectroscopy greatly enhances the structure and hence makes it possible to resolve critical points much more clearly than in the normal static methods.

The electroreflectance spectroscopy is probably the easiest of all modulation techniques from the experimental point of view.[256] However, the electroreflectance spectra in general are strongly dependent on the magnitude of the modulating field and on experimental conditions and the modulating field destroys translational invariance of solids along its direction, so the determination of material parameters from these spectra is a difficult and uncertain process. The stress modulation preserves the translational invariance. The thermal modulation occupies a hybrid positon: the thermal expansion preserves the translational invariance while the electron-phonon interaction does not. Consequently, research effort has tended to concentrate on first-derivative techniques such as thermoreflectance, piezoreflectance and wavelength-derivative spectroscopy in which experimental spectra are broader but can be analyzed in relatively simple terms.

Resonant light scattering in semiconductors has recently attracted increasing attention, since it has been found to be intimately related to the optical properties of semiconductors. Light scattering is known to be a kind of modulation spectroscopy (i.e., the optical constants of a solid are modulated by phonons).[41] The inelastic-light-scattering experiments yield more information than its conventional modulation counterpart. A measurement of the spectral dependence of the Brillouin- (Raman-) scattering intensities yields the energies of critical points in a manner similar to more conventional modulation experiments. The spectrometer analysis yields the frequency and sound velocity (acoustical phonon) of the corresponding

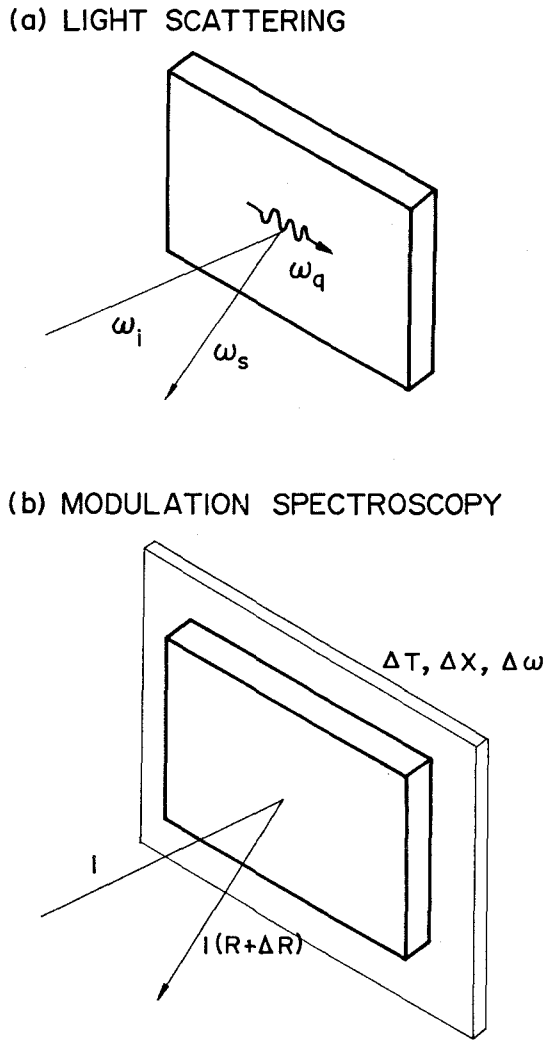

FIG. 8-1. Schematic representations of the measurement techniques for (a) inelastic light scattering and (b) modulation spectroscopy (reflectance).

excitation, without counterpart in the conventional modulation experiment. An absolute determination of the Brillouin- (Raman)- scattering intensity yields the deformation potential, which is the tensorial constant and represents the interaction of the elementary excitation (phonon) with the electronic transitions (electron-phonon interaction) [see Fig. 8-1].

In this Chapter, a discussion is given on resonant Brillouin scattering in connection with first-derivative modulation spectroscopy such as thermoreflectance, piezoreflectance and wavelength-derivative spctroscopy.[257] In Section 8.2, a detailed survey is given of a relation between the expressions for resonant Brillouin scattering based upon Loudon's light-scattering theory and the quasi-static approximation and also of a comparison of them with the first-derivative modulation spectroscopy. In Section 8.3, we compare the experimentally derived Brillouin-scattering efficiencies with the first-derivative modulation spectra in some semiconductors (ZnSe, ZnTe and GaAs). It will be demonstrated there that a good agreement between them may be obtained when the lifetime-broadening effect is taken into account in the resonant-Brillouin-scattering analysis.

8.2 THEORETICAL DESCRIPTION

In this Section, we shall show that the resonant-Brillouin-scattering process can be described by a phenomenological formalism analogous to that of the first-derivative modulation spectroscopy such as thermoreflectance, piezoreflectance and wavelength-derivative spectroscopy.[43,44]

8.2.1 Resonant Brillouin Scattering

First, we consider two-band contribution to the resonant-Brillouin-scattering process in which intermediate electronic transitions are necessarily intraband [i.e., $\hbar\omega_\alpha(\vec{k}) = \hbar\omega_\beta(\vec{k})$]. The energy denominators in Eq. (2.24) may

be written for the Stokes process as

$$[(\omega_\alpha(\vec{k}) - \omega_i)(\omega_\alpha(\vec{k}) - \omega_s)]^{-1} = \omega_q^{-1}[(\omega_\alpha(\vec{k}) - \omega_i)^{-1} - (\omega_\alpha(\vec{k}) - \omega_i + \omega_q)^{-1}]$$

$$\simeq \omega_q^{-1}\{[(\omega_\alpha(\vec{k}) - \omega_i)^{-1} + (\omega_\alpha(\vec{k}) + \omega_i)^{-1}]$$

$$- [(\omega_\alpha(\vec{k}) - \omega_i + \omega_q)^{-1} + (\omega_\alpha(\vec{k}) + \omega_i - \omega_q)^{-1}]\} \quad , \tag{8.1}$$

where we have assumed that $\omega_i \gg \omega_q$. The dielectric function of a solid is known to be given by the following form:[43]

$$\varepsilon(\omega) = \frac{4\pi}{\omega^2} \sum_{\alpha,\vec{k}} |\langle|p|\rangle|^2 \times [(\omega_\alpha(\vec{k}) - \omega)^{-1} + (\omega_\alpha(k) + \omega)^{-1}] \ . \tag{8.2}$$

Comparing Eq. (8.1) with Eq. (8.2), we find that the resonant-Brillouin term R_{is} [Eq. (2.24)] can be written in terms of the frequency-dependent dielectric constant $\varepsilon(\omega_{g\alpha},\omega)$ based on the dielectric theory as

$$R_{is} = A \sum_\alpha \Xi_{\alpha\alpha} \frac{1}{\omega_q} [\varepsilon(\omega_{g\alpha},\omega_i) - \varepsilon(\omega_{g\alpha},\omega_i-\omega_q)] \quad , \tag{8.3}$$

where $A = \hbar m^2\omega_i^2/4\pi e^2\omega_q$. Since $\hbar\omega_q$ is sufficiently smaller than $\hbar\omega_i$ (especially for the case of the Brillouin-scattering process), Eq. (8.3) can be written to a good approximation as

$$\lim_{\omega_q\to 0} R_{is} \simeq A \sum_\alpha \Xi_{\alpha\alpha} \frac{\partial}{\partial\omega} \varepsilon(\omega_{g\alpha},\omega_i)$$

$$\simeq -A \sum_\alpha \Xi_{\alpha\alpha} \frac{\partial}{\partial\omega_{g\alpha}} \varepsilon(\omega_{g\alpha},\omega_i) \quad , \tag{8.4}$$

where we have neglected an additional term arising from A which results in a structureless contribution to Eq. (8.4).

Next, we consider tree-band contribution to the resonant-Brillouin-scattering process in which intermediate electronic transitions are necessarily interband [i.e., $\hbar\omega_\alpha(\vec{k}) = \hbar\omega_\beta(\vec{k})$]. The energy denominators in Eq. (2.24) may

be written for the Stokes process as

$$[(\omega_\alpha(\vec{k}) - \omega_i)(\omega_\beta(\vec{k}) - \omega_s)]^{-1} = (\Delta + \omega_q)^{-1}[(\omega_\alpha(\vec{k}) - \omega_i)^{-1} - (\omega_\beta(\vec{k}) - \omega_i + \omega_q)^{-1}] \quad , \qquad (8.5)$$

where

$$\Delta = \omega_\beta(\vec{k}) - \omega_\alpha(\vec{k}) \qquad (8.6)$$

is the difference of the interband-transition energies (*e.g.*, the spin-orbit splitting energy for the zincblende-type crystals). Introducing the dielectric theory into Eq. (8.5), we obtain

$$\lim_{\omega_q \to 0} R_{is} \propto \frac{2}{\Delta}(\varepsilon^+ - \varepsilon^-) \quad , \qquad (8.7)$$

where ε^+ and ε^- are the contributions of the ω_α and ω_β gaps to the dielectric constant, respectively.

Consequently, we find that the expression for the Brillouin-scattering efficiency based on the quantum-mechanical approach has the same form as that derived from the quasi-static approximation [see Section 5.2.1]. The most dispersive contribution to the resonant-Brillouin process (i.e., two-band contribution) can, thus, be expressed by the first derivative of ε with respect to the incident-light frequency (or equivalently to the band-gap energy). It is easy to show that Eq. (2.55) can also be expressed by the same form as Eq. (8.4) or (8.7) when we use dielectric function valid for the exciton model instead of the free electron-hole pair model.

8.2.2 Modulation Spectroscopy

The reflectivity R of a material is a quantity which can be measured in a straightforward manner. For normal incidence of light, it has the form

$$R = \frac{(n-1)^2 + k^2}{(n+1)^2 + k^2} \quad . \tag{8.8}$$

The reflectivity can also be expressed as a function of the real and imaginary components of the dielectric constant by substitution of Eq. (6.39) into Eq. (8.8). This gives

$$R = \frac{(\varepsilon_1^2 + \varepsilon_2^2) - [2\varepsilon_1 + 2(\varepsilon_1^2 + \varepsilon_2^2)^{\frac{1}{2}}]^{\frac{1}{2}} + 1}{(\varepsilon_1^2 + \varepsilon_2^2) + [2\varepsilon_1 + 2(\varepsilon_1^2 + \varepsilon_2^2)^{\frac{1}{2}}]^{\frac{1}{2}} + 1} \quad . \tag{8.9}$$

The effect on reflectivity of the changes $\Delta\varepsilon_1$ and $\Delta\varepsilon_2$ induced by the modulation is made explicitly by differentiating Eq. (8.9). The result has the form[226]

$$\frac{\Delta R}{R} = \alpha(\varepsilon_1, \varepsilon_2)\Delta\varepsilon_1 + \beta(\varepsilon_1, \varepsilon_2)\Delta\varepsilon_2 \quad , \tag{8.10}$$

where

$$\alpha = C_1[(\varepsilon_1 - 1)A_+ + \varepsilon_2 A_-] \quad , \tag{8.11a}$$

$$\beta = C_2[(\varepsilon_1 - 1)/A_+ - \varepsilon_2/A_-] \quad , \tag{8.11b}$$

with

$$A_\pm \equiv \pm \frac{\sqrt{2}[(\varepsilon_1^2 + \varepsilon_2^2)^{\frac{1}{2}} \pm \varepsilon_1]^{\frac{1}{2}}}{(\varepsilon_1^2 + \varepsilon_2^2)^{\frac{1}{2}}} \quad , \tag{8.12a}$$

$$C_1 \equiv [(\varepsilon_1 - 1)^2 + \varepsilon_2^2]^{-1} \quad , \tag{8.12b}$$

$$C_2 \equiv 2\varepsilon_2/[(\varepsilon_1 - 1)^2 + \varepsilon_2^2](\varepsilon_1^2 + \varepsilon_2^2) \quad . \tag{8.12c}$$

The fractional coefficients α and β are functions of photon energy, and their sign and relative magnitude determine the result of the analysis in the different spectral regions. These coefficients are usually called as the Seraphin coefficients. Figure 8-2 plots the Seraphin coefficients for (a) ZnSe, (b) ZnTe and (c) CdS ($\vec{E} \perp \vec{c}$), as calculated from experimental values

of the optical constants.[190,192,203] The three diagrams are very similar: A low-energy region, which contains the fundamental absorption edge, is dominated by α. Raising β and falling α produce a crossover in the region of 3 — 4 eV. We have previously obtained the fractional coefficients α_r and β_i, like to the Seraphin coefficients, to analyze the piezobirefringence coefficient (see Section 6.4). Figure 8-3 plots the fractional coefficients α_r and β_i in Eq. (6.40) for (a) ZnSe, (b) ZnTe and (c) CdS ($\vec{E} \perp \vec{c}$), as calculated from experimental values of the optical constants.[190,192,203] (Note that Fig. 8-3 (a) is the same as Fig. 6-13). The coefficients α_r and β_i are found to have the same physical meanings as the Seraphin coefficients α and β, i.e., they determine the fractional contributions of the changes $\Delta\varepsilon_1$ and $\Delta\varepsilon_2$ induced by the stress (modulation parameters) to the piezobirefringence effect (modulation-spectroscopy response). It is obvious from a comparison of Fig. 8-2 with Fig. 8-3 that the spectral dependence of α and β (Seraphin coefficients) is very similar to that of α_r and β_i. We find from Fig. 8-2 that in the region near the fundamental absorption edge of II-VI compounds such as ZnSe and ZnTe only the first term of Eq. (8.10) is important, and therefore the behavior of $\frac{\Delta R}{R}$ is determined predominantly by the nature of the function $\Delta\varepsilon_1(\omega)$.

The function $\Delta\varepsilon_1(\omega)$ with various modulation parameters can be given by[43,44]

Temperature: ΔT (Thermoreflectance)

$$\Delta\varepsilon_1(\omega) = \left(\frac{\partial\varepsilon_1}{\partial E_g}\frac{\partial E_g}{\partial T} + \frac{\partial\varepsilon_1}{\partial\Gamma}\frac{\partial\Gamma}{\partial T} \right)\Delta T$$

$$\simeq \frac{\partial\varepsilon_1}{\partial E_g}\frac{\partial E_g}{\partial T}\Delta T = \frac{\partial\varepsilon_1}{\partial E_g}\Delta E_g \quad , \qquad (8.13)$$

Stress: ΔX (Piezoreflectance)

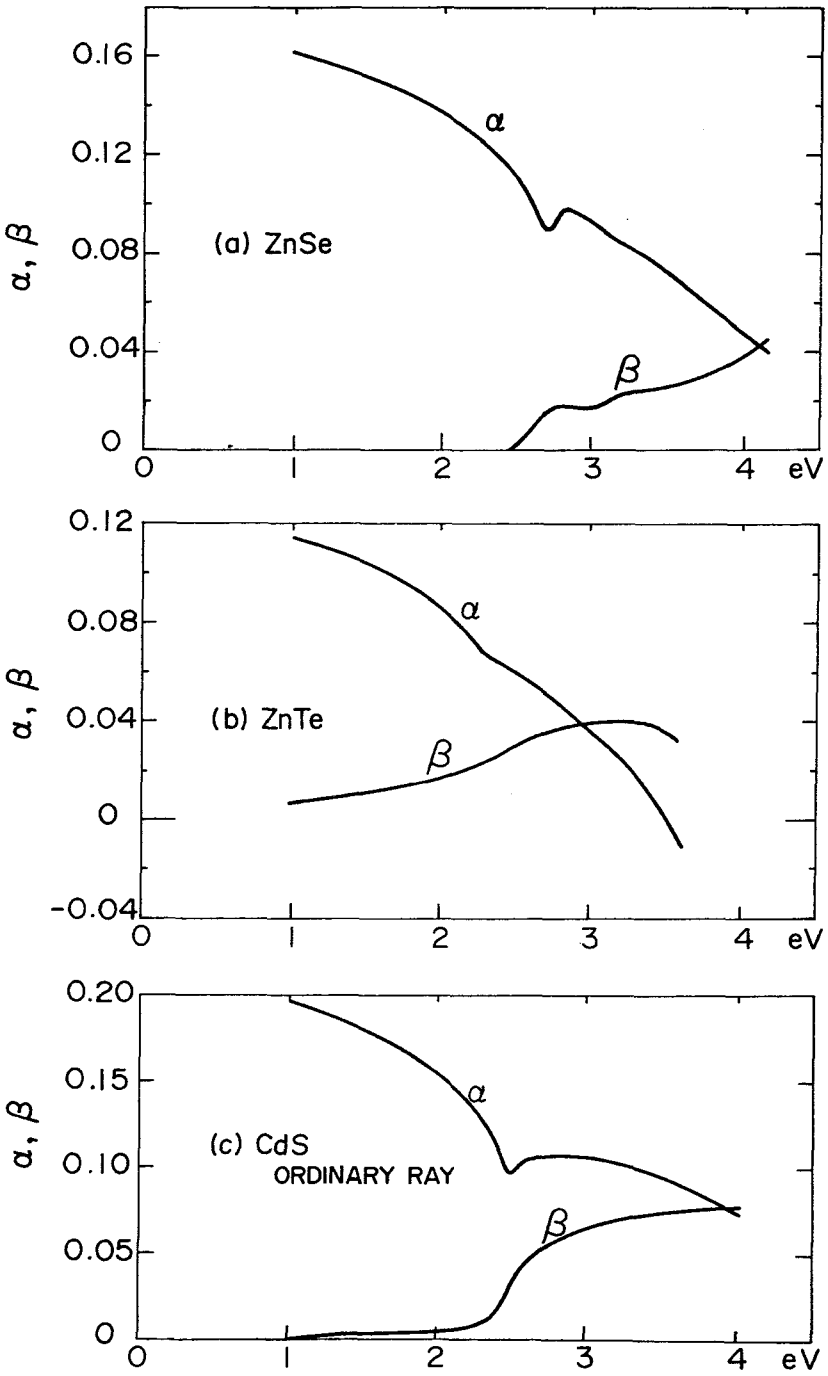

FIG. 8-2. Fractional coefficients α and β in Eq. (8.10) for (a) ZnSe, (b) ZnTe and (c) CdS ($\vec{E} \perp \vec{c}$).

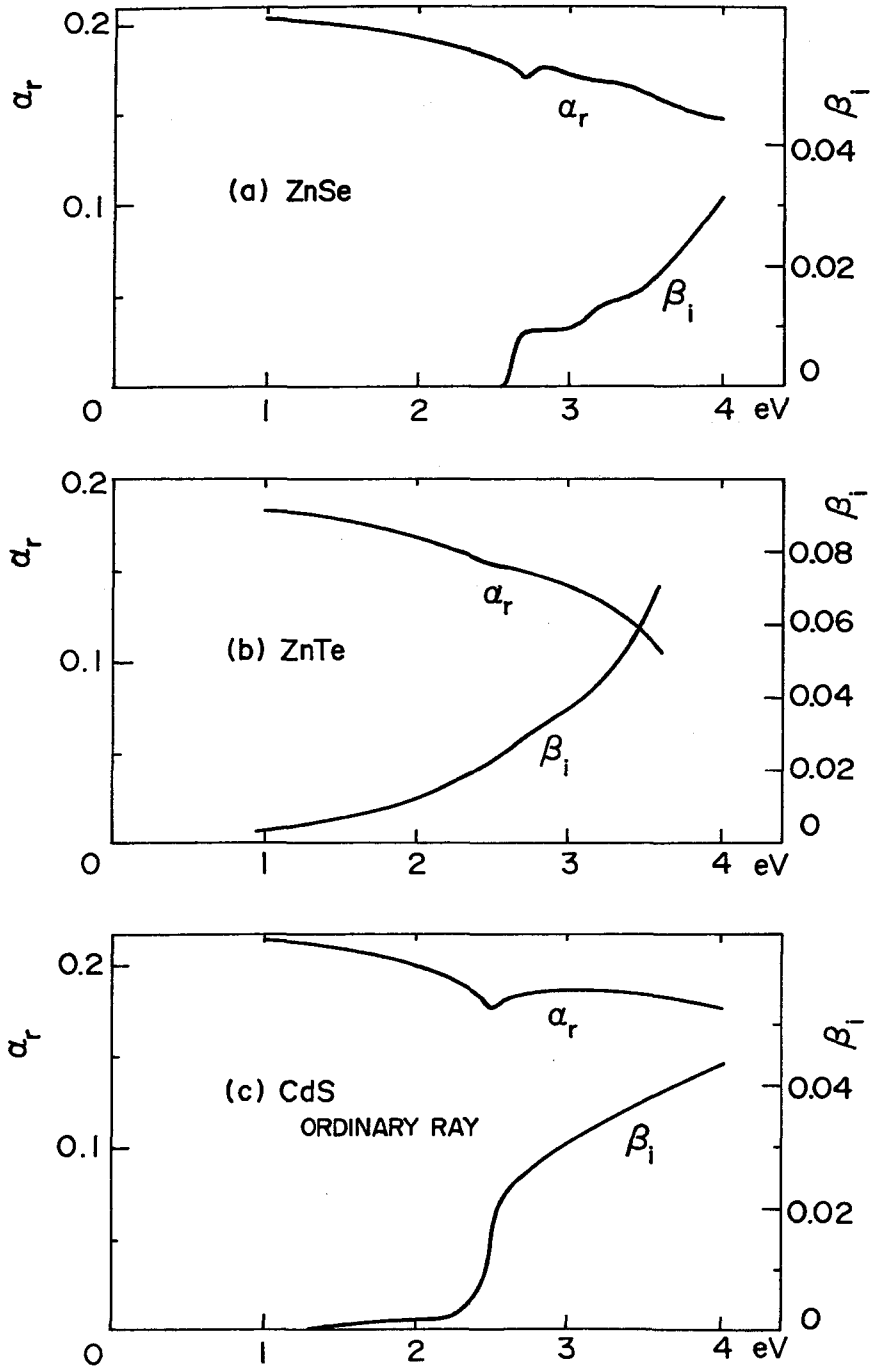

FIG. 8-3. Fractional coefficients α_r and β_i in Eq. (6.40) for (a) ZnSe, (b) ZnTe and (c) CdS ($\vec{E} \perp \vec{c}$).

$$\Delta\varepsilon_1(\omega) = \left(\frac{\partial\varepsilon_1}{\partial E_g}\frac{\partial E_g}{\partial X} + \frac{\partial\varepsilon_1}{\partial M}\frac{\partial M}{\partial X} \right)\Delta X$$

$$\simeq \frac{\partial\varepsilon_1}{\partial E_g}\frac{\partial E_g}{\partial X}\Delta X = \frac{\partial\varepsilon_1}{\partial E_g}\Delta E_g \quad , \tag{8.14}$$

Wavelength: $\Delta\omega$ (Wavelength modulation)

$$\Delta\varepsilon_1(\omega) = \frac{\partial\varepsilon_1}{\partial\omega}\Delta\omega \quad , \tag{8.15}$$

Electric field: ΔE (Electroreflectance)

$$\Delta\varepsilon_1(\omega) = \frac{\Omega^3}{3\omega^2}\frac{d^3}{d\omega^3}(\omega^2\varepsilon_1) \quad , \tag{8.16a}$$

where

$$(\hbar\Omega)^3 = e^2\hbar^2E^2/8\mu \quad . \tag{8.16b}$$

In Eqs. (8.13) — (8.16), E_g is the band-gap energy, Γ is the broadening parameter, M is the squared-p matrix element and μ is the interband reduced mass. The thermoreflectance, piezoreflectance and wavelength-modulation spectra reflect the first derivative of the unperturbed dielectric constant (first-derivative modulation spectroscopy). The electroreflectance (low-field) spectrum, on the other hand, reflects the third derivative of the unperturbed dielectric constant (third-derivative modulation spectroscopy). In thermoreflectance spectroscopy, the modulation of temperature results in a change in ε_1 of the crystal which is induced by a shift of the band-gap energy E_g and by a change of the broadening parameter Γ. The contribution to the reflectance modulation caused by the shift of E_g is usually larger than that caused by the change of Γ. Under this condition, the thermoreflectance and wavelength-modulation spectroscopy should be equivalent, except for a scaling factor related to the temperature coefficient of the band-gap energy $\partial E_g/\partial T$. The stress modulation (piezoreflectance) can be represented by the

same expression as that for the piezobirefringence [see Eq. (2.221)]. Therefore, it can be concluded that such types of modulation spectroscopy can be described by the first derivative of ε_1 with respect to the band-gap energy (thermoreflectance or piezoreflectance) or equivalently to the light wavelength (wavelength-derivative spectroscopy).

Let us now consider the derivative of the dielectric constant with respect to the interband energy E_g at various types of critical points. The complex dielectric constant for a critical point of type M_r is known to be written from simple theory in the following form (without including exciton effect):[184]

$$\varepsilon \propto i^{r+1} (\hbar\omega - E_g)^{\frac{1}{2}} \quad , \tag{8.17}$$

where E_g is the interband energy at the critical point. The lifetime-broadening effect can be accounted in the expression for phenomenologically by replacing $\hbar\omega$ by $\hbar\omega + i\Gamma$, where Γ is positive (Lorentzian broadening). This substitution yields

$$\varepsilon \propto i^{r+1} (\hbar\omega + i\Gamma - E_g)^{\frac{1}{2}} \quad . \tag{8.18}$$

Introducing the reduced variable $x = (\hbar\omega - E_g)/\Gamma$, we obtain

$$\varepsilon \propto i^{r+1} \Gamma^{\frac{1}{2}} (x + i)^{\frac{1}{2}} \quad . \tag{8.19}$$

The separation of the real and imaginary parts leads to the result

$$\varepsilon \propto i^{r+1} \Gamma^{\frac{1}{2}} [\phi(x) + i\phi(-x)] \quad , \tag{8.20}$$

where

$$\phi(x) = [x + (x^2 + 1)^{\frac{1}{2}}]^{\frac{1}{2}} \quad . \tag{8.21}$$

The derivative of the dielectric constant ε with respect to the interband energy E_g can be obtained from Eq. (8.20) in the following form:

$$\frac{d\varepsilon}{dE_g} \propto -\frac{1}{2}\, i^{r+1}\, \Gamma^{-\frac{1}{2}}\, [F(x) - iF(-x)] \quad , \tag{8.22}$$

where

$$F(x) = [(x^2 + 1)^{\frac{1}{2}} + x]^{\frac{1}{2}}/(x^2 + 1) \quad . \tag{8.23}$$

The behaviors of the derivatives of ε_1 (solid lines) and ε_2 (dashed lines) with respect to the interband energy E_g represented by Eq. (8.22) are shown in Fig. 8-4 for the four types of the critical points M_0, M_1, M_2 and M_3. It is interesting to point out that the sign of the derivative $d\varepsilon_1/dE_g$ (solid lines) is negative for the M_0 and M_3 critical points while positive for the M_1 and M_2 critical points, and the magnitude of the contribution from the M_2 critical point is considerably large at a low-energy region (which contains the M_0 critical point). This fact reasonably explains the possibility of cancellation (isotropic point) in the Brillouin-scattering process (piezobirefringence), i.e., the M_0-gap resonance component should be cancelled mainly by the M_2-gap nonresonance component. As mentioned in Section 6.2, the M_2-gap component can also be estimated by using the Penn-gap model, where the Penn gap lies in the neighborhood of which most of the optical density of states is concentrated (i.e., near the E_2 critical point).

Aspnes[258] has verified that the electric-field-induced change in the dielectric constant, determined from low-field electroreflectance measurement, is shown to be in qualitative agreement with the third derivative of the unperturbed dielectric constant measured by high-resolution ellipsometry. He has also verified the relationship of electroreflectance spectra to those obtained by first-derivative modulation techniques such as thermoreflectance, piezoreflectance and wavelength-derivative spectroscopy. Similarly, we have already verified in Chapter V that the spectral dependence of the Brillouin-scattering cross sections shows a quite good agreement with the numerically

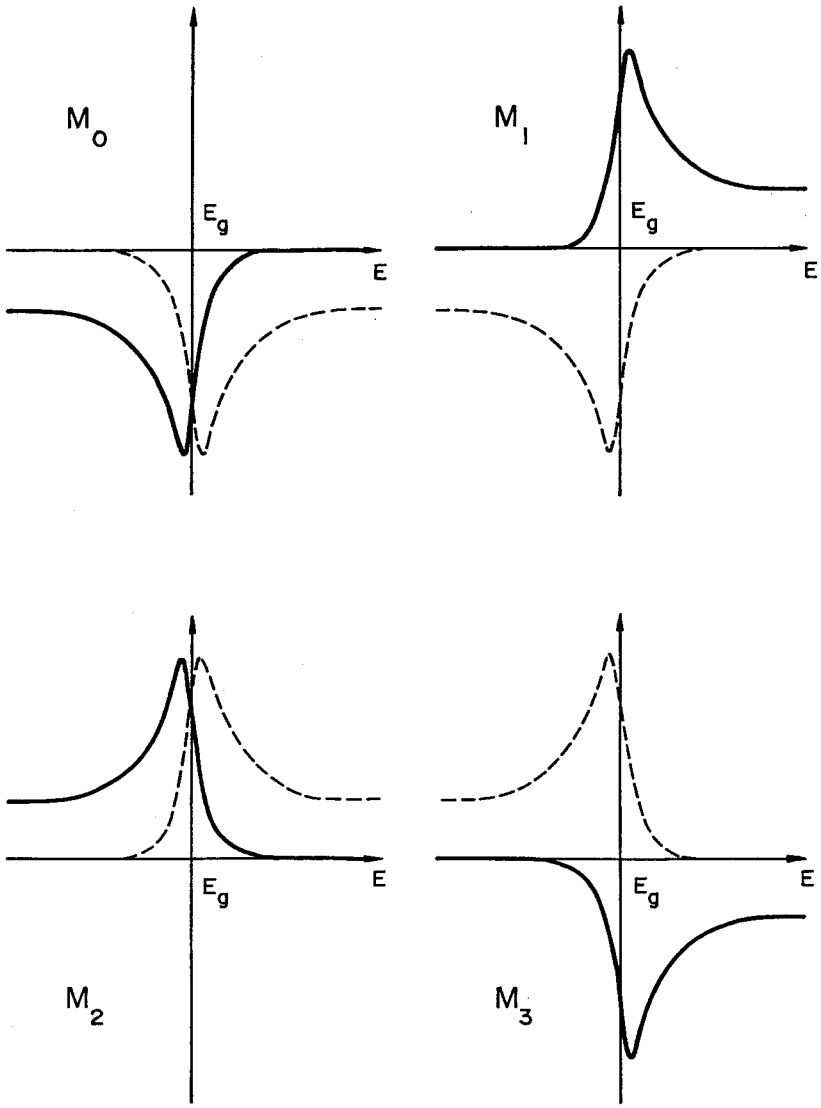

FIG. 8-4. First derivatives of ε_1 (solid lines) and ε_2 (dashed lines) with respect to the interband energy E_g represented by Eq. (8.22) for the four types of critical points.

differentiated first-derivative spectra of the dielectric constant. It is apparent from the present discussion that resonant Brillouin scattering is quite equivalent to the first-derivative modulation spectroscopy. In the next Section, indeed, we try and compare experimentally derived Brillouin-tensor term R_{is} with experimental spectra of the first-derivative modulation spectroscopy in some semiconductors (ZnSe, ZnTe and GaAs).

8.3 EXPERIMENTAL VERIFICATION

Figure 8-5 shows a comparison of the resonant-Brillouin term R_{is} with the thermoreflectance modulation spectrum of ZnSe at room temperature. The Brillouin-scattering data ($\sigma_B^{\frac{1}{2}} \propto |R_{is} + R_0|$) were obtained from TA-phonon domains injected from CdS into ZnSe by using the acoustical-domain injection method. The TA-phonon domains in ZnSe propagate in the [001] direction with shear polarization parallel to the [110] direction (fast-TA phonons). The experimentally derived thermoreflectance spectrum is from Matatagui *et al.*[184] They are fitted by adjusting a multiplicative constant in R_{is} since the measured scattering intensities were not absolute values. The square root of σ_B contains the nonresonant term R_0 arising from the dispersionless contribution to the Brillouin-scattering process. It is reasonable to consider that the nonresonant contribution R_0 is not generally equal to that of the background component contained in $\frac{\Delta R}{R}$. When the spectrum of $\sigma_B^{\frac{1}{2}}$ is compared with that of $\frac{\Delta R}{R}$ measured by the modulation spectroscopy, we have to take into account such a nonresonant contribution to $\sigma_B^{\frac{1}{2}}$. In the present analyses, we shifted the zero point of $\sigma_B^{\frac{1}{2}}$ to fit it to the spectrum of $\frac{\Delta R}{R}$, and adjusted the absolute value by the procedure stated above.

The theoretical line shape of R_{is} (solid line) is calculated from Eq. (2.55) with the following numerical values: $\hbar\omega_{gA} = \hbar\omega_{gB} = 2.68$ eV; $\hbar\omega_{gC} =$

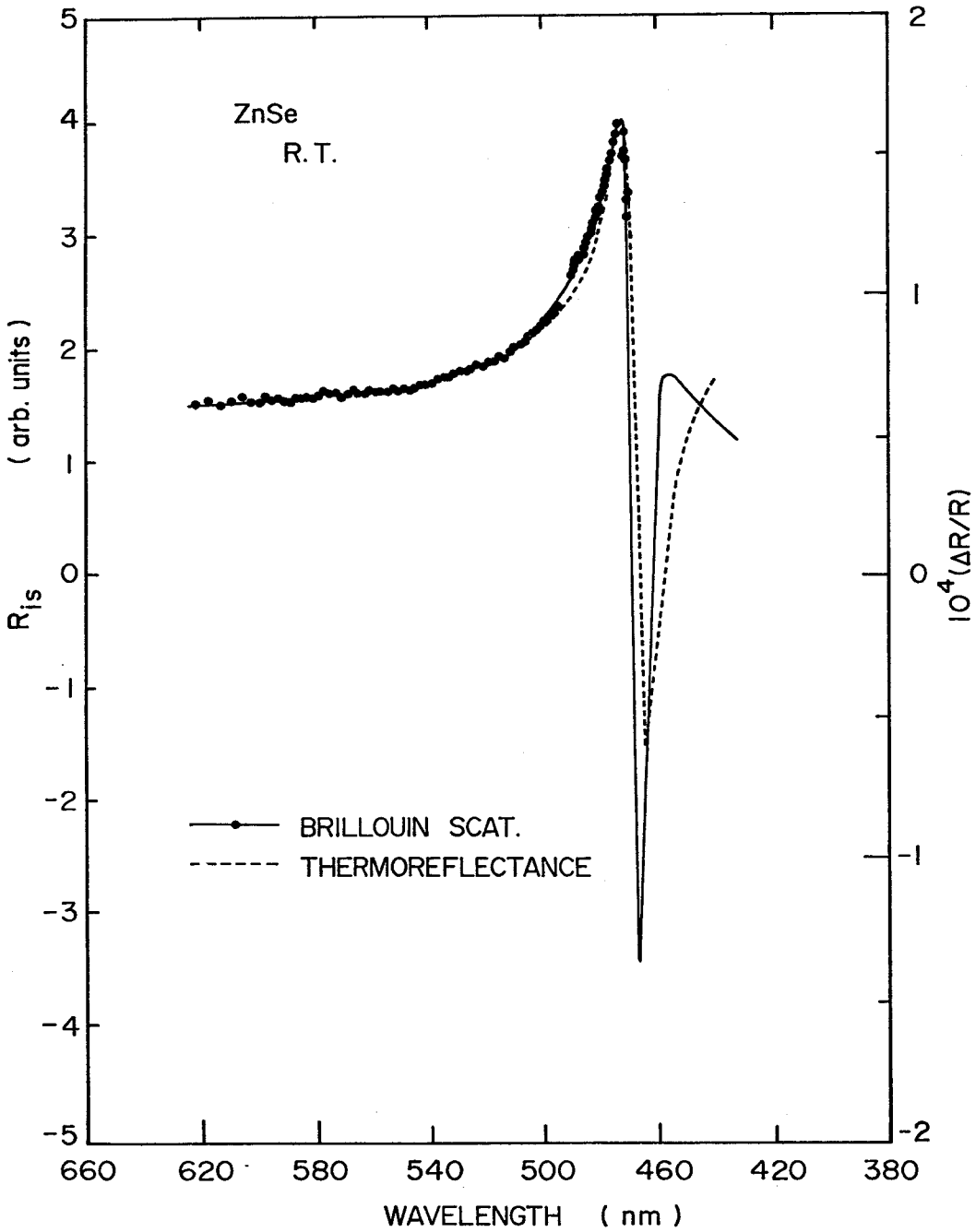

FIG. 8-5. Comparison of the Brillouin term R_{is} with the thermoreflectance spectrum of ZnSe at room temperature. The line shape of R_{is} (solid line) is calculated from Eq. (2.55) with Γ=56 meV. The thermoreflectance spectrum (dashed line) is from Matatagui *et al* (Ref. 184).

3.09 eV; Ξ_{BA} = 3.81 eV; Ξ_{CB} = 2.69 eV; Ξ_{CA} = 4.67 eV; $\hbar R^*$ = 19 meV; a_0^* = 51 Å; $P^i_{\alpha 0} = P^s_{0\beta}$; and Γ = 56 meV, where we have assumed $P^i_{\alpha 0} = P^s_{0\beta}$ = const. since the detailed values are not well known at present. (Note, however, that Lawaetz[259] has developed a semiempirical model to describe the dependence of the matrix elements on lattice constant, ionicity and *d*-electron shells in the cores of various semiconductors). It is believed that the structure appearing in the neighborhood of 460 nm is the result of the M_0 critical point (contribution from the unbound continuum exciton and free electron-hole pair) plus discrete-exciton interaction [see Fig. 8-9]. It is obvious that a reasonable fit between the line shape of R_{is} and the thermoreflectance spectrum can be obtained.

In Fig. 8-6, we compare the theoretical line shape of R_{is} (solid line), fitted with the experimental data (filled circles), with the thermoreflectance spectrum of ZnTe. The Brillouin-scattering data were obtained from fast-TA phonon domains at 77 K. The experimentally derived thermoreflectance spectrum (dashed line) is from Matatagui *et al.*[184] The line shape of R_{is} is calculated from Eq. (2.55) with the following numerical values: $\hbar\omega_{gA} = \hbar\omega_{gB}$ = 2.379 eV; $\hbar\omega_{gC}$ = 3.309 eV; Ξ_{BA} = 4.61 eV; Ξ_{CB} = 3.26 eV; Ξ_{CA} = 5.64 eV; $\hbar R^*$ = 10 meV; a_0^* = 45 Å; $P^i_{\alpha 0} = P^s_{0\beta}$ = const.; and Γ = 26 meV.

Figure 8-7 shows a comparison of R_{is} (same as that of Fig. 8-6) with the piezoreflectance modulation spectrum of ZnTe. The experimentally derived piezoreflectance spectrum (dashed line) is from Mathieu *et al.*[260] As compared with the thermoreflectance spectroscopy, the uniaxial stress modulation has an interesting new feature; the stress may lower the symmetry of the crystal and thus introduce anisotropy in the modulation spectra. The piezoreflectance spectra of cubic material, for instance, are expected to depend on the polarization of light.[261] We should, thus, regard from a phenomenological aspect that the piezoreflectance spectroscopy is quite equivalent to the piezo-

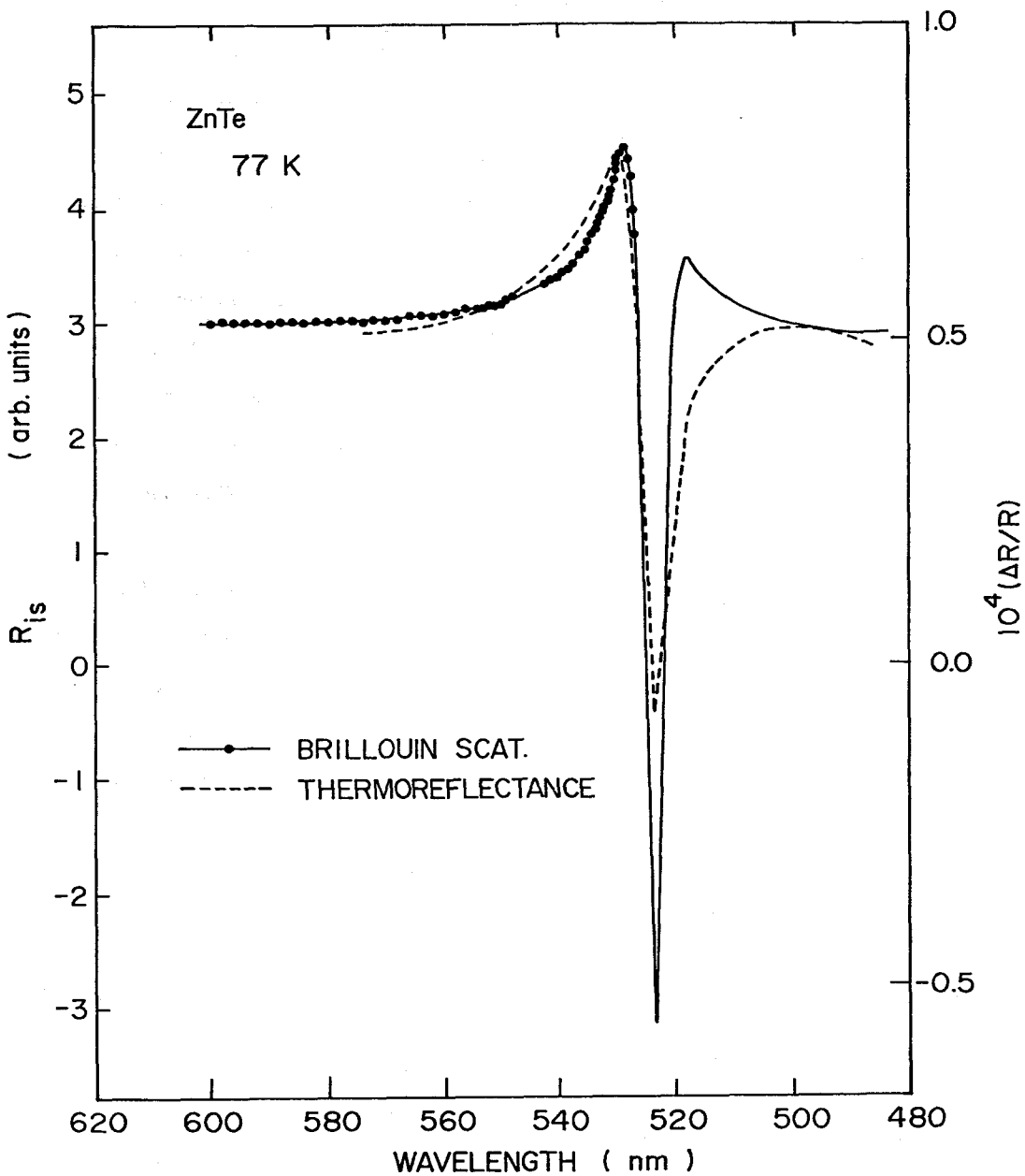

FIG. 8-6. Comparison of the Brillouin term R_{is} with the thermoreflectance spectrum of ZnTe at 77 K. The line shape of R_{is} (solid line) is calculated from Eq. (2.55) with Γ=26 meV. The thermoreflectance spectrum (dashed line) is from Matatagui *et al* (Ref. 184).

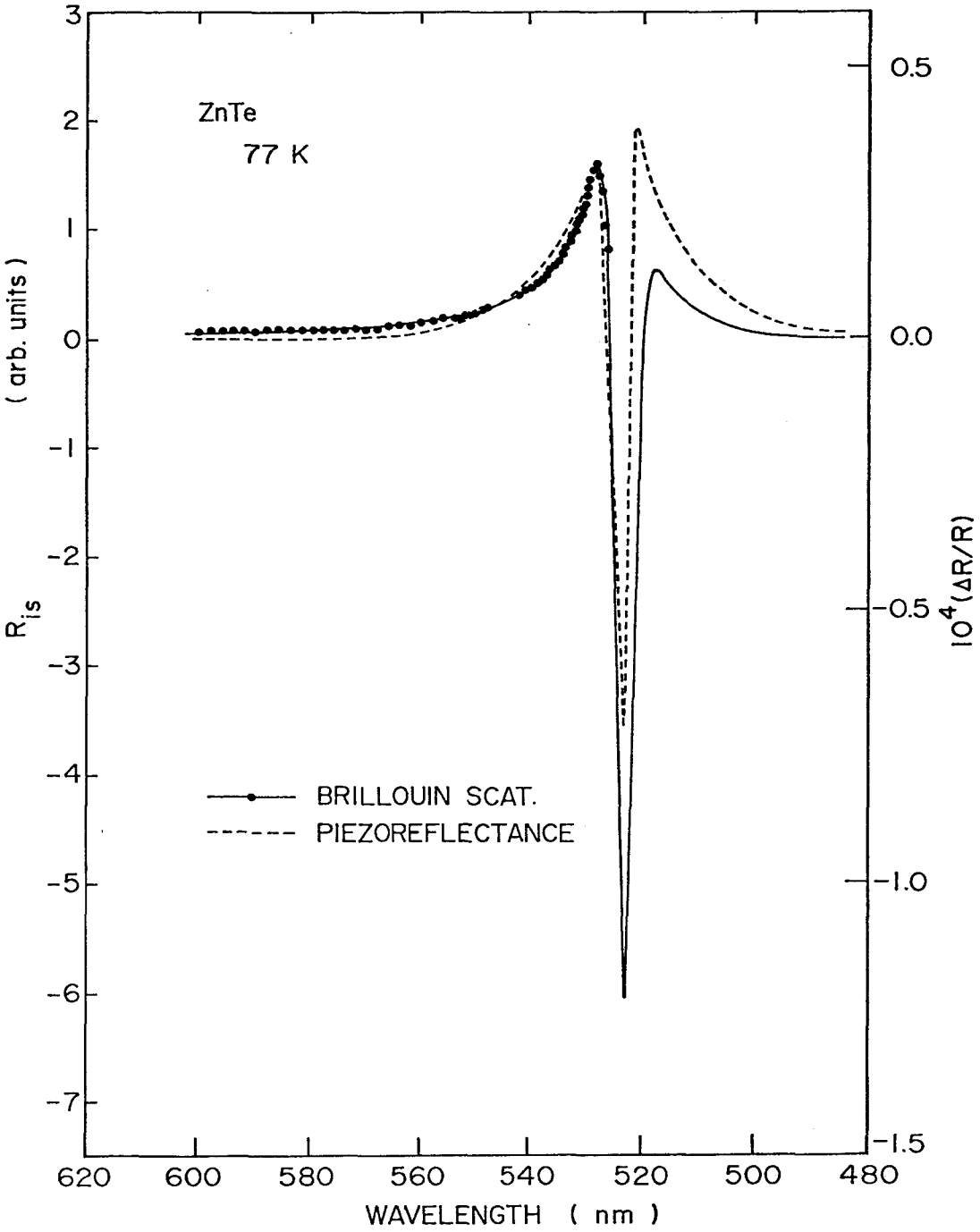

FIG. 8-7. Comparison of the Brillouin term R_{is} (same as Fig. 8-6) with the piezoreflectance spectrum of ZnTe at 77 K. The piezoreflectance spectrum (dashed line) is from Mathieu *et al* (Ref. 260).

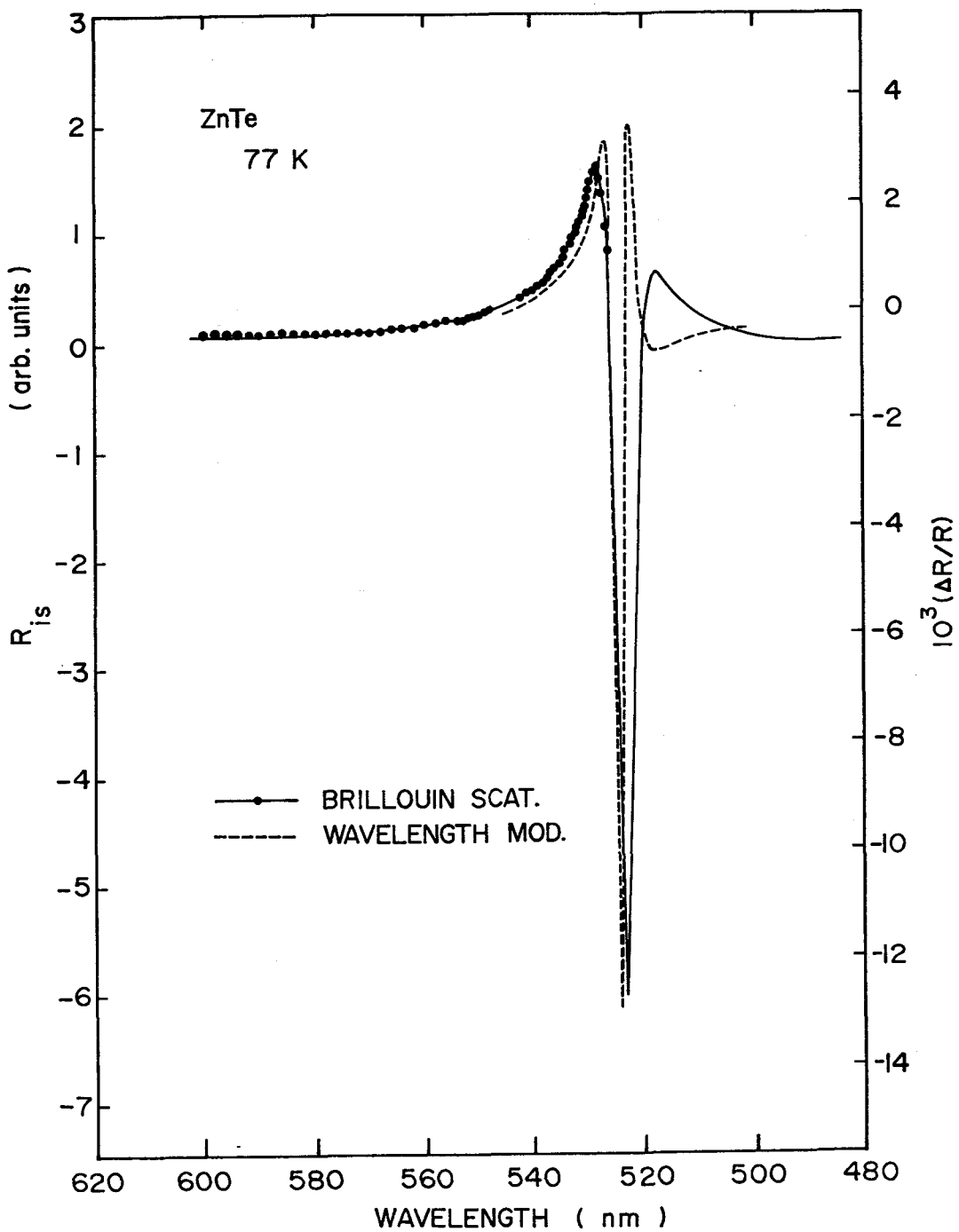

FIG. 8-8. Comparison of the Brillouin term R_{is} (same as Fig. 8-6) with the wavelength-derivative spectroscopy of ZnTe at 77 K. The wavelength-derivative spectroscopy is from Barbier *et al* (Ref. 262).

birefringence. An excellent agreement between the line shape of R_{is} and the piezoreflectance spectrum is seen in the figure.

Figure 8-8 shows a comparison of R_{is} (same as that of Fig. 8-6) with the wavelength-derivative spectroscopy. The experimental wavelength-derivative spectrum is from Barbier *et al.*[262] In the wavelength-derivative modulation, an external perturbation is not applied to the sample. This modulation, thus, gives essentially the derivative of the optical constants and hence its interpretation involves only the theory of those optical constants. It is obvious from Fig. 8-8 that a reasonable agreement between the line shape of R_{is} and the wavelength-derivative spectrum can be obtained.

We have also found that the line shapes of R_{is} [Figs. (8-5) — (8-8)] are very similar to the wavelength-modulated reflectance spectra obtained in semiconductors such as ZnSe, ZnTe and CdS.[263-266]

Let us now consider the reflectance structure appearing in the vicinity of the M_0 critical point [see Figs. (8-5) — (8-8)]. The calculated line shapes of the first derivatives presented in Fig. 8-4 are based on the simple model in which only the transition between one-electron energy bands is taken into account. The exciton effects are known to affect significantly the one-electron optical constants in the neighborhood of critical points. Figure 8-9 shows the line shapes of the first derivatives of the model dielectric constants for the band-to-band transitions [Eq. (2.184)] and discrete-exciton transitions [Eq. (2.199)] in the vicinity of the M_0 critical point. In the calculations, the damping parameter is properly taken into account in a way as described previously. It is clear from the figure that only the first derivative of the dielectric constant for the discrete-exciton transitions gives sharp negative peak in the region of the ground-state exciton energy (E_{x1}). The sharp negative peaks observed in the modulation spectra are, therefore, easily understood to be due to the discrete-exciton transitions.

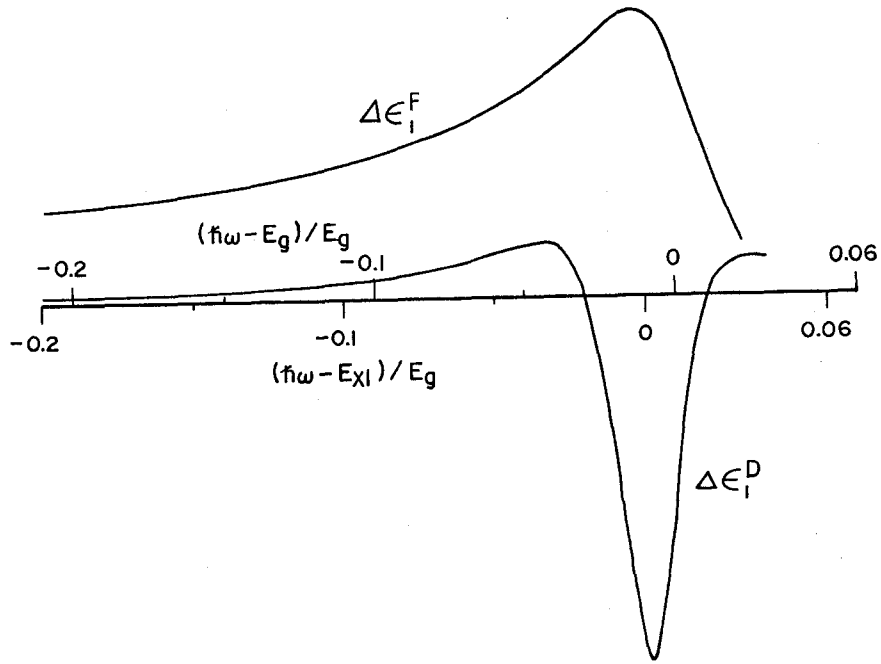

FIG. 8-9. Line shapes of the first derivatives of the model dielectric constants for the band-to-band transitions [Eq. (2.184)] and discrete-exciton transitions [Eq. (2.199)] in the vicinity of the M_0 critical point. The damping parameter is taken into account in the calculations.

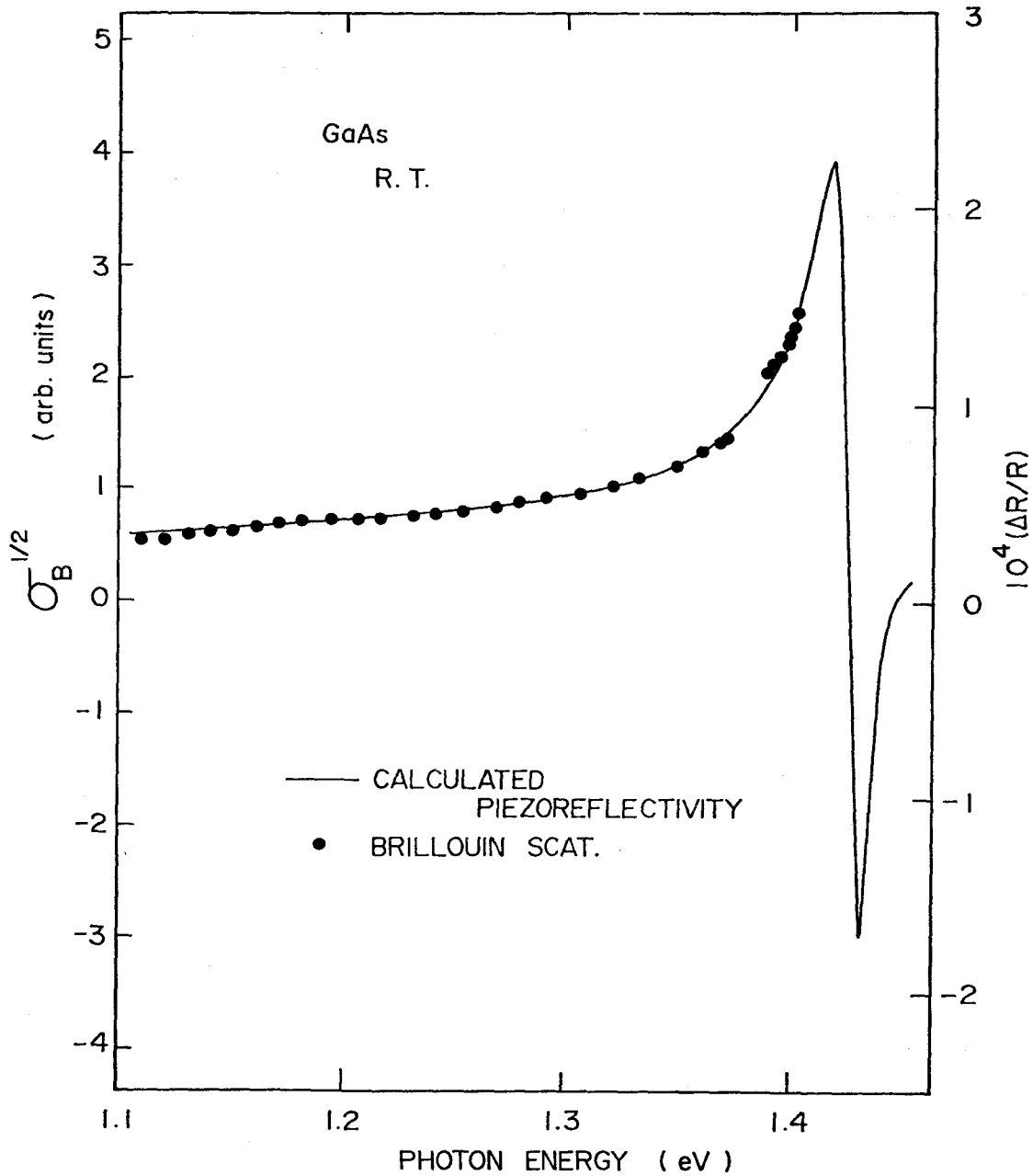

FIG. 8-10. Comparison of the calculated piezoreflectivity (solid curve) from Engeler *et al.* (Ref. 267) with the experimentally derived Brillouin-scattering data of GaAs. The Brillouin-scattering data are from Garrod and Bray (Ref. 25).

In Fig. 8-10, we show a comparison of the calculated piezoreflectivity with the experimentally derived Brillouin-scattering data ($\sigma_B^{\frac{1}{2}}$) of GaAs. The Brillouin-scattering data are from Garrod and Bray.[25] By means of the K-K relations [Eq. (2.189)], the relative reflectivity change can be related to a change of the absorption coefficient $\Delta\alpha(\omega)$:

$$\frac{\Delta R}{R} = A\int_0^\infty \frac{\Delta\alpha(\omega')d\omega'}{(\omega')^2 - \omega^2} + B\Delta\alpha(\omega) \quad , \qquad (8.24)$$

where A and B are constants corresponding to the fractional coefficients α and β of Eq. (8.10), respectively. The first and second terms of Eq. (8.24) correspond to the contributions of the changes $\Delta\varepsilon_1$ and $\Delta\varepsilon_2$ to the piezoreflectance spectroscopy, respectively. [Note that the absorption coefficient is directly related to the imaginary part of the dielectric constant through Eq. (2.198)]. The spectral shape of the stress-induced change in the absorption coefficient $\Delta\alpha(\omega)$ can be calculated by taking account of the rigid shift of the band-gap energy with stress. Then, the piezoreflectivity can be obtained from Eq. (8.24). The spectrum shown in the figure is calculated by Engeler *et al.*[267] using this procedure. Good agreement between the calculation (piezoreflectivity) and experiment (Brillouin scattering) is clearly seen in the figure.

We have demonstrated in Chapter V that the resonance features of the Brillouin-scattering efficiencies should be estimated sufficiently from the numerically calculated spectral dependence of the derivatives of the optical constants. The results presented in this Chapter, moreover, demonstrate that the experimental spectra of the first-derivative modulation spectroscopy are very suitable for the purpose of direct comparison with the resonance curves of the Brillouin-scattering efficiencies.

CHAPTER IX

RESONANT BRILLOUIN SCATTERING IN GaP NEAR THE INDIRECT ABSORPTION EDGE

9.1 INTRODUCTION

Resonance phenomena of the Raman- and Brillouin-scattering intensities in direct-gap semiconductors have recently received a considerable attention both theoretically and experimentally. Resonance effect involving indirect [268-273] or dipole forbidden transitions[274,275] has also been examined by several authors. Experimental data of resonant Raman scattering in the indirect-gap materials such as Si,[269,270] GaP[268,270] and AgBr[271] showed very weak or nonresonance feature in the indirect-gap region. Recently, Chiang *et al.*[276] have reported no existence of resonance behavior in the Brillouin-scattering cross sections of the indirect-gap layer compound GaSe. On the contraty, we have observed a weak resonant cancellation of the Brillouin-scattering cross section in the region near the fundamental absorption edge of the indirect-gap layer compounds GaSe and GaS.[277] The resonance behaviors have been successfully interpreted in terms of the direct- and indirect-gap resonances for GaSe and GaS, respectively. This difference arises from the fact that the separation between the indirect- and direct-gap energies in these materials is relatively small for GaSe (a few tens of meV) but large for GaS (0.4 eV), and thus for GaSe the indirect-gap resonance should be masked off by the much stronger direct-gap one. (Details will be discussed

in the next Chapter).

The GaP crystal is a more suitable material to study some of the indirect-gap resonance behaviors, since it has three indirect gaps, $\Gamma_8^v \rightarrow X_6^c$ near 2.25 eV (room temperature), $\Gamma_8^v \rightarrow X_7^c$ near 2.48 eV (room temperature) and $\Gamma_8^v \rightarrow L_6^c$ near 2.67 eV (78 K), as well as the lowest direct gap $\Gamma_8^v \rightarrow \Gamma_6^c$ near 2.75 eV (room temperature). This material was in fact the first indirect-gap material examined by resonant-Raman-scattering experiments by Scott *et al.*[268] Subsequent resonant-Raman-scattering experiments on GaP have been studied by Bell *et al.*[54] and Weinstein and Cardona[53] in the region of the lowest-direct gap E_0, but no careful study has yet been undertaken of indirect-gap resonance in this material. Recently, Valdez[278] has observed significant resonant enhancement of the Raman-scattering efficiency near the 2.25 eV $\Gamma_{15}^v \rightarrow X_1^c$ ($\Gamma_8^v \rightarrow X_6^c$) indirect gap, but found no enhancement near the 2.67 eV $\Gamma_{15}^v \rightarrow L_1^c$ ($\Gamma_8^v \rightarrow L_6^c$) indirect gap. Trommer and Cardona[273] have observed selective resonant enhancement of the Raman-scattering efficiency in GaAs near the indirect $\Gamma_8^v \rightarrow L_6^c$ and $\Gamma_8^v \rightarrow X_6^c$ gaps. They have also found that the L-point conduction-band minima lie below those at the X points. Jain and Jayanthi[279] have recently analyzed the experimental data of Trommer and Cardona[273] and Klein *et al.*[270] by their proposed theoretical model of the indirect-gap resonance, and obtained a good agreement between the experiment and calculation.

In this Chapter, we shall report the resonance phenomena of the Brillouin-scattering cross sections in GaP by the transverse acoustical phonons in the region of the lowest indirect-gap energy by making use of the acoustical-domain injection method.[280] In Section 9.2, we present some physical properties of this material. The indirect-gap resonance process may be described by the 5th-order perturbation theory, i.e., the perturbation is two orders higher than that for the direct-gap resonance process [see Section 2.2]. In Section 9.3, we present theories of the indirect-optical transition and resonant

Brillouin scattering near an indirect absorption edge of semiconductors. A comparison of our data with theoretical calculation is made in Section 9.4. The spectral dependence of the photoelastic constants, $|p_{11} - p_{12}|$ and $|p_{44}|$, is also determined as a by-product of the Brillouin-scattering data.

9.2 PROPERTIES OF GaP

9.2.1 Electronic Band Structure

The III-V compound GaP forms crystal with the zincblende structure as shown in Fig. 4-1 (a) [solid circles: gallium atoms, open circles: phosphorus atoms]. The Brillouin zone for GaP is, thus, drawn in Fig. 4-2 (b). The electronic band structure of GaP has been studied by a number of groups, including Zallen and Paul,[282] Cohen and Bergstresser[141] and Walter and Cohen.[283] We show in Fig. 9-1 (a) the electronic band structure of GaP obtained from Zallen and Paul.[282] The states are labeled using the notation for the irreducible representations of the single group of the zincblende lattice. The lowest-lying conduction band is at the X point, 2.25 eV above the valence-band minimum at the Γ point. Dean and Thomas[284] have studied the fundamental absorption edge of GaP at many temperatures between 1.6 and 300 K. The corresponding transitions are found to be of the allowed indirect type and involve the creation of free excitons and electron-hole pairs. From the band-structure calculations, Cohen and Bergstresser[141] have predicted a conduction-band $X_1 - X_3$ heteropolar splitting in GaP of about 300 meV. Spitzer *et al.*[285] have observed an infrared absorption band in degenerate material, which they have attributed to the $X_1 \rightarrow X_3$ transition (310 meV). The next lowest conduction-band minimum is at the L point, at about 2.67 eV (78 K).[286] Dean *et al.*[287] have observed an unresolved indirect transition at 2.67 eV, which they have attributed to the $\Gamma_{15}^{v} \rightarrow X_3^{c}$ transition. However, Kyser and

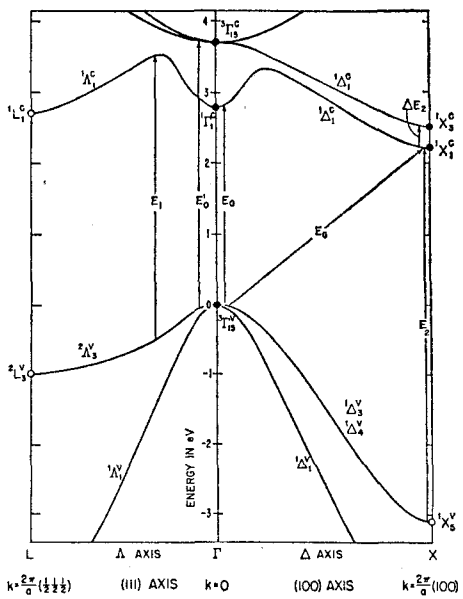

FIG. 9-1 (a). Electronic band structure of GaP obtained from Zallen and Paul (Ref. 282). The states are labeled using the notation for the irreducible representations of the single group of the zincblende lattice.

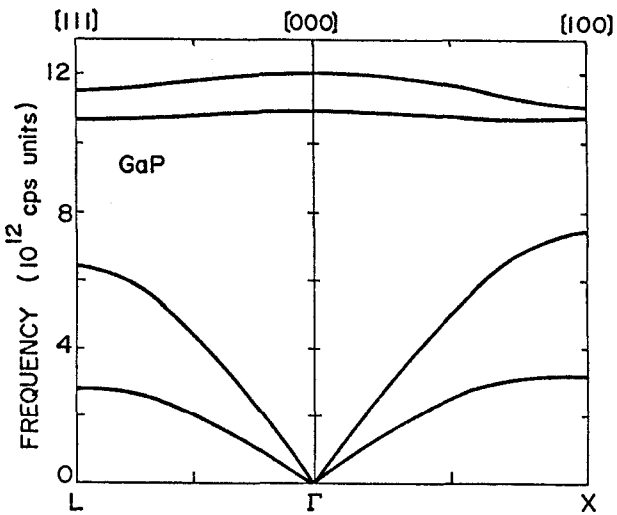

FIG. 9-1 (b). Phonon dispersion relations for PaP along directions Γ-L and Γ-X at room temperature (from Ref. 288).

Rehn[286] have recently studied this indirect-transition band by means of transverse-electroabsorption measurements, and concluded that the band is shown to be from Γ_{15}^{v} to L_1^c, contrary to the previous assignment. The lowest direct gap is at the Γ point (2.75 eV). Dean *et al.*[287] have examined this direct gap from an experimental aspect. Thompson *et al.*[45] have measured the electroreflectance spectra of a series of GaP-GaAs alloys and determined the direct interband transition energies such as E_0. $E_0+\Delta_0$, E_1, $E_1+\Delta_1$, E_0', $E_0'+\Delta_0'$, E_2 and $E_2+\delta$. Matatagui *et al.*[184] have also studied optical properties of GaP by means of the thermoreflectance technique.

9.2.2 Physical Properties

In this subsection, we shall summarize some physical properties of GaP which are of interest to us in the present work. The lattice dynamics of GaP crystal has been investigated by Banerjee and Varshni.[288] Figure 9-1 (b) shows the phonon dispersion relations for GaP along directions Γ-L and Γ-X.[288] The elastic compliance, elastic stiffness and static dielectric constants of the zincblende GaP crystal are listed in Table 9-1. The deformation potentials b and d of the Γ_{15} valence bands, lattice parameter a and crystal density g of GaP are also listed in this table. The elastic stiffness constants were measured by Weil and Groves by means of ultrasonic phase-comparison method. Yamada *et al.*[290] have recently determined the elastic constants of GaP from the Brillouin-scattering measurements using a Fabry-Perot interferometer. Their results are in good agreement with those listed in Table 9-1. The deformation potentials b and d (Pikus-Bir's notation) are from Glurdzhidze *et al.*[206] determined from the piezobirefringence measurements. Recently, Humphreys *et al.*[291] have also determined these deformation potentials to be b = -1.8 and d = -4.6 eV. Onton and Morgan[292] has studied the effect of a uniaxial stress on bound-exciton lines in GaP and found that the deformation potentials of the excitons are approximately an order of magnitude smaller

Table 9-1. Elastic compliance (S_{ij}), elastic stiffness (C_{ij}), static dielectric constant (ε_{11}), deformation potentials of the Γ_{15} valence bands (b and d), lattice parameter (a) and crystal density (g) of GaP at room temperature. S in 10^{-10} m^2/N; C in 10^{10} N/m^2; b and d in eV; a in Å; and g in g/cm^3.

Symbol	Numerical value
S_{11}	0.973[a]
S_{12}	-0.299[a]
S_{44}	1.419[a]
C_{11}	14.12[a]
C_{12}	6.253[a]
C_{44}	7.047[a]
$\varepsilon_{11}^{S}/\varepsilon_0$	10.18[b]
b	-1.8[c]
d	-4.0[c]
a	5.4504[d]
g	4.130[a]

[a]Reference 289.
[b]Reference 296.
[c]Reference 206.
[d]Reference 297.

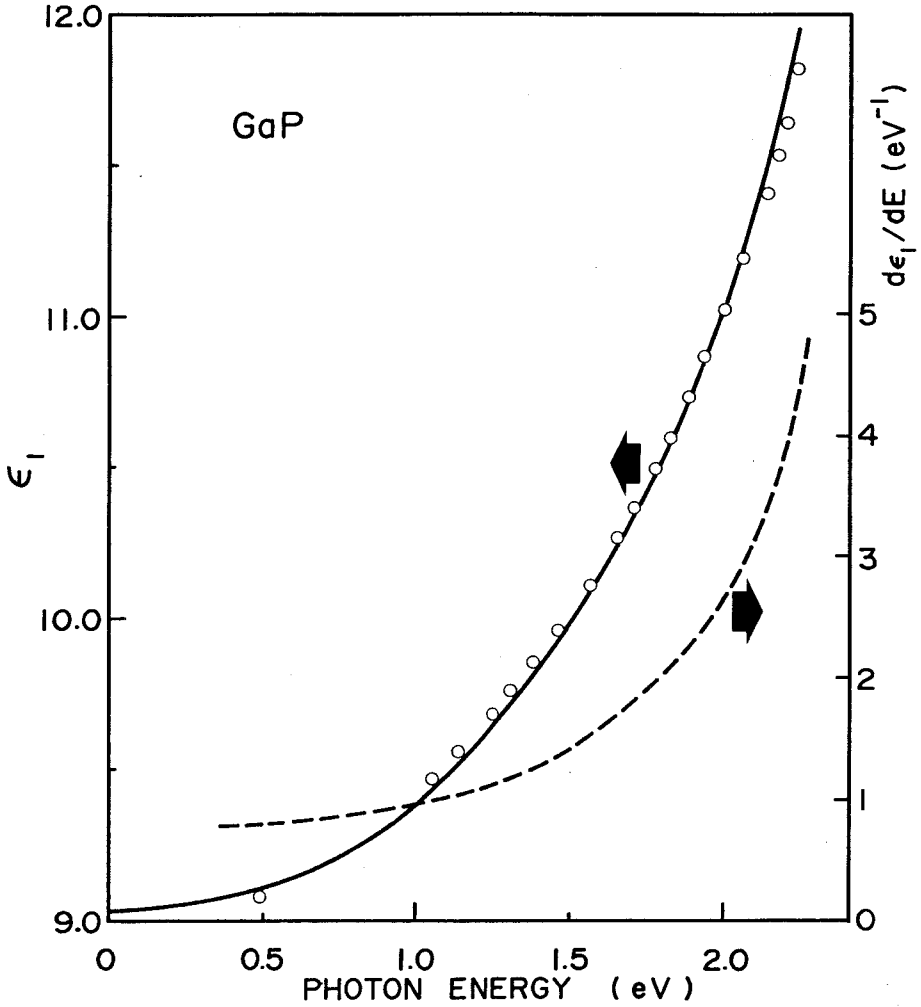

FIG. 9-2. Dielectric constant of GaP at room temperature in the region of transparency (from Ref. 294). The photon-energy derivative of the dielectric constant (in eV^{-1}) is also shown in the figure by dashed line.

than the corresponding free-hole deformation potentials. The stress-induced coupling between X_1^c and X_3^c conduction-band minima in GaP has recently been studied by Merle *et al.*[293] by means of the wavelength-modulated transmission spectroscopy and determined deformation potential of the X conduction band to be $|E_3| = 13$ eV.

Figure 9-2 shows the dielectric constant ε_1 for GaP as a function of photon energy at room temperature taken from the data of Ref. 294. The solid line is a fit of Eq. (6.1) to the experimental data. The photon-energy derivative of the dielectric constant, $d\varepsilon_1/dE$ (in eV^{-1}), is also shown in the figure by dashed line obtained by numerical differentiation.

9.3 THEORY OF LIGHT SCATTERING IN THE INDIRECT ABSORPTION EDGE

9.3.1 Indirect Optical Absorption

The band structure of GaP is schematically drawn in Fig. 9-3 in which the top of the valence band VB and the direct DCB (Γ point) and indirect ICB minima (X and L points) of the conduction bands are shown. The states labeled are those for the irreducible representations of the double group of the zincblende lattice. E_g^{ID} and E_g^D denote the lowest indirect- (≃ 2.25 eV) and direct-gap energies (≃ 2.75 eV), respectively.

We shall now consider a theory of the indirect optical absorption neglecting the electron-hole interaction (exciton interaction). The theory of indirect optical transitions can be developed by considering the perturbation Hamiltonian:[295]

$$H^{(p)} = H_{eR} + H_{eL} \quad , \tag{9.1}$$

with

$$H_{eR} = \sum_{cv\lambda K} \{f_{\chi e}(cv\lambda K)a^{\dagger}_{\lambda K}(c,v)c_{\chi e}\delta_{K,\chi} + f^*_{\chi e}(cv\lambda K)a_{\lambda K}(c,v)c_{\chi e}\delta_{K,-\chi}\}$$

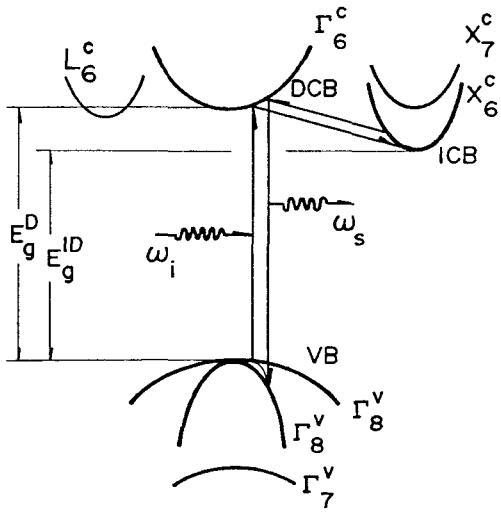

FIG. 9-3. Schematic diagram showing the indirect optical transition and Brillouin-scattering process. VB is the valence band and DCV and ICB are the direct and indirect conduction bands, respectively.

$$+ \text{c.c.}, \qquad (9.2)$$

$$H_{eL} = \sum_{\substack{cv\lambda K, c'v'\lambda'K' \\ \eta\xi}} \{h_{\eta\xi}(cv\lambda K, c'v'\lambda'K')a^{\dagger}_{\lambda K}(c,v)a_{\lambda' K'}(c',v')b^{\dagger}_{\eta\xi}\delta_{K-K',-\eta}$$

$$+ h^{*}_{\eta\xi}(cv\lambda K, c'v'\lambda'K')a^{\dagger}_{\lambda K}(c,v)a_{\lambda' K'}(c',v')b_{\eta\xi}\delta_{K-K',\eta}\} , \qquad (9.3)$$

where $f_{\chi e}$, $f^{*}_{\chi e}$, $h_{\eta\xi}$ and $h^{*}_{\eta\xi}$ are coupling parameters, and the subscripts c, v, λ, K ····, etc., have similar meanings to those appeared in Section 2.2. H_{eR} is the electron-radiation perturbation which is linear in both electron ($a^{\dagger}_{\lambda K}$ and $a_{\lambda K}$) and photon creation-annihilation operators ($c^{\dagger}_{\chi e}$ and $c_{\chi e}$), and H_{eL} is the electron-lattice perturbation which is linear in phonon creation-annihilation operator ($b^{\dagger}_{\eta\xi}$ and $b_{\eta\xi}$) but bilinear in electron one. The total Hamiltonian is now taken from Eqs. (2.1) and (9.1) as

$$H = H^{(0)} + H^{(p)} \qquad . \qquad (9.4)$$

We perform the cannonical transformation of the form [see Section 2.2]

$$\tilde{H} = e^{-iS}He^{iS} = H - i[S, H] \qquad , \qquad (9.5)$$

where S is chosen such that

$$S = \frac{1}{i}[S, H^{(0)}] = H^{(p)} \qquad . \qquad (9.6)$$

Using Eq. (2.18), we obtain

$$S = \frac{1}{i}(X + X' + Y + Y') \qquad , \qquad (9.7)$$

where

$$X = -\sum_{\substack{cv\lambda K \\ \chi e}} \frac{f_{\chi e}(cv\lambda K)a^{\dagger}_{\lambda K}(c,v)C_{\chi e}}{E_{\lambda K} - \hbar\omega_{\chi e}} \delta_{K,\chi} + \text{c.c.}, \qquad (9.8a)$$

$$X' = \sum_{\substack{cv\lambda K \\ \chi e}} \frac{f^{*}_{\chi e}(cv\lambda K)a_{\lambda K}(c,v)c_{\chi e}}{E_{\lambda K} + \hbar\omega_{\chi e}} \delta_{K,-\chi} - \text{c.c.}, \qquad (9.8b)$$

$$Y = - \sum_{\substack{cv\lambda K, c'v'\lambda'K' \\ \eta\xi}} \frac{h_{\eta\xi}(cv\lambda K, c'v'\lambda'K') a^{\dagger}_{\lambda K}(c,v) a_{\lambda', K'}(c',v') b^{\dagger}_{\eta\xi}}{(E_{\lambda K} - E_{\lambda' K'}) + \hbar\omega_{\eta\xi}} \delta_{K-K',-\eta} \quad , \tag{9.8c}$$

$$Y' = \sum_{\substack{cv\lambda K, c'v'\lambda'K' \\ \eta\xi}} \frac{h^{*}_{\eta\xi}(cv\lambda K, c'v'\lambda'K') a^{\dagger}_{\lambda K}(c,v) a_{\lambda', K'}(c',v') b_{\eta\xi}}{(E_{\lambda K} - E_{\lambda' K'}) - \hbar\omega_{\eta\xi}} \delta_{K-K',\eta} \quad . \tag{9.8d}$$

Substituting Eq. (9.4) into Eq. (9.5), we obtain

$$\tilde{H} = H^{(0)} - i[S, H^{(p)}] \quad . \tag{9.9}$$

The lowest-order commutator that contributes to the indirect optical absorption can, thus, be written as

$$\begin{aligned} H^{ID} &= i[S, H^{(p)}] = [(X + X' + Y + Y'), H^{(p)}] \\ &= [(X + X' + Y + Y'), (H_{eR} + H_{eL})] \quad . \end{aligned} \tag{9.10}$$

Rejecting the terms which do not contain photon operator and omitting two-photon transition processes, one can rewrite Eq. (9.10) as

$$H^{ID} = XH_{eL} + (Y + Y')H_{eR} - H_{eL}X - H_{eR}(Y + Y') \quad . \tag{9.11}$$

The transition probability per unit time of a process is, thus, given by

$$W \propto |\langle f| H^{ID} |i\rangle|^2 \, \delta(\omega_i - \omega_f) \quad , \tag{9.12}$$

where $|i\rangle$ and $|f\rangle$ are the initial and final states, respectively. From Eq. (9.12), we obtain the following expression for a typical process sketched in Fig. 9-3:

$$W \propto \left| \frac{\langle f|H_{eL}|m\rangle\langle m|H_{eR}|i\rangle}{E^{D}_{g}(\vec{k}_1) - \hbar\omega} \right|^2 \delta(E_c(\vec{k}_2) - E_v(\vec{k}_1) - \hbar\omega + \hbar\omega_q) \quad , \tag{9.13}$$

where $\vec{k}_1$ and $\vec{k}_2$ are the wave vectors at the Γ and X points, respectively.

We suppose that the quantity

$$C_1 \equiv \sum_f \left| \sum_m \frac{\langle f|H_{eL}|m\rangle\langle m|H_{eR}|i\rangle}{E_g^D(\vec{k}_1) - \hbar\omega} \right| \tag{9.14}$$

to a good degree of approximation is regarded as independent of the wave vectors $\vec{k}_1$ and $\vec{k}_2$ in the vicinity of the extrema. This is, in fact, a good approximation for allowed transitions when the energy denominator in Eq. (9.13) is not too small. Equation (9.13) corresponds to the process in which the valence electron is scattered to the conduction state (ICB) and a photon of energy $\hbar\omega$ and a phonon of momentum $\vec{q} = \vec{k}_2 - \vec{k}_1$ (and energy $\hbar\omega_q$) are both absorbed. $\langle m|H_{eR}|i\rangle$ is the momentum matrix element between the VB and DCB extrema located near Γ point and separated by $E_g^D(\vec{k}_1)$, and $\langle f|H_{eL}|m\rangle$ is the matrix element of the phonon-assisted transition from DCB to ICD, where for GaP they involve the TA, LA, TO and TA + LO^{Γ} phonons.[284] Considering the case of indirect-optical transitions between spherical bands and summing over $\vec{k}_1$ and $\vec{k}_2$ of Eq. (9.13) in the Brillouin zone, we obtain the following expression for the absorption coefficient $\alpha(\omega)$:

$$\alpha(\omega) \begin{cases} \propto C_1(\hbar\omega - E_g^{ID}(0) + \hbar\omega_q)^2 & \text{for } \hbar\omega > E_g^{ID}(0) - \hbar\omega_q \\ = 0 & \text{for } \hbar\omega < E_g^{ID}(0) - \hbar\omega_q . \end{cases} \tag{9.15}$$

The absorption of light begins at $\hbar\omega = E_g^{ID}(0) - \hbar\omega_q$, as seen in Eq. (9.15). Another contribution to the indirect-optical transition is due to the emission of a phonon and can be obtained using the same procedure, where the only difference from the above case is the sign of the photon energy.

9.3.2 Resonant Light Scattering

The indirect-gap Brillouin-scattering process is described by a 5th-order time-dependent perturbation,[281] i.e., the perturbation is two orders higher

than that for the direct-gap resonance. This process contains in part the indirect optical transition as discussed in Section 9.3.1. One of such processes may be explained as follows [see Fig. 9-3]; (i) A photon (ω_i) incident on a crystal in the ground state $|0\rangle$ creates a virtual electron-hole pair state $|\alpha\rangle$ in bands DCB and VB. (ii) The electron in the $|\alpha\rangle$ state is scattered to ICB by the phonon-assisted transition, forming a new pair state $|\beta\rangle$ in bands ICB and VB. (iii) The electron or hole then interacts with an acoustical phonon *via* deformation potential, changing its state to a $|\beta'\rangle$ state. (iv) The electron in the $|\beta'\rangle$ state is scattered to DCB by the phonon-assisted transition, forming a pair state $|\alpha'\rangle$ in bands DCB and VB. (v) The system returns from $|\alpha'\rangle$ to the ground state $|0\rangle$ with emission of a scattered photon (ω_s).

According to Loudon,[281] the Brillouin-tensor term arising from such an indirect-gap resonance process may be given by

$$R_{is}^{ID} \propto \left| \sum_{\alpha,\beta,\beta',\alpha'} \frac{\langle 0|H_{eR}|\alpha'\rangle\langle\alpha'|H_{eL}^{A}|\beta'\rangle\langle\beta'|H_{eL}^{B}|\beta\rangle}{(E_{\alpha'}(\vec{k}_1,\vec{k}_1)-\hbar\omega_s)(E_{\beta'}(\vec{k}_2,\vec{k}_1)-\hbar\omega_q-\hbar\omega_s)} \right.$$

$$\left. \times \frac{\langle\beta|H_{eL}^{A}|\alpha\rangle\langle\alpha|H_{eR}|0\rangle}{(E_{\beta}(\vec{k}_2,\vec{k}_1)-\hbar\omega_q-\hbar\omega_i)(E_{\alpha}(\vec{k}_1,\vec{k}_1)-\hbar\omega_i)} \right| , \qquad (9.16)$$

where the matrix element $\langle|H_{eL}^{A}|\rangle$ represents the phonon-assisted transition through the deformation-potential scattering, $\langle|H_{eL}^{B}|\rangle$ represents the deformation-potential scattering arising from an acoustical-phonon interaction of the intermediate electronic state, responsible for the Brillouin process, and $E_{\alpha}(\vec{k}_1,\vec{k}_1) = E_{\alpha c}(\vec{k}_1) - E_{\alpha v}(\vec{k}_1)$ is the electronic-energy difference between the conduction and valence bands in the pair state $|\alpha\rangle$ and so forth. The matrix element $\langle|H_{eL}^{B}|\rangle$ has already been calculated to explain the direct-gap resonance data for both the zincblende- and wurtzite-type crystals [see Section 2.2.3].

Equation (9.16) can be simplified under the following assumption: the

factor

$$C_2 \equiv \left| \sum_{\alpha,\beta,\beta',\alpha'} \frac{\langle 0|H_{eR}|\alpha'\rangle\langle\alpha'|H^A_{eL}|\beta'\rangle\langle\beta'|H^B_{eL}|\beta\rangle\langle\beta|H^A_{eL}|\alpha\rangle\langle\alpha|H_{eR}|0\rangle}{(E_{\alpha'}(\vec{k}_1,\vec{k}_1)-\hbar\omega_s)(E_\alpha(\vec{k}_1,\vec{k}_1)-\hbar\omega_i)} \right| \quad (9.17)$$

is independent of the wave vectors $\vec{k}_1$ and $\vec{k}_2$ in the vicinity of the extrema of the bands, as similar to Eq. (9.14). Such an assumption was found to be valid for the analysis of the absorption data.[284] Equation (9.16) is, thus, reduced to the form:

$$R^{ID}_{is} \propto C_2 \sum_{\vec{k}_1,\vec{k}_2} \left| \frac{1}{(E_\beta(\vec{k}_2,\vec{k}_1)-\hbar\omega_q-\hbar\omega_s)(E_\beta(\vec{k}_2,\vec{k}_1)-\hbar\omega_q-\hbar\omega_i)} \right| . \quad (9.18)$$

This expression is similar to that obtained in the case of the forbidden yellow exciton in Cu_2O.[275] We can, therefore, calculate Eq. (9.18) in the same way as was done in this Reference. The result is written by the following equation:

$$R^{ID}_{is} \begin{cases} \propto C_2 \dfrac{\alpha(\omega)}{\Gamma(\omega)} & \text{for } \hbar\omega > E^{ID}_g(0) - \hbar\omega_q \\ = 0 & \text{for } \hbar\omega < E^{ID}_g(0) - \hbar\omega_q \end{cases} , \quad (9.19)$$

where $\alpha(\omega)$ is the absorption coefficient given by Eq. (9.15), $\Gamma(\omega)$ is the lifetime-broadening energy of the scattering state, and $\hbar\omega$ is the photon energy. It is clear from Eq. (9.19) that the indirect-gap resonance begins as the incident-photon energy exceeds the energy of $E^{ID}_g(0) - \hbar\omega_q$.

9.4 EXPERIMENTAL RESULTS AND DISCUSSION

9.4.1 Brillouin-Scattering Cross Section

Figures 9-4 and 9-5 show the spectral dependence of the Brillouin-scattering cross sections in GaP for the T1- and T2-mode phonons, respectively, measured at room temperature in the region near the indirect-gap energy. All the data

points were obtained by carrying out a correction for absorption of light. The phonon frequency was selected to be 0.4 GHz for both phonon modes by properly setting the incident and scattering angles [see Section 3.3.3]. It was confirmed that the sound velocity of each mode domain agrees well with those obtained from the ultrasonic phase-comparison method[289] and Brillouin-scattering technique using a Fabry-Perot interferometer.[290]

The data of the Brillouin-scattering cross sections show a monotonic decrease when the incident-photon energy is near resonance with the indirect gap of GaP. Such a decrease implies a cancellation between the resonant (indirect gap) and nonresonant (direct gap) contributions in the Brillouin tensor. However, the resonant cancellation observed here is not complete in contrast to the case for the direct-gap semiconductors such as ZnSe and ZnTe, as discussed in Chapter IV. It seems that this is due to the weak resonance nature in the indirect gap, implying that the resonance is two perturbation orders higher than for the direct-gap resonance.

It was demonstrated in Chapter V that the resonance behaviors of Brillouin (Raman) scattering in the direct-gap semiconductors can be predicted from an expression based on the quasi-static approximation, where in this appriximation the phonons are assumed to act like static perturbations of the electronic structure of the crystal through the electron-phonon interaction. This perturbation causes a change in the dielectric constant of the crystal. The quasi-static approximation shows that the direct-gap term of the Brillouin-scattering efficiency is proportional to the first derivative of the dielectric constant with respect to the incident-photon energy. Accordingly, we can express the direct-gap (nonresonant) terms in the Brillouin tensor of GaP as follows:

$$R^{D}_{is} \propto \frac{d\varepsilon}{dE} \qquad (9.20)$$

and

$$R_0 \ (= \text{const.}) \quad , \tag{9.21}$$

where R_{is}^D arises from the lowest direct gaps (Γ point) such as E_0 and $E_0+\Delta_0$ gaps, R_0 arises from the higher direct gaps such as E_1, $E_1+\Delta_1$ and E_2 gaps, and E in Eq. (9.20) is the incident-photon energy. The term R_{is}^D and R_0 are opposite in sign to the indirect-gap resonance term R_{is}^{ID} as suggested to account for the resonant cancellation.

From Eqs. (9.19) — (9.21), the Brillouin-scattering cross section can be written as

$$\sigma_B \propto |R_{is}^{ID} + R_{is}^D + R_0|^2 \quad . \tag{9.22}$$

In Figs. 9-4 and 9-5, the theoretical curves obtained from Eq. (9.22) are shown by the solid lines. The indirect-gap resonance term R_{is}^{ID} is obtained from the absorption data measured by Dean and Thomas[284] using Eq. (9.19) with neglecting a dependence of Γ on ω. The direct-gap resonance term R_{is}^D is calculated by differentiating the data of dielectric constant reported in Ref. 294 [see Fig. 9-2]. The constant term R_0 is adjusted to give best fitting with the experimental data. It has been reported that three types of the indirect transitions are present in GaP below the direct $\Gamma_8^v \rightarrow \Gamma_6^c$ gap; $\Gamma_8^v \rightarrow X_6^c$ transition near 2.25 eV (room temperature),[284] $\Gamma_8^v \rightarrow X_7^c$ transition near 2.48 eV (room temperature)[287] and $\Gamma_8^v \rightarrow L_6^c$ transition near 2.67 eV (78 K).[286] It is obvious that the indirect-gap resonance observed here is arising from only the $\Gamma_8^v \rightarrow X_6^c$ transition, since the measured photon-energy region is limited up to 2.30 eV (540 nm). The dashed lines in the figures are also calculated from Eq. (9.22) without taking into account the constant term R_0. The solid lines show a quite good agreement with the experimental data. The best-fitting values of the constant term R_0 are found to be 8.0 and 14.0 (in units of eV^{-1}) for the T1- and T2-modes, respectively. These values are relatively large and opposite in sign to those obtained in the direct-gap

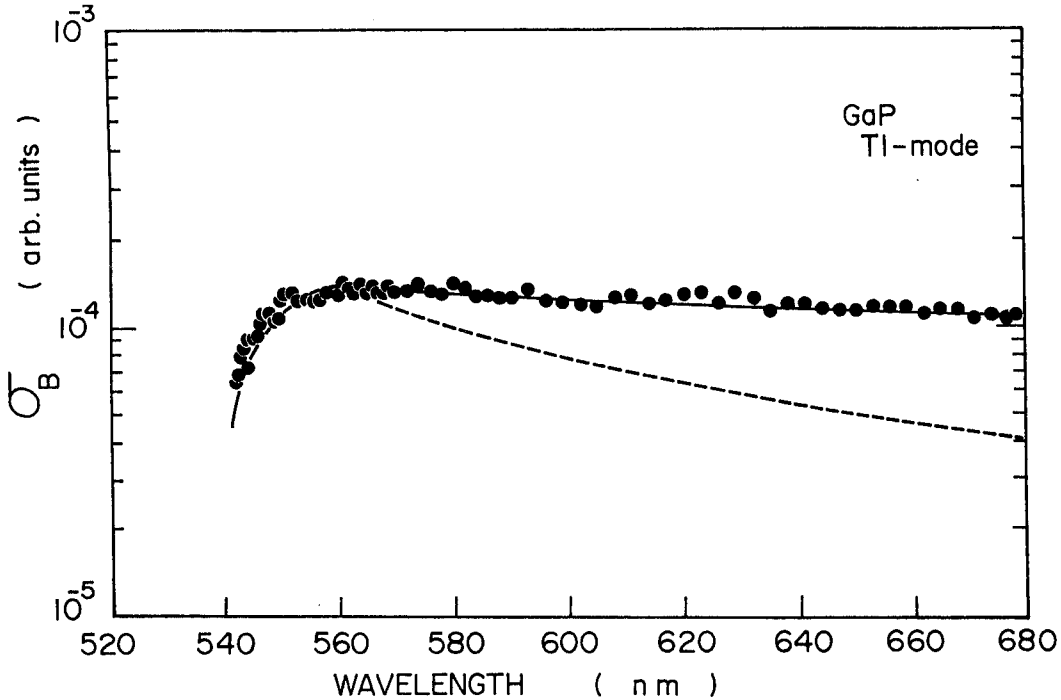

FIG. 9-4. Spectral dependence of the Brillouin-scattering cross sections by 0.4 GHz Tl-mode phonons in GaP at room temperature. The solid and dashed lines are obtained from theory in the text.

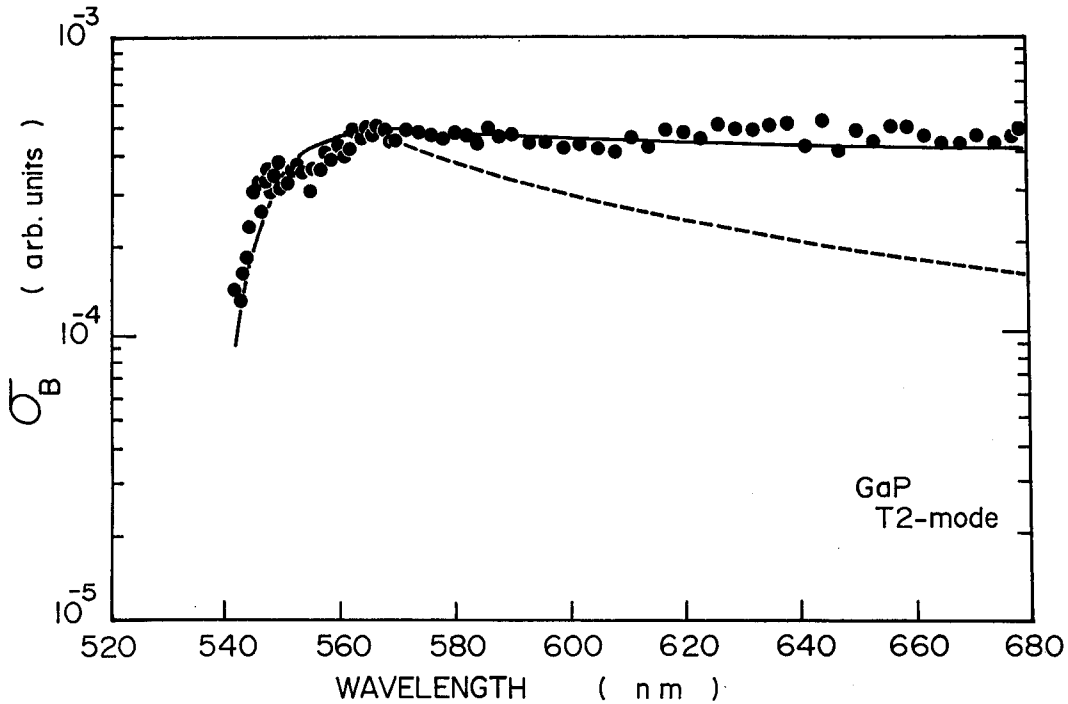

FIG. 9-5. Spectral dependence of the Brillouin-scattering cross sections by 0.4 GHz T2-mode phonons in GaP at room temperature. The solid and dashed lines are obtained from theory in the text.

semiconductors such as ZnSe, ZnTe and CdS [see Chapter V]. Similar results have also been found in other indirect-gap semiconductors GaSe and GaS [see next Chapter].

The indirect-gap resonance is sometimes masked off by the strong direct-gap resonance. In the present study, however, the weak resonant cancellation has been clearly found in the indirect absorption edge of GaP. This is presumably accounted for the fact that the separation between the indirect and direct gaps of this material is considerably large ($\simeq$ 0.5 eV) and thus the direct-gap resonance is relatively weak in the photon-energy region near the indirect gap. Equation (9.19) clearly indicates that the indirect-gap resonance depends on the lifetime broadening of the scattering states, i.e., the resonance becomes strong with decreasing Γ. The effect of the lifetime broadening on the Brillouin-scattering intensity has been found by the present auther in the direct-gap semiconductors [Chapter VII]. The resonance curves of the direct-gap semiconductors have clearly shown that the lifetime broadening suppresses the direct-gap resonances and consequently a new resonant cancellation appears in the region very close to the discrete exciton states. In the present study, unfortunately, we were not able to determine the value of Γ from the fit to the experimental data with Eq. (9.22), since the indirect-gap term R_{is}^{ID} in Eq. (9.19) contains the prefactor C_2 (C_2/Γ) as an adjustable parameter.

9.4.2 Photoelastic Constant

It has been shown by Dixon[46] that the GaP crystal is exceptionally good material for use in light deflectors and modulators. If an acoustical strain S_{kl} propagates in a crystal the induced change in the dielectric constant is $\Delta(1/\varepsilon)_{ij} = p_{ijkl}S_{kl}$, where p_{ijkl} is the component of the photoelastic tensor. Modulation of the dielectric constant induced by the acoustical strain results in a diffraction of an incident light beam. It is, therefore, very important

to investigate the spectral dependence of the photoelastic constant. The components of the photoelastic tensor, $p_{11} - p_{12}$ and p_{44}, are involved in the Brillouin-scattering cross section from the T1- and T2-mode phonons, respectively. In a macroscopical point of view, as discussed in Chapter VI, the Brillouin-scattering cross section is proportional to the square of the relevant photoelastic constant. The spectral dependence of the photoelastic constants can, thus, be easily determined from the Brillouin-scattering data.

Figures 9-6 (a) and (b) show the spectral dependence of $|p_{11} - p_{12}|$ and $|p_{44}|$, respectively. Absolute values of these constants are given in the figures; they were determined by normalizing our data to the absolute ones measured by Dixon[46] and Yamada *et al.*[290] at a light wavelength of 632.8 nm. The solid curves in the figures are not theoretical ones but probable curves of the experimental data. Note that the spectral dependence of the photoelastic constants obtained here shows very weak dispersion at light wavelength longer than 550 nm. This arises from the fact that the photoelastic constants show no sign reversal in the region below the indirect-gap energy, namely R_{is}^{D} and R_0 of Eq. (9.22) have the same sign (i.e., plus), in contrast to the case for the direct-gap materials such as ZnSe, ZnTe and CdS. Therefore, we can conclude that the GaP crystal is potentially useful in device application such as deflectors and modulators of light wavelengths longer than 550 nm.

Recently, Canal *et al.*[207] have reported experimental data of the photoelastic constants in GaP in the region below and above the indirect $\Gamma_8^v \rightarrow X_6^c$ gap obtained from the piezobirefringence measurements employing the Raman-scattering technique as a probe. Our data show a reasonable agreement with those reported by Canal *et al.*, but they analyzed their data by taking into account only the real part of the dielectric constant of the direct gaps (neglecting the contribution from the imaginary part of the dielectric constant). We have proposed in Section 6.4 new method of the piezobirefringence analysis

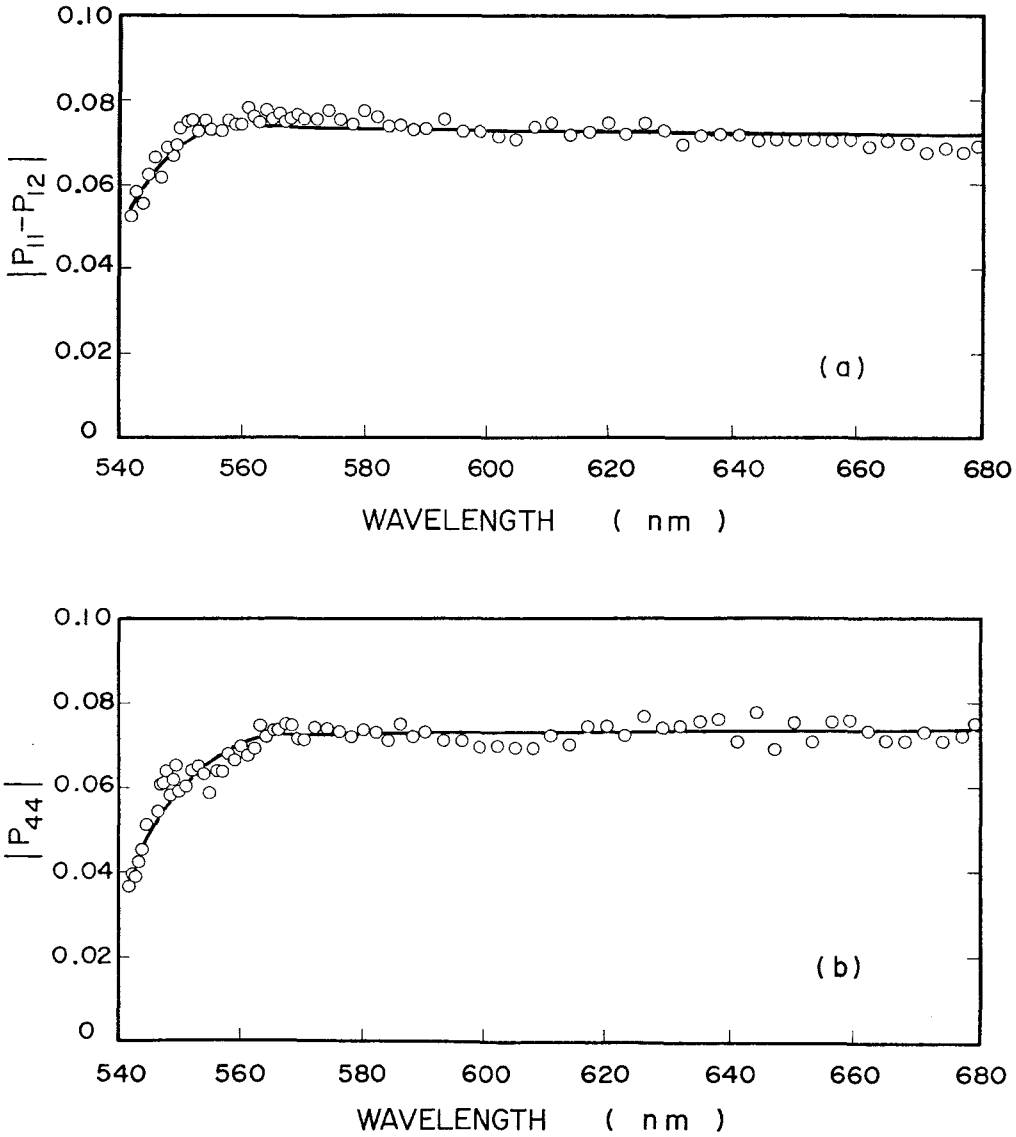

FIG. 9-6. Spectral dependence of the photoelastic constants in GaP. (a) $|p_{11} - p_{12}|$; (b) $|p_{44}|$. They are determined by normalizing our data to the absolute ones measured by Dixon (Ref. 46) and Yamada *et al.* (Ref. 290) at a light wavelength of 632.8 nm.

in an opaque region of materials in which the stress-induced changes in both the real and imaginary parts of the dielectric constant are properly taken into account. Using our proposed model, we have confirmed that their analysis is thought to be a good degree of approximation.

CHAPTER X

RESONANT BRILLOUIN SCATTERING IN THE LAYER-TYPE COMPOUNDS GaSe AND GaS

10.1 INTRODUCTION

The layer-type semiconductors GaSe and GaS are III-VI compounds which present a strong anisotropic behavior of their physical properties due to the singularity of the crystal structures.[47,298] These compounds have been shown to have fine structures associated with strong excitonic transitions in the vicinity of the fundamental absorption edges. In recent years, there have been extensive studies on resonant light scattering around excitonic transitions in various semiconductors.[8] Resonant Raman scattering around the direct-exciton levels in GaSe has already been reported by several authors.[299-303] Resonant Raman scattering in mixed GaS_xSe_{1-x} crystals ($0 \leq x \leq 0.23$) has also been studied by Chiang, Camassel, Voitchovsky and Shen.[302,304] The resonance-Raman spectra in such semiconductors have clearly shown resonant enhancement around the direct-excitonic-transition region. Resonant Brillouin scattering in the layer-type compound (GaSe) has first been reported by Chiang, Dumas and Shen.[276] However, the measured spectral dependence of the Brillouin-scattering cross section has shown no obvious resonance feature in the region near the direct-excitonic-transition region. The absence of resonance feature is thought to be due to that the exciton-acoustical phonon coupling for the electronic states near the band gap is rather weak so that the nonresonant contribution always

dominates in the Brillouin-scattering process.

Until now, at least in our knowledge, no attempt has been made on resonant Brillouin (Raman) scattering in GaS. The absorption edge of GaS is characterized by the indirect-optical transitions,[305-309] in contrast to that of GaSe (direct-optical transitions).[306,307,310,311] The resonance effect in the direct-gap region has been the subject of a number of reports, but the same effect involving the indirect-energy gap has received little attention. The GaS crystal is thought to be more suitable material to study some of the indirect-gap resonance effects since the separation between the indirect- and direct-gap energies of this material is relatively large (about 0.4 eV),[305,307] as similar to that of GaP (Section IX). Therefore, it is interesting to study some of the resonance effects especially around the indirect-energy gap of GaS.

In this Chapter, we investigate resonant Brillouin scattering in the layer-type semiconductors GaSe and GaS by the pure-transverse (PT) acoustical phonons in the photon-energy ranges of 1.55 — 1.99 eV (GaSe) and 1.70 — 2.59 eV (GaS). Previous work by Chiang *et al.*[276] was limited to the photon-energy range of 1.92 — 2.00 eV in GaSe using a tunable dye laser combined with a 3-path feedback-controlled Fabry-Perot interferometer (Brillouin scattering by thermal quasi-transverse acoustical phonons). We have carried out the resonant-Brillouin-scattering measurements by using the amplified acoustical-domain injection method, where the amplified acoustical domains provide strong scattering signals and thus enable us the use of a non-coherent light source (Xe-flash tube) instead of a laser. This technique also enables us to discuss accurate resonance behaviors at a region very close to the fundamental absorption edge.

The crystal structures of GaSe and GaS are reviewed in Section 10.2. The electronic band structure and lattice dynamics of the layer-type compounds are also presented in this Section. The experimental method is described in Section 10.3. In Section 10.4, we present the experimental results and compare them

with the theoretical models based upon the quasi-static approximation and Loudon's light-scattering theory. The measured spectral dependence of the Brillouin-scattering cross sections shows a monotonic decrease (i.e., resonant cancellation) at photon energies very close to the n = 1 direct-exciton state for GaSe and beyond the indirect-energy gap for GaS. The resonant cancellation can be well interpreted by taking into account the direct-gap (direct-exciton) and indirect-gap resonance processes for GaSe and GaS, respectively. The experimental data also show that the Brillouin-scattering efficiency depends strongly on the lifetime-broadening effect of the intermediate electronic states. The theoretical description and comparison of it with the experimental data, moreover, clearly indicate that the nonresonant contribution (nonresonant electronic transition) dominates in the Brillouin-scattering process for both GaSe and GaS especially in the region far from the fundamental absorption edges.

10.2 PROPERTIES OF GaSe AND GaS

10.2.1 Crystal Structure and Electronic Energy Band

The basic crystal structure of GaSe and GaS is the hexagonal unit layer with a point-group symmetry of D_{3h} and two molecules per unit cell.[47] The binding between the layers is of the van der Waals type, whereas it is covalent within each layer. In GaS, only one way of stacking of adjacent layers exists and the crystal has a symmetry of point group D_{6h} with two layers (four molecules) per unit cell. A layer of GaSe is represented in Fig. 10-1 (a), where one recognizes that each Ga atom has one Ga and three Se neighbours. The Se atoms have three neighbours only within the same layer. Three different modifications of GaSe have been reported in the literature,[312] as γ, β and ε modifications, respectively. A rhombohedral γ modification with three layers per unit cell and two hexagonal structures β and ε. The β-type structure is

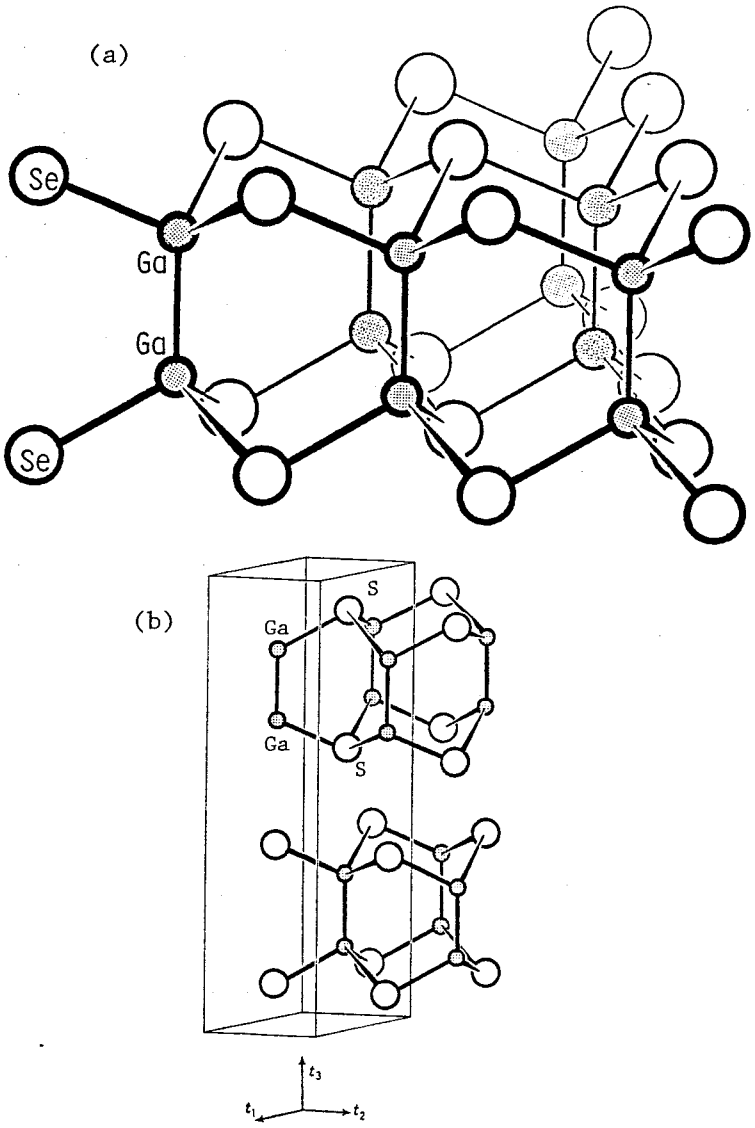

FIG. 10-1. Crystal structure of the layer-type compounds. (a) Perspective view of the one-sandwich arrangement of ε-GaSe; (b) Unit cell of β-GaS.

identical with that of GaS [see Fig. 10-1 (b)]. The ε-type structure has a D_{3h} point-group symmetry with two layers per unit cell. According to Terhell and Lieth,[313] β-type GaSe does not seem to exist as a crystal, although powder X-ray pictures of iodine-transport grown crystals always indicate β-type stacking. The γ-type structure (point group C_{3v}) is found in pure form in sublimation-grown needle crystals and is very rare.

The study of the electronic structure of layer-type compounds has attracted much attention in the last few years, essentially because of their bidimensional character. The principal theoretical works on this subject are by Bassani and Parravicini,[314] Kamimura and Nakao,[315] Fong and Cohen,[316] Schlüter,[47] Mooser and Schlüter,[298] Schlüter and Cohen[317] and Bordas *et al.*[318] The electronic band structures of the layer-type compounds GaSe and GaS have been calculated by Bassani and Parravicini[314] by using the two-dimensional tight-binding approach in a semi-empirical way. The band structure of GaSe has also been calculated by Schlüter[47] by using the empirical pseudopotential method and considering interaction between the layers. The energy bands of β-GaSe along the main symmetry axes calculated on the basis of the empirical pseudopotential method are shown in Fig. 10-2 (after Schlüter).[47] Note that differences between the one-electron energies corresponding to the three modifications are of the order of the weak interlayer coupling and thus do not influence the main features of the band structure. Among the three modifications, γ, β and ε, β modification has the highest symmetry.

In ε-GaSe with the space group D^1_{3h}, the lowest-lying conduction-band minimum is at the M point (M_3), a few tens of meV lower than the lowest-direct conduction band. The lowest direct gap occurs at the center of the Brillouin zone (Γ point), the top of the valence band having the symmetry Γ_1 and the minimum of the direct conduction band that Γ_4. In β-GaS with the space group D^4_{6h}, the lowest-lying conduction-band minimum is at the M point (M_3^+), 2.5 eV

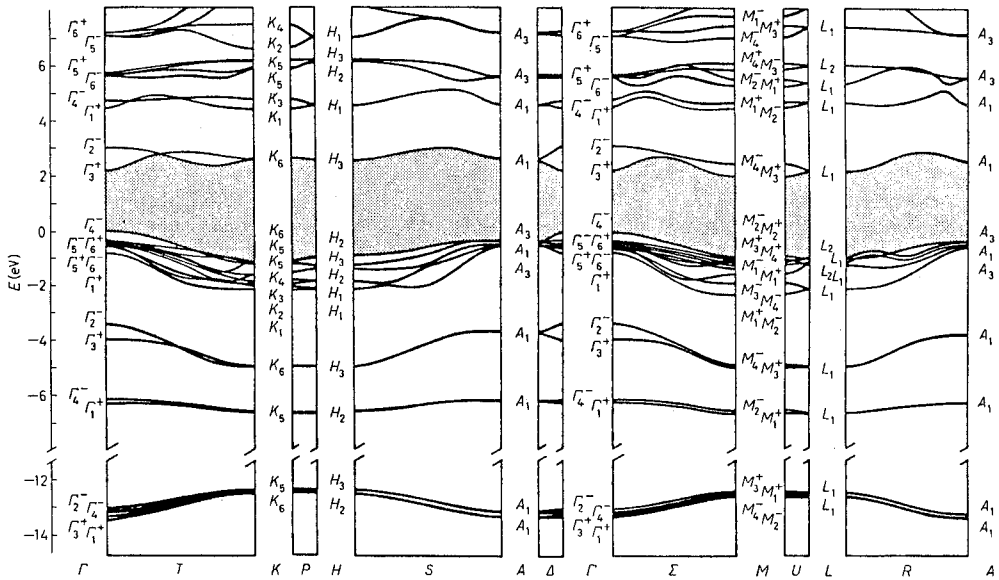

FIG. 10-2. Electronic band structure of β-GaSe along the main symmetry axes calculated on the basis of the empirical pseudopotential method. (From Ref. 47).

above the valence-band maximum at the Γ point. The lowest direct gap occurs at the Γ point, the top of the valence band having the symmetry Γ_4^- and the minimum of the direct conduction band that Γ_3^+. The direct-gap energies of GaSe and GaS are 2.02 and 2.90 eV, respectively, at room temperature.[305,319]

10.2.2 Lattice Dynamics

There has been considerable interest in recent years in the properties of layer structures particularly in the extent to which their two-dimensional nature influences these properties. Measurement of the phonon dispersion curves is known to be a powerful method for obtaining information about the interatomic forces. The inelastic-neutron-scattering measurements have been performed to obtain the phonon dispersion relations in GaSe by Brebner *et al.*[320] and Jandl *et al.*[321] Powell *et al.*[322] have recently made the analysis of lattice vibrations and inelastic-neutron-scattering measurement in GaS. The data of Jandl *et al.* (GaSe)[321] and Powell *et al.* (GaS)[322] are shown in Fig. 10-3 (a) and (b), respectively. These results have shown that the interlayer force constants are very small compared with the intralayer ones. The results have also been used to calculate the Debye temperature and lattice specific heat of GaSe and GaS.[321,322]

The elastic properties of GaSe and GaS have been extensively studied by means of ultrasonic pulse-echo method,[323] inelastic neutron scattering[320,322] and Brillouin scattering.[277,324] The elastic constants of GaSe and GaS obtained from these methods are listed in Table 10-1. The use of Brillouin-scattering technique has recently been developed by many workers who used a Fabry-Perot interferometer to determine the elastic constants of GaSe.[324,325] The five independent elastic constants, C_{11}, C_{12}, C_{13}, C_{33} and C_{44}, have been deduced from a best-fit procedure of these constants [see Table 10-1], but there remains uncertainty to determine the non-diagonal component C_{12}. On the other hand,

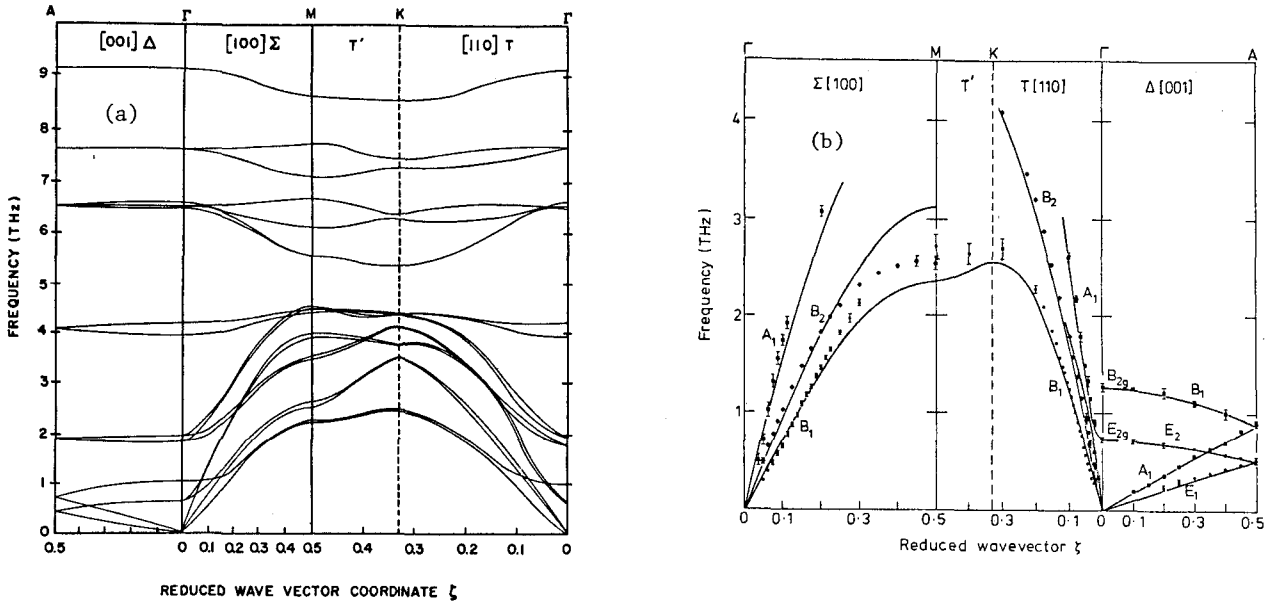

FIG. 10-3. Phonon dispersion relations for (a) GaSe and (b) GaS at room temperature. (From Refs. 321 and 322).

Table 10-1. Elastic constants of GaSe and GaS.

GaSe	(10^{11} dyn/cm^2)		
	B.S.*a	I.N.S.**b	U.P.E***c
C_{11}	10.5	——	10.24
C_{12}	3.25(3.77†)	——	3.24
C_{12}	1.26	——	——
C_{33}	3.51	3.83	3.07
C_{44}	1.04	1.03	0.70

GaS	(10^{11} dyn/cm^2)	
	B.S.*d	I.N.S.**e
C_{11}	15.7	15.5
C_{12}	3.32	(5.35†)
C_{13}	1.50	——
C_{33}	3.58	3.64
C_{44}	0.81	1.33

*Brillouin Scattering
**Inelastic Neutron Scattering
***Ultrasonic Pulse Echo
†Present Work

[a]Reference 276.
[b]Reference 320.
[c]Reference 323.
[d]Reference 335.
[e]Reference 322.

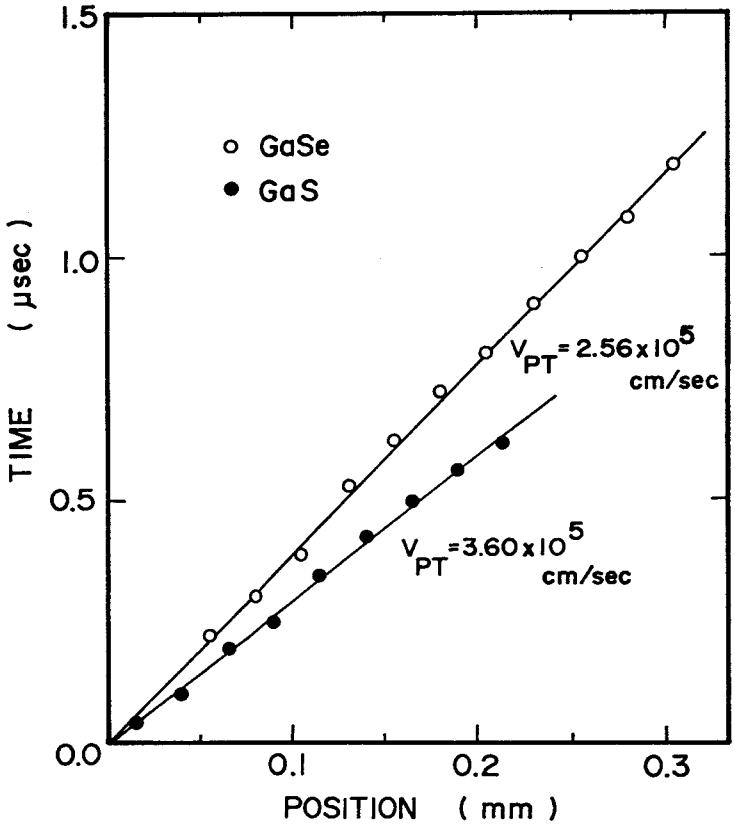

FIG. 10-4. Plot of domain-transit time versus light-spot position for GaSe and GaS from the Brillouin-scattering measurements. The slope of each line gives the domain velocity consisting of the PT-mode phonons (see text).

Powell *et al.*[322] have determined only the diagonal components C_{11}, C_{33} and C_{44} of GaS from the inelastic-neutron-scattering measurements. We determine here the non-diagonal elastic constants C_{12} of GaSe and GaS by measuring the sound velocities of the PT-mode phonon domains in these materials by means of Brillouin scattering, as a by-product of the resonant-Brillouin-scattering measurements. Figure 10-4 represents the plots of domain-transit time versus light-spot position for GaSe and GaS using a He-Ne laser as a light source. (The experimental detail is given in the next Section). The slope of each line gives the domain velocity v_{PT} consisting of the PT-mode phonons, which is determined to be 2.56×10^5 cm/sec for GaSe and 3.60×10^5 cm/sec for GaS. The sound velocity of the PT-mode phonons is given by

$$v_{PT} = [(C_{11} - C_{12})/2\rho]^{\frac{1}{2}} \quad , \qquad (10.1)$$

where ρ is the mass density (5.135 g/cm^3 for GaSe and 3.916 g/cm^3 for GaS). It is clear that the non-diagonal component C_{12} can be determined from Eq. (10.1) when the diagonal component C_{11} is known. We can determine the value of C_{12} by using the previously reported value of C_{12}. The results are as follows: $C_{12} = 3.77$ with $C_{11} = 10.5$ for GaSe[276] and $C_{12} = 5.35$ with $C_{11} = 15.5$ for GaS[322] in units of 10^{11} dyn/cm^2 [see also Table 10-1]. The value of C_{12} (GaSe) agrees well with that reported previously.[276,324]

10.3 EXPERIMENTAL PROCEDURE

The GaSe and GaS crystals used in this experiment were grown by the Bridgman technique and had ε- (D^1_{3h} symmetry) and β-type (D^4_{6h} symmetry) structures, respectively.[326] In order to obtain a strong phonon flux, the acoustical domains amplified in CdS were transmitted into the GaSe and GaS samples through the end-bonded surfaces by making use of the acoustical-domain injection method [see

Section 3.3.4]. The GaSe and GaS crystals were cut in the form of parallelepipeds with dimensions of about 0.5 × 1.5 × 5.0 mm, where the optical-flat surfaces (layer planes) perpendicular to the c-axis were obtained by cleavage using a razor blade. Indium layers were deposited by vacuum evaporation onto the end-surfaces of CdS and layer-type specimens, and they were carefully bonded by heating the evaporated indium layers so as to give a good contact for the acoustical-domain injection from CdS into the layer-type specimens. The acoustical domains injected into the specimens travel in the direction perpendicular to the c-axis with shear polarization perpendicular to the c-axis (PT-mode phonons). The apparatus used in this experiment is almost the same as those described in Section 3.3.

10.4 EXPERIMENTAL RESULTS AND DISCUSSION

10.4.1 Optical Absorption

Let us first consider selection rule of the optical transitions (dipole transitions) by the aid of group theory.[327] The polarization vectors $\vec{E} \perp \vec{c}$ and $\vec{E} \parallel \vec{c}$ of the spece group D_{3h}^{1} (ε-GaSe) belong to Γ_6 and Γ_4, respectively. The highest valence and lowest conduction bands of ε-GaSe have Γ_1 and Γ_4 symmetries, respectively, for the irreducible representation of the single group.[298] The optical transitions between the highest valence and lowest conduction bands can, thus, be given by the direct product:

$$\Gamma_1 \times \Gamma_4 = \Gamma_4 \quad . \tag{10.2}$$

This representation contains only for the $\vec{E} \parallel \vec{c}$ polarization. Experimental data confirs that the light of this polarization is strongly absorbed in GaSe in the region near and above the fundamental absorption edge.[310,311,328] However, there is also an absorption for $\vec{E} \perp \vec{c}$ in this region, which is only

about one to two orders of magnitude weaker than that for $\vec{E} \parallel \vec{c}$. This can be understood if we consider the spin-orbit interaction (spin-orbit coupling). The spin-orbit coupling results from interband mixing and is known to be relatively weak.[298] The extra representations of the double group, now, go from Γ_1 to Γ_7 (the highest valence band) and from Γ_4 to Γ_8 (the lowest conduction band), and then the product

$$\Gamma_7 \times \Gamma_8 = \Gamma_3 + \Gamma_4 + \Gamma_6 \tag{10.3}$$

contains the representations of both $\vec{E} \parallel \vec{c}$ and $\vec{E} \perp \vec{c}$. Similarly, the polarization vectors $\vec{E} \perp \vec{c}$ and $\vec{E} \parallel \vec{c}$ of the space group D^4_{6h} (β-GaS) belong to Γ^-_5 and Γ^-_2 symmetries, respectively, for the irreducible representation of the single group. The highest valence and lowest conduction bands of β-GaS have Γ^-_4 and Γ^+_3 symmetries, respectively.[298] The direct product

$$\Gamma^-_4 \times \Gamma^+_3 = \Gamma^-_2 \tag{10.4}$$

contains only the representation of symmetry Γ^-_5 ($\vec{E} \parallel \vec{c}$). The extra representations of the double group go from Γ^-_4 to Γ^-_8 (the highest valence band) and from Γ^+_3 to Γ^+_8 (the lowest conduction band), and the product

$$\Gamma^-_8 \times \Gamma^+_8 = \Gamma^-_2 + \Gamma^-_5 + \Gamma^-_1 \tag{10.5}$$

contains the representations of both $\vec{E} \parallel \vec{c}$ and $\vec{E} \perp \vec{c}$. In Fig. 10-5, we show the selection rules of the direct optical transitions at Γ point in ε-GaSe (D^1_{3h}) and β-GaS (D^4_{6h}), obtained in a way described above, based on the irreducible representation of the single group. Dashed lines indicate the compatibility relation between D^1_{3h} and D^4_{6h} symmetries.

GaSe and GaS are known to have indirect-energy gaps at energies below the lowest direct-energy gaps. The energy separations between the indirect and direct gaps of these compounds are found to be about 25 meV for GaSe and 0.4 eV

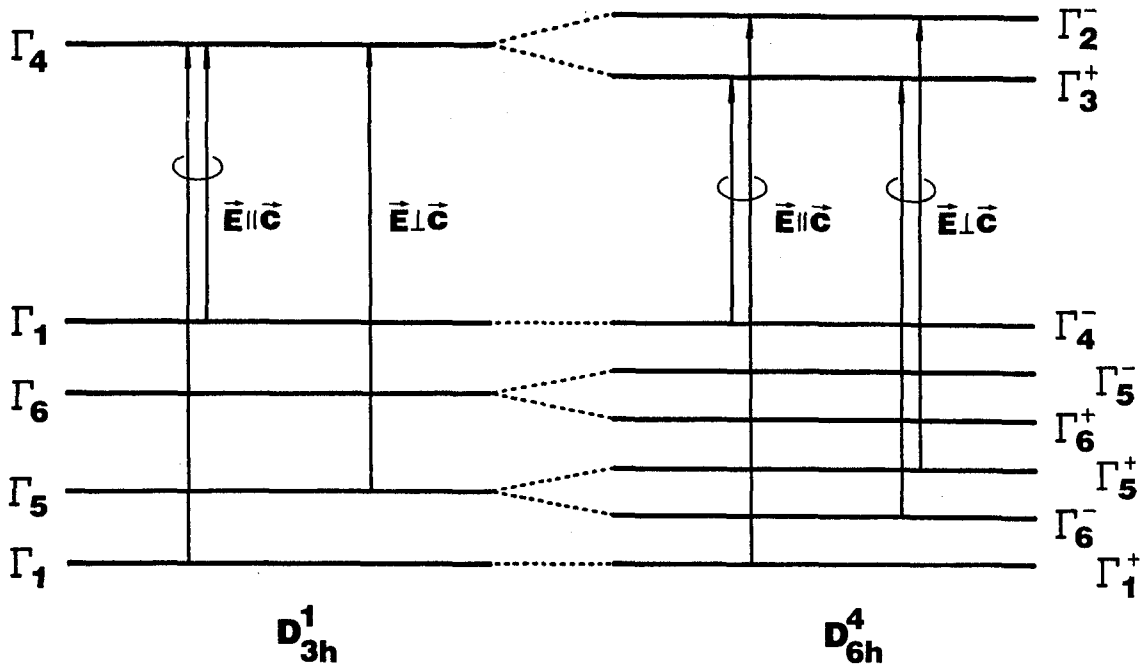

FIG. 10-5. Band structures and selection rules of the direct optical transitions at Γ point in ε-GaSe and β-GaS. Dashed lines indicate the compatibility relation between D^1_{3h} and D^4_{6h} symmetries.

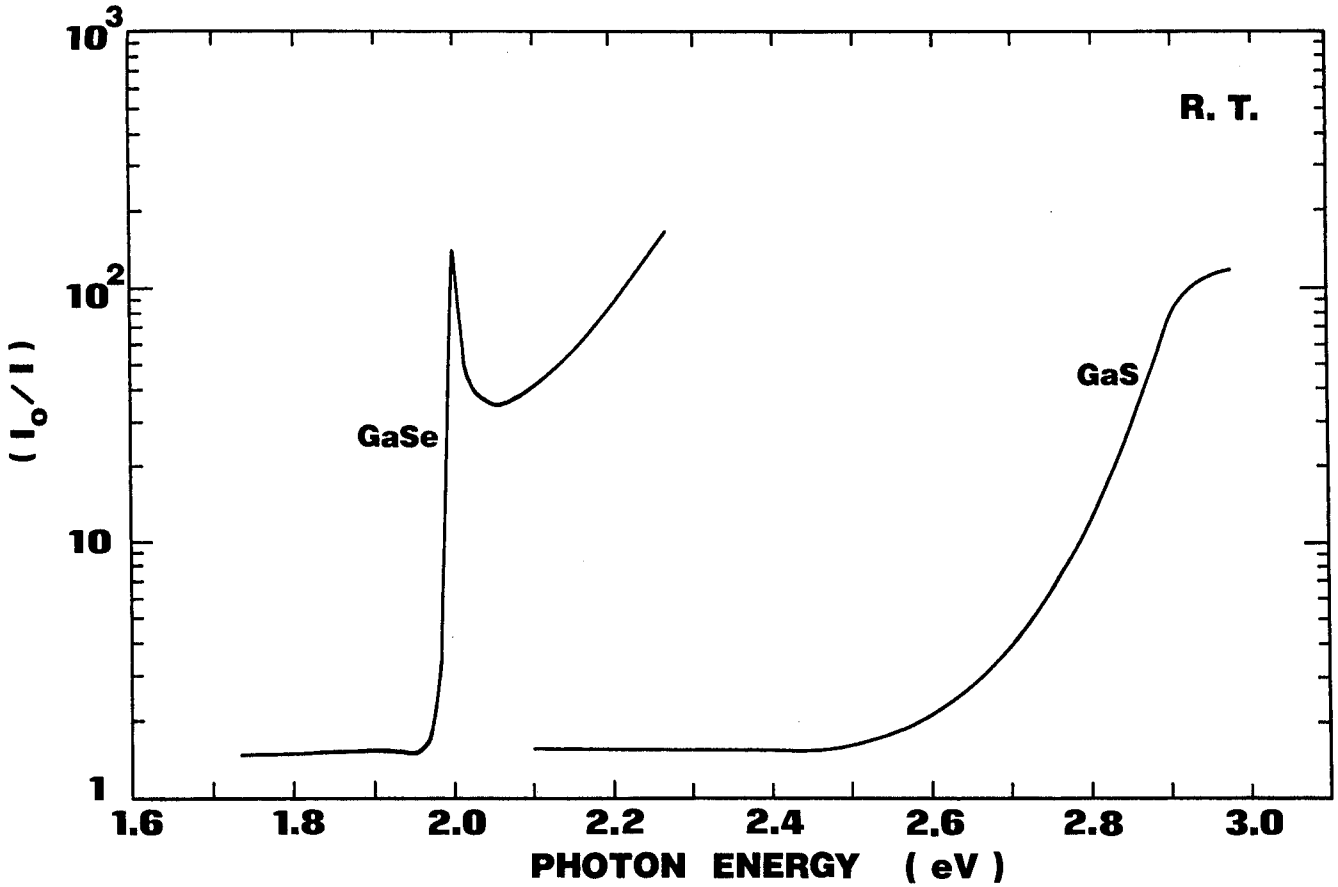

FIG. 10-6. Optical absorption spectra for the ordinary ray of GaSe and GaS single crystals used in the present measurements at room temperature.

for GaS.[307] Figure 10-6 shows the optical absorption spectra of GaSe and GaS used in the present work in the region of the fundamental absorption edge. The spectra have been obtained at room temperature from the $\vec{E} \perp \vec{c}$ polarization measurements. The behavior of the optical absorption seems to be direct for GaSe and, at energies below 2.9 eV, indirect for GaS. The optical absorption of GaSe shows a sharp peak at 2.00 eV which can be explained in terms of formation of direct excitons (n = 1) due to the Coulomb interaction between the electron and hole produced in the optical transition near the fundamental absorption edge.[298] In GaSe, however, the characteristic indirect-optical transitions could not be clearly found in the absorption spectrum which arises from the fact that the much stronger direct-optical transition should completely mask off the weaker indirect-optical transition. On the other hand, since the energy separation between the indirect and direct gaps of GaS is considerably large, the indirect-optical transition could be clearly fonund in the absorption spectrum. We can obtain from the figure that the indirect-gap energy of GaS is about 2.50 eV which agrees well with the value obtained from the emission and absorption spectra of this material.[305,307,329] It is also important to note that in both GaSe and GaS the absorption coefficient for $\vec{E} \perp \vec{c}$ is much weaker than that for $\vec{E} \parallel \vec{c}$ at the band-edge region,[310,311,328] since the optical transition is fully allowed only in the later polarization, as discussed previously.

10.4.2 Quasi-Static Analysis

Figure 10-7 shows the spectral dependence of the Brillouin-scattering cross sections in GaSe obtained at room temperature in the region of transparency. The acoustical-domain frequency has been selected to be 0.2 GHz by properly setting the incident and scattering angles. All the data points have been obtained by carrying out a correction for absorption of light. The following scattering configurations have been used in the present study by taking into

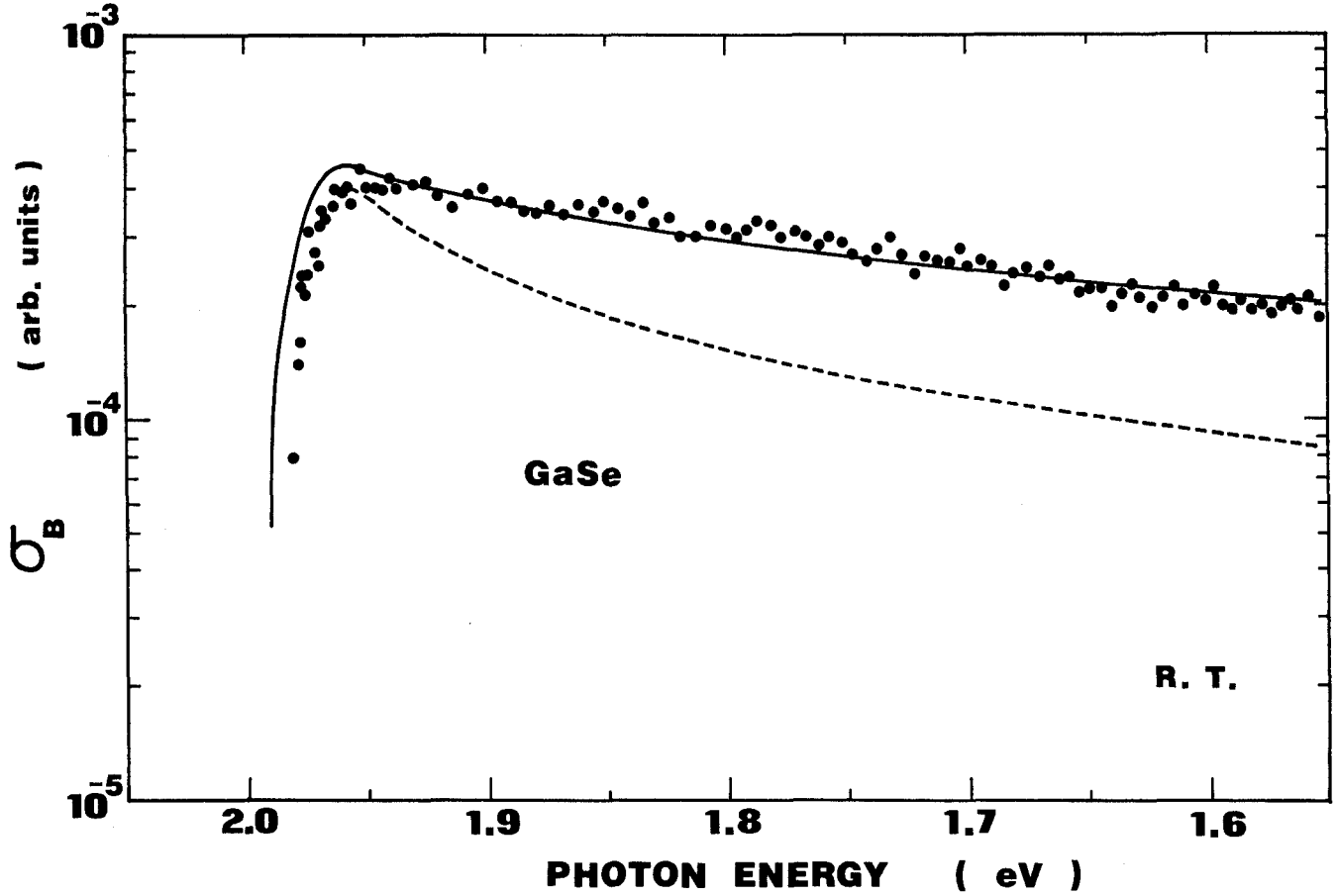

FIG. 10-7. Spectral dependence of the Brillouin-scattering cross sections by the 0.2 GHz PT-mode phonon domains in GaSe. The dashed and solid lines are calculated from Eq. (10.6) with B = 0 and 1.5 (in eV^{-1}), respectively.

account the polarization selection rules: $\vec{e}_i \perp \vec{c}$, $\vec{e}_s \perp \vec{c}$ and $\vec{e}_i \perp \vec{e}_s$, where $\vec{e}_i$ and $\vec{e}_s$ are the unit vectors in polarization direction of the incident and scattered lights, respectively. It can be found in the figure that the spectral dependence of the Brillouin-scattering cross sections shows very weak resonant enhancement in the region of transparency. The spectral dependence is very similar to that reported previously in GaSe [Ref. 276]. Such a resonance feature is in contrast to those found in the direct-gap semiconductors such as GaAs,[25] CdSe,[31] CdS,[27,30,39] ZnO,[30] ZnTe[71] and ZnSe,[95] where in these direct-gap semiconductors the spectral dependence of the Brillouin-scattering cross sections shows clear resonance features (resonant enhancement and cancellation) in the region near the lowest direct gaps. It should be noted here that the present data shows a monotonic decrease in the region very close to the fundamental absorption edge which were not clearly found in the previous work by Chiang *et al.*[276]

Figure 10-8 shows the spectral dependence of the Brillouin-scattering cross sections by the 0.8 GHz PT-mode phonon domains in GaS obtained at room temperature in the region of transparency. The observed spectral dependence is essentially the same as that in GaSe. The monotonic decrease of the Brillouin-scattering cross sections has also been found in GaS in the region of the fundamental absorption edge ($\sim$ 2.5 eV).

We have demonstrated in Chapter V that the qualitative features of resonant Brillouin scattering can be predicted from an expression based on the quasi-static approximation, where in this approximation the phonons are assumed to act like static perturbations of the electronic band structure of the crystal. This perturbation reflects a change in the dielectric constant ε of the crystal. The Brillouin-scattering cross section derived on the basis of the quasi-static approximation can be written as [same as Eq. (5.10)]

$$\sigma_B = A \left(\frac{d\varepsilon_{mn}}{dE} + B \right)^2 \quad , \qquad (10.6)$$

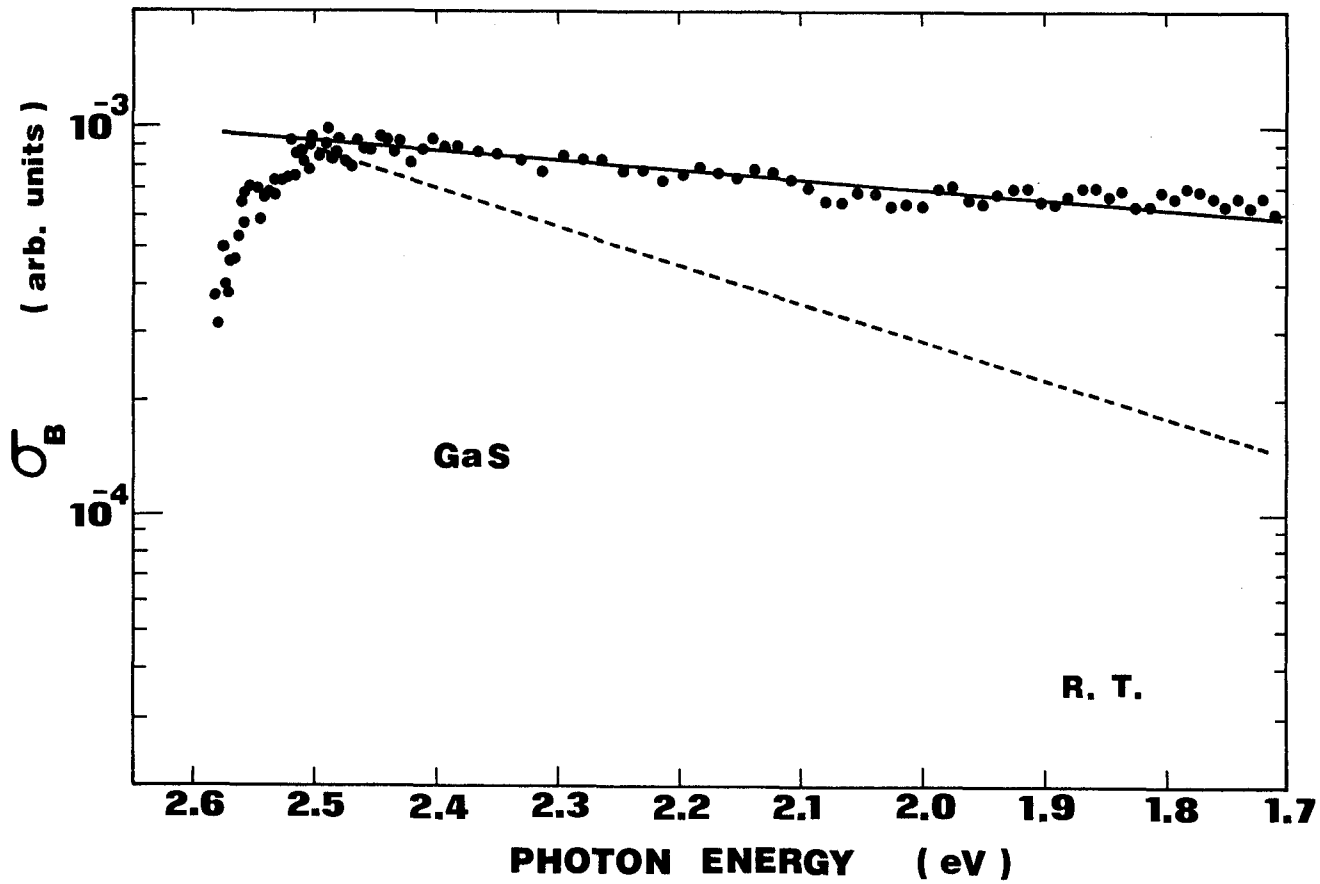

FIG. 10-8. Spectral dependence of the Brillouin-scattering cross sections by the 0.8 GHz PT-mode phonon domains in GaS. The dashed and solid lines are calculated from Eq. (10.6) with B = 0 and 2.5 (in eV^{-1}), respectively.

where A is a constant, E is the incident-photon energy and B is a nonresonant term (background contribution) arising from the far-off critical points in the band structure. The subscripts m and n are the directions of the incident and scattering fields, respectively. In order to obtain Eq. (10.6), we made the usual approximation:

$$\frac{d\varepsilon_{mn}}{dE} = -\frac{d\varepsilon_{mn}}{dE_g} \quad . \tag{10.7}$$

This relation is obtained by making use of the fact that near resonance the dielectric constant can be approximated by a function of $(E - E_g)$ only.

Figure 10-9 shows the dielectric constants for the ordinary ray of GaSe and GaS as a function of photon energy at room temperature (dashed lines) taken from the data of Refs. 310 (GaSe) and 330 (GaS). The photon-energy derivatives of these constants are also shown in the figure by solid lines. The theoretical curves calculated from Eq. (10.6) are shown in Figs. 10-7 and 10-8 by dashed (B = 0) and solid lines (B $\neq$ 0). The photon-energy derivatives of the dielectric constant (in eV^{-1}) has been obtained by differentiating the date of Refs. 310 and 330 (GaSe) and 330 (GaS) [see Fig. 10-9]. We have used the data of the dielectric constants for the ordinary ray ($\vec{E} \perp \vec{c}$) which correspond to the present Brillouin-scattering configurations ($\varepsilon_{mn} = \varepsilon_{11} = \varepsilon_{\perp}$). The constants A and B have been adjusted to give the best fitting. The best results can be obtained by taking into account the nonresonant contributions of B = 1.5 and 2.5 (in units of eV^{-1}) for GaSe and GaS, respectively, as shown in the figures by solid lines. This fitting procedure deduces an interesting fact that for both GaSe and GaS the Brillouin-scattering process arises mainly from the dispersionless contributions due to the nonresonant electronic transitions. Moreover, the nonresonant term B has a positive sign in contrast to that for the direct-gap II-VI compounds [see Table 5-1]. Such facts explain reasonably why the dispersion curves of the Brillouin-scattering intensity in both GaSe

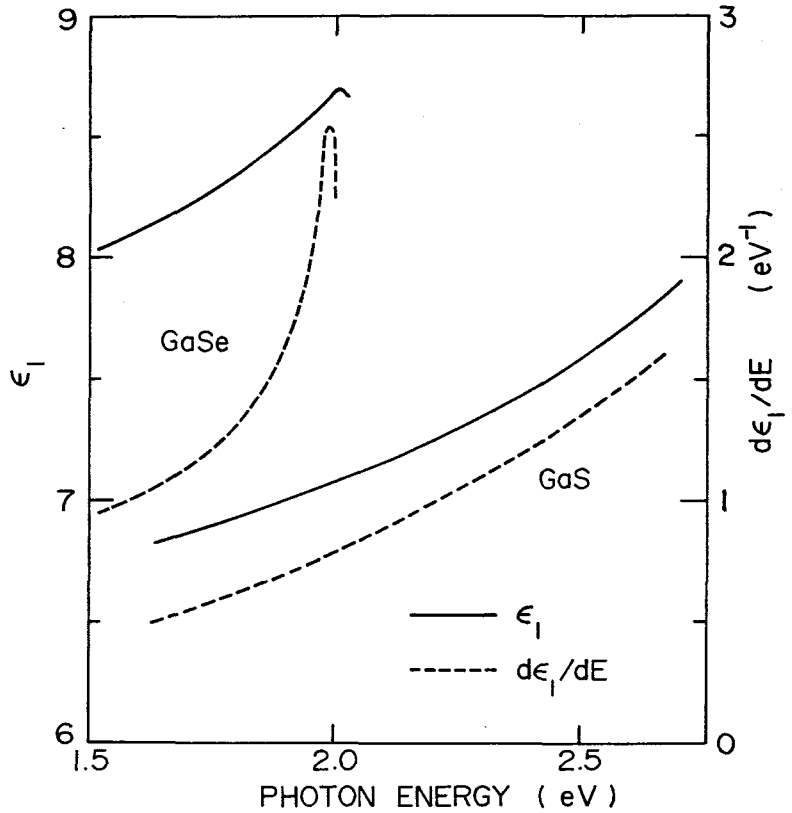

FIG. 10-9. Dielectric constants of GaSe and GaS at room temperature in the region of transparency. The photon-energy derivatives of the dielectric constants (in eV^{-1}) are also shown in the figure by dashed lines.

and GaS did not show any clear resonant cancellation (except in the region above the band-edge region) and enhancement. The quasi-static analysis for the case of II-VI compounds showed that the resonant contribution was dominant in the Brillouin-scattering process and thus the resonant cancellation could be clearly found in the region below the lowest direct gap. The resonant cancellation reflected the sign opposite relation between the resonant and non-resonant contributions [see Chapter V]. The weak resonant enhancement observed in the present study can be understood from a phenomenological aspect by taking into account the following fact; In the layer-type semiconductors such as GaSe and GaS, the absorption coefficient for the $\vec{E} \perp \vec{c}$ polarization is much weaker than that for $\vec{E} \parallel \vec{c}$ near the excitonic-transition region which is attributed to the symmetry of the electronic bands being such that for $\vec{E} \parallel \vec{c}$ the optical transitions are fully allowed while for $\vec{E} \perp \vec{c}$ they are allowed only because of the presence of spin-orbit coupling. This means that the oscillator strength for $\vec{E} \perp \vec{c}$ is much weaker than that for $\vec{E} \parallel \vec{c}$. Therefore, we can expect that the resonance effect near the band-edge region is rather weak so that tne nonresonant electronic transition is always dominant for the $\vec{e}_i \perp \vec{c}$ and $\vec{e}_s \perp \vec{c}$ scattering configurations. (Note that the Brillouin-scattering intensity is proportional to the fourth power of the corresponding momentum matrix element). On the contrary, the strong resonance effect should be expected when we proceed the Brillouin-scattering measurements in the $\vec{e}_i(\vec{e}_s) \parallel \vec{c}$ configuration. The quasi-static approximation easily supports this expectance because the spectral dependence of the dielectric constant $\varepsilon_{\parallel}$ (ε_{33}) shows a strong dispersion near the band-edge region, i.e., the first term in the bracket of Eq. (10.6) gives considerably large value. Unfortunately, however, the incident and scattering angles for this scattering configuration can not be determined from the usual procedure of Dixon[117] because of the strong anisotropic nature of the refractive indices in the layer-type compounds.

As shown in Figs. 10-7 and 10-8, we have observed clear resonant cancellation of the Brillouin-scattering cross sections in GaSe and GaS at a region very close to the fundamental absorption edges. The resonant cancellation in GaSe is found to be well interpreted in terms of the dielectric theory of resonant Brillouin scattering given by Eq. (10.6), whereas the resonant cancellation in GaS can not be successfully explained when we use the data of dielectric constant (Ref. 330) which do not show any clear structure or maximum at the fundamental absorption edge [see Fig. 10-9]. Note here that $d\varepsilon/dE$ becomes zero at a maximum of $\varepsilon(E)$ and thus the resonant cancellation occurs near the maximum of $\varepsilon(E)$. The solid line of Fig. 10-8 does not show a decrease near the fundamental absorption edge ($\sim$ 2.50 eV), reflecting the structureless nature of $\varepsilon(E)$ in the region. The dielectric constant of GaS reported by Akhundov *et al.*,[328] on the other hand, exhibits a clear maximum at a photon energy of about 2.65 eV, and thus the observed resonant cancellation can be interpreted by Eq. (10.6). However, the data of Akhundov *et al.* show optically positive nature ($\varepsilon_{\perp} < \varepsilon_{\parallel}$) which is in contrast to those of GaS[330,331] and GaSe.[310,330] Thus, we need more detailed measurements on the dielectric constant of GaS for the analysis of the quasi-static approximation.

10.4.3 Microscopical Analysis

In this subsection, we analyze the Brillouin-scattering data from a microscopical point of view, based upon Loudon's light-scattering theory.[35] The resonant cancellation observed in both GaSe and GaS will be successfully interpreted by the proposed theoretical model.

The layer-type compounds GaSe and GaS are known to be indirect-gap semiconductors, as mentioned previously. The top of its valence band lies at Γ point and the bottom of the conduction band at M point. Relative minima of the conduction band at Γ point are situated a few tens of meV for GaSe and about

0.4 eV for GaS above the minima at M point. A common feature of theoretical expressions for the Brillouin-scattering intensity of a substance is the presence of terms which either divergence or become relatively large when the frequency of the exciting radiation is equal to an allowed optical-transition frequency of the substance. The Brillouin scattering cross section can be given in terms of the frequency-dependent Brillouin tensor $R(-\omega_i,\omega_s,\omega_q)$ by

$$\sigma_B \propto | R(-\omega_i,\omega_s,\omega_q) |^2 \quad . \tag{10.8}$$

For the case of the indirect-gap materials such as GaSe and GaS, we can separate the Brillouin-tensor term into three independent components [see Chapter IX]:

$$R = R_{is}^{ID} + R_{is}^{D} + R_0 \quad , \tag{10.9}$$

where R_{is}^{ID} and R_{is}^{D} are the indirect-gap and lowest direct-gap resonance terms, respectively, and R_0 is the nonresonant term arising from the far-off critical points in the band structure. The indirect-gap resonance process, which contains in part the indirect-optical transition, is described theoretically by the 5th-order time-dependent perturbation [see Chapter IX]. The expression of R_{is}^{ID} is given by the same form as Eq. (9.19). The absorption coefficient can now be written in terms of the density of states of the indirect-energy gap as[305,306]

$$\alpha(\omega) \propto (\hbar\omega - E_g^{ID} \pm \hbar\omega_q)^2 \quad . \tag{10.10}$$

As mentioned in Section 2.2, the direct-gap resonance process is described by the 3rd-order time-dependent perturbation and is given by the same form as Eq. (2.55).

Let us now consider the direct-gap Brillouin-scattering process by the aid of group theory. The direct gap with which the exciton series of interest here are associated occurs at the center of the Brillouin zone (Γ point). The

Brillouin-scattering process can be deduced from the symmetry properties of the intermediate electronic states and corresponding acoustical vibrations. The strain component induced by acoustical phonons is defined by Eq. (2.70). The PT-mode phonons propagating in GaSe, thus, induce the non-zero strain component $e_{\pm} = e_{xx} - e_{yy} \pm 2ie_{xy}$ which has the symmetry of Γ_6 (space group D^1_{3h}). The initial-intermediate-electronic state can be assumed to have Γ_6 symmetry, since in the present study it is produced by the $\vec{e}_i \perp \vec{c}$ (Γ_6) radiation After being the deformation-potential interaction with the PT-mode phonons, the intermediate electronic state will have the symmetry given by the following product:

$$\Gamma_6(\vec{e}_i \perp \vec{c}) \times \Gamma_6(e_{\pm}) = \Gamma_1 + \Gamma_2 + \Gamma_6 \quad . \qquad (10.11)$$

The right-hand side of Eq. (10.11) contains the representation of symmetry Γ_6, and as a result the scattered-intermediate-electronic state can produce the radiation having polarization of $\vec{e}_s \perp \vec{c}$ (Γ_6). The above result possibly suggests that in the case of GaSe the exciton (electron)-acoustical phonon interaction is necessarily intraband, i.e., the Brillouin-scattering process can be described only by the two-band model. The schematic diagram of this process is represented in Fig. 10-10 (a), where $|0\rangle$ represents the electronic ground state and $|\alpha\rangle$ and $|\beta\rangle$ represent the intermediate electronic states. The same result can also be obtained in the case of GaS (space group D^4_{6h}). The PT-mode phonons propagating in GaS induce the non-zero strain component of $e_{\pm} = e_{xx} - e_{yy} \pm 2ie_{xy}$ which has the symmetry of Γ_6^+. The symmetry of the scattered-intermediate electronic state is, therefore, given by the product

$$\Gamma_5^-(\vec{e}_i \perp \vec{c}) \times \Gamma_6^+(e_{\pm}) = \Gamma_3^- + \Gamma_4^- + \Gamma_5^- \quad , \qquad (10.12)$$

which contains the representation of symmetry Γ_5^- $(\vec{e}_s \perp \vec{c})$. Thus, the direct-gap Brillouin-scattering process in GaS can also be described only by the two-band

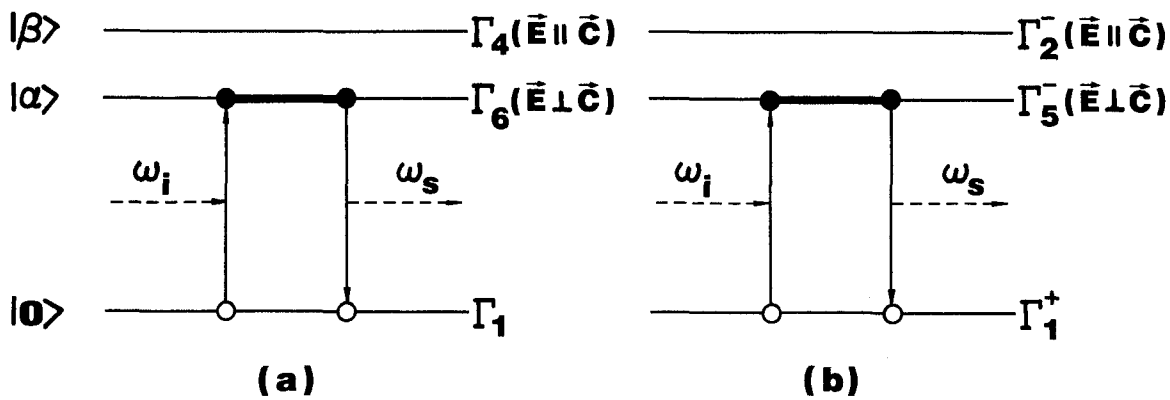

FIG. 10-10. Schematic description of the Brillouin-scattering process. (a) ε-GaSe (D^1_{3h} symmetry) and (b) β-GaS (D^4_{6h} symmetry). The dashed arrows indicate photons. The heavy lines indicate the transition processes of virtual intermediate electronic states *via* deformation-potential interaction.

model (i.e., intraband electronic transition). The schematic diagram of the Brillouin-scattering process in the case of the space group D_{6h}^{4} (GaS) is represented in Fig. 10-10 (b).

Figure 10-11 shows the theoretical curves of the Brillouin-scattering cross sections in GaSe, calculated from Eq. (10.8), along with the experimental data. The vertical arrow indicates the position of the n = 1 discrete-exciton energy (E_{x1}). The indirect-gap resonance is usually weaker than the direct-gap one because of the higher perturbation orders of the indirect-gap resonance process. The energy separation between the indirect and direct gaps of GaSe is too small (a few tens of meV). It can, therefore, be reasonably considered that in GaSe the indirect-gap resonance term R_{is}^{ID} is negligibly small compared with the direct-gap resonance term R_{is}^{D}, i.e., the indirect-gap resonance should be masked off by the much stronger direct-gap one. Similar phenomena can also be expected in other optical processes such as absorption and emission of light [see, *e.g.*, Fig. 10-6]. From the above fact, we have neglected the indirect-gap resonance term for GaSe and then calculated theoretical curves using the following Brillouin tensor instead of Eq. (10.9):

$$R = R_{is}^{D} + R_{0} \quad . \tag{10.13}$$

The numerical values used in the calculations are listed in Table 10-2. The theoretical curves have been taken into account four different lifetime-broadening energies; Γ = 0 meV (dash-dotted line), Γ = 30 meV (dashed line), Γ = 60 meV (solid line) and Γ = 90 meV (dotted line). The group-theoretical analysis discussed before indicated that for both GaSe and GaS the direct-gap resonance process can be treated only by the two-band model. We have, thus, mode in Eq. (2.55) that

$$\omega_{g\alpha} = \omega_{g\beta} \quad , \quad P_{\alpha 0}^{i} = P_{0\beta}^{s} \quad \text{and} \quad \Xi_{\beta\alpha} = \Xi_{\alpha\alpha} \quad . \tag{10.14}$$

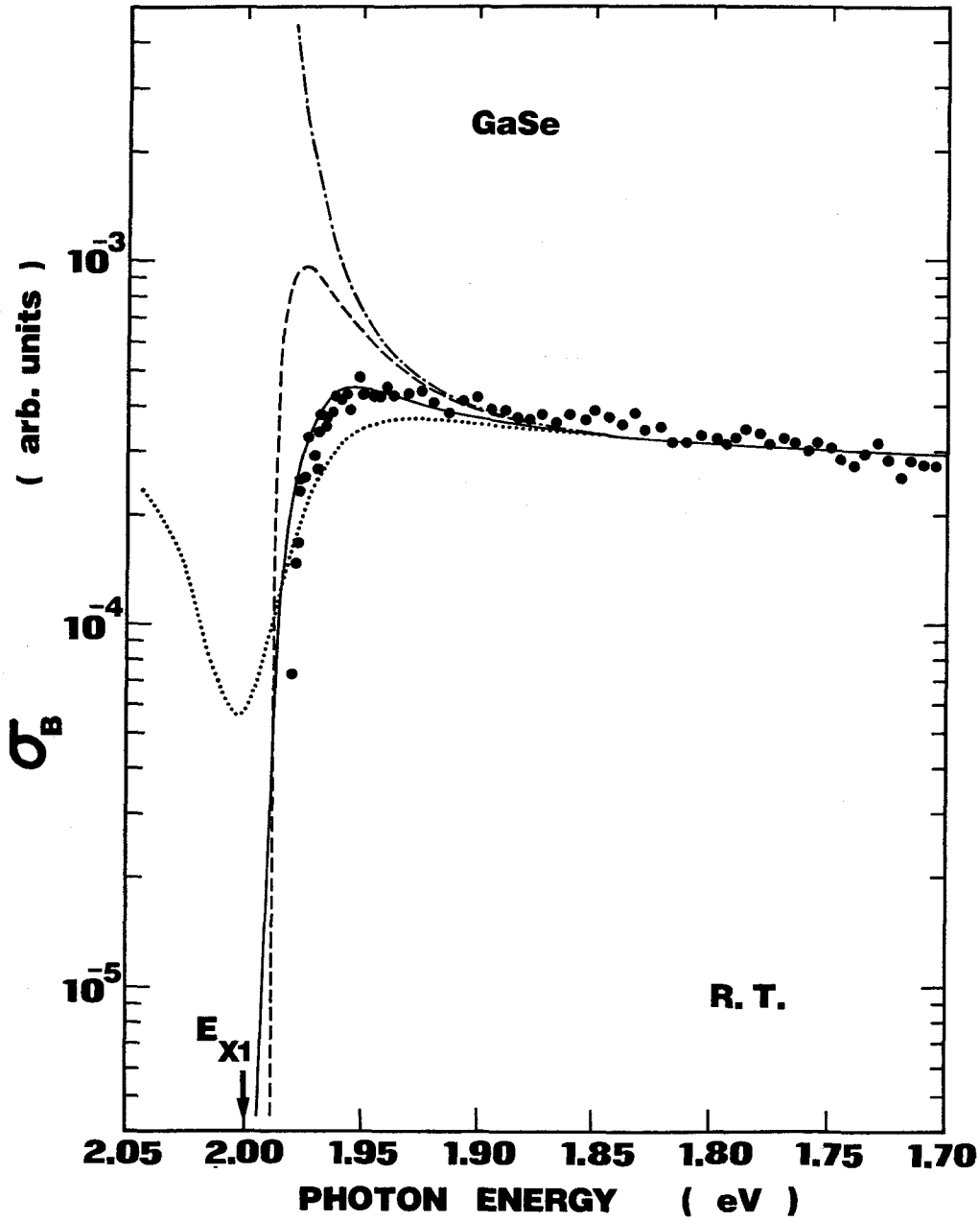

FIG. 10-11. Dispersion curve of the Brillouin-scattering cross sections for the 0.2 GHz PT-mode phonon domains in GaSe. The theoretical curves are obtained from Eq. (10.13) with Γ=0 meV (dash-dotted line), Γ=30 meV (dashed line), Γ=60 meV (solid line) and Γ=90 meV (dotted line). The vertical arrow indicates the position of the n = 1 direct-exciton energy (E_{x1}).

Table 10-2. Numerical parameters used to calculate the spectral dependence of the Brillouin-scattering cross sections.

	GaSe	GaS
$E^{D}_{g\alpha}$ [eV]	2.02[a]	2.90[b]
E^{ID}_{g} [eV]	——	2.495[c]
$\hbar R^*$ [meV]	20[d]	67[e]
a_0^* [Å]	41.5[d]	14[e]
μ	0.11[d]	0.3[e]

[a]Estimated from our experimental data (Fig. 10-6).

[b]Reference 305 and estimated from our experimental data (Fig. 10-6).

[c]Reference 329 and estimated from our experimental data (Fig. 10-6).

[d]Reference 336.

[e]Reference 337.

It is obvious from Fig. 10-11 that the lifetime-broadening effect strongly broadens resonance features especially near the direct-exciton resonance region (E_{x1}). The best-fitting value of the lifetime-broadening energy is determined to be Γ = 60 meV (solid line).

Figure 10-12 shows the theoretical curves of the Brillouin-scattering cross sections in GaS, calculated from Eq. (10.8), along with the experimental data. The vertical arrows in the figure indicate the positions of the indirect-gap (E_g^{ID}) and n = 1 direct-exciton (E_{x1}) energies. The solid and dashed lines have been calculated from the Brillouin tensors of Eqs. (10.9) and (10.13), respectively. The numerical values used are listed in Table 10-2. In the calculation of the direct-gap resonance term R_{is}^{D}, we have taken into account the lifetime-broadening energy of Γ = 200 meV.[332] The dashed line in which the indirect-gap resonance is not taken into account shows a decrease in the region near the n = 1 direct-exciton state (E_{x1}) arising from the lifetime broadening of the exciton states. However, the agreement between the theoretical curve and experimental data is very poor in the region near the fundamental absorption edge. As already mentioned in Section 10.4.1, GaS has an indirect-energy gap below the lowest direct one and this gap sufficiently aparts from the lowest direct gap. As a result, the absorption spectrum of this material clearly shows an indirect-gap characteristic at energies below 2.9 eV. This fact enables us to consider that the indirect-gap resonance should be occured without masking off by the strong direct-gap resonance as the photon energy approaches and extends beyond the indirect-energy gap E_g^{ID}. It should be important to point out that the indirect-gap resonance expressed by Eq. (9.19) begins as the incident-photon energy extends beyond the energy of ($E_g^{ID} - \hbar\omega_q$). One can find from Fig. 10-12 that the theoretical curve calculated from Eq. (10.9) well interpretes the measured monotonic decrease of the Brillouin-scattering cross sections, as shown by solid line. In the calculation, we have assumed to account

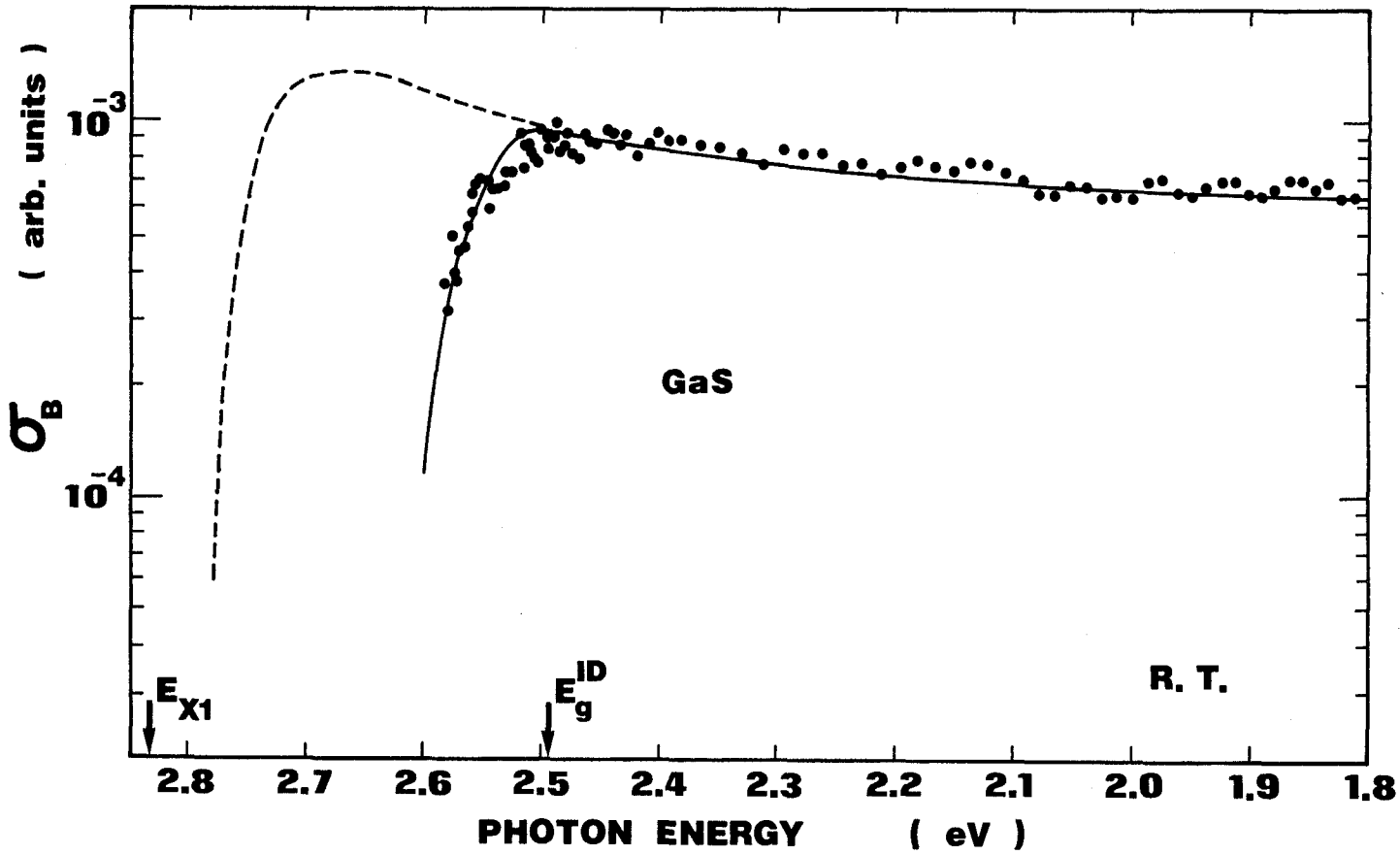

FIG. 10-12. Dispersion curve of the Brillouin-scattering cross sections for the 0.8 GHz PT-mode phonon domains in GaS. The theoretical curves are obtained from Eqs.(10.9) [solid line] and (10.13) [dashed line], respectively. The lifetime-broadening energy of Γ=200 meV is taken into account in the calculation of the direct-gap resonance term R_{1s}^{D}. The vertical arrows indicate the positions of the indirect-gap (E_g^{ID}) and n = 1 direct-exciton energy (E_{x1}).

the cancellation that the the indirect-gap resonance term (R_{is}^{ID}) has a opposite sign to the direct-gap (R_{is}^{D}) and nonresonant terms (R_0). The monotonic decrease is, thus, considered to be the result of cancellation between the R_{is}^{ID} and R_{is}^{D} (plus R_0) terms. Similar resonant cancellation has also been found in the indirect gap of Si[269] from the Raman-scattering measurements as the resonance with the indirect-energy gap is approached. Unfortunately, we were not able to determine the value of $\Gamma(\omega)$ from the fit to the experimental data with Eq. (10.9), since the term R_{is}^{ID} contains the prefactor C_2 as an adjustable parameter.

Figure 10-13 shows the theoretical line shapes of the Brillouin tensor R of GaSe calculated from Eq. (10.13) in the neighborhood of the excitonic structure with three different broadening energies; Γ = 40 meV (dashed line), Γ = 60 meV (solid line) and Γ = 90 meV (dotted line). The experimental data ($\sigma_B^{\frac{1}{2}} \propto |R|$) are plotted in the figure by solid circles. The corresponding nonresonant term R_0 is also shown by solid line. The vertical arrow indicates the position of the n = 1 direct-exciton state E_{x1}. One can find from the figure that the calculated curves show sharp peaks at arround 2.00 eV arising from the direct-exciton resonance. Note that the absorption spectrum [Fig. 10-6] also showed sharp peak at the same photon energy due to the n = 1 direct-exciton transition. The resonance behaviors are clearly found to be strongly affected by the lifetime broadening of the exciton states. The calculation has required a fit to the experimental data with Γ = 60 meV (solid line; see also Fig. 10-11). The figure clearly indicates that at photon energies below 1.95 eV the nonresonant contribution (nonresonant electronic transition) is dominant in the Brillouin-scattering process; We obtain, for example, that the ratio of each contribution R_{is}^{D}/R_0 is about 1/7.5 at photon energy of 1.85 eV. Such a result agrees reasonably with that obtained from the quasi-static analysis, as mentioned in Section 10.4.2.

It is interesting to note here that the line shape of R [Fig. 10-13] is

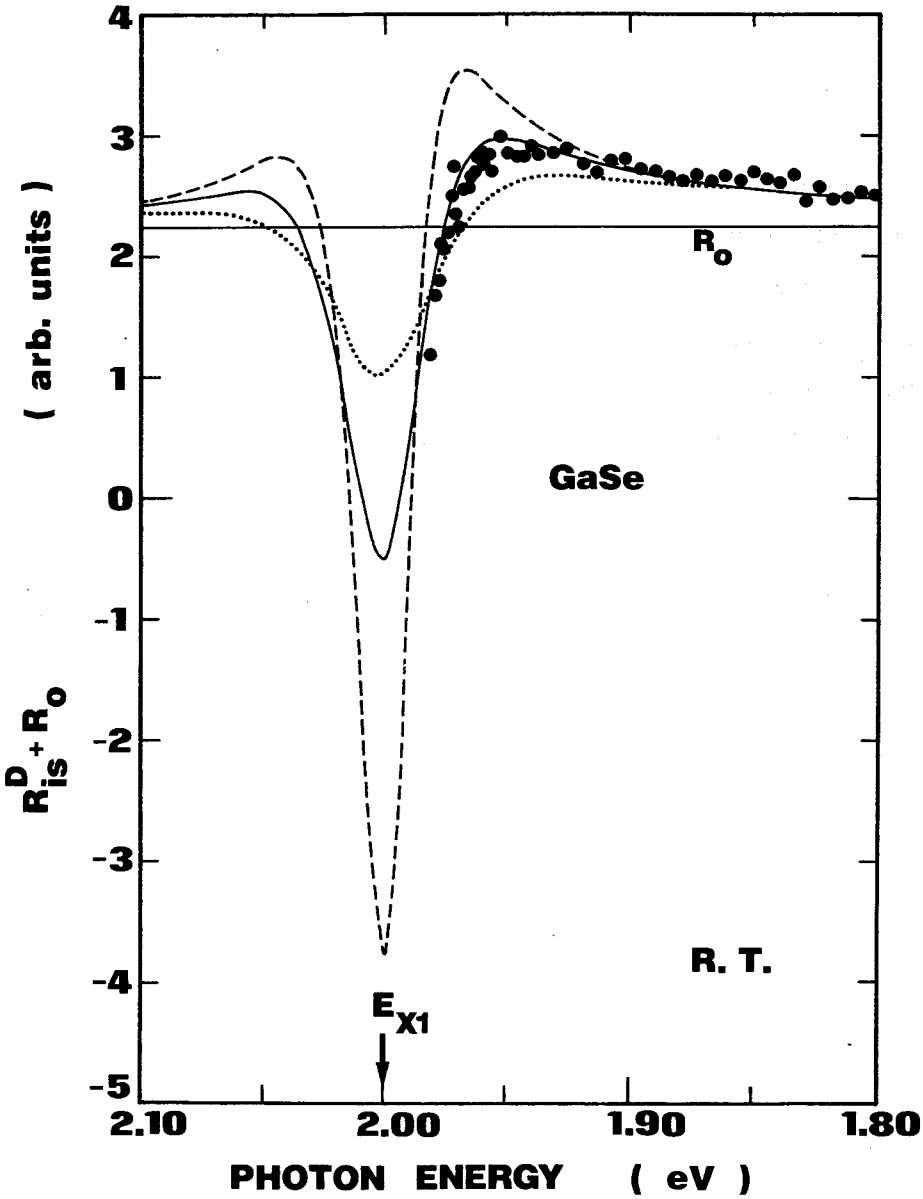

FIG. 10-13. Theoretical line shapes of R in the neighborhood of the fundamental absorption edge along with the experimental data for GaSe. The theoretical curves are obtained from Eq. (10.13) with Γ=40 meV (dashed line), Γ=60 meV (solid line) and Γ=90 meV (dotted line). The corresponding non-dispersive term (R_0) is also shown in the figure by solid line. The vertical arrow indicates the position of the n = 1 direct-exciton energy (E_{x1}).

very similar to that of the first-derivative modulation spectroscopy. We have discussed in Chapter VIII that resonant Brillouin scattering is quite equivalent to the first-derivative modulation spectroscopy such as thermoreflectance, piezoreflectance and wavelength-derivative spectroscopy. Indeed, the thermoreflectance spectrum of GaSe[333,334] showed a sharp peak due to the n = 1 excitonic structure at a region close to the direct-energy gap, which is very similar to the line shape of R given in Fig. 10-13.

Figure 10-14 shows the theoretical line shapes of the Brillouin tensor R of GaS in the neighborhood of the fundamental absorption edge. The solid line is calculated from Eq. (10.9), where the lifetime-broadening energy of Γ = 200 meV is taken into account in the calculation of Eq. (2.55). The theoretical line shapes are also calculated from Eq. (10.13) with three different broadening energies; Γ = 0 meV (dash-dotted line), Γ = 200 meV (dashed line) and Γ = 300 meV (dotted line). The experimental data ($\sigma_B^{\frac{1}{2}} \propto |R|$) are plotted in the figure by solid circles. The corresponding nonresonant term R_0 is also shown by solid line. The vertical arrows indicate the positions of the indirect-gap (E_g^{ID}) and n = 1 direct-exciton (E_{x1}) energies. The figure clearly indicates that the monotonic decrease observed in the region of the indirect-energy gap can not be successfully interpreted only by the direct-gap resonance process, in contrast to the case of GaSe. The indirect-gap resonance term R_{is}^{ID}, on the other hand, completely interpretes the observed monotonic decrease, as shown by solid line. We can also show in the figure that the nonresonant term R_0 is always dominant especially at energies below E_g^{ID}. This result is similar to the case of GaSe. An examination of analogous data allows one to argue possibility of the indirect-gap resonance in GaS. For example, we have reported in Chapter IX the results of resonant Brillouin scattering in GaP. The GaP crystal is an indirect-gap semiconductor and is thought to be excellent material to study some of the indirect-gap resonance effects, since the energy

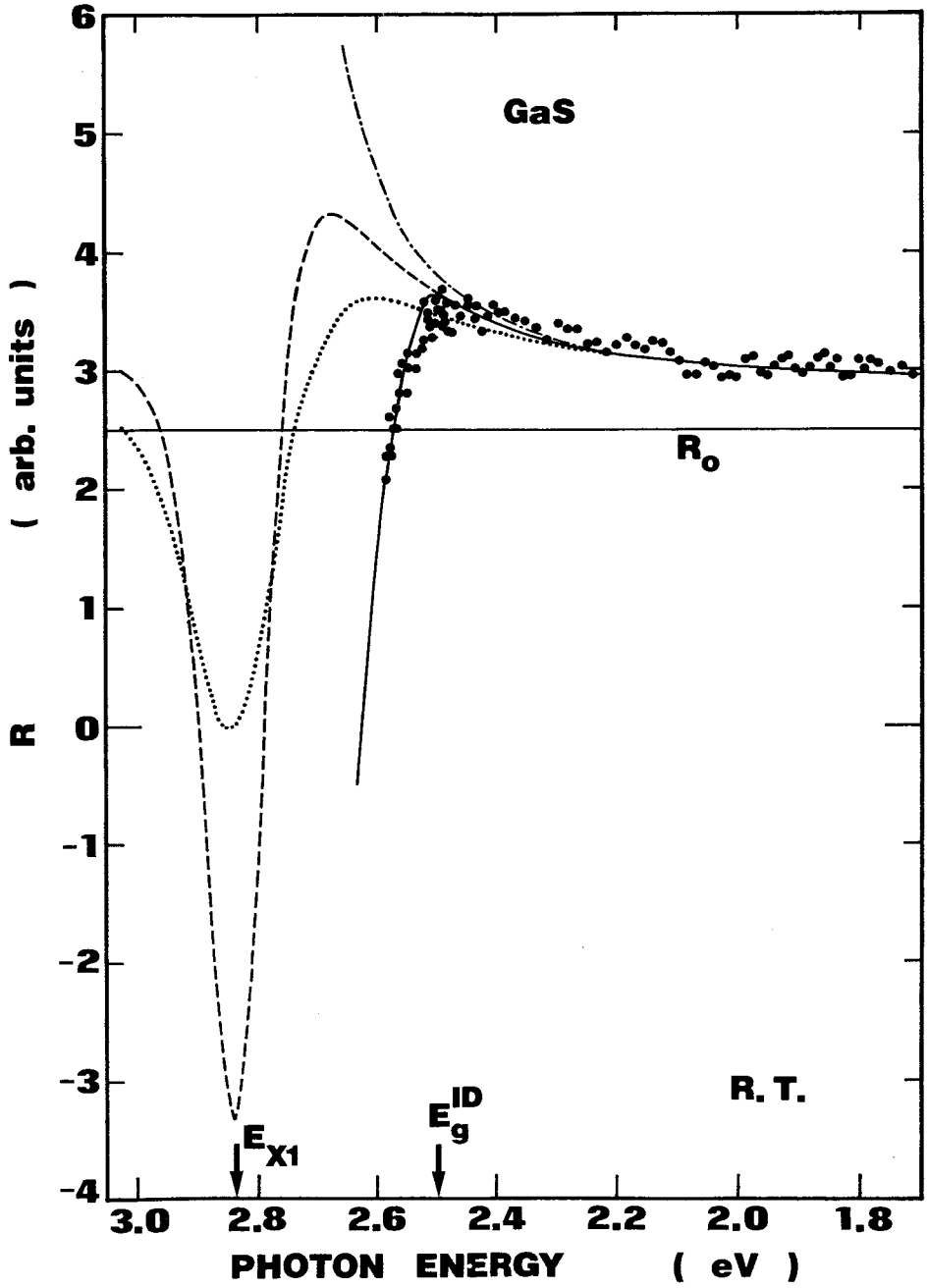

FIG. 10-14. Theoretical line shapes of R in the neighborhood of the fundamental absorption edge along with the experimental data for GaS. The theoretical curves are obtained from Eq. (10.9) with Γ=200 meV (solid line) and from Eq. (10.13) with Γ=0 meV (dash-dotted line), Γ=200 meV (dashed line) and Γ=300 meV (dotted line), where Γ is the direct-exciton lifetime-broadening energy. The corresponding nondispersive term (R_0) is also shown in the figure by solid line. The vertical arrows indicate the positions of the indirect-gap (E_g^{ID}) and n = 1 direct-exciton energy (E_{x1}).

separation between the indirect and direct gaps of this material is relatively large (≃ 0.5 eV). The measured spectral dependence of the Brillouin-scattering cross sections in GaP also showed weak resonant cancellation as the incident-photon energy extends beyond the indirect-energy gap of this material.

CHAPTER XI

SUMMARY AND CONCLUSION

Resonant Brillouin scattering has been investigated in II-VI, III-V and III-VI semiconductors. The results and conclusions obtained in the present work are summarized as follows.

Resonant Brillouin scattering in ZnSe and ZnTe has been studied at room temperature and 77 K by making use of the acoustical-domain injection method. The spectral dependence of the Brillouin-scattering cross sections in these semiconductors for the T1- (slow TA) and T2-mode (fast TA) phonons has shown resonant enhancement and cancellation in the region near the fundamental absorption edge. The Brillouin-scattering cross section has been found to depend strongly on the lifetime-broadening effect of the intermediate electronic states near the resonance region. The resonance-Brillouin effect has also been studied in $Zn_xCd_{1-x}Te$ solid solutions by making use of the acoustical-domain injection method. The relative concentration of the participants in solid solutions determines the band-gap energy which usually falls within the range of the band-gap energies of the two pure compounds. The band-gap energy plays a significant role in the resonance features through the intraband and interband electronic transitions. It has been clearly found that the resonance curve observed shifts toward longer wavelength side as the molar composition x decreases, originating from the shift of the band-gap energy with x. The resonance behavior of the Brillouin-scattering cross

sections in CdS has been measured by using the acoustoelectrically amplified phonon domains [T2-mode (slow TA)]. The resonance data of Brillouin scattering by the T1-mode (fast TA) and PL-mode (pure longitudinal) phonon domains have also been obtained in CdS by the mode conversion upon partial reflection of the T2-mode domains at the anode-end surface. The data have shown resonant enhancement and cancellation for the T1- and T2-mode phonon domains in the region near the fundamental absorption edge, while only weak resonant enhancement has been found for the PL-mode phonon domains in the region below the intrinsic absorption edge. The experimental data obtained have been compared with the theoretical prediction based upon Loudon's light-scattering theory assuming the free electron-hole pairs or Wannier-Mott excitons as the intermediate electronic states. It has been found that the Wannier-Mott exciton model shows a quite good agreement with the present experimental results when the lifetime-broadening effect is phenomenologically taken into account in the calculation.

The resonance data of Brillouin scattering in ZnSe, ZnTe and CdS have been analyzed with a theoretical prediction based on the quasi-static approximation. This analysis indicates that for the allowed scattering the Brillouin-scatteing efficiency (Brillouin tensor) is proportional to the first derivative of the dielectric constant ε with respect to the incident-photon energy while for the forbidden scattering proportional to the second derivative of ε with respect to the incident-photon energy. The theoretical calculation has been performed by numerically differentiating the experimental data of the dielectric constant. The resonance behaviors of Brillouin scattering have been well interpreted by the quasi-static approximation when the non-dispersive contributions are properly taken into account. This analysis has also clearly indicated that resonant Brillouin scattering is quite equivalent to the conventional modulation spectroscopy such as thermoreflectance spectro-

scopy. Resonance forbidden Brillouin scattering has been observed in CdS by the T2-mode phonon domains in several scattering configurations (parallel-parallel and parallel-perpendicular configurations). The data have been well interpreted with a dielectric theory based on the second derivative of ε with respect to the incident-photon energy, as expected from the quasi-static approximation. Although the forbidden-scattering mechanism observed here has not yet been completely explained, it may be pointed out that the strong longitudinal field associated with the T2-mode phonon domain is one of the causes.

From a macroscopical point of view, the Brillouin-scattering cross section is proportional to the square of the corresponding photoelastic constant which can be obtained independently from the piezobirefringence experiment. The spectral dependence of the photoelastic constants, $p_{11} - p_{12}$ and p_{44} for ZnSe and ZnTe and p_{66} $[\frac{1}{2}(p_{11}-p_{12})]$, p_{44} and p_{31} for CdS, has been determined from the present data by introducing the piezobirefringence analysis. The photoelastic constant has been found to depend strongly on the lifetime-broadening effect of the electronic states especially near the band-edge region as in the Brillouin-scattering efficiency. Moreover, it has been reported a new method to analyze the piezobirefringence coefficient in an opaque region of solids. This method takes into account the contributions from the stress-induced changes in both the real ($\Delta\varepsilon_1$) and imaginary part ($\Delta\varepsilon_2$) of the dielectric constant. New coefficients, which determine the fractional contributions of $\Delta\varepsilon_1$ and $\Delta\varepsilon_2$ to the piezobirefringence coefficient, have been derived from an analytical point of view. The experimental data of Si and ZnSe have been analyzed by using the present model. Good agreement between the experiment and calculation has been found. The present method is thought to provide a guiding principle for analyzing the piezobirefringence coefficient in an opaque region.

The effect of the lifetime broadening on resonant Brillouin scattering has been studied in more detail by using the acoustical-domain injection method. Two kinds of ZnTe and ZnSe single crystals have been used to investigate some effects of the crystalline imperfections on the spectral dependence of the Brillouin-scattering cross sections. Moreover, the measurements have been made at room temperature and low temperature (77 K) to investigate some temperature effects on the lifetime broadening. It has been found that the lifetime-broadening energy does not depend strongly on the temperatures but on the kinds of the crystals. The lifetime-broadening energy of the high-purity ZnTe (ZnSe) determined from the Brillouin-scattering measurements is Γ = 26 meV (44 meV) at 77 K, which is very large compared with the value of $\Gamma \simeq$ 2 meV (3 meV) obtained from reflectance spectrum. The results are interpreted in terms that the lifetime broadening is caused mainly by an interaction of the intermediate electronic states with the high-intensity phonon domains and crystalline imperfections.

The common feature of all modulation techniques of optical spectroscopy is the measurement of the derivative of some optical properties with respect to some parameters such as temperature, stress, wavelength, electric field and magnetic field. Such a modulation spectroscopy yields information about the structures and properties of optical critical points and profiles of the exciton lines. A detailed discussion has been given on resonant Brillouin scattering in connection with the first-derivative modulation spectroscopy such as thermoreflectance, piezoreflectance and wavelength-modulation spectroscopy. It has been shown that the Brillouin-scattering efficiency is expected by the first derivative of the dielectric constant with respect to the incident-light wavelength or equivalently to the band-gap energy, which is the same as the expression for the first-derivative modulation spectroscopy. A comparison of the Brillouin-scattering efficiencies derived experimentally

with the first-derivative modulation spectra has shown that they agree quite well with each other and also with the theoretical curves of the Brillouin-scattering efficiency when the lifetime-broadening is taken into account in the Brillouin-scattering analyses. It has been concluded from these results that the resonant-Brillouin process can be described by a phenomenological formalism analogous to that of the first-derivative modulation spectroscopy.

Resonant Brillouin scattering in III-V semiconductor GaP by the transverse acoustical phonons has been studied at room temperature in the region of the indirect absorption edge by making use of the acoustical-domain injection method. The GaP crystal is a more suitable material to study some of the indirect-gap resonance behaviors, since the energy separation between the indirect and direct gaps in this material is relatively large ($\simeq$ 0.5 eV). The spectral dependence of the Brillouin-scattering cross sections has shown a monotonic decrease (resonant cancellation) as the incident-photon energy extends beyond the indirect-gap energy. It has been formulated a theory of resonant Brillouin scattering at the indirect gap of semiconductors. The experimental data have been well interpreted by this theoretical model (indirect-gap resonance) and an additional dielectric theory of the direct-gap resonance (quasi-static approximation). The spectral dependence of the photoelastic constants, $|p_{11} - p_{12}|$ and $|p_{44}|$, has also been determined as a by-product of the Brillouin-scattering data.

The strong anisotropic nature of the layer-type, III-VI semiconductors GaSe and GaS makes it a very interesting subject of investigation from both theoretical and experimental aspects. Resonant Brillouin scattering in GaSe and GaS has first been investigated at room temperature by making use of the acoustical-domain injection method. The GaSe and GaS crystals are well known to have indirect gaps below the lowest direct gaps; the top of its valence band lies at Γ point and the bottom of the conduction band at M point.

Relative minima of the conduction band at Γ are situated a few tens of meV for GaSe and about 0.4 eV for GaS above the minima at M. The group-theoretical analysis has indicated that the two-band process (intraband electronic transition) plays an important role in the direct-gap resonance of the Brillouin-scattering mechanism by the pure-transverse phonons. The experimental data obtained have shown clear resonant cancellation for both GaSe and GaS in the region very close to the fundamental absorption edges. It has been found that the Brillouin-scattering intensity depends strongly on the lifetime-broadening effect of the intermediate electronic states. The spectral dependence of the Brillouin-scattering cross sections has shown a good agreement with the theoretical predictions based on the quasi-static approximation and Loudon's light-scattering theory. The resonant cancellation has been successfully interpreted by the direct-gap (direct-exciton) and indirect-gap resonance processes for GaSe and GaS, respectively. Such analyses, moreover, have clearly indicated that the nonresonant electronic transitions are dominant in the Brillouin-scattering process even in the region near the fundamental absorption edges.

LIST OF REFERENCES

1. L. Rayleigh: Phil. Mag. 47(1899)375.
2. L. Brillouin: Ann. Phys. (Paris) 17(1922)88.
3. A. Smekal: Naturwiss. 11(1923)873.
4. C. V. Raman: Ind. J. Phys. 2(1928)387.
5. G. Landsberg and L. Mandelstam: Naturwiss. 16(1928)57.
6. E. Gross: Nature 126(1930)603.
7. E. H. L. Meyer and W. Ramm: Physik. Z. 33(1932)270.
8. See, for example, *Light Scattering in Solids*, ed. M. Cardona (Springer-Verlag, Berlin, 1975).
9. R. C. C. Leite and S. P. S. Porto: Phys. Rev. Lett. 17(1966)10.
10. J. M. Ralston, R. L. Wadsack and R. K. Chang: Phys. Rev. Lett. 25(1970)814.
11. A. S. Pine: Phys. Rev. B5(1972)3003.
12. A. R. Hutson, J. H. McFee and D. L. White: Phys. Rev. Lett. 7(1961)237.
13. A. R. Hutson and D. L. White: J. Appl. Phys. 33(1962)40.
14. D. L. White: J. Appl. Phys. 33(1962)2547.
15. J. Zucker and S. Zemon: Appl. Phys. Lett. 9(1966)398.
16. D. L. Spears: Phys. Rev. B2(1970)1931.
17. E. D. Palik and R. Bray: Phys. Rev. B3(1971)3302.
18. M. Yamada, C. Hamaguchi, K. Matsumoto and J. Nakai: Phys. Rev. B7(1973) 2682.
19. M. San'Ya, M. Yamada, C. Hamaguchi and J. Nakai: Jpn. J. Appl. Phys. 13(1974)611.
20. J. Zucker, S. Zemon and J. H. Wasko: *II-VI Semiconducting Compounds*, ed. D. G. Thomas (Benjamin, New York, 1967) p. 919.
21. W. Wettling and M. Bruun: Phys. Lett. A27(1968)123.
22. S. Zemon and J. Zucker: IBM J. Res. Develop. (1969)494.

23. R. Mauro and W. C. Wang: Phys. Rev. B1(1970)683.

24. E. M. Conwell and A. K. Ganguly: Phys. Rev. B4(1971)2535.

25. D. K. Garrod and R. Bray: Phys. Rev. B6(1972)1314; *Proceedings of the Eleventh International Conference on the Physics of Semiconductors*, Warsaw 1972 (p. 1167).

26. M. Yamada, K. Ando and C. Hamaguchi: J. Phys. Soc. Jpn 34(1973)1696.

27. K. Ando and C. Hamaguchi: Phys. Rev. B11(1975)3876.

28. U. Gelbart and A. Many: Phys. Lett. A43(1973)329.

29. R. Berkowicz and D. H. R. Price: Solid State Commun. 14(1974)195.

30. R. Berkowicz and T. Skettrup: Phys. Rev. B11(1975)2316.

31. K. Yamamoto, K. Misawa, H. Shimizu and K. Abe: J. Phys. Chem. Solids 37(1976)181.

32. See, for example, N. I. Meyer and M. H. Jørgensen: *Advances in Solid State Physics*, ed. O. Madelung (Pergamon, Vieweg, 1970) p. 21.

33. K. Yamabe, K. Ando and C. Hamaguchi: Jpn. J. Appl. Phys. 16(1977)747.

34. C. Hamaguchi, K. Yamabe, K. Ando and S. Adachi: *Proceedings of the Sixth International Conference on Internal Friction and Ultrasonic Attenuation in Solids*, ed. R. R. Hasiguti and N. Mikoshiba (University of Tokyo, Tokyo, 1977) p. 183.

35. R. Loudon: Proc. Roy. Soc. Lond. A275(1963)218.

36. R. Loudon: J. Phys. (Paris) 26(1965)677.

37. A. K. Ganguly and J. L. Birman: Phys. Rev. 162(1967)806.

38. G. B. Benedek and K. Fritch: Phys. Rev. 149(1966)647.

39. S. Adachi and C. Hamaguchi: Phys. Lett. A66(1978)401; J. Phys. Soc. Jpn 45(1978)505.

40. Y. Itoh, K. Yamabe, S. Adachi and C. Hamaguchi: J. Phys. Soc. Jpn 46(1979)542.

41. A. Pinczuk and E. Burstein: *Light Scattering in Solids*, ed. M. Cardona

(Springer-Verlag, Berlin, 1975) p.23.

42. J. F. Nye: *Physical Properties of Crystals* (Clarendon, Oxford, 1960) p. 235.

43. M. Cardona: *Modulation Spectroscopy* (Academic, New York, 1969).

44. B. O. Seraphin, R. L. Aggarwal, D. F. Blossey, P. Handler, I. Balsley, D. E. Aspnes and N. Bottka: *Semiconductors and Semimetals*, ed. R. K. Willardson and A. C. Beer (Academic, New York, 1972) Vol. 9.

45. A. G. Thompson, M. Cardona and K. L. Shaklee: Phys. Rev. 146(1966)601.

46. R. W. Dixon: J. Appl. Phys. 38(1967)5149.

47. M. Schlüter: Nuovo Cimento B13(1973)313.

48. R. M. Martin: Phys. Rev. B4(1971)3676.

49. M. Cardona: Solid State Commun. 9(1971)819.

50. F. Cerdeira, W. Dreybrodt and M. Cardona: *Proceedings of the Eleventh International Conference on the Physics of Semiconductors*, Warsaw 1972 (p. 1142).

51. F. Cerdeira, W. Dreybrodt and M. Cardona: Solid State Commun. 10(1972)591.

52. W. Dreybrodt, W. Richter and M. Cardona: Solid State Commun. 11(1972)1127.

53. B. A. Weinstein and M. Cardona: Phys. Rev. B8(1973)2795.

54. M. I. Bell, R. N. Tyte and M. Cardona: Solid State Commun. 13(1973)1833.

55. M. A. Renucci, J. B. Renucci, R. Zeyher and M. Cardona: Phys. Rev. B10 (1974)4309.

56. R. L. Schmidt, B. D. McCombe and M. Cardona: Phys. Rev. B11(1975)746.

57. W. Kiefer, W. Richter, R. L. Schmidt and M. Cardona: *Light Scattering in Solids*, ed. M. Balkanski, R. C. C. Lite and S. P. S. Porto (Flammarion, Paris, 1975) p. 98.

58. J. M. Calleja and M. Cardona: Phys. Rev. B16(1977)3753.

59. N. Sinyukov, R. Trommer and M. Cardona: Phys. Status Solidi B86(1978)563.

60. R. Trommer and M. Cardona: Phys. Rev. B17(1978)1865.

61. W. Richter, R. Zeyher and M. Cardona: Phys. Rev. B18(1978)4312.

62. D. F. Nelson, P. D. Lazay and M. Lax: Phys. Rev. B6(1972)3109.

63. C. Hamaguchi: J. Phys. Soc. Jpn 35(1973)832.

64. C. W. Higginbotham, M. Cardona and F. H. Pollak: Phys. Rev. 184(1969)821.

65. R. Claus, L. Merten and J. Brandmuller: *Light Scattering by Phonon-Polaritons* (Springer-Verlag, Berlin, 1975).

66. W. Brenig, R. Zeyher and J. L. Birman: Phys. Rev. B6(1972)4617.

67. W. Jones and N. H. March: *Theoretical Solid State Physics* (John Wiley & Sons, London, 1973) Vol. 2, p. 880.

68. R. S. Knox: *Theory of Excitons* (Academic, New York, 1963).

69. D. C. Reynolds, C. W. Litton and T. C. Collins: Phys. Status Solidi 9(1965)645.

70. R. J. Elliott: Phys. Rev. 108(1957)1384.

71. S. Adachi and C. Hamaguchi: J. Phys. Soc. Jpn 43(1977)1637.

72. G. L. Bir and G. E. Pikus: *Symmetry and Strain-Induced Effects in Semiconductors* (John Wiley & Sons, New York, 1974).

73. C. Kittel: *Quantum Theory of Solids*, (John Wiley & Sons, New York, 1963).

74. G. E. Pikus and G. L. Bir: Sov. Phys.-Solid State 1(1959)136.

75. F. H. Pollak and M. Cardona: Phys. Rev. 172(1968)816.

76. H. Fröhlich: Advan. Phys. 3(1954)325.

77. H. Ehrenreich: J. Phys. Chem. Solids 2(1957)131.

78. L. I. Schiff: *Quantum Mechanics* (McGraw-Hill, New York, 1955).

79. J. F. Nye: *Physical Properties of Crystals* (Clarendon, Oxford, 1960) p. 93.

80. D. G. Thomas and J. J. Hopfield: Phys. Rev. 116(1959)573.

81. J. J. Hopfield: J. Phys. Chem. Solids 15(1960)97.

82. G. E. Pikus: Sov. Phys.-Solid State 6(1964)261.

83. B. Segall: *Physics and Chemistry of II-VI Compounds*, ed. M. Aven and J. S. Prener (North-Holland, Amsterdam, 1967) p. 1.

84. J. C. Slater: *Insulators, Semiconductors and Metals* (McGraw-Hill, New York,

1967).

85. M. Cardona: *Solid State Physics, Nuclear Physics and Particle Physics*, ed. I. Saavedra (Benjamin, New York, 1968) p. 737.

86. F. Stern: *Solid State Physics*, ed. F. Seitz and D. Turnbull (Academic, New York, 1963) Vol. 15.

87. L. I. Korovin: Sov. Phys.-Solid State 1(1960)1202.

88. D. F. Blossey: Phys. Rev. B2(1970)3976; B3(1971)1382.

89. R. Berkowicz: Ph. D. Thesis (Technical University of Denmark, 1975).

90. B. Segall and D. T. F. Marple: *Physics and Chemistry of II-VI Compounds*, ed. M. Aven and J. S. Prener (North-Holland, Amsterdam, 1967) p. 317.

91. D. G. Thomas: J. Appl. Phys. Suppl. 32(1961)2298.

92. P. Y. Yu and M. Cardona: J. Phys. Chem. Solids 34(1973)29.

93. E. O. Kane: *Semiconductors and Semimetals*, ed. R. K. Willardson and A. C. Beer (Academic, New York, 1966) Vol. 1, p. 75.

94. See, for example, G. Dresselhaus, A. F. Kip and C. Kittel: Phys. Rev. 98(1955)368.

95. S. Adachi and C. Hamaguchi: Phys. Rev. B19(1979)938.

96. S. Adachi and C. Hamaguchi: J. Phys. Soc. Jpn 44(1978)343.

97. See, for example, G. A. Wolff and A. I. Mlavsky: *Crystal Growth, Theory and Techniques*, ed. C. H. L. Goodman (Plenum, New York, 1974) Vol. 1, p. 193.

98. M. Aven and H. H. Woodbury: Appl. Phys. Lett. 1(1962)53.

99. R. W. Smith: Phys. Rev. Lett. 9(1962)87.

100. J. H. McFee, P. K. Tien and H. L. Hodges: J. Appl. Phys. 38(1967)1721.

101. W. H. Haydl, K. Harker and C. F. Quate: J. Appl. Phys. 38(1967)4295.

102. M. Kikuchi: Jpn. J. Appl. Phys. 2(1963)807; 2(1963)812; 3(1964)448.

103. S. Yee, A. Kawai and M. L. Neudorfer: Solid-State Electronics 12(1969)191

104. M. Kikuchi: Jpn. J. Appl. Phys. 4(1965)233.

105. A. I. Morozov: Sov. Phys.-Solid State 10(1969)2844.

106. J. H. McFee: J. Appl. Phys. 34(1963)1548.

107. N. I. Meyer, M. H. Jørgensen and I. Balslev: Solid State Commun. 3(1965) 393.

108. W. E. Spear and P. G. Le Comber: Phys. Rev. Lett. 13(1964)434.

109. C. Hervouet, J. Lebailly, P. L. Hugon and R. Veilex: Solid State Commun. 3(1965)413.

110. H. Hayakawa, M. Kikuchi and Y. Abe: Jpn. J. Appl. Phys. 5(1966)734.

111. P. O. Sliva and R. Bray: Phys. Rev. Lett. 14(1965)372.

112. J. B. Ross: Ph. D. Thesis (Purdue University, 1972).

113. G. Quentin and J. M. Thuiler: *Proceedings of the Seventh International Conference on the Physics of Semiconductors*, Paris 1964 (p. 571).

114. J. Mort: Phys. Rev. Lett. 18(1967)540.

115. R. Klein: Solid State Commun. 7(1969)917.

116. D. L. Spears and R. Bray: Phys. Lett. A29(1969)670; D. L. Spears: Ph. D. Thesis (Purdue University, 1969).

117. R. W. Dixon: IEEE J. Quantum Electronics QE-3(1967)85.

118. K. Ando, M. Yamada and C. Hamaguchi: Jpn. J. Appl. Phys. 13(1974)1467.

119. K. Ando and C. Hamaguchi: Solid State Commun. 16(1975)57.

120. K. Ando, K. Yamabe, S. Hamada and C. Hamaguchi: J. Phys. Soc. Jpn 41(1976) 1593.

121. B. A. Auld: *Acoustic Fields and Waves in Solids* (John Wiley & Sons, New York, 1973).

122. H. J. Maris: *Physical Acoustics*, ed. W. P. Mason and R. N. Thurston (Academic, New York, 1971) Vol. VIII.

123. K. Dransfeld and E. Salzmann: *Physical Acoustics*, ed. W. P. Mason and R. N. Thurston (Academic, New York, 1970) Vol. VII.

124. J. Zucker, S. A. Zemon and J. H. Wasko: *Proceedings of the Nineth*

International Conference on the Physics of Semiconductors, Moscow 1968 (p. 904).

125. S. Adachi and C. Hamaguchi: Technol. Rept. Osaka Univ. Vol. 28, No. 1410, p. 141.

126. K. Tsubouchi, S. Kameoka and T. Arizumi: J. Phys. Soc. Jpn 37(1974)1305.

127. K. Tsubouchi and N. Mikoshiba: Jpn. J. Appl. Phys. 14(1975)309.

128. H. Jaffe and D. A. Berlincourt: Proc. IEEE 53(1965)1372.

129. D. Berlincourt, H. Jaffe and L. R. Shiozawa: Phys. Rev. 129(1963)1009.

130. G. Arlt and P. Quadflieg: Phys. Status Solidi 25(1968)323.

131. C. Hamaguchi, S. Adachi and Y. Itoh: Solid-State Electronics 21(1978)1585.

132. W. L. Roth: *Physics and Chemistry of II-VI Compounds*, ed. M. Aven and J. S. Prener (North-Holland, Amsterdam, 1967) p. 117.

133. E. P. Warekois, M. C. Lavine, A. N. Mariano and H. C. Gatos: J. Appl. Phys 33(1962)690.

134. L. K. Vodop'yanov, E. A. Vinogradov, A. M. Blinov and V. A. Rukavishnikov: Sov. Phys.-Solid State 14(1972)219.

135. K. Saito, A. Ebina and T. Takahashi: Solid State Commun. 11(1972)657.

137. A. Ebina, K. Saito and T. Takahashi: J. Appl. Phys. 44(1973)3659.

138. V. A. Tyagai, O. V. Snitko, V. N. Bondarenko, N. I. Vitrikhovskii, V. B. Popov and A. N. Krasiko: Sov. Phys.-Solid State 16(1974)885.

139. S. G. Kroitoru, O. G. Maksimova and V. V. Sobolev: Sov. Phys.-Semicond. 9(1976)1191.

140. See, for example, D. L. Greenaway and G. Harbeke: *Optical Properties and Band Structure of Semiconductors* (Pergamon, Oxford, 1968).

141. M. L. Cohen and T. K. Bergstresser: Phys. Rev. 141(1966)789.

142. T. K. Bergstresser and M. L. Cohen: Phys. Rev. 164(1967)1069.

143. J. P. Walter, M. L. Cohen, Y. Petroff and M. Balkanski: Phys. Rev. B1 (1970)2661.

144. B. H. Lee: J. Appl. Phys. 41(1970)2984.

145. B. H. Lee: J. Appl. Phys. 41(1970)2988.

146. I. Strzalkowski, S. Joshi and C. R. Crowell: Appl. Phys. Lett. 28(1976) 350.

147. J. C. Irwin and J. LaCombe: Can. J. Phys. 50(1972)2596.

148. N. Vagelatos, D. Wehe and J. S. King: J. Chem. Phys. 60(1974)3613.

149. M. A. Nusimovici and J. L. Birman: Phys. Rev. 156(1967)925.

150. A. D. Bruce and R. A. Cowley: J. Phys. C 5(1972)595.

151. R. Haberkorn, M. Buchanan and H. Bilz: Solid State Commun. 12(1973)681.

152. D. W. Langer, R. N. Euwema, K. Era and T. Koda: Phys. Rev. B2(1970)4005.

153. B. Segall: *Proceedings of the Nineth International Conference on the Physics of Semiconductors*, Moscow 1968 (p. 425).

154. B. Bendow and B. Lengeler: *Electronic Structure of Noble Metals and Polariton-Mediated Light Scattering* (Springer-Verlag, Berlin, 1978) p. 69.

155. R. Zeyher, C. S. Ting and J. L. Birman: Phys. Rev. B10(1974)1725.

156. R. G. Ulbrich and C. Weisbuch: Phys. Rev. Lett. 38(1977)865.

157. R. G. Ulbrich and C. Weisbuch: *Advances in Solid State Physics*, ed. O. Madelung, H. J. Queisser and J. Treusch (Vieweg-Verlag, Wiesbaden, 1978) p. 217.

158. G. Winterling and E. Koteles: Solid State Commun. 23(1977)95.

159. E. S. Koteles and G. Winterling: J. Luminescence 18/19(1979)267.

160. R. H. Bruce and H. Z. Cummins: Phys. Rev. B16(1977)4462.

161. G. Winterling, E. S. Koteles and M. Cardona: Phys. Rev. Lett. 39(1977)1286.

162. P. Y. Yu and F. Evangelisti: Solid State Commun. 27(1978)87.

163. P. Y. Yu and F. Evangelisti: Phys. Rev. Lett. 42(1979)1642.

164. C. Hermann and P. Y. Yu: Solid State Commun. 28(1978)313.

165. Y. Oka and M. Cardona: Solid State Commun. 30(1979)447.

166. T. C. Damen and J. F. Scott: Solid State Commun. 9(1971)383.

167. R. H. Callender, S. S. Sussman, M. Selders and R. K. Chang: Phys. Rev. B7(1973)3788.

168. R. H. Callender, M. Balkanski and J. L. Birman: *Light Scattering in Solids*, ed. M. Balkanski (Flammarion, Paris, 1971) p. 40.

169. J. L. Lewis, R. L. Wadsack and R. K. Chang: *Light Scattering in Solids*,

170. A. A. Kaplyanskii and L. G. Suslina: Sov. Phys.-Solid State 7(1966)1881.

171. M. Hayek and O. Brafman: *Light Scattering in Solids*, ed. M. Balkanski (Flammarion, Paris, 1971) p. 76.

172. M. A. Renuccim J. B. Renucci and M. Cardona: Phys. Status Solidi B49 (1972)625.

173. A. A. Klochikhin, A. G. Plyukhin, L. G. Suslina and E. B. Shadrin: Sov. Phys.-Solid State 18(1976)1112.

174. See, for example, I. F. Chang and S. S. Mitra: Advan. Phys. 20(1971)359.

175. J. A. Van Vechten and T. K. Bergstresser: Phys. Rev. B1(1970)3351.

176. E. Gutsche and J. Voigt: *II-VI Semiconducting Compounds*, ed. D. G. Thomas (Benjamin, New York, 1967) p. 337.

177. C. E. Bleil and J. G. Gay: *II-VI Semiconducting Compounds*, ed. D. G. Thomas (Benjamin, New York, 1967) p.360.

178. T. M. Bieniewski and S. J. Czyzak: J. Opt. Soc. Am. 53(1963)496.

179. D. Dutton: Phys. Rev. 112(1958)785.

180. A. G. Fischer and R. J. Paff: J. Phys. Chem. Solids 23(1962)1479.

181. S. Larach, R. E. Shrader and C. F. Stocker: Phys. Rev. 108(1957)587.

182. A. D. Stuckes and G. Farrell: J. Phys. Chem. Solids 25(1964)477.

183. W. R. Cook, Jr.: J. Am. Ceram. Soc. 51(1968)518.

184. E. Matatagui, A. G. Thompson and M. Cardona: Phys. Rev. 176(1968)950.

185. G. E. Hite, D. T. F. Marple, M. Aven and B. Segall: Phys. Rev. 156(1967) 850.

186. E. Loh and R. Newman: J. Phys. Chem. Solids 21(1961)324.

187. M. Cardona, K. L. Shaklee and F. H. Pollak: Phys. Rev. 154(1967)696.

188. S. Adachi and C. Hamaguchi: J. Phys. Soc. Jpn 46(1979)1546.

189. K. Ando and C. Hamaguchi: Phys. Lett. A58(1976)41.

190. S. Adachi and C. Hamaguchi: J. Phys. Soc. Jpn 46(1979)1385.

191. E. O. Kane: Phys. Rev. 178(1969)1368.

192. P. J. Colwell and M. V. Klein: Solid State Commun. 8(1970)2095.

193. P. F. Williams and S. P. S. Porto: *Light Scattering in Solids*, ed. M. Balkanski (Flammarion, Paris, 1971) p. 70.

194. R. M. Martin and T. C. Damen: Phys. Rev. Lett. 26(1971)86.

195. G. W. Rubloff, E. Anastassakis and F. H. Pollak: Solid State Commun. 13(1973)1755.

196. W. Dreybrodt, W. Richter, F. Cerdeira and M. Cardona: Phys. Status Solidi B60(1973)145.

197. D. T. F. Marple: J. Appl. Phys. 35(1964)539.

198. M. Aven, D. T. F. Marple and B. Segall: J. Appl. Phys. Suppl. 32(1961)2261.

199. T. R. Sliker and J. M. Jost: J. Opt. Soc. Am. 56(1966)130.

200. M. Cardona: J. Appl. Phys. 36(1965)2181.

201. G. D. Mahan and J. J. Hopfield: Phys. Rev. Lett. 12(1964)241.

202. E. S. Kohn and M. A. Lampert: Phys. Rev. B4(1971)4479.

203. M. Cardona and G. Harbeke: Phys. Rev. 137(1965)A1467.

204. M. Iliev and I. Assenov: Phys. Status Solidi 42(1970)383.

205. A. Ferdman and D. Horowitz: J. Appl. Phys. 39(1968)5597.

206. L. N. Glurdzhidze, A. P. Izergin, Z. N. Kopylova and A. D. Remenyuk: Sov. Phys.-Semicond. 7(1973)305.

207. F. Canal, M. Grimsditch and M. Cardona: Solid State Commun. 29(1979)523.

208. A. Yu. Shileika, M. Cardona and F. H. Pollak: Solid State Commun. 7(1969)1113.

209. P. Y. Yu, M. Cardona and F. H. Pollak: Phys. Rev. B3(1971)340.

210. V. D. Kulakovskii, V. I. Grinev and M. P. Kulakov: Sov. Phys.-Solid State 19(1977)345.

211. K. K. Dubenskii, A. A. Kaplyanskii and N. G. Lozovskaya: Sov. Phys.-Solid State 8(1967)1644.

212. W. Wardzynski: J. Phys. C 3(1970)1251.

213. D. K. Biegelsen, J. C. Zesch and C. Schwab: Phys. Rev. B14(1976)3578.

214. A. A. Reza and G. A. Babonas: Sov. Phys.-Solid State 16(1974)909.

215. M. H. Grimsditch, E. Anastassakis and M. Cardona: Phys. Rev. B19(1979) 3240.

216. R. W. Dixon and M. G. Cohen: Appl. Phys. Lett. 8(1966)205.

217. M. Chandrasekhar, M. H. Grimsditch and M. Cardona: J. Opt. Soc. Am. 68(1978)523.

218. M. Chandrasekhar, M. H. Grimsditch and M. Cardona: Phys. Rev. B18(1978)4301.

219. S. Adachi and C. Hamaguchi (to be published).

220. D. R. Penn: Phys. Rev. 128(1962)2093.

221. J. A. Van Vechten: Phys. Rev. 182(1969)891.

222. B. Tell, J. M. Worlock and R. J. Martin: Appl. Phys. Lett. 6(1965)123.

223. C. Hamaguchi, K. Ando, M. San'Ya and M. Yamada: *Symp. on Microwave Acoustics*, Lancaster 1974 (unpublished).

224. H. R. Philipp and H. Ehrenreich: Phys. Rev. 129(1963)1550.

225. Y. Tsay, B. Bendow and S. S. Mitra: *Light Scattering in Solids*, ed. M. Balkanski, R. C. C. Leite and S. P. S. Porto (Flammarion, Paris, 1976) p. 442.

226. B. O. Seraphin and N. Bottka: Phys. Rev. 145(1966)628.

227. Y. Toyozawa: Prog. Theor. Phys. (Kyoto) 20(1958)53; J. Phys. Chem. Solids 25(1964)59.

228. D. T. F. Marple and M. Aven: *II-VI Semiconducting Compounds*, ed. D. G. Thomas (Benjamin, New York, 1967) p. 315.

229. S. Adachi, Y. Itoh and C. Hamaguchi: Jpn. J. Appl. Phys. 18(1979)575.

230. J. Carides and A. G. Fischer: Solid State Commun. 2(1964)217.

231. R. Triboulet and G. Didier: J. Crystal Growth 28(1975)29.

232. T. Taguchi, J. Shirafuji and Y. Inuishi: Jpn. J. Appl. Phys. 17(1978)1331.

233. M. Aven and B. Segall: Phys. Rev. 130(1963)81.

234. M. Aven: J. Appl. Phys. 42(1971)1204.

235. M. Yamaguchi and T. Shigematsu: Jpn. J. Appl. Phys. 17(1978)335.

236. D. T. F. Marple (unpublished).

237. Y. Toyozawa and J. Hermanson: Phys. Rev. Lett. 21(1968)1637.

238. M. Aven and D. A. Cusano: J. Appl. Phys. 45(1974)1444.

240. M. E. Özsan and J. Woods: Solid-State Electronics 18(1975)519.

241. S. Adachi and Y. Machi: Jpn. J. Appl. Phys. 15(1976)1513.

242. S. Adachi (unpublished).

243. G. B. Stringfellow and R. H. Bube: Phys. Rev. 171(1968)903.

244. R. E. Halsted, M. Aven and H. D. Coghill: J. Electrochem. Soc. 112(1965)177.

245. S. Iida: J. Phys. Soc. Jpn 26(1969)1140.

246. F. J. Bryant and P. S. Manning: J. Phys. Chem. Solids 35(1974)97.

247. T. Koda and S. Shionoya: Phys. Rev. 136(1964)A541.

248. W. C. Holton, M. de Wit and T. L. Estle: *International Symposium on Luminescence*, München 1965 (p. 454).

249. S. Iida: J. Phys. Soc. Jpn 25(1968)177.

250. J. C. Bouley, P. Blanconnier, A. Herman, Ph Ged, P. Henoc and J. P. Noblanc: J. Appl. Phys. 46(1975)3549.

251. D. C. Reynolds, L. S. Pedrotti and O. W. Larson: J. Appl. Phys. Suppl. 32(1961)2250.

252. P. J. Dean and J. L. Merz: Phys. Rev. 178(1969)1310.

253. A. W. Livingstone and J. W. Allen: Appl. Phys. Lett. 20(1972)207.

254. J. B. Bouley, P. Blanconnier, A. Herman, G. Jacottin, Ph Ged and J. P. Noblanc: *European Solid State Device Research Conference*, Nottingham 1974

(unpublished).

255. D. L. Spears and R. Bray: Appl. Phys. Lett. 12(1968)118.

256. D. E. Aspnes: Surface Science 37(1973)418.

257. S. Adachi and C. Hamaguchi: J. Phys. C 12(1979)2917.

258. D. E. Aspnes: Phys. Rev. Lett. 28(1972)168.

259. P. Lawaetz: Phys. Rev. B4(1971)3460.

260. H. Mathieu, J. Camassel and D. Auvergne: Phys. Status Solidi B68(1975)797.

261. G. W. Gobeli and E. O. Kane: Phys. Rev. Lett. 15(1965)142.

262. D. barbier, B. Montegu and A. Laugier: Solid State Commun. 28(1978)525.

263. A. N. Georgobiani, Yu. V. Ozerov and H. Friedrich: Sov. Phys.-Solid State 15(1974)1991.

264. A. N. Georgobiani, Yu. V. Ozerov and H. Friedrich: Phys. Status Solidi B68(1975)663.

265. D. Barbier and A. Laugier: Solid State Commun. 23(1977)435.

266. H. Friedrich, Yu. V. Ozerov, R. Strehlow and A. N. Georgobiani: Phys. Status Solidi B89(1978)603.

267. W. E. Engeler, H. Fritzsche, M. Garfinkel and J. J. Tiemann: Phys. Rev. Lett. 14(1965)1069.

268. J. F. Scott, T. C. Damen, R. C. C. Leite and W. T. Silfvast: Solid State Commun. 7(1969)953.

269. J. M. Ralston, R. L. Wadsack and R. K. Chang: Phys. Rev. Lett. 25(1970)814

270. P. B. Klein, H. Masui, Jin-Joo Song and R. K. Chang: Solid State Commun. 14(1974)1163.

271. W. von der Osten, J. Weber and G. Schaack: Solid State Commun. 15(1974) 1561.

272. M. Yamada, C. Hamaguchi and J. Nakai: Solid State Commun. 17(1975)879.

273. R. Trommer and M. Cardona: Solid State Commun. 21(1977)153.

274. A. Compaan and H. Z. Cummins: Phys. Rev. Lett. 31(1973)41.

275. P. Y. Yu and Y. R. Shen: Phys. Rev. B12(1975)1377; B17(1978)4017.

276. T. C. Chiang, J. Dumas and Y. R. Shen: Solid State Commun. 28(1978)173.

277. S. Adachi and C. Hamaguchi: Solid State Commun. 31(1979)245.

278. J. B. Valdez: Ph. D. Thesis (University of California Irvine, 1978).

279. K. P. Jain and C. S. Jayanthi: Phys. Rev. B19(1979)4198.

280. S. Adachi and C. Hamaguchi: Physica B (in press).

281. R. Loudon: *The Quantum Theory of Light* (Clarendon, Oxford, 1973) p. 267.

282. R. Zallen and W. Paul: Phys. Rev. 134(1964)A1628.

283. J. P. Walter and M. L. Cohen: Phys. Rev. 183(1969)763.

284. P. J. Dean and D. G. Thomas: Phys. Rev. 150(1966)690.

285. W. G. Spitzer, M. Gershenzon, C. J. Frosch and D. F. Gibbs: J. Phys. Chem. Solids 11(1959)339.

286. D. S. Kyser and V. Rehn: Phys. Rev. Lett. 40(1978)1038.

287. P. J. Dean, G. Kaminsky and R. B. Zetterstrom: J. Appl. Phys. 38(1967)3551.

288. R. Banerjee and Y. P. Varshni: J. Phys. Soc. Jpn 30(1971)1015.

289. R. Weil and W. O. Groves: J. Appl. Phys. 39(1968)4049.

290. M. Yamada, K. Wasa and C. Hamaguchi: Jpn. J. Appl. Phys. 15(1976)1107.

291. R. Humphreys, U. Rössler and M. Cardona (to be published).

292. A. Onton and T. N. Morgan: Phys. Rev. B1(1970)2592.

293. P. Merle, J. Camassel and H. Mathieu: Solid State Commun. 28(1978)75.

294. A. N. Pikhtin and D. A. Yas'kov: Sov. Phys.-Solid State 9(1967)107.

295. F. Bassani and G. P. Parravicini: *Electronic States and Optical Transitions in Solids* (Pergamon, Oxford, 1975) p. 168.

296. S. Shionoya: *Luminescence of Inorganic Solids*, ed. P. Goldberg (Academic, New York, 1966) p. 205.

297. A. Addamiano: J. Am. Chem. Soc. 82(1960)1537.

298. E. Mooser and M. Schlüter: Nuovo Cimento B18(1973)164.

299. R. M. Hoff and J. C. Irwin: Phys. Rev. B10(1974)3464.

300. J. Reydellet and J. M. Besson: Solid State Commun. 17(1975)23.

301. J. Camassel, T. C. Chiang, Y. R. Shen, J. P. Voitchovsky and N. M. Amer: Solid State Commun. 19(1976)483.

302. T. C. Chiang, J. Camassel, J. P. Voitchovsky and Y. R. Shen: Nuovo Cimento B38(1977)301.

303. M. Balkanski, J. Reydellet, C. Hirlimann and M. Kanehisa: J. Luminescence 18/19(1979)665.

304. T. C. Chiang, J. Camassel, Y. R. Shen and J. P. Voitchovsky: Solid State Commun. 19(1976)157.

305. J. L. Brebner and G. Fischer: Can. J. Phys. 41(1963)561.

306. J. L. Brebner: 25(1964)1427.

307. E. Aulich, J. L. Brebner and E. Mooser: Phys. Status Solidi 31(1969)129.

308. B. S. Razbirin, M. I. Karaman, V. P. Mushinskii and A. N. Starukhin: Sov. Phys.-Semicond. 7(1973)753.

309. G. L. Belenkii and M. O. Godzhaev: Phys. Status Solidi B85(1978)453.

310. J. D. Wasscher and J. Dieleman: Phys. Lett. A39(1972)279.

311. R. Le Toullec, N. Piccioli, M. Mejatty and M. Balkanski: Nuovo Cimento B38(1977)159.

312. M. Schlüter, J. Camassel, S. Kohn, J. P. Voitchovsky, Y. R. Shen and M. L. Cohen: Phys. Rev. B13(1976)3534.

313. J. C. J. M. Terhell and R. M. A. Lieth: Phys. Status Solidi A10(1972)529.

314. F. Bassani and G. P. Parravicini: Nuovo Cimento B50(1967)95.

315. H. Kamimura and K. Nakao: J. Phys. Soc. Jpn 24(1968)1313.

316. C. Y. Fong and M. L. Cohen: Phys. Rev. B5(1972)3095.

317. M. Schlüter and M. L. Cohen: Phys. Rev. B14(1976)424.

318. J. Bordas, J. Robertson and A. Jakobsson: J. Phys. C 11(1978)2607.

319. S. Adachi and C. Hamaguchi (to be published).

320. J. L. Brebner and S. Jandl: Solid State Commun. 13(1973)1555.

321. S. Jandl and J. L. Brebner: Phys. Rev. B13(1976)686.

322. B. M. Powell, S. Jandl, J. L. Brebner and F. Lèvy: J. Phys. C 10(1977)3039.

323. K. M. Khalilov and K. I. Rzaev: Sov. Phys.-Crystallography 11(1967)786.

324. M. Tanaka, M. Yamada and C. Hamaguchi: J. Phys. Soc. Jpn 38(1975)1708; 40(1976)1778.

325. J. R. Sandercock: RCA Rev. 36(1975)89.

326. Y. Sasaki: Ph. D. Thesis (Osaka University, 1975).

327. The group-theoretical symbols used here are taken from G. F. Koster, J. O. Dimmock, R. G, Wheeler and H. Statz: *Properties of the Thirty-Two Point Groups* (MIT, Mass., 1963).

328. G. A. Akhundov, S. A. Musaev, A. E. Bakhyshev, N. M. Gasanly and L. G. Musaeva: Sov. Phys.-Semicond. 9(1975)94.

329. Y. Sasaki (private communication).

330. T. A. McMath and J. C. Irwin: Phys. Status Solidi A38(1976)731.

331. J. L. Brebner and J. A. Deverin: Helv. Phys. Acta 38(1965)650.

332. M. Grandolfo, F. Somma and P. Vecchia: Phys. Rev. B5(1972)428.

333. A. Balzarotti, M. Grandolfo, F. Somma and P. Vecchia: Phys. Status Solidi B44(1971)713.

334. S. Antoci and L. Mihich: Solid State Commun. 12(1973)649.

335. C. Hamaguchi, K. Wasa and M. Yamawaki: Sci. Repts Res. Inst. Tohoku Univ., Ser. A, Suppl. (1979).

336. Y. Suzuki, Y. Hamakawa, H. Kimura, H. Komiya and S. Ibuki: J. Phys. Chem. Solids 31(1970)2217.

337. S. G. Abdullayeva, V. A. Gadjiyev, T. G. Kerimova and E. Yu. Salayev: Nuovo Cimento B38(1977)459.

APPENDIX

CRYSTAL GROWTH: TRAVELING HEATER METHOD

A. INTRODUCTION

The most important factor in the characterization of materials is the ability to prepare structually and chemically pure crystals (i.e., both from the point of view of natural defects and foreign impurities). Single crystals of fair perfection have been grown by a variety of techniques from vapor, gaseous phase, melt and solution. Although growth from the melt is the most common technique used in crystal growth of elemental materials, this method is not readily applicable to the higher band-gap II-VI compounds. The high melting temperatures and non-insignificant pressures developed near the stoichiometric melting points are important reasons for growth from the vapor phase at considerably lower temperatures and pressures. Vapor growth, however, has its limitaions with regard to purity, crystal size and especially the time required for growing sizable crystals. Moreover, the gaseous and vapor growth should suffer from local supersaturation and local undercooling. The high-temperature melt growth should also suffer from uncontrollable temperature fluctuations. The growth of crystals from solution, in particular from metallic solution, on the other hand, is much less susceptible to such disturbances. The traveling heater method (THM) is a kind of solution growth [1], and is advantageous for the growth of large single crystals with little contamination and good crystalline perfection.

The THM has been applied to obtain high-purity semiconductors such as III-V (GaSb[2], InSb[2], GaP[3] and GaAs[4]) and II-VI compounds (CdTe[5], ZnTe[6] and ZnO[7]). This method has also been found to be advantageous for the growth of crystals of solid solutions of homogeneous composition, and has been applied to the growth of a range of solid solutions such as Ga(As,P) [8], (Ga,In)P [4], (Ga,Al)As [4], (Zn,Hg)Te [8] and Zn(Te,Se) [9]. In the course of this work, we have grown ZnTe, CdTe and (Zn,Cd)Te single crystals by the THM from tellurium solution. The methodology and growth technique are as follows.

B. CRYSTAL GROWTH OF ZnTe, CdTe AND $Zn_xCd_{1-x}Te$

(a) Phase Diagram of Zn-Te, Cd-Te and Pseudobinary ZnTe-CdTe Systems

The knowledge of the phase diagram is of importance for crystal growth especially from the melt. The phase-diagram study on Zn-Te system has been carried out by Carides and Fischer [10]. The result obtained is shown in Fig. A-1 (a). The melting point of stoichiometric ZnTe is about 1298°C. The phase diagram of the system Cd-Te has been studied by Lorenz [11]. He has obtained that solid stability reaches a maximum at 1092°C in the vicinity of the equimolar ratio, but the maximum melting point is not coincident with the stoichiometric composition. TheII-VI compounds ZnTe and CdTe form a complete series of solid solutions with cubic zincblende structure and with band-gap energies varying from 1.5 to 2.25 eV at room temperature [see Fig. 4-16]. The phase diagram of the Zn-Cd-Te ternary system has been studied by Steininger *et al.* [12] and Steininger and Strauss [13]. The ZnTe-CdTe system shows a typical lens-shaped phase diagram with sublinear variations in temperature with composition and relatively narrow liquidus-solidus gaps, as shown in Fig. A-1 (b).

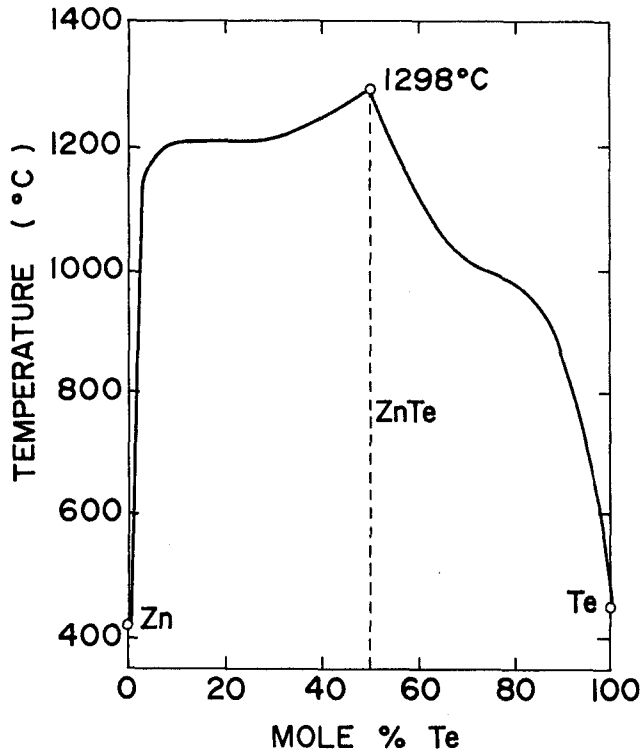

FIG. A-1 (a). Phase diagram of the system Zn-Te [10].

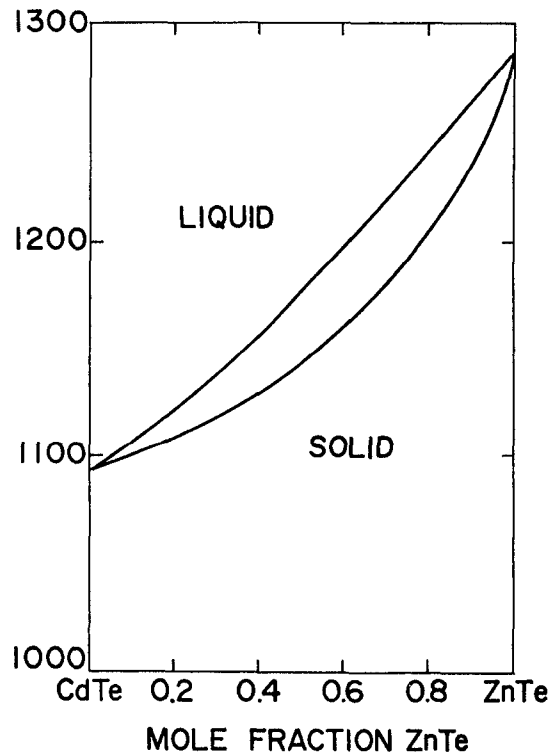

FIG. A-1 (b). Phase diagram of the CdTe-ZnTe pseudobinary system [12,13].

(b) Source Materials

The elements, Zn (6N from Cominco), Cd (6N from Osaka Asahi Metal) and Te (6N from Osaka Asahi Metal), are used in shots to limit their surface of contact with air during the manipulations. Zinc and cadmium are etched in a solution of 4 % HNO_3 in ethanol and tellurium in a dilute HCl.

(c) Synthesis of Feed Crystals

Polycrystalline ingots of ZnTe, CdTe and $Zn_xCd_{1-x}Te$ were prepared by melting the component elements in evaquated quartz tubes (Bridgman method). A 8 mm I.D. quartz tube was first cleaned with an aqueous solution of HF, graphitized by cracking of acetone vapors at 1100°C, and then baked out under $10^{-5} - 10^{-6}$ Torr for several hours at about 1000°C. The graphitized quartz ampule was filled by a charge of Zn:Te = 4:6, Cd:Te = 4.7:5.3 or (Zn_x,Cd_{1-x}):Te = 4.6:5.4 (in atomic ratio) and sealed off under 10^{-6} Torr. The temperature profile of a vertical Bridgman furnace is schematized on Fig. A-2 (a). The direct synthesis from the elements is often explosive. Therefore, the temperature was increased slowly over a 48-h period to 1180°C, held constant for 5 h, and then the ampule was slowly lowered in the steep temperature gradient of about 20 deg/cm at 2 mm/h. The ingots obtained in all preparation trials consisted of few grains of single crystals.

(d) Crystal Growth by THM

In the THM, a molten solvent zone is made to move through a solid source material by the slow movement of the charge material relative to the solution-zone heater, or *vice versa*. In this process, the dissolution of feed material occurs at the receding liquid-solid interface, and the crystallization of the dissolved feed occurs at the advancing liquid-solid interface. The schematic diagram of the THM furnace used and its temperature profile are shown in Fig. A-2 (b). A 8 mm I.D. quartz tube was cleaned with an aqueous solution of

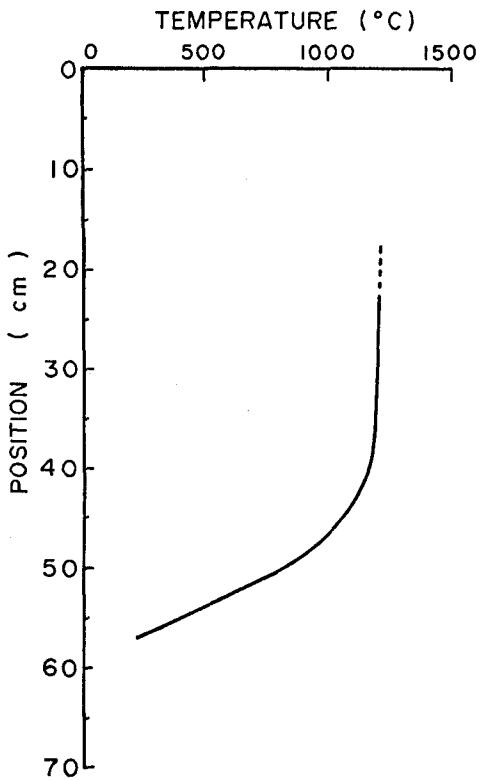

FIG. A-2 (a). Temperature profile of vertical Bridgman furnace.

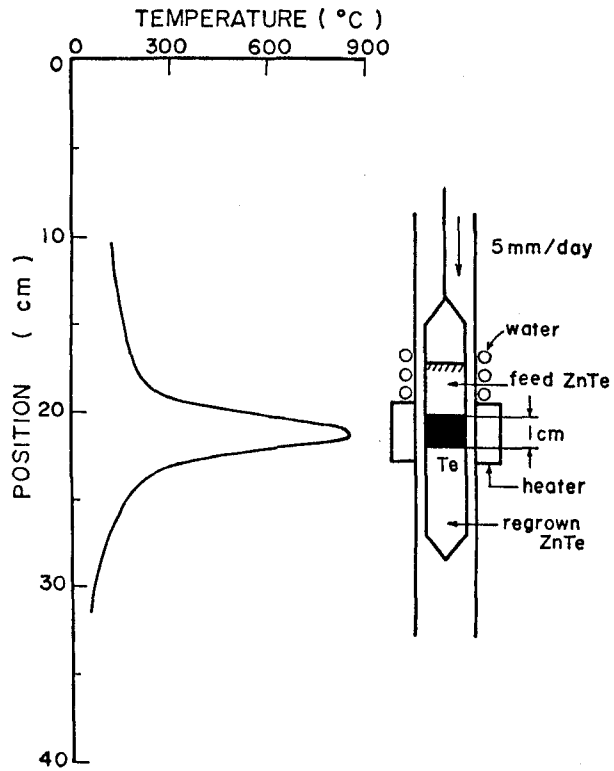

FIG. A-2 (b). Schematic diagram of the THM furnace and its temperature profile.

HF and baked our under $10^{-5} - 10^{-6}$ Torr for several hours at about 1000°C. The quartz tube contained Te ingot (solvent) [6N from Osaka Asahi Metal] and feed crystal was then sealed off under 10^{-6} Torr. The single crystals were grown by the THM with a growth rate of 5 mm/day. The maximum temperature of the THM furnace was adjusted to be 850, 700 and 700 — 850°C for the growth of ZnTe, CdTe and $Zn_xCd_{1-x}Te$, respectively. The solubilities of ZnTe and CdTe into Te solvent were about 12 and 17 mol % at these temperatures, respectively.

The material-transport mechanism in THM can be easily understood by the following expression [8]:

$$\frac{1}{f}\frac{d[A]_l}{dt} = [\ (A)_{eq0} - (A)_{eql}\ ]\cdot\frac{D}{l} \quad , \qquad \text{(A-1)}$$

where f is the cross section of ingot, $[A]_l$ is the actual concentration in solid at the receding liquid-solid interface, $(A)_{eq0}$ and $(A)_{eql}$ are the equilibrium concentrations in the solution at the advancing and receding liquid-solid interfaces, respectively, D is the diffusion constant within the solution zone, and l is the zone length. From this equation, the material transport is found to be probably due to a diffusion controlled growth, and to be very sensitive in temperature (solubility) and zone length.

We have obtained the inclusion-free, high-quality single crystals of ZnTe, CdTe and $Zn_xCd_{1-x}Te$ by the THM from tellurium solution. It has been confirmed that the THM can be taken as a useful method to grow reproducibly large crystals of II-VI compounds at low growth temperatures with low dislocation densities. The extraction effect of the tellurium solvent and low growth temperature should lead to materials of good crystalline perfection. The crystalline-imperfection effect on resonant Brillouin scattering is discussed in detail in Chapter VII.

ADDENDUM

[1] For review of THM see, G. A. Wolff and A. I. Mlavsky: *Crystal Growth, Theory and Techniques*, ed. C. H. L. Goodman (Plenum, New York, 1974) Vol. 1, p. 193.

[2] K. W. Benz and G. Müller: J. Crystal Growth 46(1979)35.

[3] J. D. Broder and G. A. Wolff: J. Electrochem. Soc. 110(1963)1150.

[4] N. Hemmat, C. B. Lamport, A. A. Menna and G. A. Wolff: *Proceedings of Materials Engrg. & Sciences Div. Biennial Conf.*, Am. Inst. Engrs., p. 112 (1970).

[5] T. Taguchi, J. Shirafuji and Y. Inuishi: Jpn. J. Appl. Phys. 17(1978) 1331.

[6] R. Triboulet and G. Didier: J. Crystal Growth 28(1975)29.

[7] G. A. Wolff and H. E. LaBelle, Jr.: J. Am. Ceram. Soc. 48(1965)441.

[8] G. A. Wolff, H. E. LaBelle, Jr. and B. N. Das: Trans. Metallurgical Soc. AIME 242(1968)436.

[9] J. Steininger and R. E. England: Trans. Metallurgical Soc. AIME 242 (1968)444.

[10] J. Carides and A. G. Fischer: Solid State Commun. 2(1964)217.

[11] M. R. Lorenz: J. Phys. Chem. Solids 23(1962)939.

[12] J. Steininger, A. J. Strauss and R. F. Brebrick: J. Electrochem. Soc. 117(1970)1305.

[13] J. Steininger and A. J. Strauss: J. Crystal Growth 13/14(1972)657.

VITA

Sadao Adachi was born in Toyama, Japan, on June 1, 1950. He received the B. S. and M. S. degrees in electrical engineering from Tokyo Electrical Engineering College, Tokyo, Japan, in 1973 and 1976, respectively. He enrolled in Osaka University, Osaka, Japan, in April 1977 and became a candidate for the degree of Doctor of Engineering in March 1980.

He is a member of the Physical Society of Japan and the Japan Society of Applied Physics.